Conceptual Design Study of the Long Baseline Neutrino Experiment (LBNE) Target and Beam Window

Final report

CJ Densham, O Caretta, TR Davenne, MD Fitton, P Loveridge, M Rooney

STFC Rutherford Appleton Laboratory
Harwell Science and Innovation Campus, DIDCOT, OX11 0QX, UK

November 2010

Contents

1. Objectives and Parameters

1.1 Introduction

This is the final report of a feasibility/design study into pion production target and beam window concepts for the proposed Long Baseline Neutrino Experiment at FNAL. The work is the result of an Accord signed in December 2009 between Fermilab and STFC Rutherford Appleton Laboratory for 'The conceptual design study of Long Baseline Neutrino Experiment (LBNE) 2 MW Target Components'.

The objectives of this study were to investigate beryllium and beryllium alloys as alternative materials to the directly water cooled graphite target that is the current LBNE baseline target technology [1]. A further objective was to study candidate materials and outline designs for a vacuum-to-air beam window for entry of the proton beam to the Target Station.

The proton beam power specified for this study was 2 or 2.3 MW at beam energies of 60 or 120 GeV respectively, the highest power envisaged for the LBNE facility. This is to ensure that the final focusing section of the proton driver and the target station infrastructure are designed to permit such an upgrade after operation and activation. However, since the initial design of the facility is for 700 kW operation, design options for this lower beam power were also considered. Each section in the report ends with a summary of findings for 700 kW operation and for 2-2.3 MW operation.

1.2 Technical Goals

The specific technical goals of the Accord are as follows:

Task A: Investigation of beryllium and AlBeMet as candidate materials for the LBNE 2 MW target considering thermal shock effects from incident proton beam with parameters shown in Table 1 (initially consider both 60 GeV and 120 GeV cases), including pulse micro-structure (bunch) effects. Initial target dimensions shall be a radius of 3 times beam sigma and length of 2 interaction lengths (about 1 meter). In addition to the ideal case of incident beam centered on the target, the case of accidental, off-centre incident proton beam (limited to 1-5 pulses) with a maximum offset of 3 times beam sigma shall be evaluated.

Task B: Investigation of time-averaged power removal (target cooling) concepts (such as water, helium, water-spray, and 2-phase water), including consideration of thermal shock effects in the cooling medium.

Task C: Conceptual design of an integrated target and horn 1 (target as inner conductor). This shall include study of magnetic field, magnetic forces and combined thermal and magnetic stresses on target/horn resulting from the horn 1 current pulse (1.0 milli-sec duration, half sine wave, 300 kA peak).

Task D: Conceptual design of a proton beam window for the same beam parameters as Task A, including time-averaged power removal, thermal stress and shock wave studies. Initial window "clear" aperture diameter shall be 50 mm. In addition to the ideal case of incident beam centered on the window, the case of accidental, off-centre incident proton beam (limited to 1-5 pulses) anywhere in the "clear" aperture area that presents the greatest threat to window survivability shall be evaluated.

1.3 Analysis Issues and Methods

The eventual aim of this study is to enable a well informed choice of target technology and parameters to be made in order to optimize the overall performance of the proposed facility. This will be optimized when the integrated neutrino flux at the far detector has been maximized over the energy range of interest. This involves consideration of both the optimum pion yield with the relevant parameters, while also achieving a sufficient target and horn lifetime that the facility can operate within a typical accelerator maintenance schedule, e.g. one major shutdown per year. Of course, the facility performance will also depend on significant target station engineering decisions which are outside the scope of this study.

The FLUKA Monte Carlo particle tracking code [2] has been used to determine heat loads and pion production for the various cases studied. A 'Figure of Merit' (FoM) for pion production described in Section 3 has been supplied by FNAL [3] in order for the pion production efficiency to be assessed. This generates a single number from a cut sum of pions weighted for higher energies leaving the surface of the target. It uses a straight transverse momentum cut and does not include any consideration of horn focusing efficiency. Note the FoM is normalized per proton and needs to be suitably scaled for beam current.

The FLUKA power deposition results permit the temperatures, static and transient thermal stresses and stress waves to be determined using the ANSYS [4] (implicit) and AUTODYN [5] (explicit) codes. Heat transfer calculations are carried out with a combination of empirical calculations and Computation Fluid Dynamics (CFD) methods using the CFX [6] code. In general, a smaller beam size and target radius is expected to give better physics performance. However from an engineering perspective a larger beam and consequently larger target radius is favoured in order to reduce the deposited power density, temperatures and thermal stresses, to reduce the radiation damage density, and for a combined target and horn to reduce the current density in the inner conductor. It may prove to be prudent to make a trade off between these factors, and tolerate a small reduction in instantaneous pion production efficiency to increase target lifetime. However, estimation of target lifetime is notoriously difficult due to a scarcity of radiation damage of materials data under the appropriate conditions, and it is likely that such a trade-off will rely as much on judgment as on analysis data.

The above issues will need to be considered before a decision can be made on whether to change the baseline target technology from graphite to beryllium or beryllium alloy. At higher beam powers, target lifetime may be expected to be dominated by radiation damage effects. Consequently it is quite possible that a different target technology may be preferred for a future 2-2.3 MW operation compared to that selected for operation at up to 0.7 MW.

1.4 Beam Parameters

The beam parameters used in the study are as shown in Table 2.1. In all cases the proton beam is assumed to have a Gaussian distribution with 'sigma' denoting one radial standard deviation.

Table 1.1 Beam Parameters

Proton Beam Energy (GeV)	Protons per Pulse	Repetition Period (sec)	Proton Beam Power (MW)	Beam sigma, radius (mm)
120	4.9e13	1.33	0.7	1.5-3.5
60	5.6e13	0.76	0.7	1.5-3.5
120	1.6e14	1.33	2.3	1.5-3.5
60	1.6e14	0.76	2	1.5-3.5
Bunch length (nano-sec)	Bunch spacing (nano-sec)	Bunches per Pulse	Protons per Bunch	Pulse length (micro-sec)
2-5	18.8	519	3.1e11	9.78

1.5 Target dimensions

At this stage in the project, a simplistic idealised target rod geometry has been considered in Tasks A – C to enable a generic study of all the phenomena identified. Pure beryllium and AlBeMet alloy target rods with the following dimensions have been considered, scaled from the range of beam size:

Rod length = 1 m (c. 2 interaction lengths)

Rod radius = 4.5 mm - 10.5 mm

1.6 Horn parameters

The horn geometry is described in document 'Specifications for Beam Simulations' Version 5, 24 May 2010 by Bob Zwaska [3]:

In this document version the horn inner conductor radius has been increased from that in an earlier version to:

Inner Conductor Radius = 20 mm (z = 0 – 1 m)

Thickness = 3 mm (z = 0 – 1 m)

Peak current = 300 kA

Current pulse length = 1.0 ms, half sine wave

1.7 Assumptions and issues for tasks

Task A (Separate target and horn, Section 3)

For the generic separate target and horn studies, several different Boundary Conditions were considered for the target supports. It is assumed that the target is supported separately from the horn upstream but that it may be possible to support the end of the target at the downstream end from the horn bore.

The horn inner conductor radius has had limited effect on this task since the study has not considered the target and horn integration in any great detail. It does however set a safety margin for target vibrations generated by an off-centre beam causing an interference with the horn.

Task B (Target Cooling, Section 4)

The horn inner conductor radius gives some flexibility to the target cooling task. For the largest target radius of 10.5 mm, there is a 9.5 mm radial space available for cooling. This space permits in principle both single pass and co-axial flow-and-return cooling, by the cooling media of water, helium or air. Water spray cooling is also considered, which would only be appropriate for Task C.

Task C (Combined Target and Horn Inner Conductor, Section 5)

In this case the target and inner horn radius are set to be equal. However this means that neither can be separately optimised. Since as already mentioned the FoM does not make any allowance for horn focusing issues, a further study would be necessary to compare the overall physics performance of the combined target and horn with that of the separate components.

Task D (Beam Window, Section 6)

The beam window is required to separate the proton beamline vacuum from the Target Station at atmospheric pressure. It must withstand the same proton beam loading issues as Task A, but in addition it must also safely withstand the pressure load. The range of potential materials includes any suitable metal or alloy that meets these requirements.

Potential cooling methods include, in order of preference: natural convection (single skin), natural convection in combination with radial conduction to an outer water cooling channel (single skin), and transverse helium cooling (double skin).

It is assumed that the window would need to be easily replaceable, for example by using inflatable pillow seals of the type invented by PSI, subsequently developed by the KEK Muon Group and reproduced to a RAL specification for the T2K project [7].

1.8 Additional Assumptions and Issues

It is assumed that there is a preference at Fermilab for the target station and pion decay tunnel to be filled with dry air at atmospheric pressure. For a design with the target separate from the horn it should be possible to replace failed targets either within the target station itself, or by lifting the complete target and horn assembly into a Hot Cell where target replacement can take place. Where the target is integral with the horn, it may be necessary to replace the complete horn assembly, although a design where the target and inner conductor could be replaced as a separate unit would be very desirable.

1.9 Material properties

The study uses material properties for pure beryllium obtained for Brush Wellman's S-65 grade [8], as quoted in the ITER Material Properties Handbook [9]. These values are less conservative than the minimum material properties quoted by Brush Wellman. S-65 is a premium structural grade that is used as the reference grade for ITER due to it's resistance to cracking under high heat flux thermal cycling. This makes it an excellent candidate for both the LBNE target and beam window.

Material properties for AlBeMet are obtained from Brush Wellman [10] and for Ti-6Al-4V from US standards [11,12]

Design stress

All target designs are assessed on the basis of a design stress limit that is equal to the Yield Stress/1.5, ie a Safety Factor of 1.5 on the yield stress at 100°C. This criterion was specified by Fermilab for this study.

The beam window uses the design stress limit for beam windows specified by Fermilab [13] which is half the ultimate tensile stress.

Table 2.2 Design stress values used in this study (at a reference temperature of 100°C)

		Aluminium alloy 6082 [15]	Beryllium [14]	AlBeMet 162 [10]	Ti-6Al-4V [12]
Target design stress = σy/1.5	(MPa)	167	167	184	-
Window design stress = UTS/2	(MPa)	-	214	-	475

It can be seen that there is an anachronism with the design stress used for the beam window being significantly larger than that used for the target. This is compounded by the fact that the consequences of a beam window failure are more significant than the mechanical failure of a target. Note that any change to such criteria would not affect the results of the studies, but could change conclusions in terms of acceptable stress levels.

Regarding the yield stress criterion used for the target studies, there are two interesting effects that occur at the yield point which may allow the design of targets with stress levels above the 'static' yield point. These effects include the yield stress reported as being increased by 25 – 40% at strain rates greater than 100 s^{-1} [16,17] and the shakedown effect that applies a pre-tension to material that has undergone a compressive yield. Detailed consideration of these effects is beyond the scope of this report.

Temperature independent material properties were used for benchmarking purposes, using properties shown in Table 2.3

Table 2.3 Material properties assumed constant with temperature (23°C)

		Aluminium	Beryllium	AlBeMet	Ti-6Al-4V
Density	(kg/m^3)	2700	1821	2100	4430
Elastic Modulus	(GPa)	69	309	193	113.8
Poisson Ratio	(-)	0.33	0.07	0.17	0.342
Linear Expansion	(/K)	23×10^{-6}	11.5×10^{-6}	13.9×10^{-6}	9×10^{-6}
Heat Capacity	(J/kg.K)	900	1829	1560	526
Thermal Conductivity	(W/m.K)	210	183	210	6.7

For simulations using codes, temperature dependent material properties were used where possible. Those used for beryllium are shown in Figure 2.1.
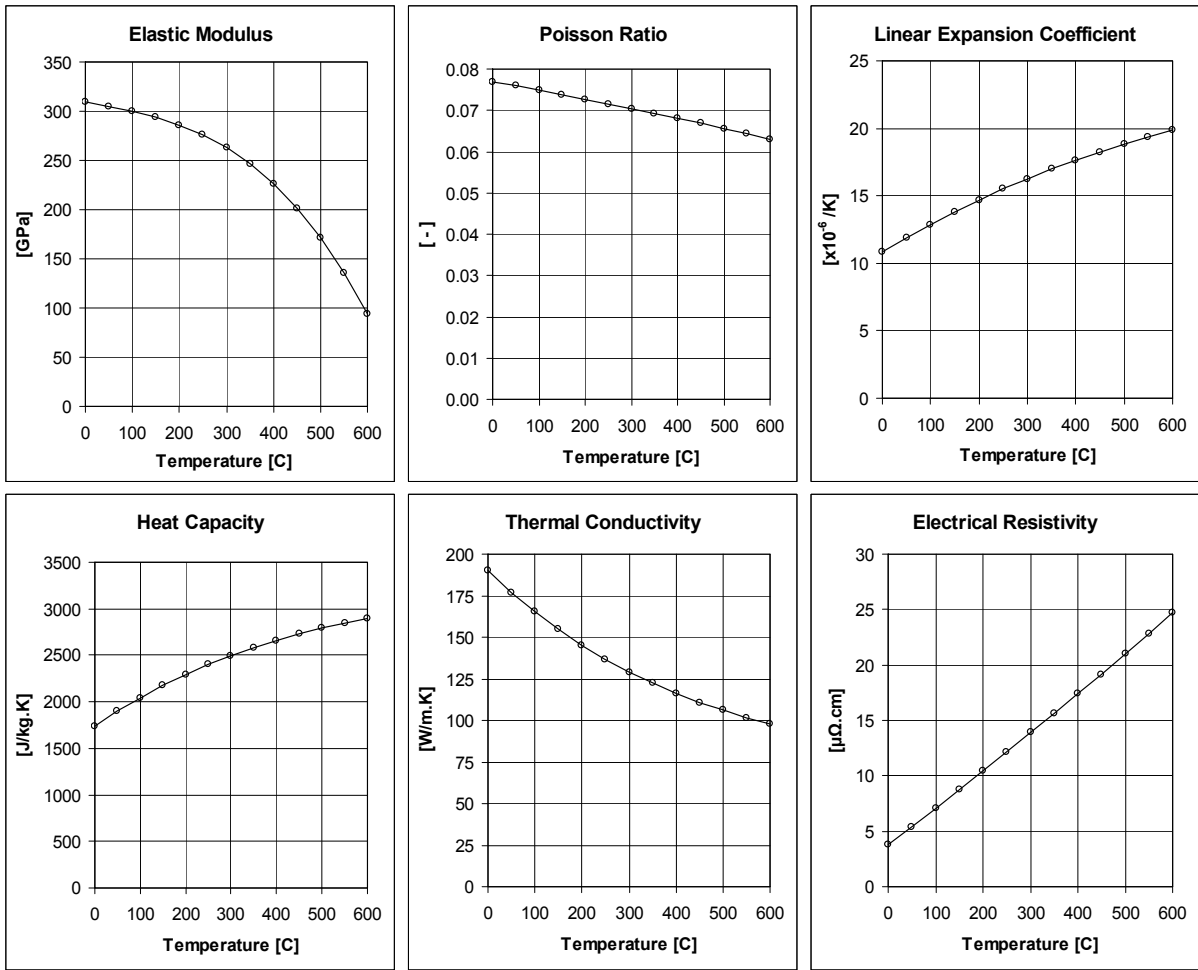
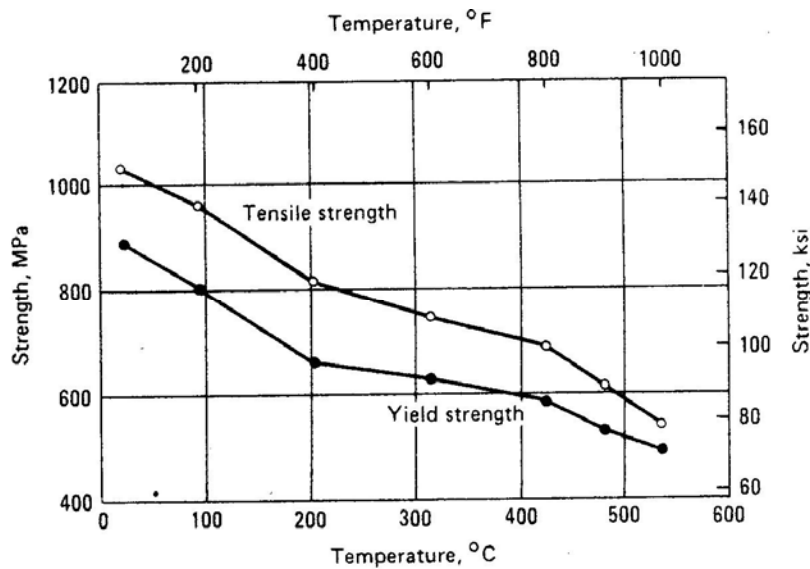*Figure 2.1 Temperature dependent material properties of beryllium [9]*

Figure 2.1 Mechanical strength of Ti-6Al-4V as a function of temperature [12]

1.10 Materials joining

The Welding Institute [18] has been briefly consulted with regard to joining beryllium to aluminium and aluminium alloys. This would be desired for the combined target and horn inner conductor option in order to minimise the use of beryllium. Initial suggestions are that at least two methods appear to be potential candidates, both of which would avoid vaporising beryllium during the bonding process. A general recommendation is to avoid joining beryllium directly to aluminium alloys, as this would increase the possibility of forming a brittle intermetallic compound at the interface. The suggested technique would involve using an intermediate pure aluminium layer between the beryllium and aluminium alloy material.

One technique would be conventional friction welding, a type of solid state forming. In this process both materials are plastically deformed to form the joint, rather than melted. It would however generate significant distortion and would require post machining.

Another, potentially more attractive technique is diffusion bonding. A suitable combination of temperature, pressure and time could form a strong joint with little if any distortion, meaning that little or no post machining would be required. The bonding process would need to take place in vacuum and so would need a large vacuum furnace and press. Due to the large loads and high temperatures required to create the bond, careful design of the joint and the joining process would be necessary.

1.11 References

1. V. Garkusha, A. Mikheyev, I. Ponimash, A. Ryabov,T. Ryabova, F. Novoskoltsev and V. Zarucheisky, *Design Study of the NuMI Target for 2 MW Upgrades*, Institute for High Energy Physics, State Research Centre of Russia, Protvino, Moscow region, Russia.

2. A. Fasso, A. Ferrari, J. Ranft, and P.R. Sala, *FLUKA: a multi-particle transport code,* CERN-2005-10 (2005), INFN/TC_05/11, SLAC-R-773.

3. B. Zwaska, *Specifications for Beam Simulations*, Version 5, 24 May 2010.
   http://lbne-docdb.fnal.gov:8080/cgi-bin/RetrieveFile?docid=161&version=5&filename=Beam_Spec_v5.pdf

4. ANSYS® Multiphysics, Release 11.0, ANSYS, Inc.

5. ANSYS® AUTODYN, Release 11.0, ANSYS, Inc.

6. ANSYS® CFX, Release 12.1, ANSYS, Inc.

7. M. Rooney, *The Current T2K Beam Window Design and Upgrade Potential*. Presentation to the Oxford-Princeton Targetry Workshop, Princeton, USA, 2008.
   www.physics.princeton.edu/mumu/target/Rooney/rooney_110608.pdf

8. *Designing with Beryllium*, Brush Wellman Engineered Materials.
   http://www.berylliumproducts.com/documents/mb-001.pdf [Accessed November 2010]

9. ITER Material Properties Handbook, 1997.
   http://fusionnet.seas.ucla.edu/fusionnetwork

10. Brush Wellman Inc. Beryllium Products.
   www.berylliumproducts.com [Accessed November 2010]

11. *Metallic Materials Properties Development and Standardization Handbook.* US Department of Transport, Office of Aviation Research, Washington, D.C., 2003.

12. *Metals handbook, Volume 2, Properties and selection: nonferrous alloys and pure metals*, American Society for Metals, Ninth edition.

13. FESHM Chapter 5033.1 – *Vacuum Window Safety*, Fermilab safety document, 2004.

14. MF Smith, RD Watson, JB Whitley and JM McDonald, *Thermomechanical Testing of Beryllium for Limiters in ISX-B and JET*, Fusion Technology 8(1) (1985) 1174.

15. *Aluminium and aluminium alloys, Extruded rod/bar, tube and profiles*, BS EN 755-2:2008, Part 2: Mechanical properties.

16. T. Nicholas, et al., *Mechanical Properties of Structural Grades of Beryllium at High Strain Rates*, AFML-TR-76-168, Air Force Materials Laboratory, Wright Patterson Air Force Base, Ohio, 1976.

17. F.L. Schierloh and S.G Babcock, *Tensile Properties of Beryllium at High Strain Rates and Temperatures*, AFML-TR-69-273, General Motors Tech Center, 1969.

18. TWI Ltd, Granta Park, Great Abington, Cambridge, CB21 6AL, UK.

2. Fluka MonteCarlo simulations

2.1 Introduction

FLUKA [1] is a fully integrated particle physics MonteCarlo simulation package that is used in this study to investigate the performance of a target in terms of (i) the power deposition and (ii) the yield of pions within an energy and transverse momentum range of interest. The power deposition (or rather, the energy deposited per pulse) is the input required to evaluate the temperatures and thermal stresses generated in a target as a result of the beam interaction. The FLUKA results for energy deposition covering the complete target parameter space as defined in Task A are given in a set of three tables, one for each of the materials considered. A benchmark simulation for a single case showed good agreement for the energy deposition between FLUKA and MARS [2] with the FLUKA integrated energy deposition being 97% of the MARS value. The FLUKA particle tracking code was also used to compare the 'useful' pion production performance of the different target parameters by generating a single Figure of Merit (FoM). In addition to the overall Figure of Merit, pion yield as a function of position in a cylindrical target rod was investigated by dividing the target into radial and longitudinal bins. The evaluation of the FoM for different target parameters leads to a discussion of the pro and cons of various design options in terms of the pion yield.

2.2 Energy Deposition

Energy Deposition in the target and beam window has been calculated for beryllium, AlBeMet and aluminium targets with beam sigmas of 1.5 mm and 3.5 mm and with the two energy levels 120 and 60 GeV. Figure 2.1 shows a typical contour plot of energy deposition as a function of radius, r, and axial position, z, in a circular cross section cylindrical target. A summary of the peak and integral energy depositions in the target are shown in table 2.1.
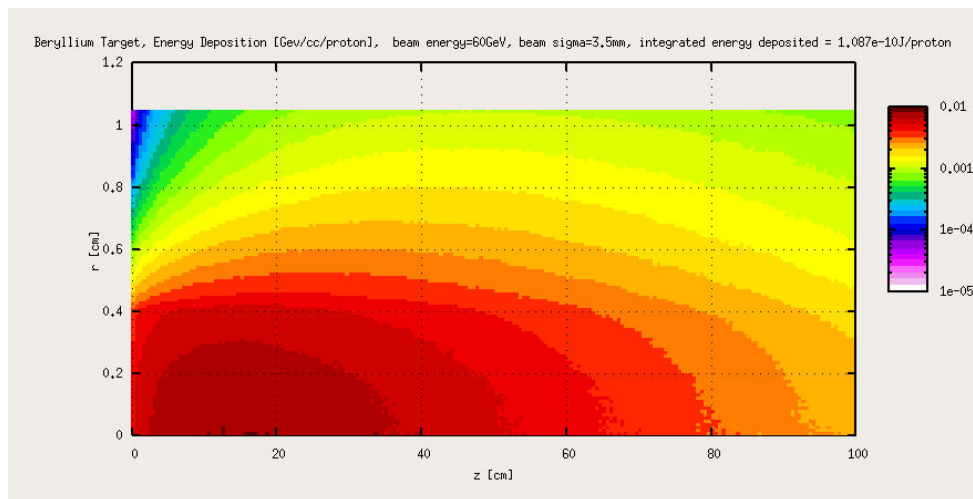

Figure 2.1 Energy deposition in beryllium target (GeV/cc/proton) with 60 GeV 3.5mm sigma proton beam, Integrated energy deposition=16.9kJ/spill

Magnetic Field

A magnetic field can be described in a Fortran subroutine which is called by the main FLUKA program. This enables the user to define a magnetic field in 3D space and then observe the effect of the field on particle yields and energy deposition. As a check to verify that the correct field has been programmed the trajectory of an electron entering a uniform field has been modelled and compared to an analytical solution (Appendix 2.1). It was found that a simple but representative magnetic field as described in Section 5 has a significant effect on the heat deposited in a target compared with modelling the target with no magnetic field, as demonstrated by comparing Figures 2.1 and 2.2. An increase of 10 to 20% was found mainly as a result of charged particles that have left the target surface being focused to re-enter the target further downstream. Also note that the peak energy deposition is more spread out longitudinally and is moved further down from the front end of the target. The magnetic field for this simple case is a function of radius as calculated in Section 5 and is shown in Figure 2.3. For simplicity the magnetic field is not included in any of the following analysis in the report, however if a detailed design is to be developed then it is recommended that detailed magnetic field maps be generated so that the effect of magnetic field on the heat deposition can be considered.
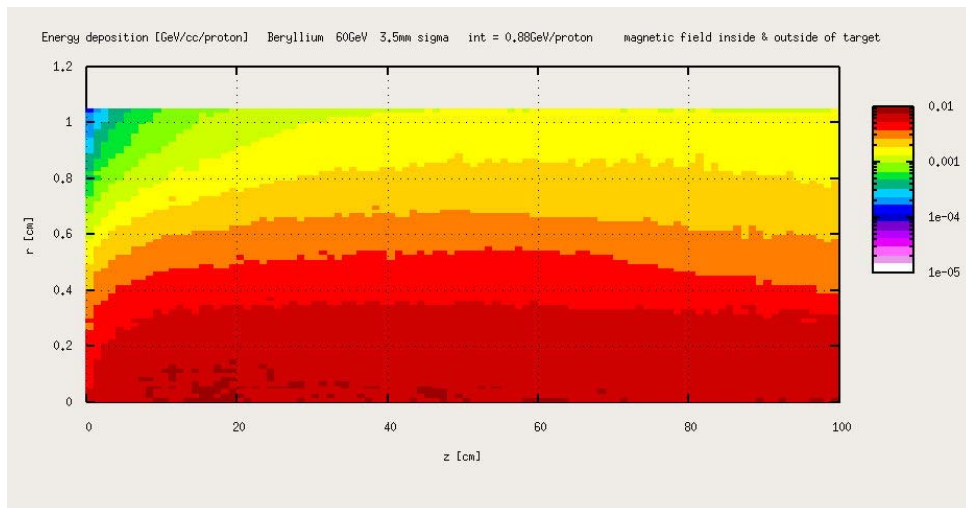

Figure 2.2 Energy deposition in Beryllium target (GeV/cc/proton) with 60 GeV 3.5mm proton beam sigma with magnetic field, Integrated energy deposition=22.6kJ/spill
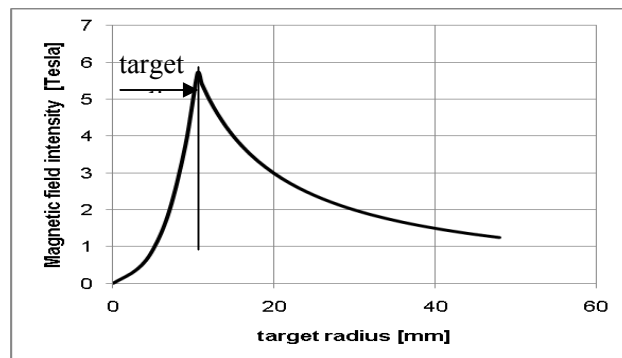

Figure 2.3 Magnetic field as a function of radius

Table 2.1 Beam heating parameter study results

Beryllium

Beam Energy (GeV)	Beam Power (MW)	Beam Sigma (mm)	Deposited Energy (kJ/spill)	Time Averaged Power (kW)	Peak Energy Density (J/cc/spill)	Max. ΔT per spill (K)
120	0.7	1.5	4.2	3.2	254	76
		3.5	9.2	6.9	74	22
60	0.7	1.5	2.9	3.8	243	73
		3.5	5.8	7.7	61	18
120	2.3	1.5	14.0	10.5	846	254
		3.5	30.7	23.1	245	74
60	2	1.5	8.4	11.1	707	212
		3.5	17.0	22.3	176	53

Aluminium

Beam Energy (GeV)	Beam Power (MW)	Beam Sigma (mm)	Deposited Energy (kJ/spill)	Time Averaged Power (kW)	Peak Energy Density (J/cc/spill)	Max. ΔT per spill (K)
120	0.7	1.5	12.2	9.2	537	221
		3.5	35.1	26.4	269	110
60	0.7	1.5	6.3	8.3	472	190
		3.5	16.6	21.8	155	60
120	2.3	1.5	40.8	30.7	1789	736
		3.5	117.1	88.1	898	365
60	2	1.5	18.2	24.0	1374	551
		3.5	48.2	63.4	451	175

AlBeMET

Beam Energy (GeV)	Beam Power (MW)	Beam Sigma (mm)	Deposited Energy (kJ/spill)	Time Averaged Power (kW)	Peak Energy Density (J/cc/spill)	Max. ΔT per spill (K)
120	0.7	1.5	6.2	4.7	321	98
		3.5	15.7	11.8	108	33
60	0.7	1.5	3.8	5.0	299	91
		3.5	8.6	11.3	77	23
120	2.3	1.5	20.6	15.5	1069	326
		3.5	52.5	39.5	359	110
60	2	1.5	11.0	14.5	869	265
		3.5	25.0	32.8	223	68

Primaries and bins

FLUKA is used to track the trajectory of a large number of primary protons entering a target and the ensuing secondary particles as they either pass through the target or are stopped by the target. The user controls how many primary particles are tracked and how the target is split into a series of 'results bins'. Each bin has a certain number of particle interactions and will thus have an energy deposition associated with those interactions. The number of primary particles is really limited by the computing time required. If the bin sizes are too small then the results are likely to be artificially noisy due to inadequate numbers of interactions in the small bins. If the bin sizes are too big then details such as peak energy deposition may be lost or smoothed out. The choice of the number of bins and number of particles is a balance as illustrated in Figure 2.4. To obtain the FLUKA results that follow five computational cycles were completed, each with at least 500000 primaries. The results from each cycle are combined and averaged.
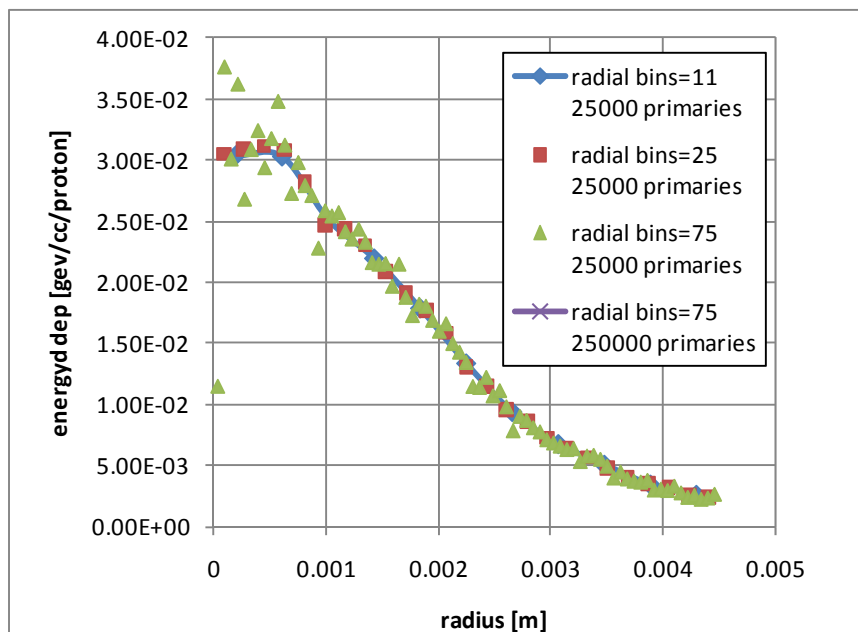

Figure 2.4 Energy deposition at z=200mm as a function of radius for different numbers of radial bins and primary particles. Beryllium target with1.5 mm beam sigma 60 GeV

Deltaray Threshold

The default deltaray production threshold in FLUKA is 1 MeV. This means that fast moving electrons caused by secondary ionisation that have energies below 1MeV will deposit their energy where they are generated and will not be tracked so as to save computational effort. If they have an energy above the 1 MeV threshold then they can potentially escape the target and take their energy with them. In the case of energy deposition in a thin beam window or wire then the selection of the deltaray threshold can be an important consideration [3]. In a thin target a significant proportion of the electrons produced by secondary ionisation can be close enough to the surface to escape and take their energy out of the target. The effect of deltaray threshold on energy deposition in a thin (0.2 mm) beryllium window has been investigated and it was found to have a fairly small effect. Although significant numbers of electrons below 1MeV do leave the window they do not have much energy and so only make a small contribution to the energy deposition. More details of this study can be found in Appendix 2.2.

2.3 Figure of Merit

The purpose of the Figure of Merit (FoM) is to generate a single, simple parameter to characterize the pion yield as part of the target design optimization process. Different target designs can be compared in terms of the useful pion yield obtained. The FoM was devised in a private note by Zwaska (appendix 2.3) and is based on the following:

- Pions leaving the target with a kinetic energy between 1.5 and 12 GeV are included
- Pions leaving the target with a transverse momentum less than 0.4 GeV/c are included
- The FoM weights pion energy with a power of 2.5, since higher energy pions have a greater probability of producing a useful neutrino interaction in the downstream detectors. This compensates for the overabundance of low energy pions which have a small probability of producing neutrino interations in the detectors.

Excluded from the Figure of Merit is consideration of a variable focusing efficiency along the length of the target, ie it is assumed that all pions leaving the target surface within the transverse momentum cut are within the depth of field of the horn focusing elements. This issue is partially addressed by evaluating high and low energy pion production along the target length. A complete study should convolute the pion production with the horn focusing, nevertheless the FoM is a valuable tool in this target design study.

The FoM is calculated using FLUKA to obtain the yield of pions of both signs emerging from the target surface. The specific output taken from FLUKA is the plain double differential yield of pions of both signs with respect to the kinetic energy and the transverse momentum of the pions, i.e.

$$\frac{\partial^2 N}{\partial E \partial p}$$

where,

- N = number of pions of both signs emerging from the target per primary particle on target
- E = kinetic energy of the pions [GeV]
- p = transverse momentum of the pions [GeV/c]

We can then obtain the yield of pions per incident proton on target as a function of energy and transverse momentum. To do this a simple numerical integration of the double differential yield is carried out between the following limits :

- kinetic energy from 1.5 GeV to 12 GeV with 21 discrete intervals of width 0.5 GeV
- transverse momentum between 0 and 0.4 GeV/c with a single interval

Figure 3.2.1 shows the resulting pion yield in histogram form. A weighting factor is then calculated for each of the 21 energy intervals which is equal to the energy at the centre of the interval raised to the power 2.5. The energy at the centre of each interval is given by :

$$Ecen = \left(\frac{Emin + Emax}{2}\right)$$

where for example for the first interval Emin=1.5 GeV and Emax=2 GeV. The FoM is calculated as the summation of the yield in each energy interval multiplied by the corresponding weighting factor for that interval expressed mathematically as follows.

$$FoM = \sum_{n=1}^{21} (Ecen_n)^{2.5} \int_{Emin_n}^{Emax_n} \int_0^{\Delta p} \frac{\partial^2 N}{\partial E \partial p} \partial p \partial E$$

Figure 2.5. indicates that the majority of the pions from the target are towards the lower end of the energy range of interest. By integrating over 30 intervals in transverse momentum from 0 GeV/c to 1.5 GeV/c for three different energy levels the yield as a function of transverse momentum is obtained (Figure 2.6).
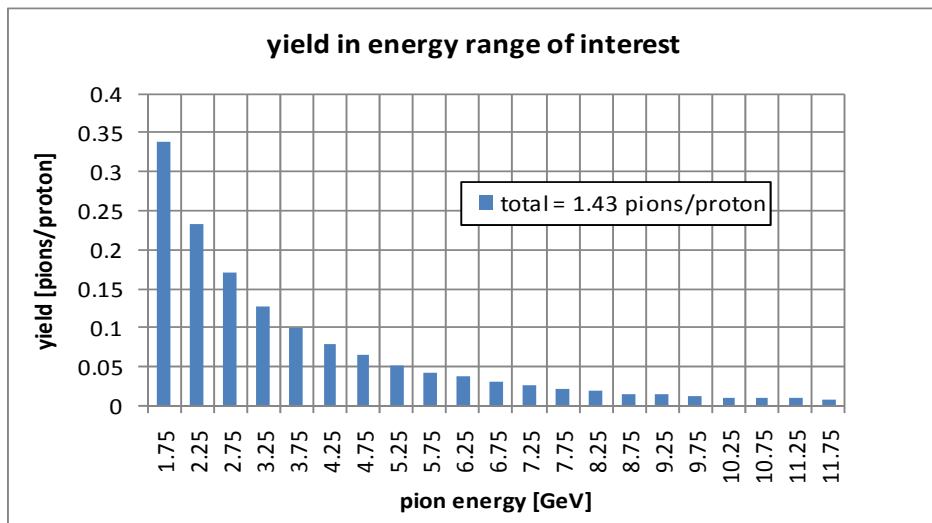
Figure 2.5 Pion yield histogram as a function of kinetic energy. Beryllium target with 60 GeV 1.5 mm beam sigma
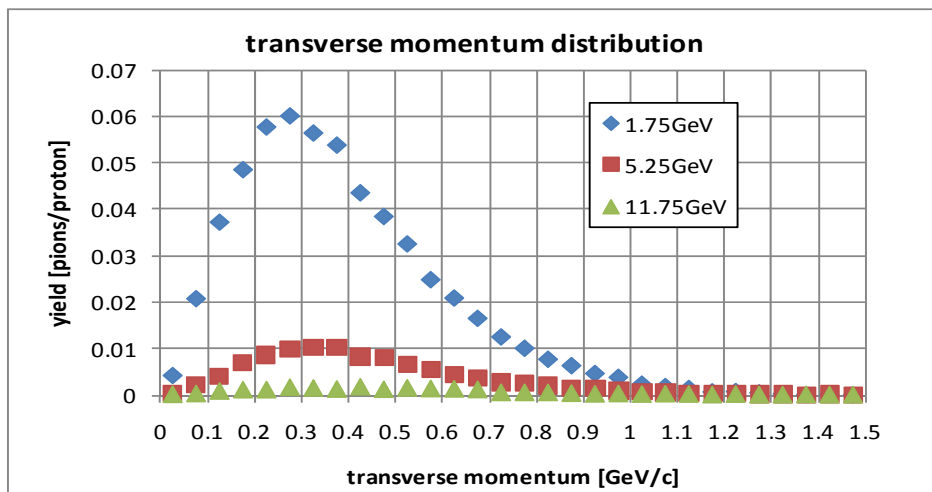

Figure 2.6 Transverse momentum of the pions with kinetic energy between 1.5 GeV and 12 GeV. Beryllium target with 60 GeV 1.5 mm beam sigma

The pion production varies throughout the volume of the target. In order to investigate the yield from different parts of the target the cylindrical target has been subdivided into both longitudinal and radial bins. For the longitudinal segmentation, the target is divided into ten bins of length 100 mm. Each one is named from tl1 to tl10 where tl1 is the first longitudinal segment that goes from 0 mm to 100 mm as shown in Figure 2.7. For the radial segmentation there are nine cylinders, the first has a circular cross section with radius 0.5 mm and then the next eight all have annular cross sections of width 0.5 mm as shown in figure 2.7. The number of pions passing from each segment to the surrounding vacuum and the number of pions passing from one segment to the following segment can be determined from the FLUKA output.

The effective pion production in each segment is calculated using the following relation:

pion production by segment = pions leaving segment – pions entering segment

We consider just pions that have an energy between 1.5 GeV and 12 GeV and a transverse momentum less than 0.4 GeV/c for the case of a 60 GeV proton beam with a 1.5 mm beam sigma.
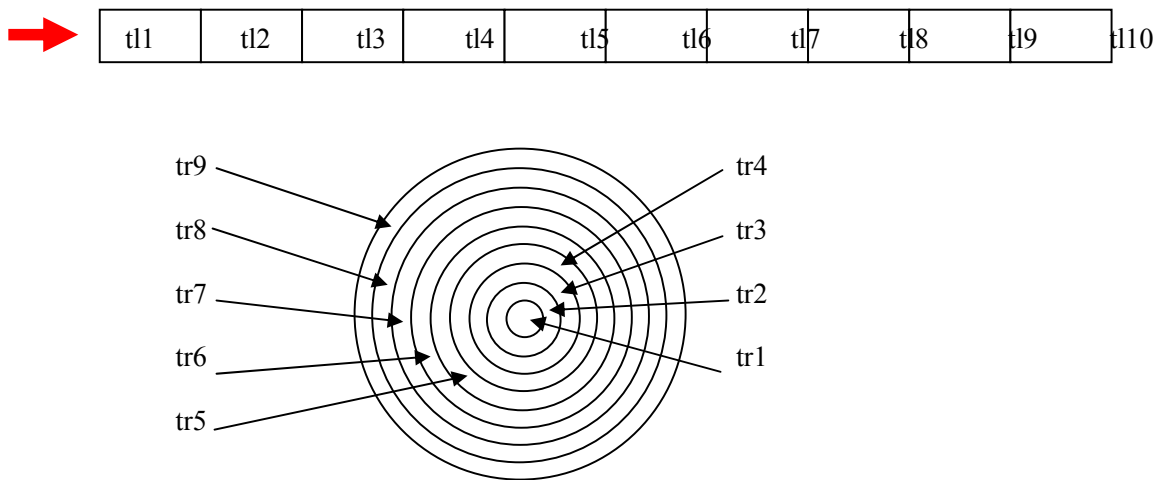
proton beam

Figure 2.7 Illustration of segmentation of the target

The longitudinal segmentation shows that pion production is biased towards the front end of the target with it gradually reducing towards the end of the target (figure 2.8). As the higher energy pions have more value it may be worth considering where pions of different energies emerge from the target. Figure 2.9 shows that there is a general trend for both low and high energy pions to be produced towards the front end of the target. The one exception is that the last segment, tl10, produces considerably more high energy pions than the preceding segments, this is due to higher energy low transverse momentum pions emerging from the end face of the target. The radial segmentation study indicates that pion production increases with radius but falls off towards the last radial segment, tr9 (Figure 2.10). The outer annular ring has an inner radius of 2.66xsigma and an outer radius of 3xsigma so only the protons in the tail of the Gaussian beam spot will land on the outer annular segment. Due to the relatively small number of protons on the outer annular segment there will correspondingly be less primary particle interaction. Figure 2.11. shows the yield from the same target with a rectangular profile beam instead of a Gaussian, with the radius of the rectangular profile equal to the radius of the target. The production does not reduce towards the surface of the target in the same way as the Gaussian beam because with the uniformly distributed rectangular beam there are still significant primary interactions taking place in the outer radial segments. However the number of pions leaving the outer radial segment and entering the vacuum is significantly lower with the rectangular beam, this is mainly due to the evenly distributed beam arising in less secondary interactions being captured. These are clearly important for the total pion production and FoM.
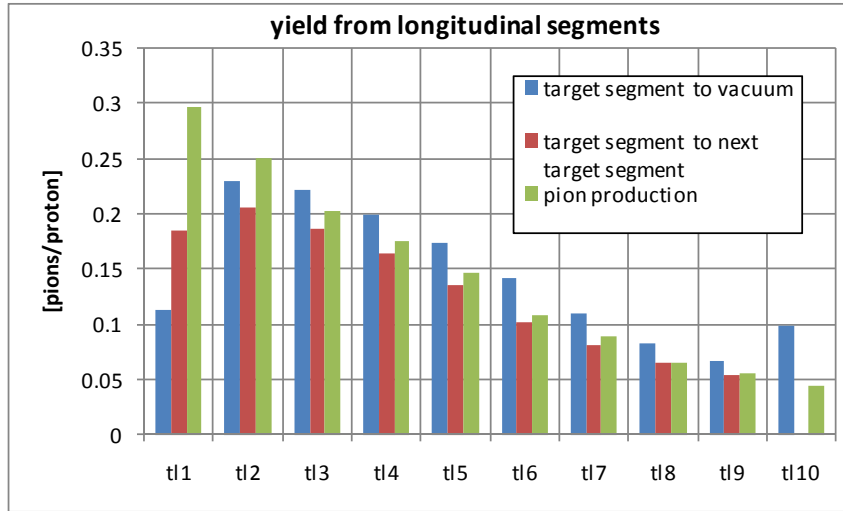
Figure 2.8 Longitudinal segmentation, location of pion production, beryllium target, 1.5 mm beam sigma, 60 GeV. Pions travelling back from a downstream segment to an upstream segment are ignored
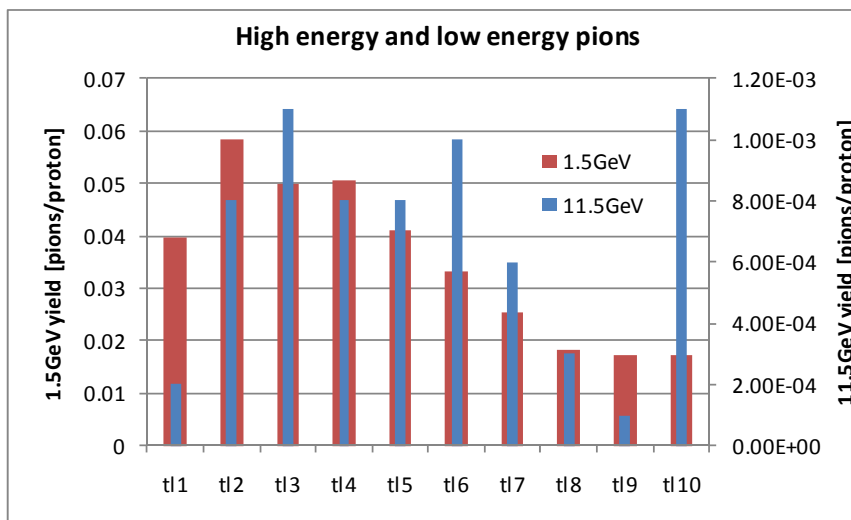

Figure 2.9 Longitudinal segmentation, location of emergence of low and high energy pions, beryllium target, 1.5 mm beam sigma, 60 GeV
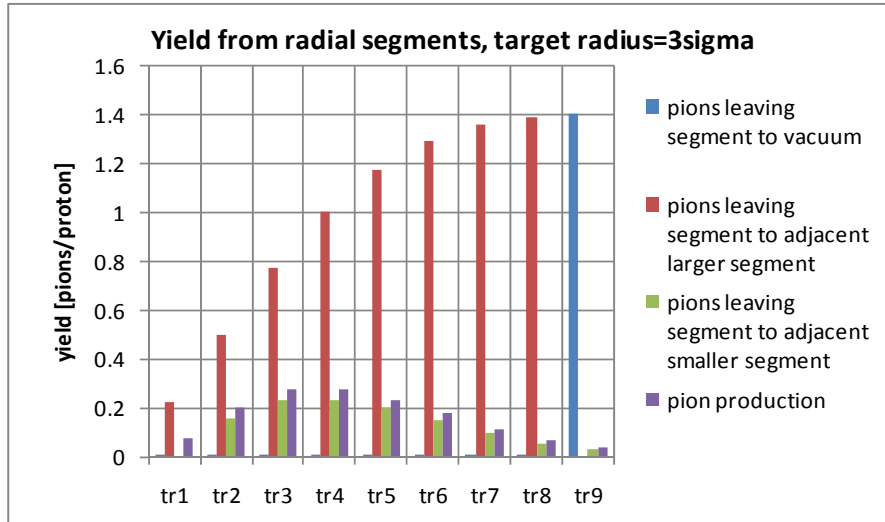
Figure 2.10 Radial segmentation, location of pion production, beryllium target, 1.5 mm beam sigma, 60 GeV, pions travelling from inner to outer and outer to inner rings are included
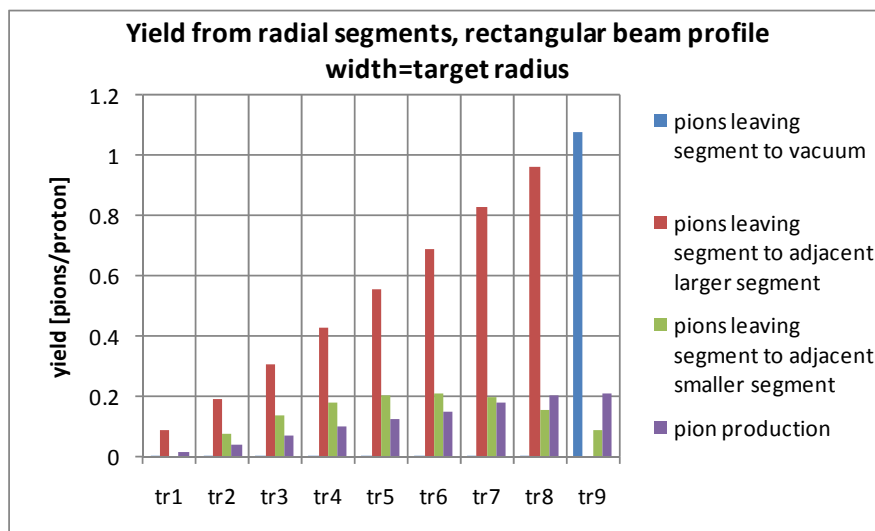

Figure 2.11 Radial segmentation, location of pion production, beryllium target, rectangular beam, beam radius=target radius, 60 GeV, pions travelling from inner to outer and outer to inner rings are included

The presence of the magnetic field in and outside of the target has a small effect on the FoM of the order of a few percent. However the FoM as defined above does not evaluate the effectiveness of the field as the field mainly focuses pions that have left the target. The FoM only considers pions leaving the target in to the vacuum. In order to evaluate the effectiveness of the magnetic field at focusing pions then the effect of the field on the pions once they have left the target needs to be incorporated into the FoM. A simple way to do this would be to evaluate the FoM at a detector positioned downstream of the target. Pions will only reach this downstream detector if they are efficiently focused by the magnetic field and so then the FoM would be a measure of both target yield and horn effectiveness. This would give significant extra scope above the current FoM for optimising designs.

2.4 Figure of Merit design indications

Three different target materials, (beryllium, AlBeMet and aluminium) have been considered for the target, as well as two different beam sigma values and two beam kinetic energy values. Figure 2.12. shows the FoM as a function of these fundamental design parameters. The first point to note is that beryllium gives the highest pion yield and aluminium the lowest. Although a fairly small difference it is more significant at lower beam energy. The small beam sigma at 1.5 mm is clearly favourable over the larger 3.5 mm beam sigma in terms of the FoM. For the high energy 120 GeV case the FoM is 17% higher with the small beam sigma. For the low energy 60 GeV case the FoM is 19% higher with the small beam sigma. Also to note from Figure 2.12 is the FoM for the 60 GeV case is very approximately half of the FoM for the 120 GeV case. This is because the FoM has units of pions/primary*GeV^2.5. To normalise for beam power, the FoM for 60 GeV should be multiplied by two for comparison with the 120 GeV result, although it is understood this is not a realistic option for the LBNE proton driver. Figure 2.13 shows the FoM for 120 GeV together with 2xFoM for 60 GeV. The result indicates that for a given beam power 120 GeV gives a better performance than 60 GeV for all materials especially aluminium and for both values of beam sigma. The weighting function in the FOM puts a lot more importance on the higher energy pions emerging from the target and so the higher energy beam is favoured here because it produces more higher energy pions.
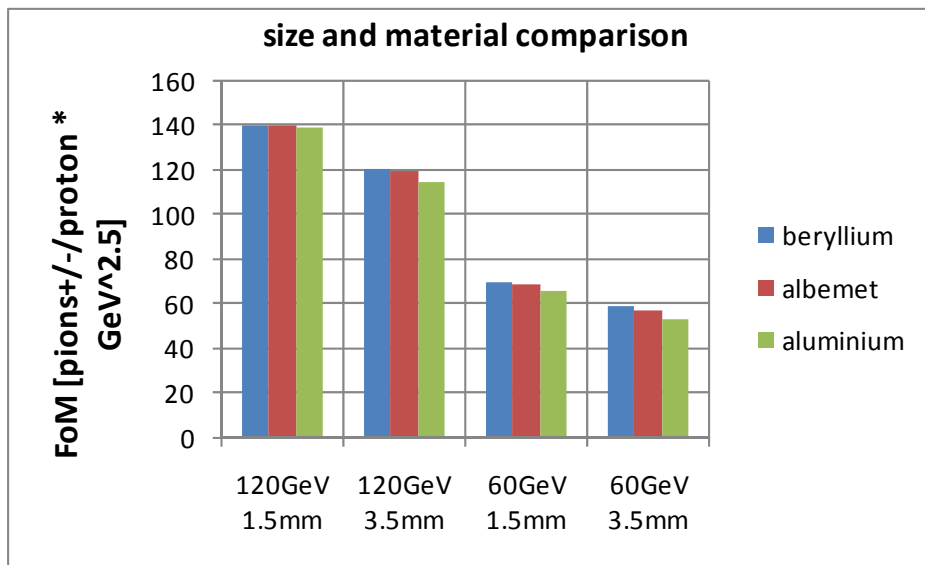

Figure 2.12 Figure of Merit comparison for material, target size and beam energy.
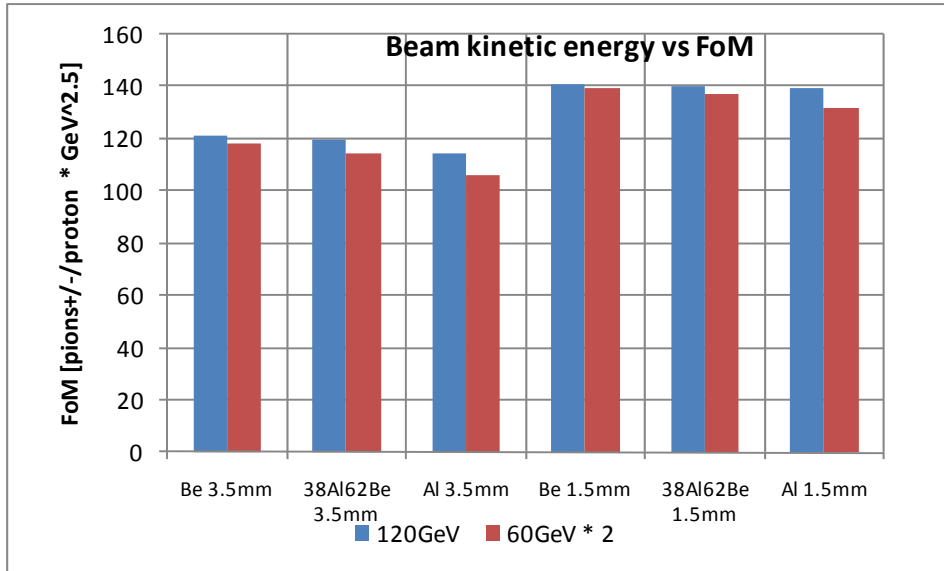
Figure 2.13 Figure of Merit comparison for beam kinetic energy, normalized for beam power

The effect on pion yield of a parallel off centre beam has been evaluated for the small and large beryllium targets. Figure 2.14 shows how the FoM decays as the beam moves off centre. The small target has a sharper drop-off in yield as the deviation off-centre increases. This is because more of the beam misses the target for a given amount of deviation off centre. The performance of the large target would thus be less sensitive to the beam being off centre.
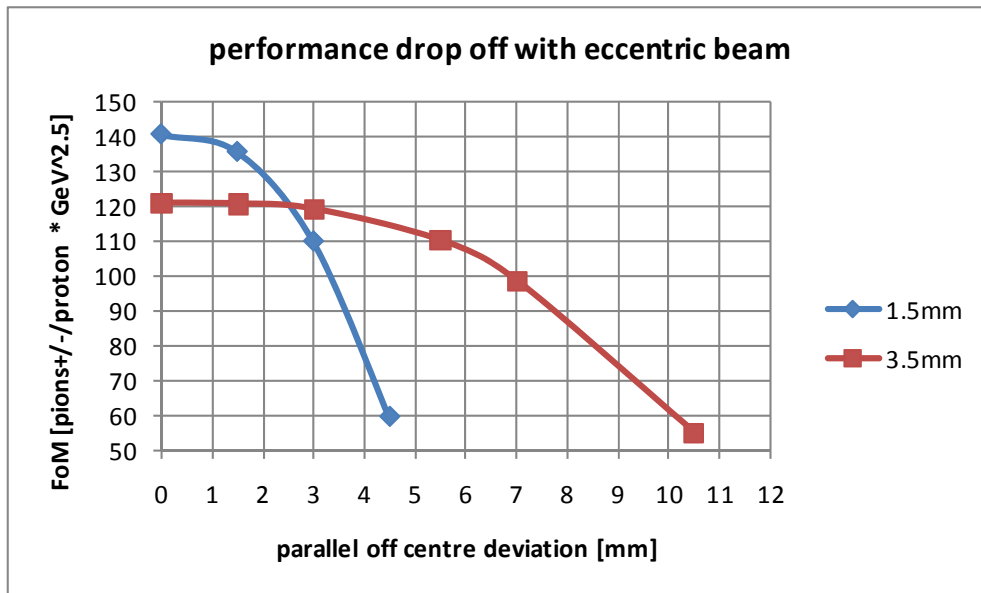

Figure 2.14 FoM variation as a result of beam off centre for 3.5 mm and 1.5 mm beam sigma beryllium targets with 120 GeV beam

Figure 2.15 shows how the FoM varies if the target radius is varied around the 3xsigma value. For the 1.5 mm beam sigma, a target radius equal to 3xsigma is the ideal dimension in terms of the FoM. For the 3.5

mm beam sigma the FoM can be marginally increased by reducing the target radius below the 3xsigma value. This is due to pions produced in the core of the target being absorbed before they reach the outer surface of the 10.5 mm radius target. A reduction to a radius of 9 mm reduces the absorption such that the FoM is increased by a couple of percent.
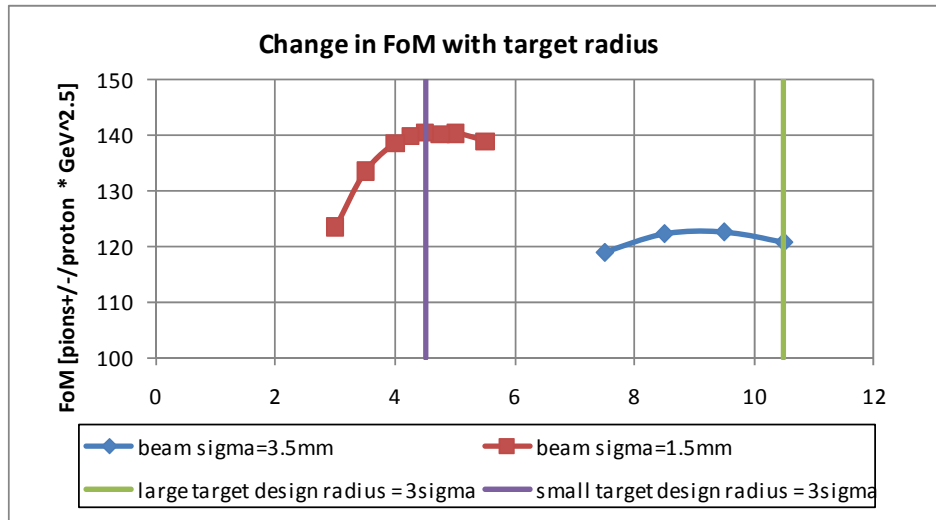

Figure 2.15 Effect on FoM of varying the target radius for fixed beam size (beryllium targets with 120 GeV beam energy)

Having fixed the beam sigma to be 1/3 of the target radius, Figure 2.16 shows the variation in the FoM as a function of the target diameter. It can be seen that the FoM for a cylindrical target decreases proportionally to increasing radius. For various engineering reasons which will be discussed later longitudinally segmenting the target has some practical advantages. One segmenting option considered in chapter 3 is a series of spheres. Included in figure 2.16 is a data point for the FoM for a series of 48 contained 21 mm diameter spheres making a target length of ≈1m. It can be seen that the FoM is equivalent for a series of spheres as compared to the cylindrical rod of the same diameter.

Figure of Merit as a function of target diameter (1 m long cylinders; sigma=r/3)
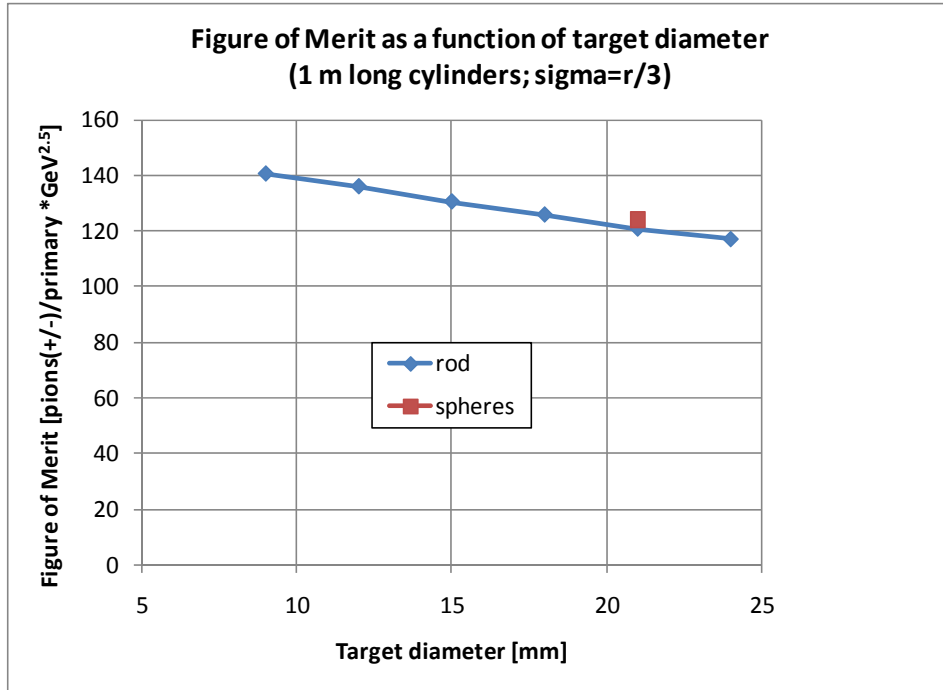
Figure 2.16 FoM is shown to be linearly proportional to target radius for a beryllium target with 120 GeV beam and beam sigma equal to one third of target radius

Figure 2.17 shows the FoM as a function of target length for 10.5 mm and 4.5 mm radii targets. It can be seen that 1m is not the optimum length for achieving the best FoM. As noted previously the FoM does not evaluate the focusing effect of the horn magnetic field and the true optimum length will be influenced by the depth of field of the magnetic horn system. Notwithstanding focusing, this study of FoM vs length does raise a question about the optimum target length. Making the target longer than 1 m has the effect of increasing the FoM. This is because a significant percentage of the protons entering the target will reach the end of a 1m beryllium target without interacting much. If the target is made longer these 'high energy' protons leaving the 1m long target have further chances to interact and augment the pion yield. Once the target length is increased to 1.5m then further increase in length results in a much smaller or negligible benefit.
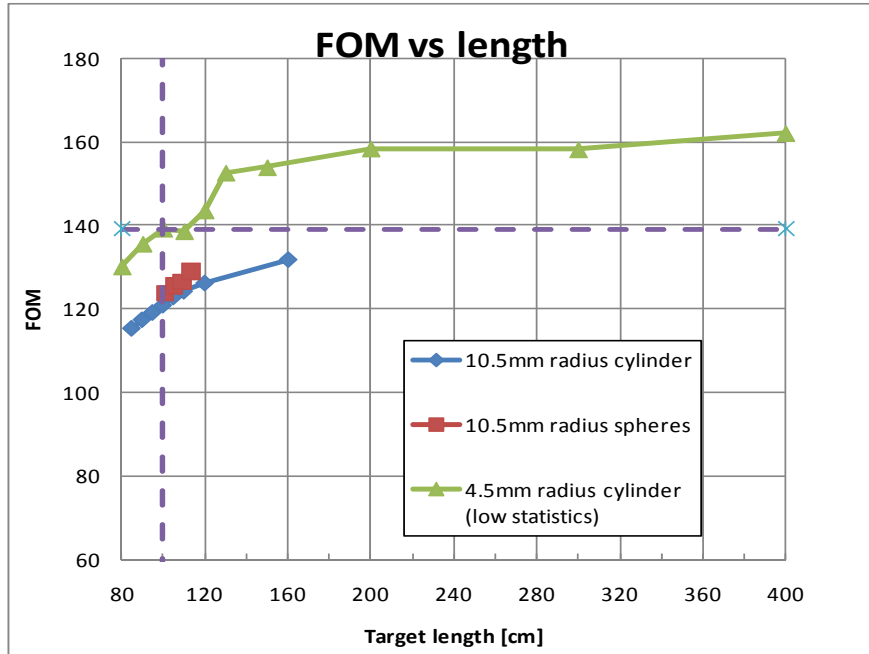
Figure 2.17 FoM as a function of target length

Larger diameter targets may be desirable from an engineering perspective but the FoM is found to reduce in proportion to increasing radius. However by increasing fractionally the target length (see Figure 2.18) it may be possible to recover the loss that would result from a larger radius, provided this is compatible with the layout of the rest of the target station.
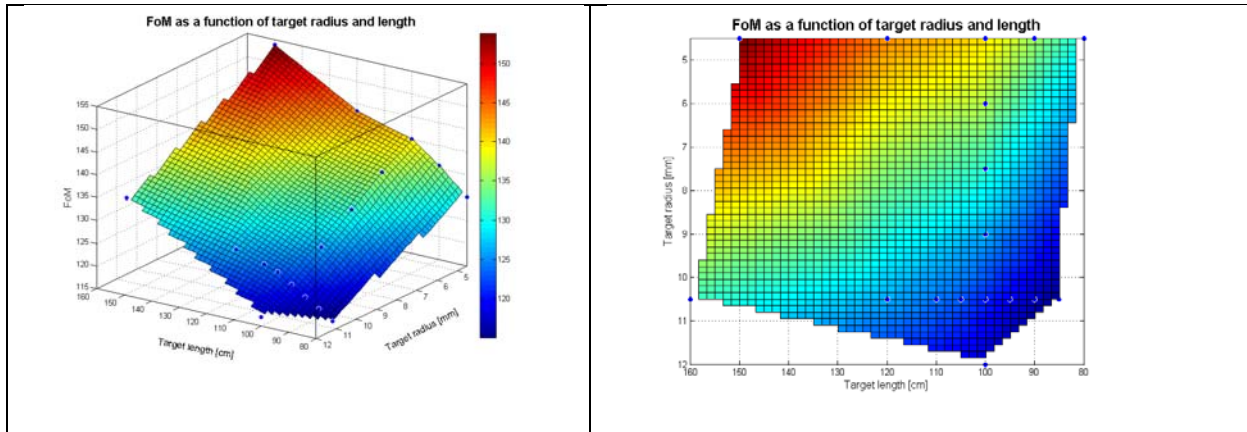

Figure 2.18 FoM as a function of target radius and length. Surface interpolation from FLUKA simulation data (blue dots)

Additional material in close proximity with the target, ie the horn inner conductor, can also have a significant effect on the FoM. The engineering issues of an integrated target and horn inner conductor are studied in detail in Section 5. Stress levels and practical constraints are found to limit the size and layout of the inner conductor, and so the FoM needs to be evaluated in addition to the engineering issues. The current horn baseline design has a 3 mm thick, 20 mm inside diameter aluminium inner conductor. This leaves a radial gap of 9.5 mm if a 10.5 mm target rod is inserted. In Figure 2.19 the FoM for the baseline

magnetic horn (green column) is compared with the integrated target and horn option (red column). In this study the integrated inner conductor is considered thicker (5mm instead of 3mm) to make up for the loss of cross sectional area due to the reduced conductor radius (NB stress levels due to magnetic end effects are discussed in detail in Chapter 5). The two intermediate steps (3 mm integrated and 5 mm separated conductor) are presented in the Figure together with the target rod without the horn (purple column) as reference points.
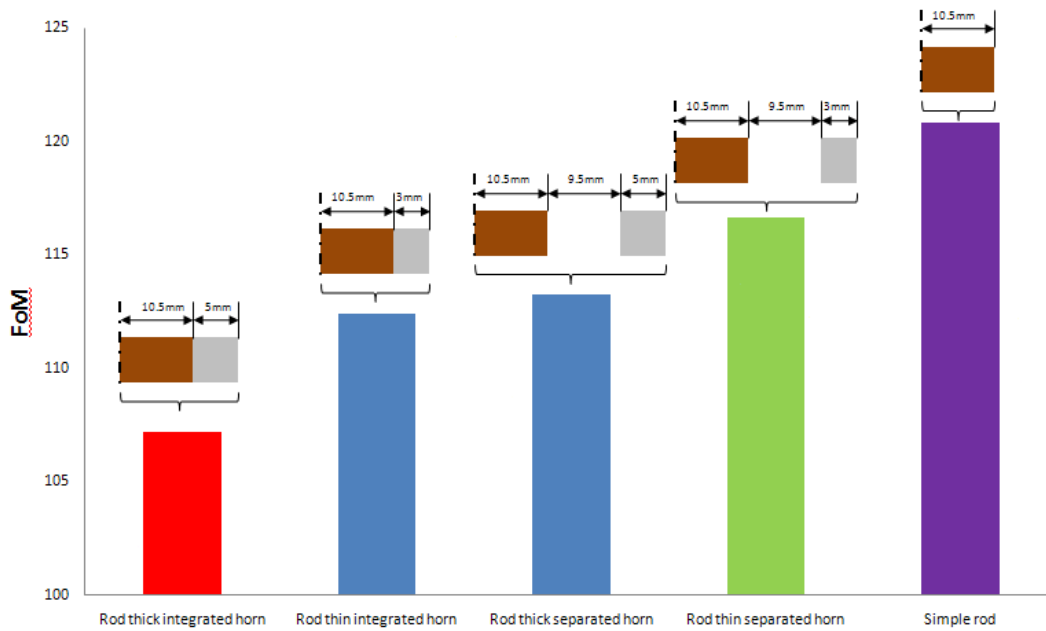

Figure 2.19 FoM as a function of the layout of the horn inner conductor

For an integrated target and horn, significant heating of the inner conductor can result from secondary particle interactions, particularly for an aluminium conductor. This effect is demonstrated by including in the model an upstream collimator of aperture radius equal to the target radius. This ensures that energy deposition in the conductor is uniquely due to secondary particles generated in the target. Figure 2.20a and 2.20b compares energy deposition in a simple beryllium target with that in an integrated beryllium target and aluminium conductor (21 mm beryllium target diameter, 5 mm thick aluminium conductor and 21 mm collimator aperture diameter). Over double the energy is deposited in the integrated target and conductor compared with the simple beryllium target. Figure 2.20c shows that when the beam is off centre by 2σ the peak energy deposition is higher in the aluminium inner conductor than it is in the beryllium target. These results highlight the importance and difficulties of material selection for the engineering of a combined target and horn as further discussed in Section 5.
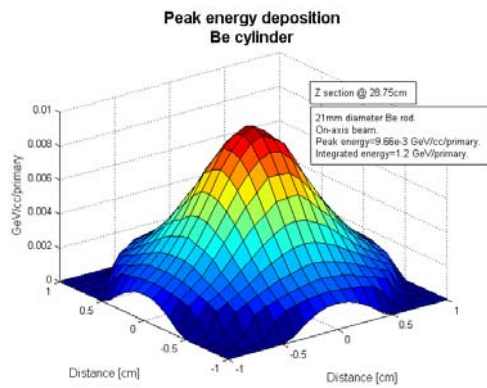
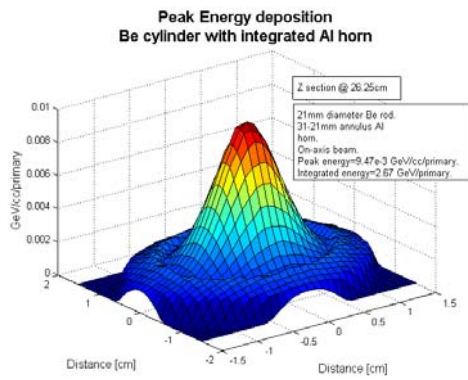*Figure 2.20 a Peak energy deposition in all beryllium target*

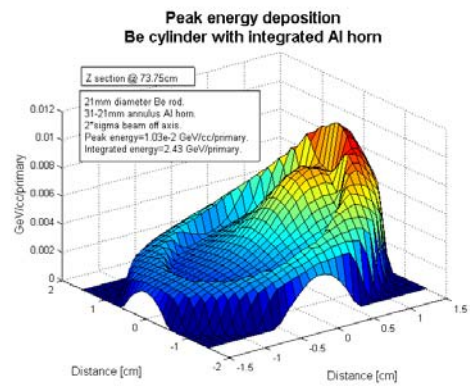*Figure 2.20 b Peak energy deposition in beryllium target with aluminium conductor*

Figure 2.20 c Peak energy deposition in beryllium target with aluminium conductor with off centre beam

2.5 Summary

FLUKA has been used to calculate the Energy deposition in three different target materials, beryllium, AlBeMet and aluminium, with two different beam sigma values and two beam kinetic energy values. The results are listed in a table and used as an input to stress calculations presented in the following sections. Beryllium was found to absorb the least energy out of the three materials. The magnetic field of the horn was found to increase energy deposition in the target by up to 20% and also move the peak energy deposition further down the target. A Figure of Merit was used to assess the pion production performance per incident proton for the three different target materials, two different beam sigma values and two beam kinetic energy values. Beryllium gave marginally the highest pion yield with aluminium giving a reduction of c. 1% at 120 GeV, with a more significant effect at 60 GeV. When normalized for beam power, the FoM result indicates that 120 GeV is marginally better than 60 GeV for all materials especially aluminium and for both values of beam sigma. In terms of the FoM the small beam sigma at 1.5 mm is clearly favourable over the larger 3.5 mm beam sigma (where the target radius equals three times sigma). For the 120 GeV case the FoM is 17% higher with the small beam sigma. For the 60 GeV case the FoM is 19% higher with the small beam sigma. However, the FoM for the smaller beam and target is more sensitive to a miss-steered proton beam; it is stable up to a beam miss-steer of 1 sigma in each case. FoM studies also raised a question about the optimum length of the target suggesting that 1m may not be long enough however it is noted that the simple FoM used does not evaluate the focusing efficiency of the horn and extra length could be outside the depth of field of the horn focusing elements. A FLUKA study of a combined target and horn has revealed a reduction in FOM and an increase in total energy deposition compared with a separate target inside the horn.

2.6 References

[1] "FLUKA: a multi-particle transport code", A. Fasso, A. Ferrari, J. Ranft, and P.R. Sala, CERN-2005-10 (2005), INFN/TC_05/11, SLAC-R-773

[2] MARS 15, N.V. Mokhov, "The MARS Code System User's Guide", Fermilab-FN-628 (1995).

[3] "The micron wire scanner at the SPS"
J.Bosser, J.Cammas, L.Evans, F.Ferioli, J.Mann, O.Olsen and R.Schmidt
CERN SPS 86-26 December 1986

Appendix 2.1

FLUKA magnetic field benchmark
Comparison of FLUKA with analytical expression for the radius of curvature of an electron entering a uniform magnetic field.

A particle with charge e moving through a field B

at a velocity v will experience a force F

$$F = ev\mathbf{x}\mathbf{B}$$

if v perpendicular to B then

$$evB = F = \frac{mv^2}{r} \quad \text{so}$$

$$Br = \frac{mv}{e} = \frac{p}{e}$$

where e = particle charge, m = particle mass,

v = particle velocity, B = field intensity, p = beam momentum

and r = radius of curvature

if p is in GeV/c and B is in Tesla then

$$r = 3.3356\frac{p}{B}[m]$$

for a 1GeV electron and B = 1T   r = 3.3m and for B = 5T

r = 0.7m

Figure a1 and Figure a2 show that the radius of curvature of a 1 GeV electron as a result of two different uniform field strengths predicted by FLUKA agrees with the analytical solution.
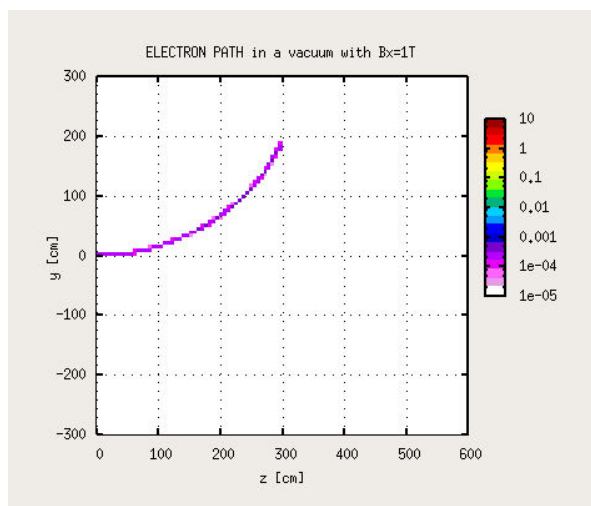

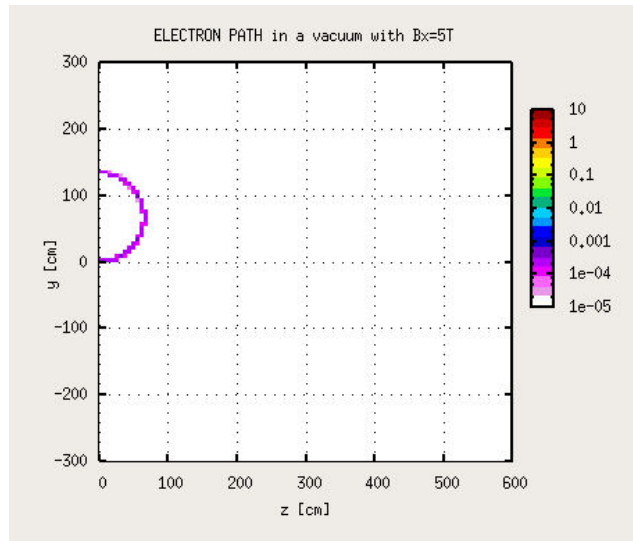*Figure a1. Trajectory of a1GeV electron in a 1Tesla uniform field*

Figure a2. Trajectory of a1GeV electron in a 5Tesla uniform field

Appendix 2.2

Deltaray threshold

The integrated energy deposition in a 0.2 mm thick window as a function of deltaray threshold is shown in figure a3. Increasing the deltaray threshold above 1MeV does effect the energy deposition but below 1MeV it has a very small effect.
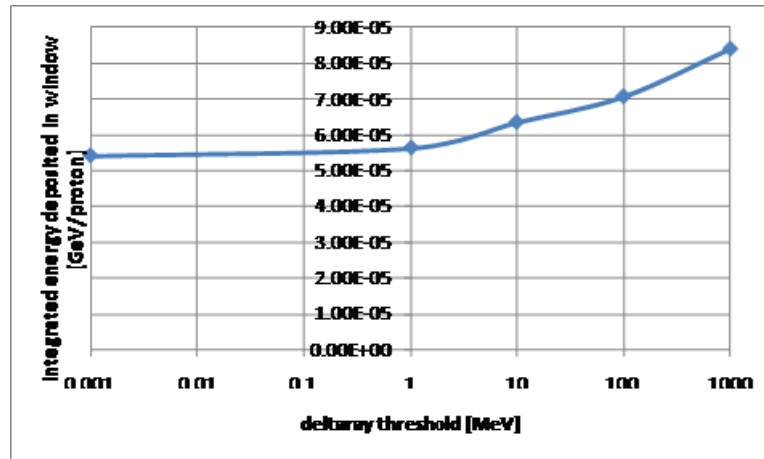

Figure a3. Energy deposition in a 0.2 mm thick beryllium window as a function of deltaray threshold

Figure a4 shows the fluence of electrons leaving the window into the surrounding vacuum. For this plot the deltaray threshold is reduced from the default value to 1keV which shows that there are electrons leaving the target at less than the default 1MeV, however it seems from figure a6 that the energy that escapes the window with these low energy escaping electrons does not make a significant difference to the integrated energy deposed in the window.
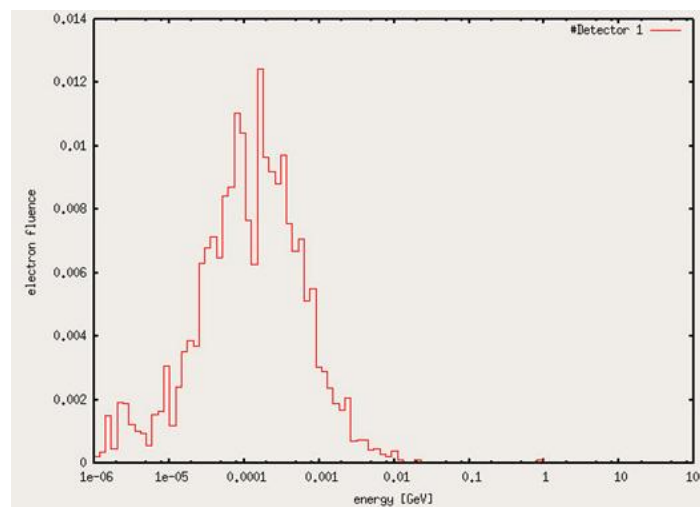

Figure a4. Fluence of electrons emerging from the 0.2 mm thick beryllium window

We also note the following comment in the FLUKA notes.

"In very thin layers, wires, or gases, Molière theory does not apply. In FLUKA, it is possible to replace the standard multiple scattering algorithm by single scattering in defined materials "

Apparently the multiple scattering Moliere method that is used by default does not apply in very thin layers. Figure a5 compares the single scattering with the default multiple scattering. It doesn't seem to have a big effect when the deltaray threshold is below the default 1MeV.
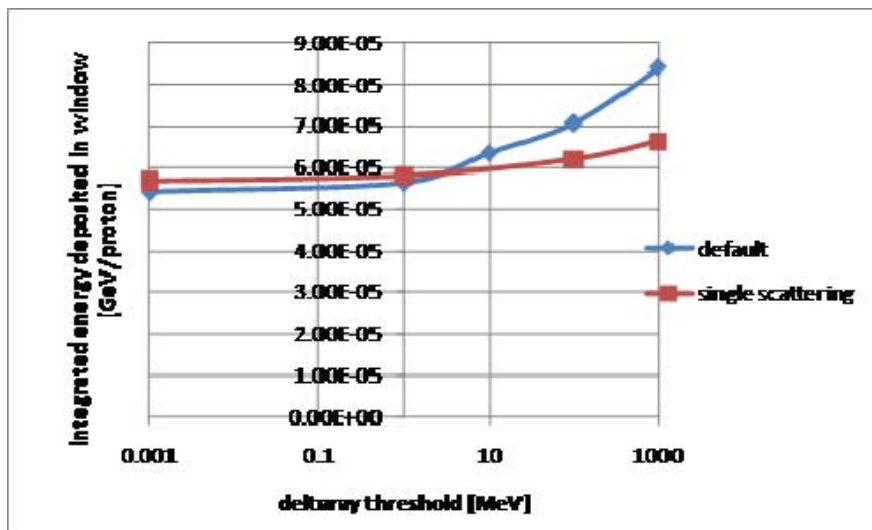

Figure a5. Energy deposition as a function of deltaray threshold for single scattering and Moliere scattering.

Appendix 2.3

Appendix 2.3 contains the original communication outlining the method for calculation of the FOM. However following analysis of initial FOM results, the original values (as stated in the document of March 23 below) for the transverse momentum cut-off, pion energy range of interest and the weighting function exponent were modified in April 2010. Both the original and new values are quoted in the table below. The new values were used to perform the FOM analysis presented in Section 2.

Parameter	Original Value (March 23 2010)	New Value (April 2010)
Transverse Momentum Cut-Off	0.5 GeV/c	0.4 GeV/c
Pion energy range of interest	1.5 – 8 GeV	1.5 to 12GeV
Weighting function exponent	2	2.5

FOM for pion Production

March 23, 2010
Bob Zwaska

This is a rough Figure of Merit contrived for use by RAL in target design optimization. A quick, simple approximation based on basic pion kinematical parameters is used.

Overview of Technique:

The objective is to get a single number to characterize the pion yield. The difficulty is caused by the overabundance of low energy pions which have very small probability of producing neutrino interactions in the detectors. Therefore, a sum of pions, irresepctive of energy, is not adequate.

Instead, we propose using an energy weighted and cut sum of pions. This could be done individually or in bins of pion energy.

Relevant parameters:

FOM: Figure of Merit

E_{pi} : Energy of pions in GeV

pT: Transverse momentum of pions in GeV/c

$N_{pi}(E)$: The number of pions produced below a certain pion energy (E)

$(d/dE) N_{pi}(E)$: The differential number of pions per energy. This corresponds to the height of a histogram bin.

w(E): Scalar weight that is a function of pion Energy.

Factors:

Pion production spectrum:

The pion production spectrum has a power law dependence such that:

$(d/dE) N\_pi(E) = const \times E^{-1.6}$

Thus, low-energy pions strongly dominate. However, these pions are much less likely to produce neutrinos. In fact, the interaction spectrum rises strongly over the first few GeV of neutrino energy, suggesting that a stronger weight scale is needed.

Pion focusing:

Wide anngle pions are not focused. As a rule, we should not consider pions with transverse momentum (pT) greater than 0.5 GeV/c. THis number is not hard and fast, so it could be subsequently reconsidered

-----

Interesting pion energies:

The neutrinos of interest are around two peaks of neutrino oscillations around 0.7 and 2.6 GeV. These correspond to a range of pion energies, such that we would like to capture pions between 1.5 and 8 GeV. Lower energies are generally undetecatble. Higher energy neutrinos are not useful

----

Recommendation:

Produce a FOM via a convolution of an energy spectrum of elected pions with a weighting function.

The cuts should be:
1.5 GeV < E_pi < 8 GeV
pT < 0.5 GeV/c

The weighting function should be
w(E) = E^2
such that w(1.5) = 2.25, w(8) = 64
Don't worry about normalization (except to the total number of protons simulated).

This could be applied either to single protons or to a histogram of the pion energy spectrum. I list a procedure for evaluating the FOM via histograms:

1. Instruct FLUKA to generate a histogram of pions, by energy as they leave the target, but instruct it to cut on transverse momentum. This may have to be performed by having it output a two-dimensional histogram with only 2 bin widths in the pT direction - one less than the 0.5 GeV/c cut, one larger. I suggest having the bin widths in momentum at 0.5 GeV or smaller.

2. Multiply the number of pions collected in each bin by the weighting function evaluated at the center of each bin. For example, for the bin containing energies 1.5 - 2.0, evaluate at 1.75 to get 3.0625. Multiply that by the bin contents.

3. Sum up the weighted entries between the energy limits of 1.5 and 8.0 GeV.

4. If not yet normalized, divide by the number of protons simulated.

You now have the FOM.

3. Report on Task A: Proton beam interactions with Beryllium and AlBeMet Targets

This section reports on the engineering implications of the interaction between the proton beam and the target. It starts with an introduction which describes the nature of the stress induced in the targets and the various timescales of importance. It also serves to define the terminology that we shall use throughout the rest of the report. Following the introduction is a description of the simulation tools (ANSYS and AUTODYN) and how they are used to calculate the stress levels induced in a target. Then there are the following 4 subsections which present the main results and finally a summary containing the conclusions.

- On-centre beam thermal stress *without* inertial effects (ANSYS)
- On-centre beam thermal stress *with* inertial effects (AUTODYN)
- Off centre beam, lateral deflection and vibration modes (ANSYS)
- Off-centre beam with thermal stress and inertial effects (AUTODYN)

3.1 Introduction

The beam induced stress in the target is a result of both relatively long term thermal stress and inertial effects of rapid energy deposition.

Thermal Stress

The beam deposits energy in the target generating a thermal gradient which is manifested as a corresponding thermal stress. The thermal stress fades as thermal conduction and cooling act to smooth out temperature gradients, distributing the deposited energy throughout the volume of the target. For LBNE it takes of the order of a second for radial temperature gradients to smooth and of the order of minutes for the longitudinal temperature gradients to smooth out.

Inertial Stress

Inertial stress occurs as a result of the energy deposition being faster than the expansion time of the target material. The expansion time is equal to the characteristic dimension divided by the speed of sound in the material. Typically a bunch length (the time scale of a single bunch of particles) is very short with respect to the expansion time of a target and so the energy deposition can be considered instantaneous. As the energy deposition is instantaneous there is no time for expansion and so it can be modelled as constant volume heating which gives rise to a stress that is proportional to the temperature jump. This stress then propagates through the target in the form of stress waves. As long as the magnitude of the stress waves is below the point where material yielding occurs then they are elastic waves (not plastic or shock waves) that travel through the target material at the speed of sound. The waves cause stress and strain oscillations in different directions at frequencies defined by the characteristic dimensions of the target and the speed of sound of the target material. The waves from successive bunches can superimpose leading to complex wave patterns where the final stress magnitude depends on the time structure of the energy deposition as well as the target shape and material. As an example of timescales the radial and longitudinal stress wave oscillations in the 2.1 cm diameter 1m long beryllium target considered for LBNE are 300 kHz and 3.3 kHz respectively.

If the beam hits the target off-centre resulting in an asymmetric temperature gradient in the target, suddenly the target will want to be bent due to one side of the target heating up more than the other. This sudden application of bending stresses can excite some natural frequencies of the target. This is an inertial effect which results in stresses that oscillate at the excited natural frequency and can give rise to higher stresses than are seen with a symmetric concentric temperature gradient. The natural frequency depends on how the target is mounted, as an example the first mode of vibration for a simply supported 21mm diameter LBNE target is 164 Hz so the period is of the order of 6 milliseconds.

As a conservative start point the analysis that follows is based on the premise that the stress induced in the target is always below the yield stress and all the results presented below are based on a linear relationship between stress and strain.

3.2 Simulation tools for evaluation of target stress

3.2.1 ANSYS models

Outline

The finite element software ANSYS was used to simulate a proton beam spill interacting with a 1m long cylindrical target. The objective was to calculate the temperature distribution and resulting thermal stress in the target for a specified range of beam parameters, materials, and geometry parameters. Included in the model are heating from an on-centre beam, thermal conduction in the target, and the calculation of transient thermal stresses. Excluded from the model is the propagation of elastic stress waves in the target. These are considered using the explicit finite element code AUTODYN in the sections that follow.

Analysis Procedure

In order to explore the entire parameter-space in a quick and efficient way while keeping the results as generic as possible, a number of simplifications were made. These included limiting the simulation to a single beam spill, applying linear rather than temperature dependent material properties, and ignoring the method of cooling by specifying an adiabatic surface boundary condition. The analysis was performed in three stages as illustrated in Figure 3.2.1.

Firstly, the beam target interaction was modelled using FLUKA in order to determine the energy density distribution in the target. The energy deposition as a function of radial and axial position was output from FLUKA in a suitable table format.

Secondly, the FLUKA data table was read into ANSYS and used as an input for a thermal transient run. The temperature distribution was calculated as a function of time, both during and after the beam spill, taking thermal conduction into account.

Thirdly, several structural static runs were carried out in ANSYS, one corresponding to the temperature profile at each time step in the previous transient thermal analysis. The thermal stresses generated by the temperature gradients in the target were evaluated.
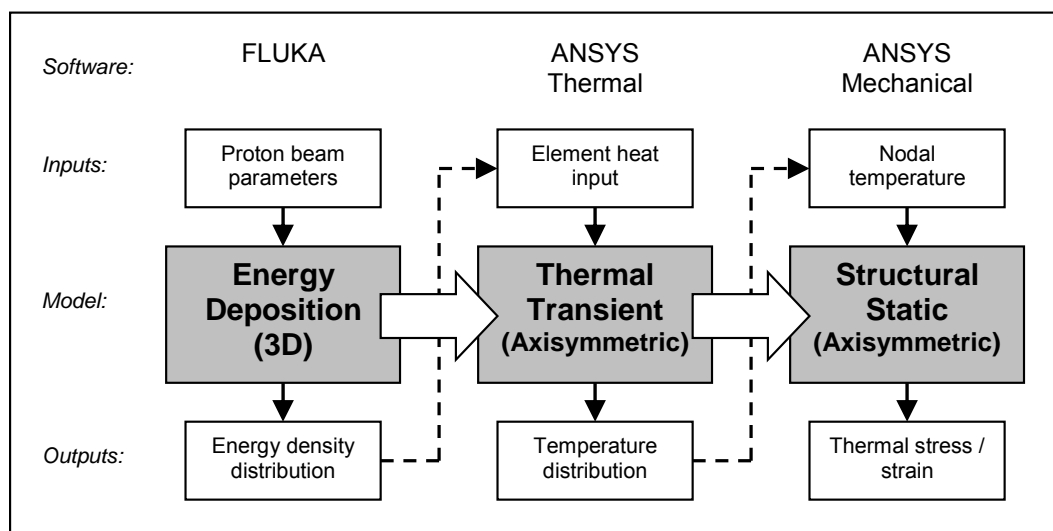

Figure 3.2.1 Analysis process, beam/target interaction

Model Description

A finite element model, comprising a 1m long solid cylindrical rod, was created in ANSYS using planar axisymmetric elements. An axisymmetric simulation has the advantage of being much less computationally expensive than the alternative full 3d approach, while still capturing the component stresses in the r, theta, and z directions. An inherent limitation is that the beam is assumed to be centred on the target, and as such, off centre beams cannot be modelled. A regular mapped mesh was used consisting of 50 radial divisions and 100 axial divisions. 8-node quad elements were used of type PLANE77 for the thermal analysis and type PLANE82 for the structural analysis. An identical mesh was used in the thermal and structural runs in order to facilitate the transfer of nodal results between the thermal and structural model environments.

The model time structure, illustrated in Figure 3.2.2, comprised the 9.78 µsec spill time during which the beam heat load was applied, and the ~1 second interval between beam spills where the thermal conduction problem was solved. The heat generation rate was stepped on at the start of the spill and stepped off at the end of the spill. The dashed line indicates the time at which the next beam spill is due to arrive. Effects of the bunch structure within the beam spill were investigated in a separate analysis using AUTODYN and are reported in the sections that follow.
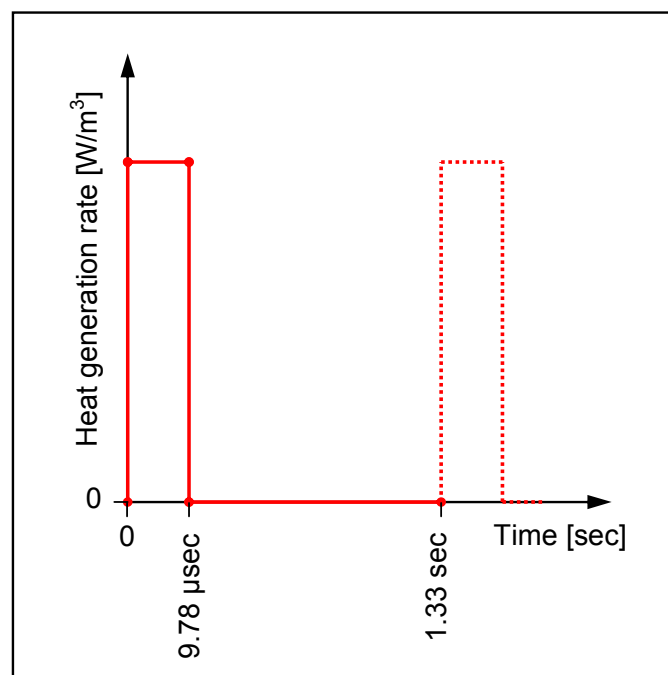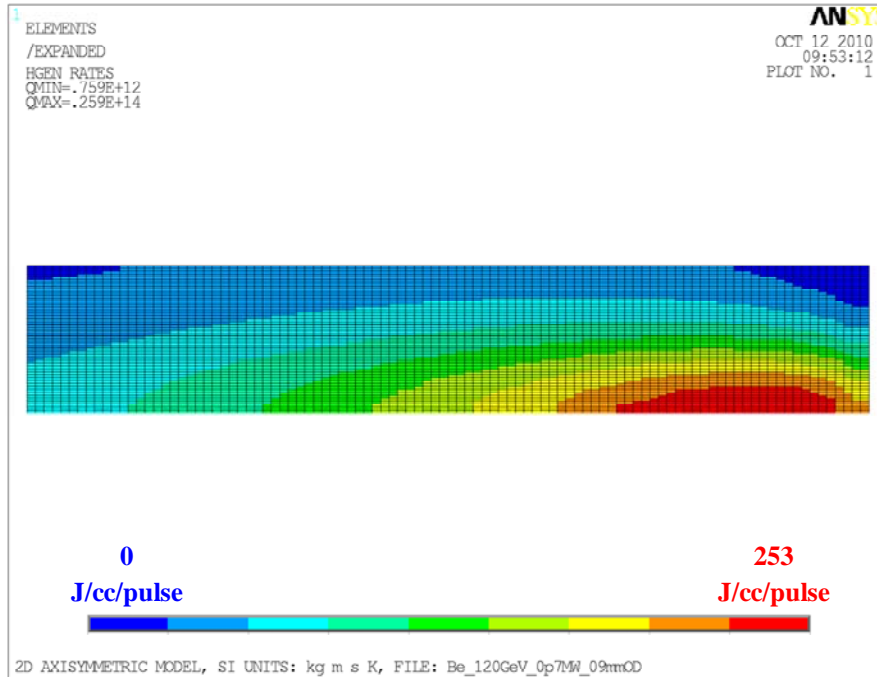

Figure 3.2.2 Model time structure

The element heat loads were read in from the FLUKA data file and converted into SI units before being applied to the ANSYS model. Figure 3.2.3 shows an example contour plot of the element heat generation rates during the beam spill for one particular case.

Figure 3.2.3 Heat generation input
Ø9mm beryllium target, 120 GeV, 0.7 MW beam

In the thermal analysis a uniform initial temperature of 300 K was applied. The heat load was applied to the model at a uniform rate during the beam spill, with adiabatic boundary conditions. The result is a permanent increase in temperature which, after a period of time, becomes uniform throughout the model due to thermal conduction within the target material.

In the structural analysis the target was fixed at the upstream end and allowed to expand axially at the downstream end. Gravity effects were not included. Static structural analyses were performed in order to deliberately exclude any dynamic (inertia) effects that would otherwise be captured. This simplifies the analysis and reduces simulation times by allowing a transient thermal stress to be calculated without solving for the dynamic (inertia) effects.

3.2.2 AUTODYN Models

The energy deposition that results from the interaction of a bunch of protons gives rise to a 'sudden' temperature gradient in a target. This results in thermal stress and inertial stresses as described in the introduction. We have used AUTODYN to model both the thermal stress and the inertial stresses. We only consider the propagation of elastic stress waves and elastic deformation of the target material.

Simulations with AUTODYN

In order to calculate stress in a target with AUTODYN we use the energy deposition data from FLUKA as an input for AUTODYN. User subroutines have been written at RAL to deposit energy into the AUTODYN model as efficiently as possible in both cartesian and polar coordinates. The subroutines interpolate between the FLUKA output data and the AUTODYN mesh so as to place the correct amount of energy in each cell and at each time step of the AUTODYN model. The processed output from FLUKA containing the energy deposition data is saved in a data file along with the beam parameters such as number of protons per bunch, number of bunches per pulse, bunch duration, etc. AUTODYN is then run using a modified execution file which calls the energy deposition subroutines and reads the energy deposition data file. The target geometry is defined with a Lagrange mesh which expands and contracts as the target changes shape. AUTODYN solves the continuity, momentum and energy equations using an equation of state to obtain closure of the complete set of equations which are listed below.

Continuity $\quad \rho = \dfrac{m}{V}$

Momentum x $\quad \rho\ddot{x} = \dfrac{\partial \sigma_{xx}}{\partial x} + \dfrac{\partial \sigma_{xy}}{\partial y} + \dfrac{\partial \sigma_{xz}}{\partial z}$

Momentum y $\quad \rho\ddot{y} = \dfrac{\partial \sigma_{yx}}{\partial x} + \dfrac{\partial \sigma_{yy}}{\partial y} + \dfrac{\partial \sigma_{yz}}{\partial z}$

Momentum z $\quad \rho\ddot{z} = \dfrac{\partial \sigma_{zx}}{\partial x} + \dfrac{\partial \sigma_{zy}}{\partial y} + \dfrac{\partial \sigma_{zz}}{\partial z}$

Energy $\quad \dot{e} = \dfrac{1}{\rho}\left(\sigma_{xx}\dot{\varepsilon}_{xx} + \sigma_{yy}\dot{\varepsilon}_{yy} + \sigma_{zz}\dot{\varepsilon}_{zz} + 2\sigma_{xy}\dot{\varepsilon}_{xy} + 2\sigma_{yz}\dot{\varepsilon}_{yz} + 2\sigma_{zx}\dot{\varepsilon}_{zx}\right)$

where the strain tensor ε_{ij}, is determined from the relation between strain rate and velocity i.e.

$$\dot{\varepsilon}_{xx} = \frac{\partial \dot{x}}{\partial x}, \qquad \dot{\varepsilon}_{yy} = \frac{\partial \dot{y}}{\partial y}, \qquad \dot{\varepsilon}_{zz} = \frac{\partial \dot{z}}{\partial z}$$

$$\dot{\varepsilon}_{xy} = \frac{1}{2}\left(\frac{\partial \dot{x}}{\partial y} + \frac{\partial \dot{y}}{\partial x}\right), \qquad \dot{\varepsilon}_{yz} = \frac{1}{2}\left(\frac{\partial \dot{y}}{\partial z} + \frac{\partial \dot{z}}{\partial y}\right), \qquad \dot{\varepsilon}_{zx} = \frac{1}{2}\left(\frac{\partial \dot{z}}{\partial x} + \frac{\partial \dot{x}}{\partial z}\right)$$

In the case of elastic dynamics, stress and strain rate tensors are simply related via Hookes law. The equation of state used takes the following form:

Mie Gruneisen Shock equation of state $\quad p = p_H + \Gamma\rho(e - e_H)$

where p_H and e_H are known functions of volume on the Shock Hugoniot curve. However when compression of the material is small which is the case for elastic compressions then

these two terms tend to zero and we are left with a much simpler equation of state which relates pressure to density and internal energy which can be written in the following way:

$$\delta p = \Gamma \rho \delta e$$

Where Γ is the Gruneisen Gamma and is defined as follows

$$\Gamma = v \frac{\partial p}{\partial e}\bigg|_v$$

It is assumed that Γ is a function of volume and not of pressure or energy (reasonable for the range of pressures and internal energies of interest). For an infinitesimal change in internal energy i.e:

For $\delta e \rightarrow 0$ then $\Gamma = V \dfrac{\delta P}{\delta e} = \dfrac{V \delta P}{C_v \delta T}$

the pressure rise due to temperature rise at constant volume is given by

$$\delta P = \propto_v K \delta T \quad and\ so \ \ \Gamma = \frac{V \propto_v K}{C_V} \ \ or \ \ \Gamma = \frac{\propto_v K}{\rho C_V}$$

Substituting this expression for Γ in to the equation of state gives

$$\delta P = \frac{\propto_v K}{C_V} \delta e = \propto_v K \delta T$$

So the equation of state is simply a thermal pressure equation of state which describes the pressure rise caused by heating at constant volume.

An explicit time stepping method is used to solve the set of equations simultaneously at each time step, this is inherently stable even with non-linear equations of state as long as the courant number stability criteria is satisfied. The courant number stability criteria ensures the time steps are small enough that the dynamics are captured and in this way the solution remains stable. Conservation of total energy is the criteria for convergence of each time step.

For all of the AUTODYN models, beryllium has been used with the material properties taken from the AUTODYN library, see Appendix 3.1. Standard AUTODYN does not have the functionality to enter material properties that vary as a function of temperature.

3.3 Proton Beam and Target Interaction Results

3.3.1. On-Centre beam, thermal stress without inertial effects (ANSYS)

The ANSYS model was run many times with varying input parameters to sweep the required design parameter space. Four primary proton beam configurations were considered (table 3.3.1). Three separate materials were investigated: aluminium, beryllium, and AlBeMET (an alloy of aluminium and beryllium). Linear (room temperature) material properties were used. These are listed in Section 1. Two target diameters were considered: 21 mm and 9 mm. The beam sigma was scaled to be one-third of the target radius.

Table 3.3.1 Proton beam configurations

Proton Beam Energy (GeV)	Repetition Period (sec)	Protons per spill (-)	Proton Beam Power (MW)
120	1.33	4.8E+13	0.7
60	0.76	5.5E+13	0.7
120	1.33	1.6E+14	2.3
60	0.76	1.6E+14	2.0

Example Results Case

By way of example, contour plots and graphs for one specific case (120 GeV, 0.7 MW, 9 mm diameter beryllium target) will be shown in detail. The results for all other parameter combinations, which follow the same trends, are summarised in Table 3.3.2.

As expected, the maximum temperature rise occurs at the target centre, at the end of the beam spill (t = 9.78 µsec in Figure 3.3.1). The spill time is short enough that no thermal conduction takes place in the timescale of the beam energy being deposited. This means that the temperature rise in the target is effectively instantaneous. During the ~1 second interval between beam spills the temperature gradients are reduced through thermal conduction in the target material. At the time when the next beam spill is due to arrive (t = 1.33 sec in Figure 3.2.4) the temperature has fully equalised radially, but an axial temperature gradient still remains.

The maximum transient thermal stress also occurs at the target centre at the end of the beam spill. The Von Mises stress at this time, together with the component radial, hoop, and axial stresses, are illustrated in Figure 3.3.2. It follows from the temperature variation that we have a compressive (negative) stress at the target centre and tensile (positive) stress at the target surface.

Figure 3.3.3 shows how the maximum and minimum temperature in the model, and the maximum Von Mises stress in the model vary with time. The two plots show the same data-set displayed over different timescales, microseconds on the left, and seconds on the right. The maximum stress and temperature rise linearly during the beam spill (first ~10 microseconds) because the heat energy deposition was spread evenly throughout the spill time. The minimum temperature, which occurs at the surface of the target, hardly increases

at all during the spill. The model runs on in time to the point at which the next beam spill is due to arrive. During this time the maximum and minimum temperatures begin to converge, and the thermal stress, which is driven by the stress gradient in the target, drops almost to zero.
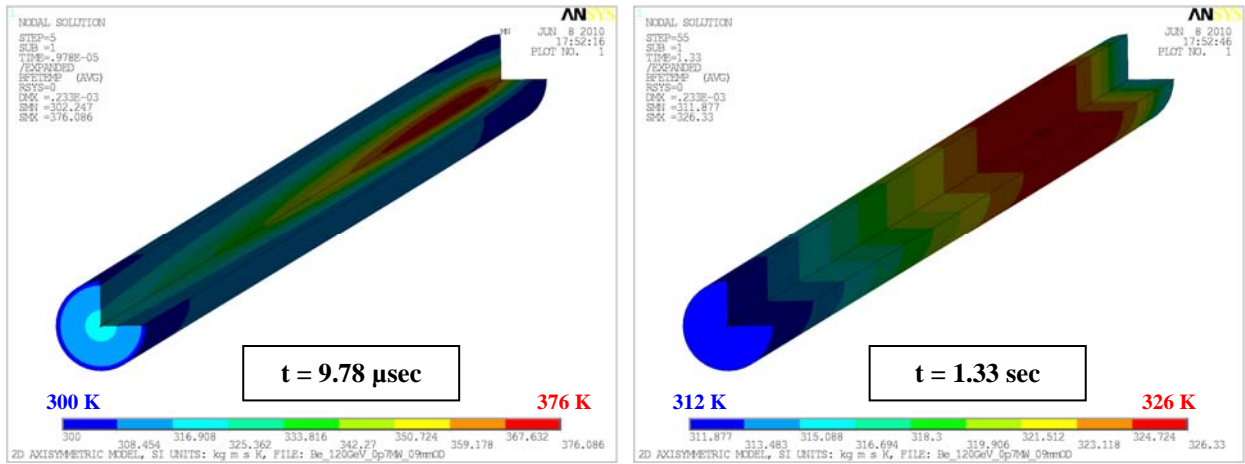
Figure 3.3.1 Temperature contour plots
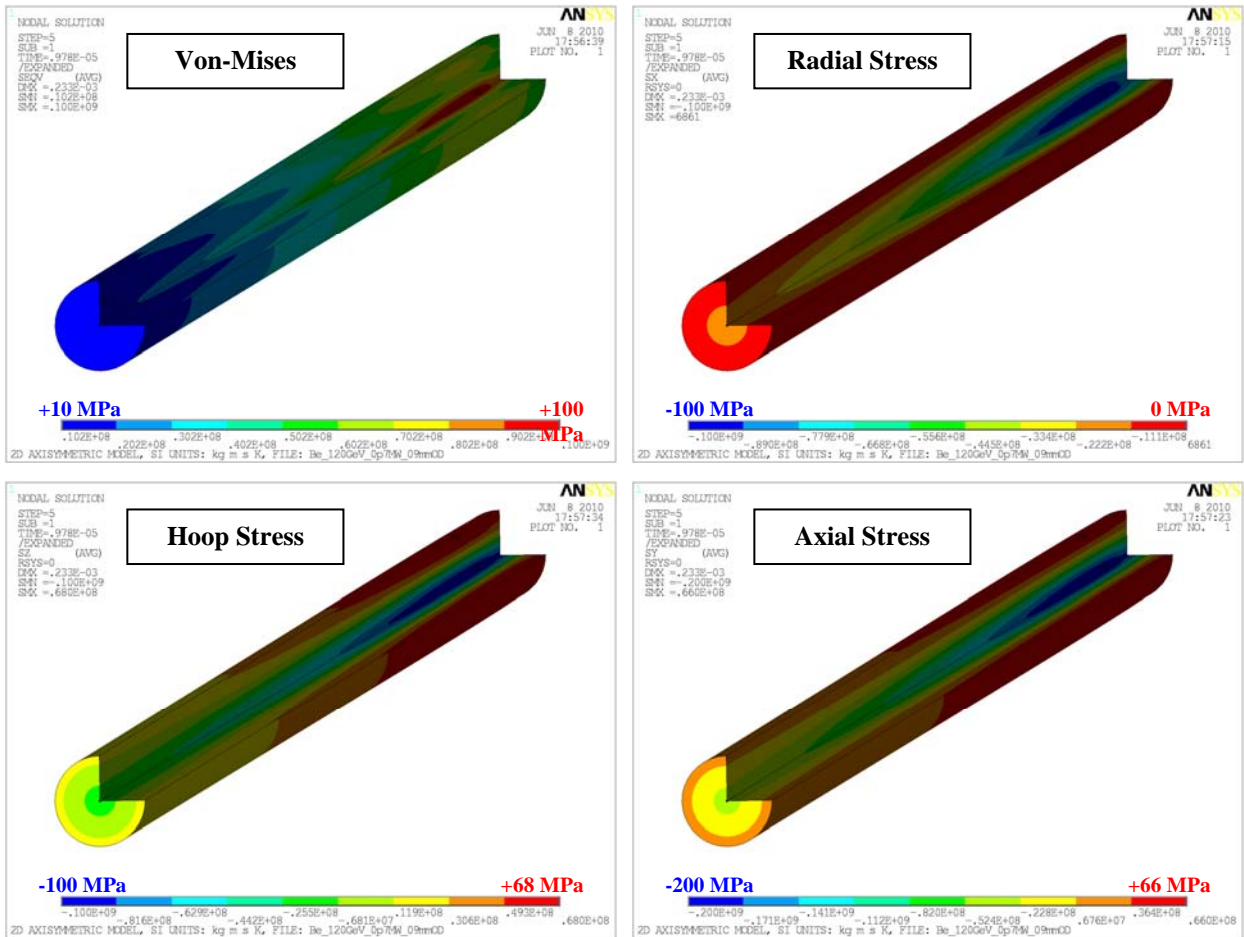*Ø9mm beryllium target, 120 GeV, 0.7 MW beam*

Figure 3.3.2 Component stress plots at the end of the beam spill, t = 9.78 µsec
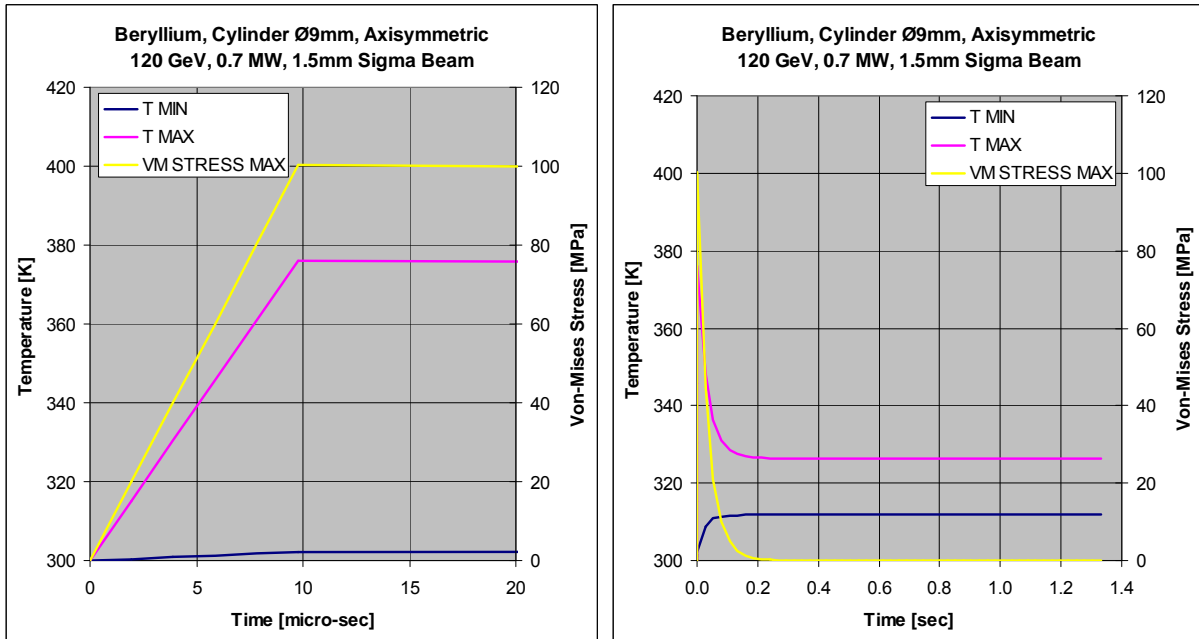*Ø9mm beryllium target, 120 GeV, 0.7 MW beam*

Figure 3.3.3 Max / min result quantities
Ø9 mm beryllium target, 120 GeV, 0.7 MW beam

The results for the full range of beam, material, and geometry parameter combinations are given in Table 3.3.2. Some of the results come directly from FLUKA, and some from ANSYS. The FLUKA results include the total energy deposited in the target by a single beam spill, and the peak energy density in the target material. The ANSYS results include the maximum temperature rise during the beam spill, and the maximum transient thermal Von Mises stress. The time averaged power comes from dividing the integrated energy deposited during a complete spill by the beam repetition period. This is the "steady-state" heat load that must be dealt with by the cooling system. Note that the beam repetition period varies according to the chosen beam configuration.

Note that the stress results quoted here are non-conservative because they do not include the following effects:

1. Multiple spills. During the first few beam spills the level of stress in the target is expected to increase up to a point where steady-state thermal operating conditions are reached.

2. Stress waves. Elastic stress waves occur over a much shorter timescale than the one investigated using ANSYS. Such stress waves are calculated using AUTODYN in the following section and act in addition to the transient thermal stresses reported here.

3. Off-centre beam. Asymmetric heating introduces additional bending stresses and dynamic effects in the target. These effects are studied in the final part of this section, and also act in addition to these results.

Table 3.3.2 Beam heating parameter study results

Beryllium

Beam Energy (GeV)	Beam Power (MW)	Beam Sigma (mm)	Deposited Energy (kJ/spill)	Time Averaged Power (kW)	Peak Energy Density (J/cc/spill)	Max. ΔT per spill (K)	Max. Von-Mises Stress (MPa)
120	0.7	1.5	4.2	3.2	254	76	100
		3.5	9.2	6.9	74	22	27
60	0.7	1.5	2.9	3.8	243	73	99
		3.5	5.8	7.7	61	18	23
120	2.3	1.5	14.0	10.5	846	254	334
		3.5	30.7	23.1	245	74	88
60	2	1.5	8.4	11.1	707	212	288
		3.5	17.0	22.3	176	53	68

Aluminium

Beam Energy (GeV)	Beam Power (MW)	Beam Sigma (mm)	Deposited Energy (kJ/spill)	Time Averaged Power (kW)	Peak Energy Density (J/cc/spill)	Max. ΔT per spill (K)	Max. Von-Mises Stress (MPa)
120	0.7	1.5	12.2	9.2	537	221	158
		3.5	35.1	26.4	269	110	71
60	0.7	1.5	6.3	8.3	472	190	158
		3.5	16.6	21.8	155	60	43
120	2.3	1.5	40.8	30.7	1789	736	525
		3.5	117.1	88.1	898	365	236
60	2	1.5	18.2	24.0	1374	551	459
		3.5	48.2	63.4	451	175	124

AlBeMET

Beam Energy (GeV)	Beam Power (MW)	Beam Sigma (mm)	Deposited Energy (kJ/spill)	Time Averaged Power (kW)	Peak Energy Density (J/cc/spill)	Max. ΔT per spill (K)	Max. Von-Mises Stress (MPa)
120	0.7	1.5	6.2	4.7	321	98	105
		3.5	15.7	11.8	108	33	30
60	0.7	1.5	3.8	5.0	299	91	104
		3.5	8.6	11.3	77	23	25
120	2.3	1.5	20.6	15.5	1069	326	351
		3.5	52.5	39.5	359	110	101
60	2	1.5	11.0	14.5	869	265	302
		3.5	25.0	32.8	223	68	73

3.3.2 On-Centre beam, thermal stress with inertial effects (AUTODYN)

When modelling beam induced heating of a target in AUTODYN the stress output is essentially composed of a superposition of two component stress fields:
1. A "quasi-static" thermal stress that is driven by temperature gradients in the target, which decay on the timescale of thermal conduction.
2. Elastic stress waves propagating at the speed of sound in the target material that are generated by the instantaneous nature of the applied heat load.

This superposition concept is illustrated schematically in Figure 3.3.4 The relative importance of the two component stress fields can be appreciated by comparing the "total" stress output from AUTODYN to the "quasi-static" component isolated using ANSYS. The "stress wave" component may then be inferred through subtraction. A headline summary of the AUTODYN results, including a breakdown of "quasi-static" and inferred "stress wave" components, is given in Table 3.3.3. Following the table, results from two example cases (700 kW 120 GeV 1.5 mm sigma 9 mm diameter beryllium rod and 2.3 MW 120 GeV 3.5 mm sigma 21 mm diameter beryllium rod) are used to describe the stress fields in a cylindrical target in more detail. In both cases the target is free, i.e. no fixed boundary conditions. The effect of fixing the ends of the target is discussed later in Section 3.3.4.
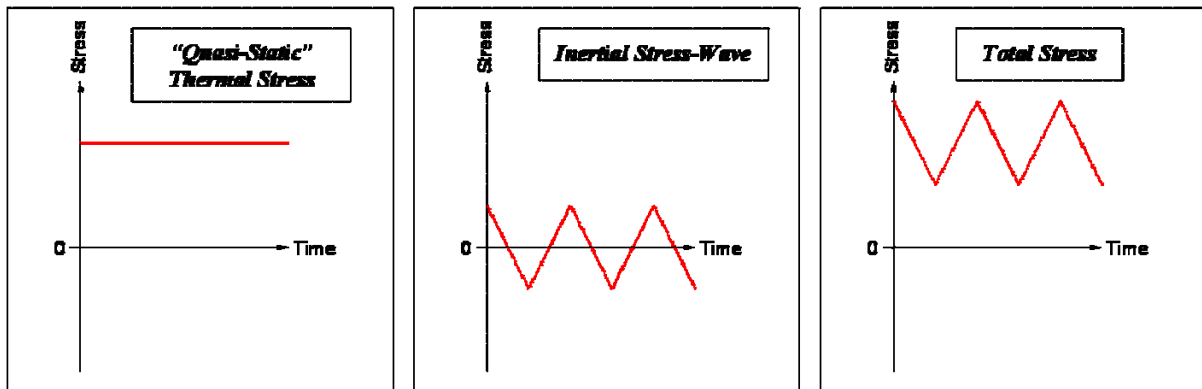
Figure 3.3.4 The total stress field is generated from a superposition of quasi-static and inertial stresses

Table 3.3.3 Summary of stress results due to temperature gradient and stress waves

Beam Energy (GeV)	Beam Power (MW)	Beam sigma (mm)	Peak "total" stress (AUTODYN) [MPa]	"Quasi-static" thermal stress component (ANSYS) [MPa]	"Stress-wave" inertial component (inferred through subtraction) [MPa]
120	0.7	1.5	177	100	77
		3.5	55*	27	28
120	2.3	1.5	575*	334	241
		3.5	180	90	90

*Scaled from beam current ratio

700 kW beryllium 120 GeV 1.5 mm sigma target

For this example 700 kW case Figure 3.3.5 shows a contour plot of the energy deposition in the target after the complete spill. Figure 3.3.6 shows a contour plot of the temperature of the target after a complete spill. A total of 4.2 kJ is deposited in the spill. Figure 3.3.7 shows the position of gauge points where output values from the simulation have been plotted. Results from the 700 kW case which follow are used to explain the formation of the stress waves during the spill and in the first millisecond afterwards.
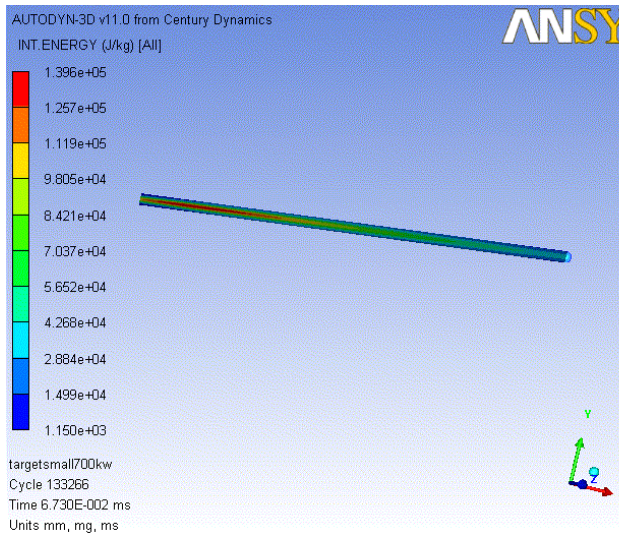
Figure 3.3.5
Internal energy deposited in beryllium target with 1.5 mm beam sigma and 120 GeV 700 kW beam
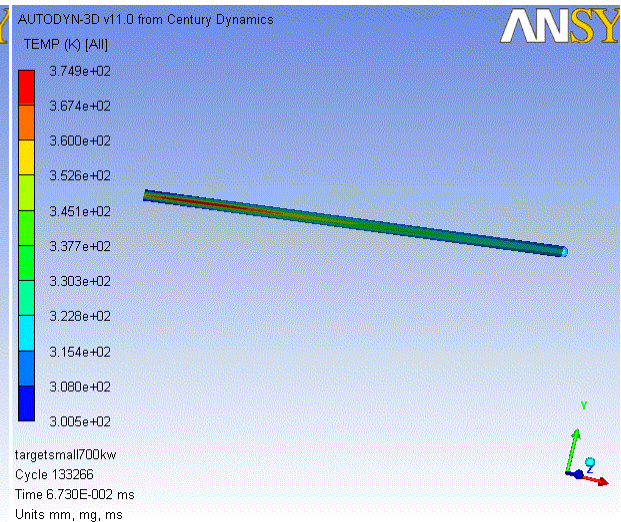
Figure 3.3.6
Temperature profile after beam spill in beryllium target with 1.5 mm beam sigma and 120 GeV 700 kW beam
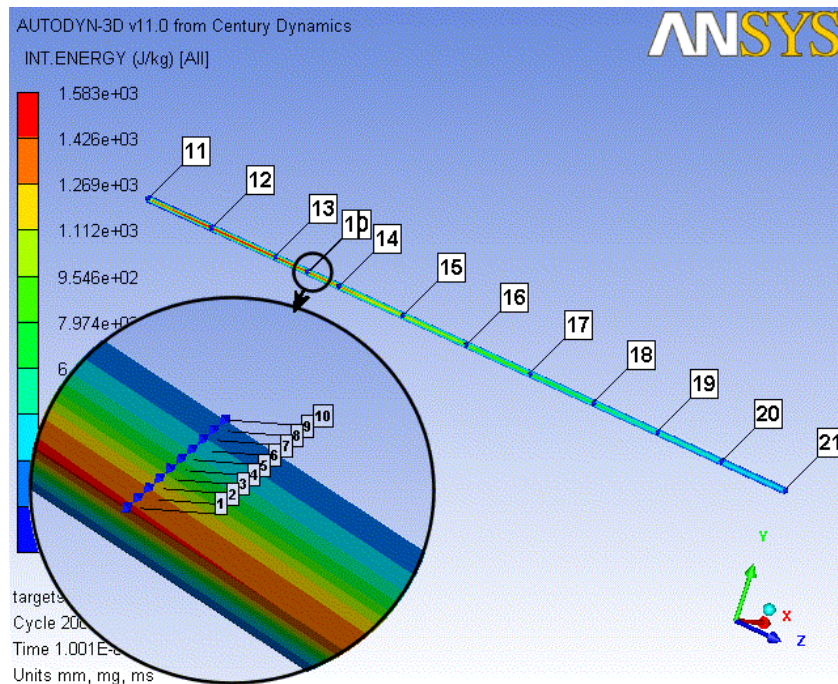
Figure 3.3.7 Gauge point positions

Figure 3.3.8 shows the typical form of the radial and hoop stress in the target as a function of time. The high frequency oscillations in stress that occur after the beam spill are radial oscillations of the target. These result from shear waves travelling in the radial direction reflecting at the surface of the target. These waves travel at the shear wave speed of the material and move perpendicular to the predominant elastic deflection of the target which is longitudinal. The amplitude of the oscillations is not that significant because the time for the target to expand in the radial direction is much less than the duration of the beam spill. Inertia effects in the form of oscillating stresses are only significant if the expansion time is long compared to the energy deposition time. The radial and hoop stress are both compressive and identical on axis at gauge point 1. The hoop stress increases to a tensile value at the surface of the target (gauge 10). The steady values reached after 0.5 ms depend on the temperature gradient in the target and so correspond to the stress levels calculated in Section 3.3.1. A slight reduction in the 'average' stress levels after 0.5 ms can be seen and this is a result of thermal conductivity smoothing out the temperature gradient. Figure 3.3.9 and 3.3.10 are contour plots of the radial and hoop stress after 0.3 ms.
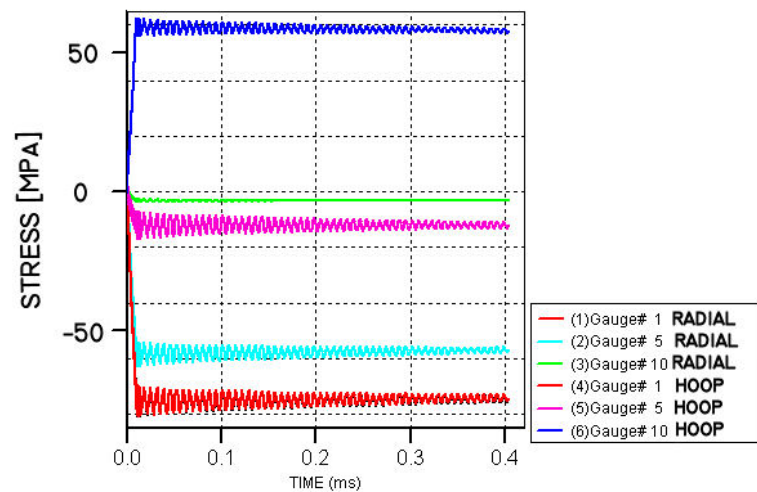
Figure 3.3.8
Radial, hoop and longitudinal stresses in beryllium target with 1.5mm beam
sigma and 120GeV 700kW beam
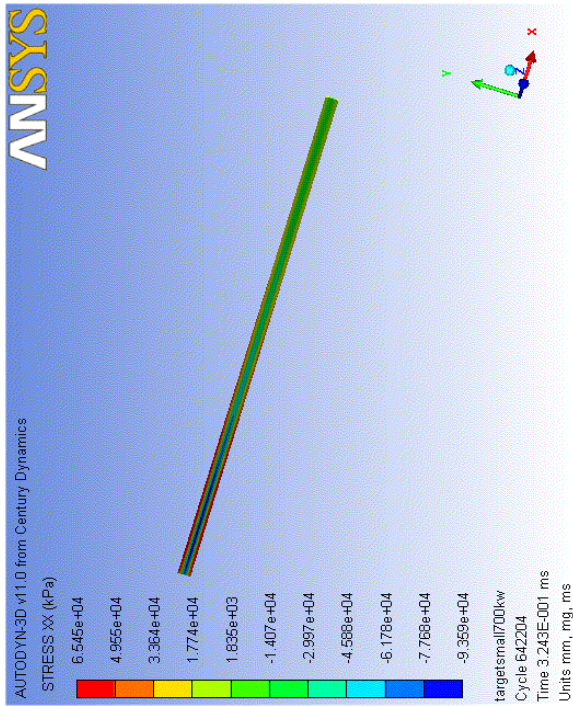
Figure 3.3.9
Radial stress in beryllium target with 1.5mm beam
sigma and 120GeV 700kW beam
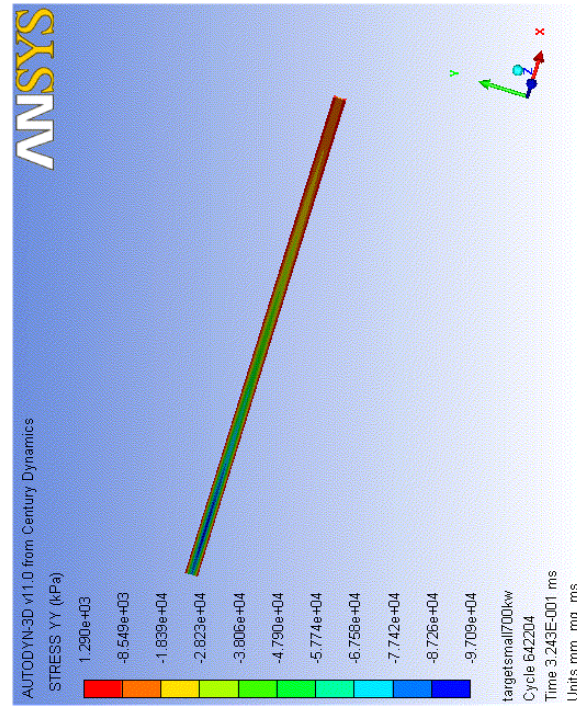
Figure 3.3.10
Hoop stress in beryllium target with 1.5mm beam
sigma and 120GeV 700kW beam

The longitudinal stress fluctuates significantly during the time period modelled as a result of stress waves travelling along the target (Figure 3.3.11). The amplitude of the oscillations is very significant because the longitudinal expansion time is large with respect to the beam spill duration. The longitudinal stress waves travel at the longitudinal sound speed because the wave direction is parallel with the direction of the predominant elastic deformation. The period of oscillation at a gauge point on the target is about 0.16 ms and this ties in with the longitudinal sound speed in beryllium. The magnitude of oscillations at the ends of the target (gauge 11 & 21) are small due to the superposition of the incoming and outgoing waves at the free ends. The most symmetrical pattern occurs at the centre of the target. The longitudinal stress is highly compressive at the central core of the target where the peak energy deposition occurs but is tensile towards the surface. The surface of the target is effectively stretched by the highly compressed core. This can be seen in Figure 3.3.12 where gauge 1 is at the centre and gauge 10 is on the surface of the target. A contour plot of the longitudinal stress clearly changes significantly with time as the stress waves can be seen moving up and down the target. Figure 3.3.13. shows the longitudinal stress at a snap shot in time, not expected to agree with the quasi-static results in Section 3.3.1 because of the significant magnitude of longitudinal stress waves that are superimposed on the thermal stress. Figure 3.3.14. illustrates the propagating longitudinal stress waves with several snap shots as a function of time. The radial and longitudinal oscillations described here can be seen in the frequency domain in a Fourier analysis presented later in Section 3.3.4 and in particular Figure 3.3.39.
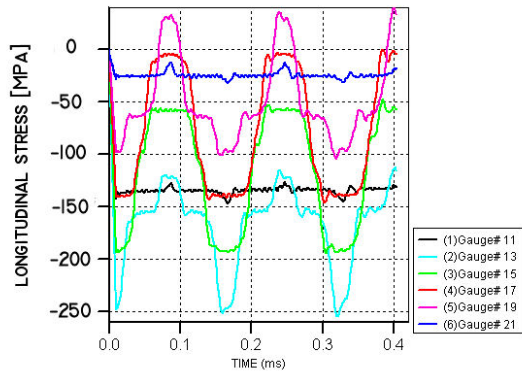
Figure 3.3.11
Longitudinal waves along the target axis in beryllium target with 1.5 mm beam sigma and 120 GeV 700 kW beam
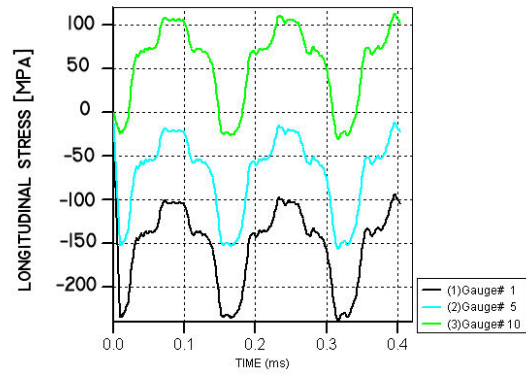

Figure 3.3.12
Longitudinal waves as a function of radius in beryllium target with 1.5 mm beam sigma and 120 GeV 700 kW beam
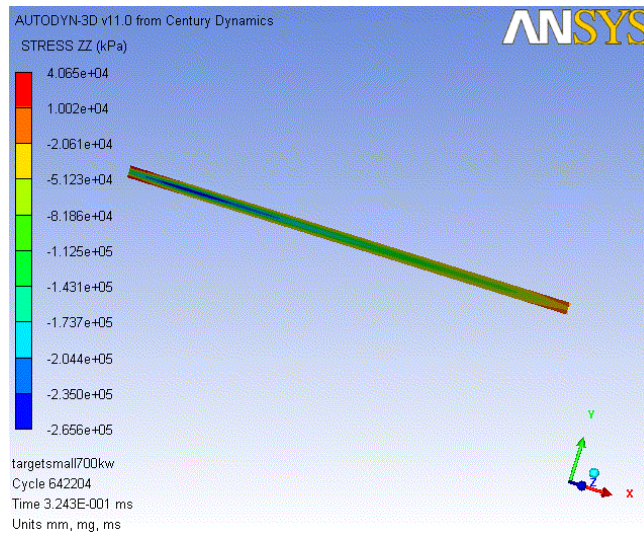

Figure 3.3.13
Contour plot of longitudinal stress at a snap shot in time in beryllium target with 1.5 mm beam sigma and 120 GeV 700 kW beam
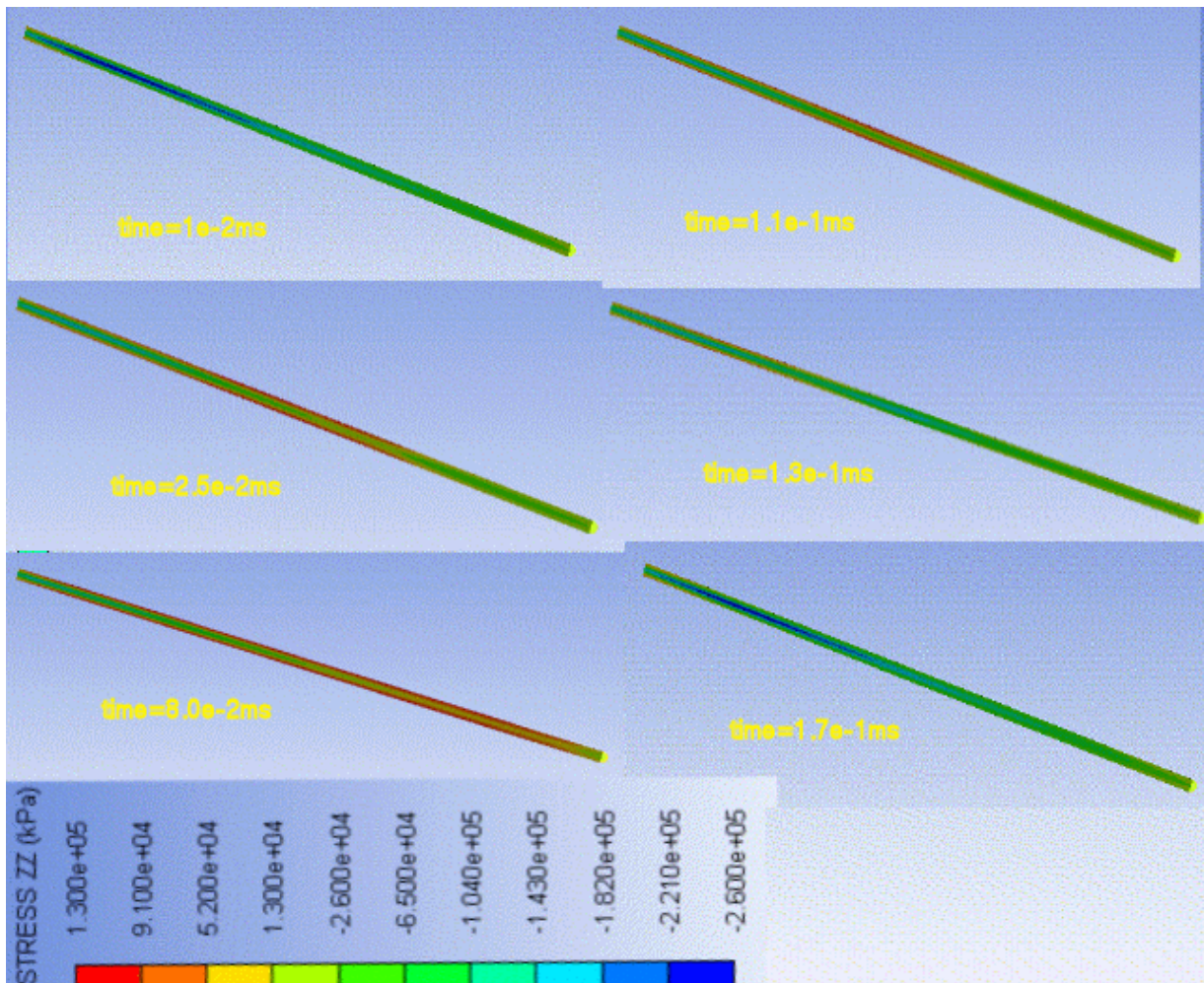
Figure 3.3.14 Longitudinal stress contour at various time increments, shows repeating pattern of fluctuating longitudinal stress waves

It can also be noted that the form of the Von Mises stress follows the dominant longitudinal stresses and reaches a maximum of about 177 MPa. This compares to the thermal stress without inertia effects of 100 MPa. Figures 3.3.15 and 3.3.16 show the oscillations of Von Mises stress at gauge point 13 (near the maximum energy deposition) and a contour plot of Von Mises stress.

In most engineering problems comparison of the Von Mises stress with the yield stress is a good measure of safety factor or indication of failure. In the case of high frequency stress waves an additional variable makes judging the failure criteria more difficult. Strain rate hardening of a material may cause the yield strength to be increased above the level obtained in standard steady tensile tests (Schierloh et al., Vaschenko et al.). Another output from AUTODYN is strain rate which is highest on axis of the target. Figures 3.3.17 and 3.3.18 show the strain rate in the target as a function of time at various positions in the target. Levels of up to 100 s^{-1} are seen. These levels may not be high enough to cause a significant increase in yield strength. However it may still be useful to note that the strain rate depends on the dimensions of the target and also the magnitude of stress applied. Smaller targets and higher applied stresses both lead to an increase in strain rate.
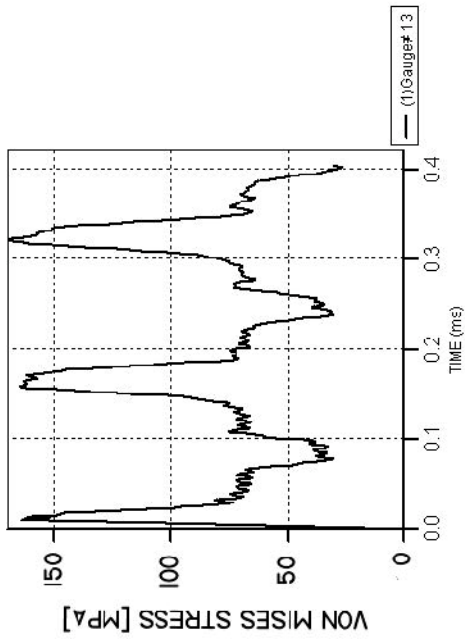
Figure 3.3.15
Von Mises stress at gauge point 13 (near the maximum energy deposition, and location of maximum Von Mises stress) in beryllium target with 1.5 mm beam sigma and 120 GeV 700 kW beam
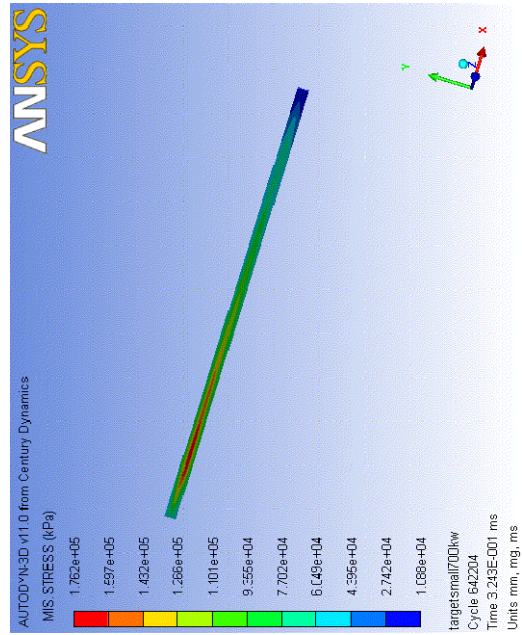

Figure 3.3.16
Contour plot of Von Mises stress at point in time when maximum occurs in beryllium target with 1.5 mm beam sigma and 120 GeV 700 kW beam
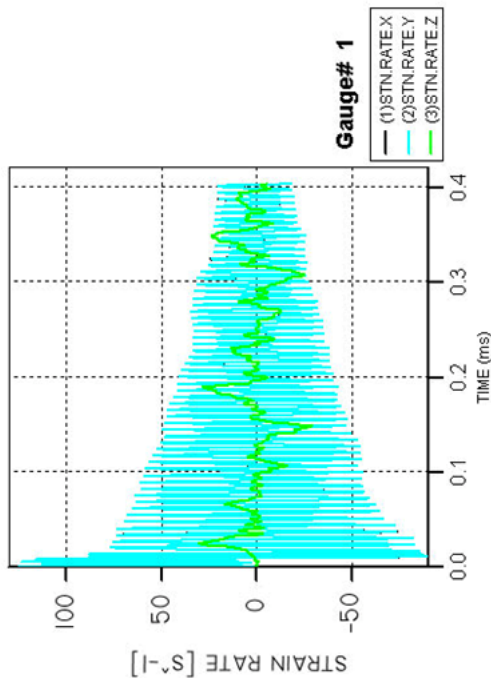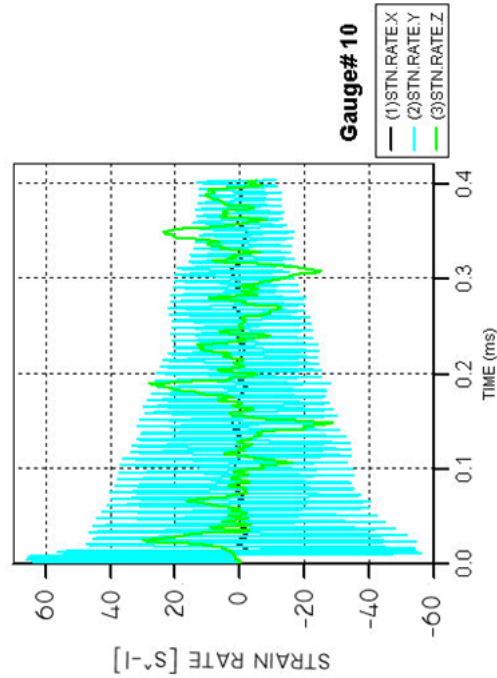

Figure 3.3.17
Components of strain rate at gauge point 1 (on axis quarter the way along target) in beryllium target with 1.5 mm beam sigma and 120 GeV 700 kW beam

Figure 3.3.18
Components of strain rate at gauge point 10 (at surface quarter the way along target) in beryllium target with 1.5 mm beam sigma and 120 GeV 700 kW beam

Stress in the 2.3 MW 3.5 mm sigma 120 GeV Beryllium target

In general, results for the 2.3 MW large beryllium target with 3.5 mm beam sigma follow the same characteristics as the 700 kW case studied in detail above. The peak stress as a result of the thermal gradient is about 90 MPa but with inertia effects included the induced stress waves cause a peak of around 180 MPa. Gauge point 1 is near the point of maximum energy deposition and also near the point where the maximum stress wave magnitude occurs (Figure 3.3.19). Figure 3.3.20 shows contour plots of Von Mises stress near the time where the peak value occurs.
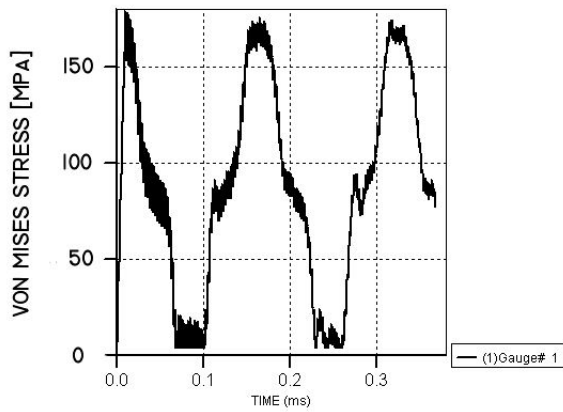
Figure 3.3.19
Von Mises stress at gauge point 1 (on-axis near peak energy deposition) in beryllium target with 3.5 mm beam sigma and 120 GeV 2.3 MW beam
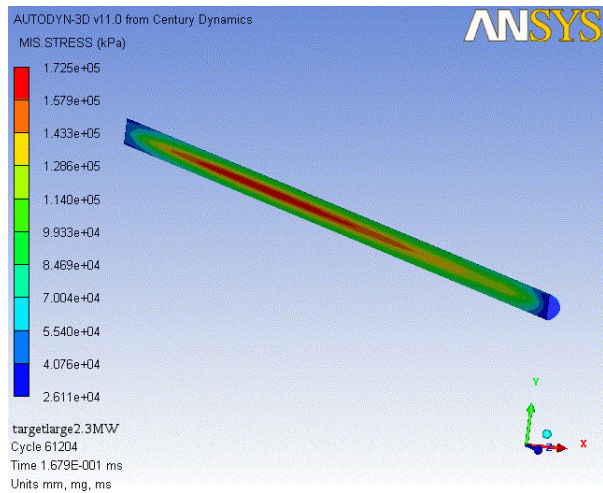
Figure 3.3.20
Contour plot of Von Mises stress near time of the occurrence of maximum Von Mises stress in beryllium target with 3.5 mm beam sigma and 120 GeV 2.3 MW beam

Spill Time and Target Segments

The peak magnitude of stress waves depend on how quickly the energy is deposited with respect to the expansion time of the target. If the energy is deposited extremely slowly with respect to the expansion time then no inertial component of stress will occur and there will just be a thermal stress component. As the energy deposition time is reduced then inertial effects and stress wave magnitudes build up until the energy deposition is effectively instantaneous with respect to the expansion time. Any further reduction in energy deposition time beyond this point has no effect. Figure 3.3.21 shows the peak stress wave magnitude as a function of spill duration. The spill duration has been varied by changing the interval between bunches.
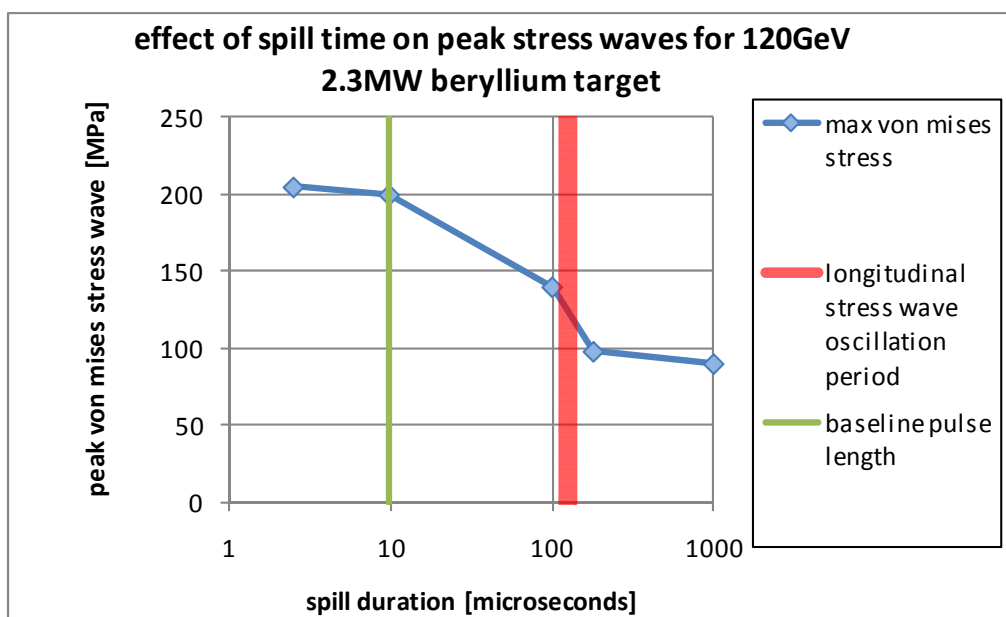

Figure 3.3.21 Effect of spill duration on peak stress wave magnitude in a 10.5 mm radius beryllium target with 120 GeV 2.3 MW beam

However a short pulse is required to maximise the signal to noise ratio at the detectors so scope for reducing the peak stress waves by increasing spill time may be limited. If the energy deposition time cannot be changed the expansion time of the target can be changed by segmenting the target. The radial expansion time is already short and radial waves are thus not significant as previously discussed, however the longitudinal expansion time could be bought down towards the baseline beam spill of 9.78 μs by segmenting the target into 20 segments of 50 mm in length. This longitudinal segmentation is depicted in Figure 3.3.22.
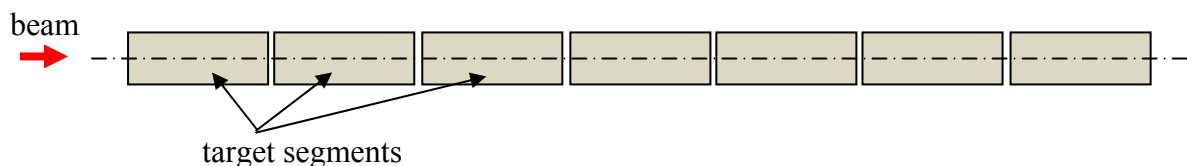

Figure 3.3.22 Illustration of target segments

Segmenting the target in this way has the same effect as increasing the spill time and significantly reduces the peak stress waves seen in the target segments. AUTODYN has been

used to model the stress waves for the 9.75µs spill time in a 50mm segment of the 21mm diameter 2.3MW beryllium target at the axial position where the peak energy deposition occurs i.e. 0.3m<z<0.35m. Figures 3.3.23 to 3.3.25 show the temperature rise after the spill, a snap shot of the stress profile and the Von Mises stress waves as a function of time. The peak Von Mises stress is about 120MPa, this compares to a value of 180MPa as seen with the standard 1m long target (Figure 3.3.20).
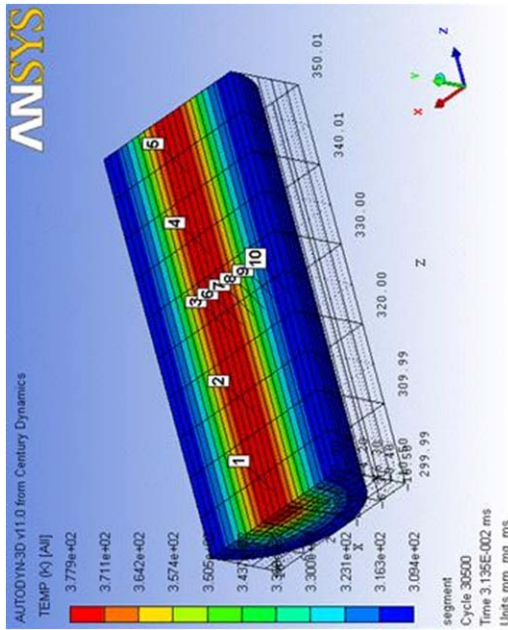

Figure 3.3.23. Temperature rise in beryllium target segment, 120 GeV, 3.5 mm sigma 2.3 MW(Gauge point positions shown)
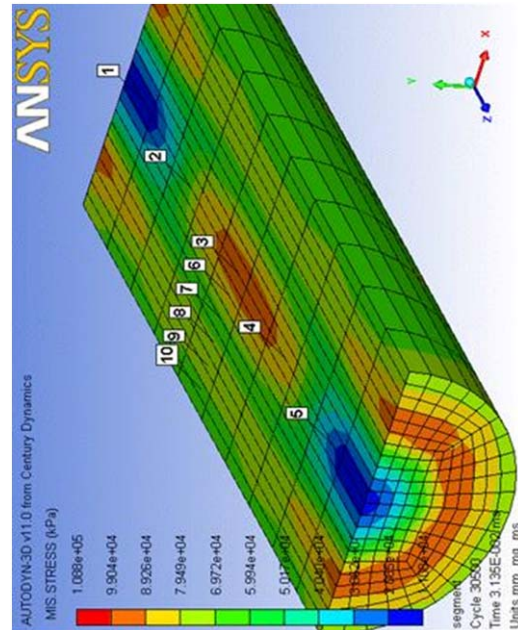

Figure 3.3.24. Snap shot contour of Von Mises stress in beryllium target segment, 120 GeV, 3.5 mm sigma, 2.3 MW
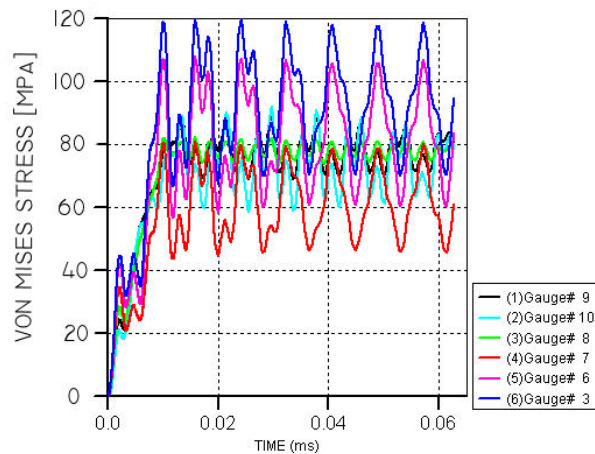

Figure 3.3.25. Peak Von Mises stress in beryllium target segment, 120 GeV, 3.5 mm sigma, (Gauge point positions shown in Figure 3.3.23)

As well as reducing the magnitude of stress waves in an ideal case where the beam hits the target on centre, segmenting the target has advantages for the case of an off-centre beam. An off-centre beam causes differential expansion of the target which results in bending stresses, deflections and vibrations. Segmenting reduces the differential expansion and reduces these bending stresses, deflections and vibrations. A thorough investigation of the performance of a segment targeted subjected to an off-centre beam is presented in Section 3.3.4.

3.3.3 Off-centre beam, Lateral deflection and vibration modes (ANSYS)

Outline

We now consider the case where, instead of being coaxial, the proton beam axis is offset from the target centreline. This generates an asymmetric temperature distribution in the target which produces an additional thermal bending effect. The objectives are to calculate the temperature distribution, thermal stress, resulting deflection and vibration modes due to the off-centre beam.

Analysis Procedure

The analysis followed the same steps used in the case of the coaxial target and beam, i.e. sequentially linked FLUKA, ANSYS thermal, and ANSYS mechanical runs. The main difference was that the previously used axisymmetric approach could no longer be used. Instead, a half-symmetry 3D approach was adopted, allowing the off-centre heating effects to be captured. As before, a single beam / target interaction was modelled.

Model Description

A 3D finite element model was constructed in ANSYS using 8-node brick elements of types SOLID70 and SOLID45 for the thermal and structural analyses respectively. A 2D free-mesh was created on the target end face, and then extruded along the target axis in equal steps to create the 3D elements. 40 axial divisions and approximately 30 radial divisions were used.

Four offset beam positions were studied, starting with a centred case, and then offsetting the beam centre by 1, 2, and 3 sigma from the target centre-line. Each case was run separately in FLUKA to calculate the distribution of deposited energy in the target material. The FLUKA energy distribution was read into ANSYS using a three-dimensional table, and converted to SI units before being applied as a heat generation rate in the ANSYS thermal simulation. The heat generation rates for these four cases are illustrated in Figure 3.3.26. For each of the four "off-centre" beam positions, two beam/target configurations were considered. These are listed in Table 3.3.4. They were chosen as "favourite" cases after examination of the parameter study results above.

Table 3.3.4 Beam / target configurations

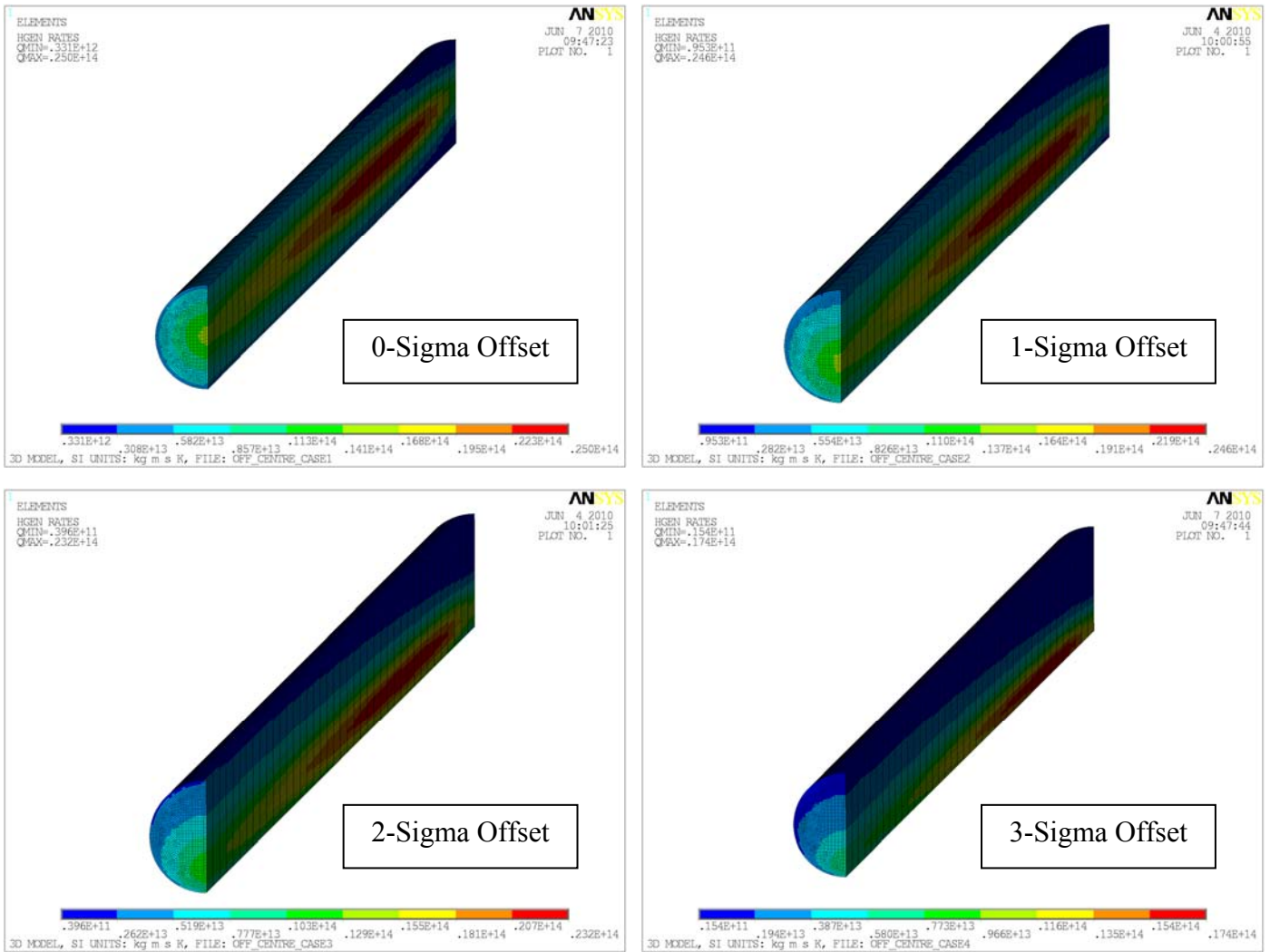| Proton Beam Energy (GeV)	Proton Beam Power (MW)	Beam Sigma (mm)	Target Diameter (mm)
120	0.7	1.5	9
120	2.3	3.5	21

Figure 3.3.26 Heat generation rate [W/m³]
Ø21 mm beryllium target, 120 GeV, 2.3 MW beam

In the structural analysis the target was fixed (cantilevered) at the upstream end and left free to deflect at the downstream end. Gravity effects were not included. The structural analyses were first run in the static, and then in the transient modes. The static structural results indicate the "steady-state" thermal deflection and thermal stress from the off-centre beam/target interaction. Inertia effects are ignored, and as such, we can say that this is the deformed shape around which the target would be expected to oscillate. The transient structural results indicate the real-time dynamic oscillations of the target, taking inertia into account.

Static Results

Example static result contour plots are included in Figure 3.3.27. The asymmetric temperature distribution is shown on the left, and the target deflection is shown on the right. The lateral deflection is plotted at true scale, with the undeformed shape indicated in outline only. With an off-centre beam one side of the target is heated more than the other. Deflection due to thermal expansion then leads to a static bending of the target. A summary of results for all of the parameter combinations considered is included in Table 3.3.5. The effect of varying the beam offset distance is summarised in Figure 3.6.28. Here, the worst

case in terms of both deflection and stress is at 2-sigma beam offset, where the increase in stress is of the order 50% compared to the zero-offset case. The peak energy density and integrated deposited energy are at a maximum when there is zero offset, and both reduce as the offset is increased.
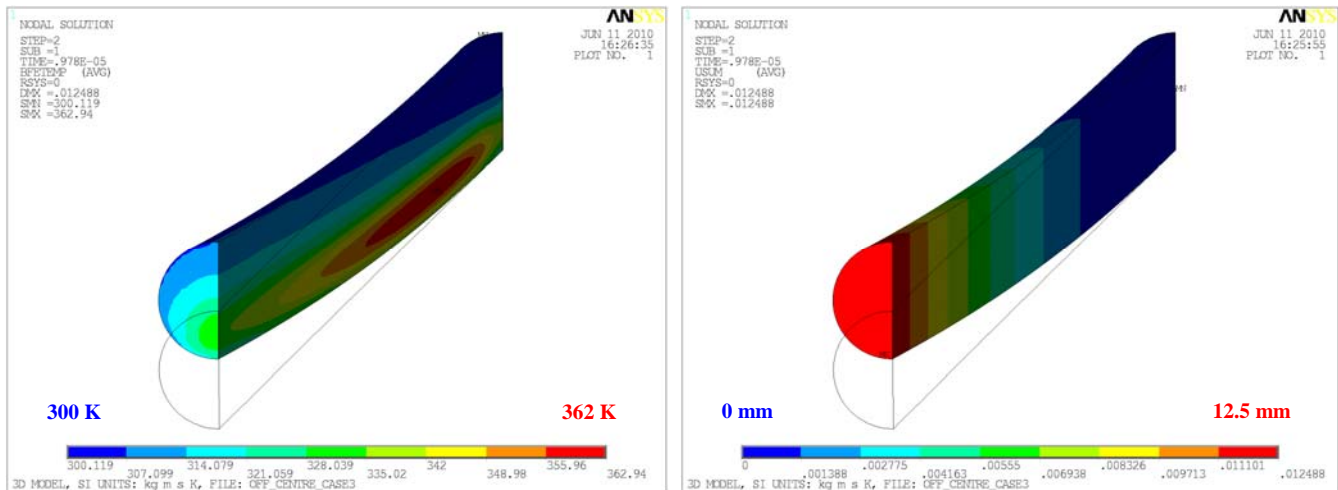

Figure 3.3.27 Temperature (left) and static deflection (right)
21 mm diameter beryllium target, 120 GeV, 2.3 MW beam, 2 sigma offset

Table 3.3.5 Static results summary, off-centre beam effects

Beam Energy (GeV)	Beam Power (MW)	Target Diameter (mm)	Beam Offset (mm)	Deposited Energy (kJ/spill)	Time Averaged Power (kW)	Peak Energy Density (J/cc/spill)	Max. ΔT per spill (K)	Max. End Deflection *static (mm)	Max. Von-Mises Stress *static (MPa)
120	0.7	9	0.0	4.2	3.2	255	69	0.0	99
120	0.7	9	1.5	3.9	3.0	257	70	19.2	124
120	0.7	9	3.0	3.0	2.3	244	67	27.0	151
120	0.7	9	4.5	1.6	1.2	200	55	15.7	159
120	2.3	21	0.0	30.8	23.1	248	68	0.0	90
120	2.3	21	3.5	28.7	21.6	245	67	9.0	122
120	2.3	21	7.0	21.8	16.4	230	63	12.5	131
120	2.3	21	10.5	11.0	8.3	175	48	8.0	129

The effect of deflection due to gravity should be added to these results. In the case of a beryllium cylinder cantilevered from one end, the gravity deflection (sag) and associated bending stress depend strongly on the cylinder diameter (Figure 3.3.29). This is the assumed method of support for a stand-alone target inserted into a magnetic horn bore. Supporting the target from both ends would significantly reduce the gravity effects.
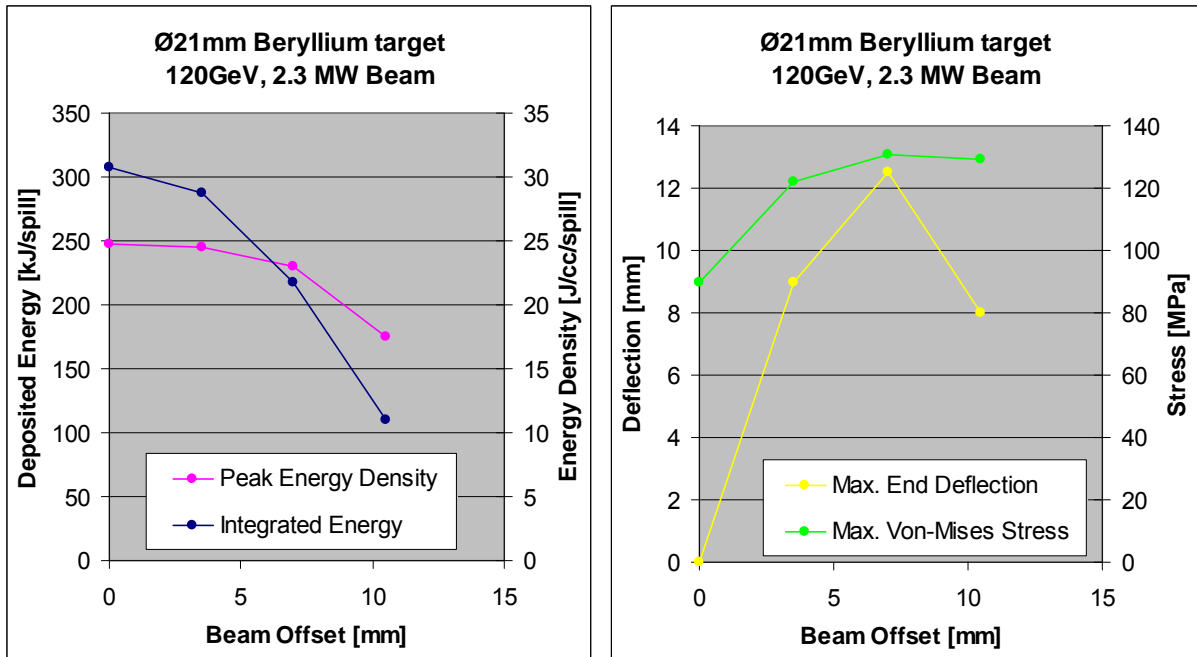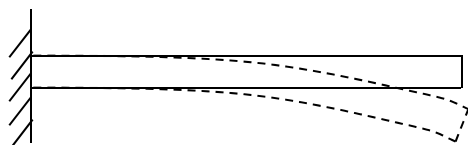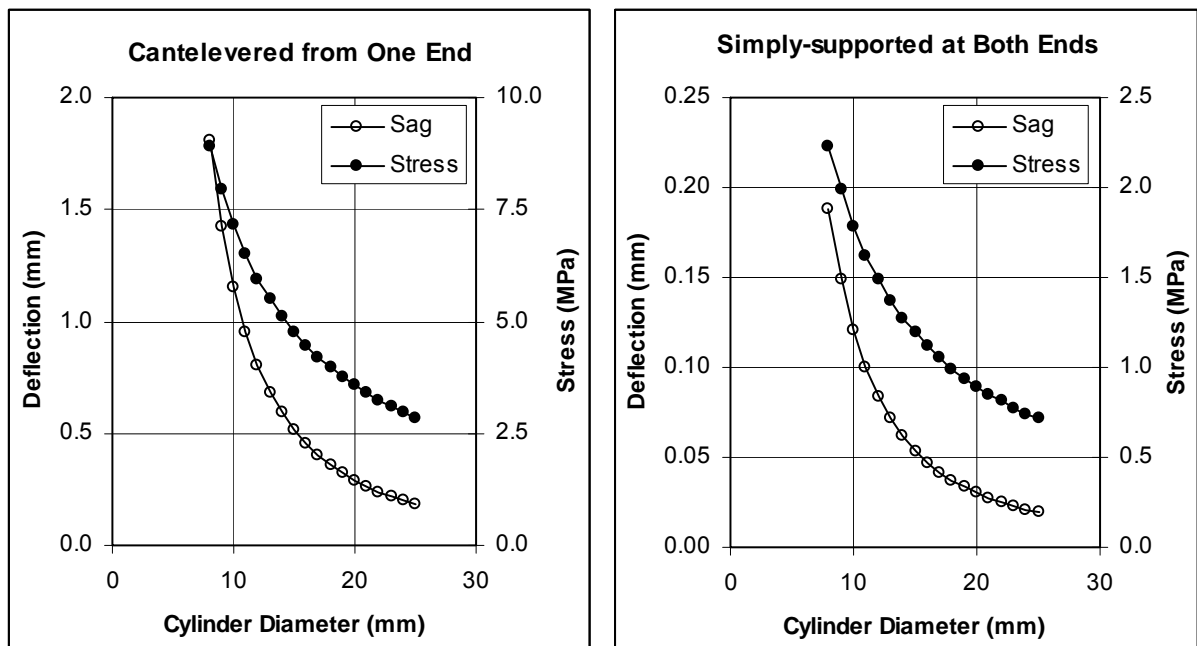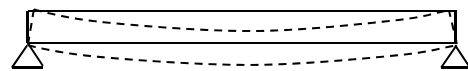
Figure 3.3.28 Static results summary

Cantilever Case:
• Max sag at free end
• Max stress at held end

Simply-supported Case:
• Max sag at centre
• Max stress at centre

Figure 3.3.29 Gravity effect on a 1m long solid beryllium cylinder

Transient Results

The apparent worst case, i.e. the 2-sigma beam offset, was chosen as the input to a transient structural analysis, i.e. turning inertia effects on. The result is plotted in Figure 3.3.30. The data points show the end deflection as a function of time. The maximum transient deflection is roughly double the static deflection, indicated by the dashed line. There are roughly 13 milliseconds between the beam heat being deposited and the target reaching its most deflected state.

The first two mode frequencies for a 21 mm diameter 1 m long cantilevered beryllium rod (Figure 3.3.31) were calculated to be 38 Hz and 240 Hz. These vibration modes correspond to the 26 milli-sec and 4 milli-sec oscillation periods that are clearly visible in the dynamic end-displacement plot. The natural frequencies and corresponding mode shapes relating to a number of potential target / constraint conditions are described in Table 3.3.6.
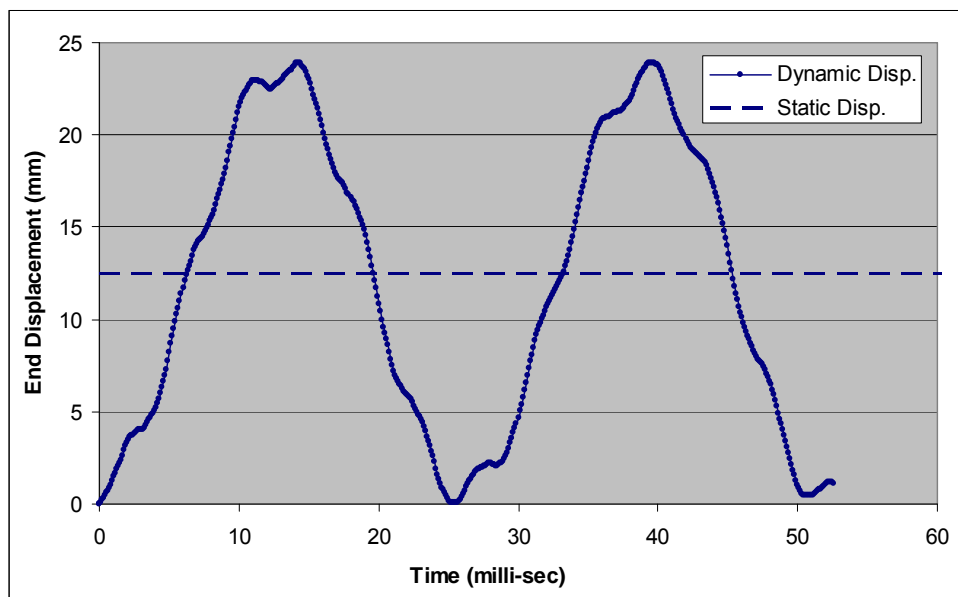

Figure 3.3.30 End deflection from structural transient analysis
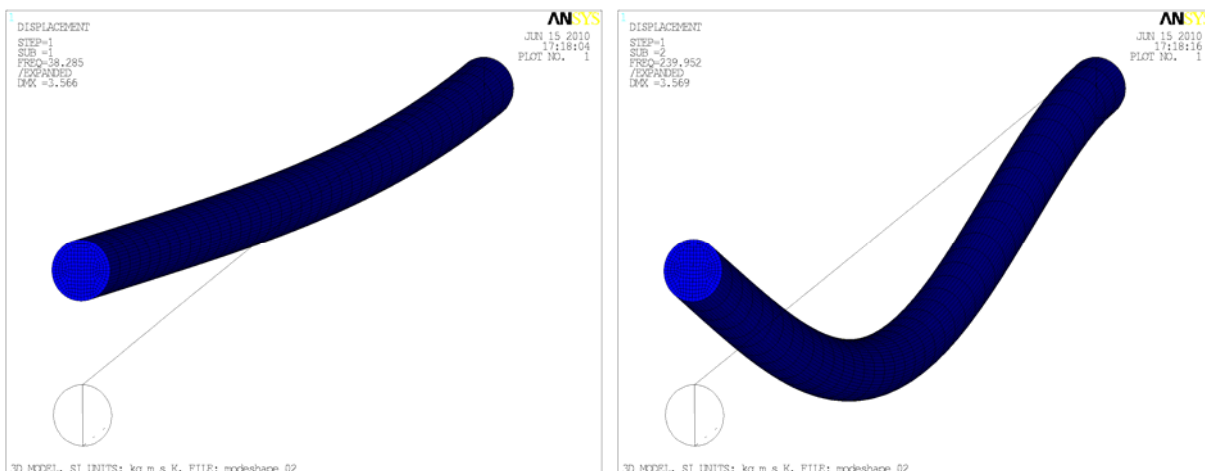*21 mm diameter beryllium target, 120 GeV, 2.3 MW beam, 2 sigma offset*
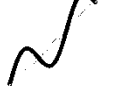
Figure 3.3.31 Mode shapes for a 21 mm diameter, 1 m long, cantilevered beryllium cylinder
1st mode = 38 Hz (left), 2nd mode = 240 Hz (right)

63

Table 3.3.6 Natural frequencies and corresponding mode shapes for a number of target / constraint conditions

Material	Radius (mm)	Length (mm)	Upstream Constraint	Downstream Constraint	1st Mode [Hz]		2nd Mode [Hz]		3rd Mode [Hz]	
Beryllium	10.5	1000	fixed	free	38.3		239		669	
Beryllium	4.5	1000	fixed	free	16.4		103		288	
Beryllium	10.5	1000	simply supported	simply supported	107		429		963	
Beryllium	4.5	1000	simply supported	simply supported	46		184		414	
Beryllium	10.5	1000	fixed	cart	168		542		1130	
Beryllium	4.5	1000	fixed	cart	71.9		233		486	

In practice, the dynamic stress will be dominated by longitudinal stress oscillations on a much shorter timescale than the ~26 milli-sec 1st mode period for the cantilevered target. These stresses can be significantly higher than the previously calculated "static" stress level quoted in Table 3.3.5. Further work to fully understand the nature of these dynamic stresses is presented in Section 3.3.4.

3.3.4 Off-centre beam with thermal stress and inertial effects (AUTODYN)

Dynamic Analysis of Off-centre Beam Heating on the Target

As explained in the previous sections, proton beam induced heating on the target rod produces a complex set of dynamic stress waves as well as residual temperature gradient stresses which fades at the rate of thermal conduction. If the beam interacts with the target entering the face of the rod out of the centreline (as can be expected to a certain extent in a real facility) the stress pattern is further complicated if compared with a symmetrical excitation. The maximum intensity of such stress field depends on the coordinates and direction of the beam at the point of interaction with the target.
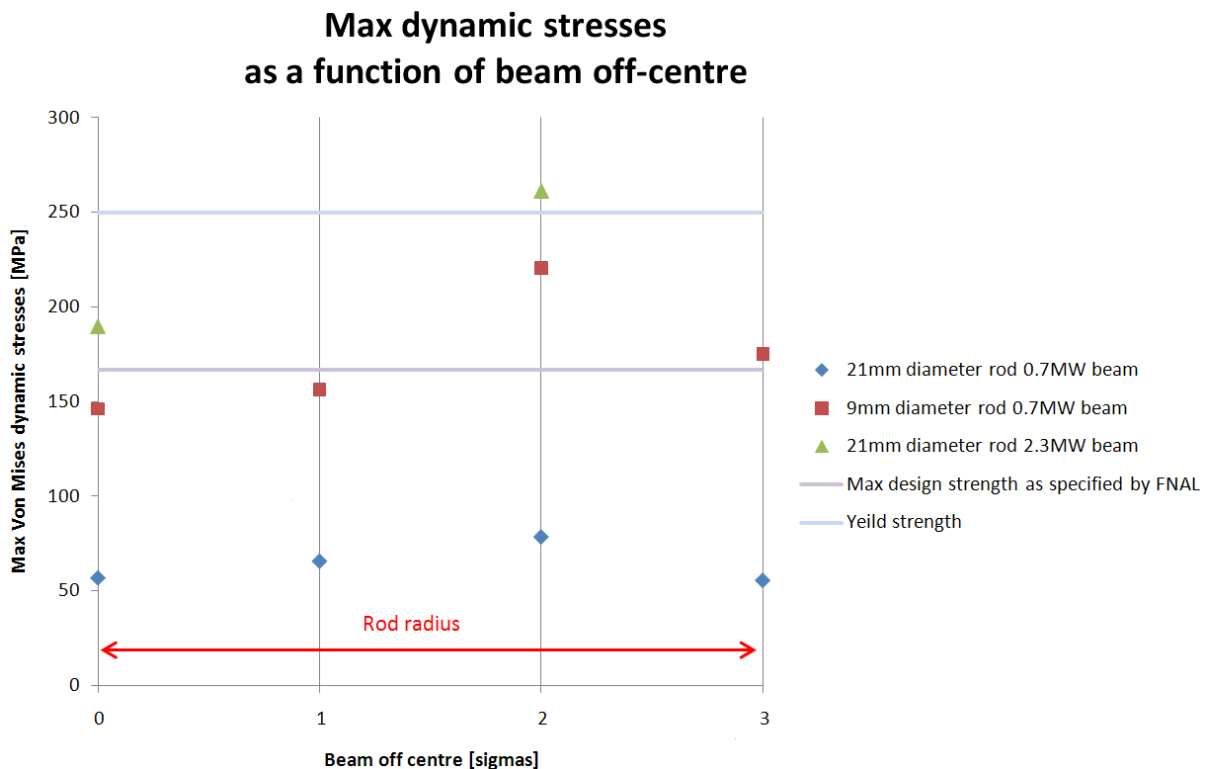
Figure 3.3.32 Effect of off-centre beam on peak dynamic stress

As shown in Figure 3.3.32, AUTODYN dynamic simulations predict that an off-centre beam could increase the maximum Von Mises stresses in a beryllium target rod by over 50%. The simulations shown in Figure 3.3.32 assume the beam to be parallel with the target rod, and off-centre by a multiple of the beam sigma (the target radius being 3 sigma). The Figure shows that the stresses increase as a function of the beam off-centre up to about 2 sigma. Moving the beam further off-centre reduces the amount of energy deposited in the target material and so when the beam is grazing the side of the target (off-centre 3 sigma) the stresses appear lower.

The remainder of this section presents results for 2 sigma beam off-centre, as this is considered to be the worst case scenario. Although this may not be a condition to be expected during the continuous operation of the accelerator, it is reasonable to assume that the beam

will not be perfectly centred. Note also that the results here presented show a higher degree of sensitivity to beam off-centre for smaller rods, where beam sigma is also smaller and the collimation more challenging.

The simulations suggest that if the target is unbound (or under-constrained, e.g. cantilevered) and the beam interaction is off-centre on the rod, then significant bowing and whipping of the free end of the rod can be expected. Figures 3.3.33 to 3.3.35 show the simulated characteristic stresses, velocities and displacement of a 21 mm cantilevered beryllium rod excited by a 0.7 MW beam, off-centre by 2 sigma. Figure 3.3.36 shows the real scale deformation of a 9 mm beryllium rod subject to the same beam conditions.
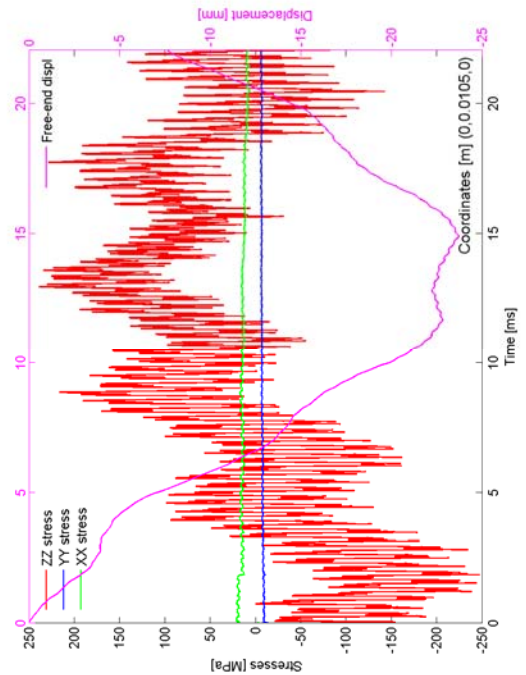
Figure 3.3.33
21 mm diameter cantilevered Be rod, 0.7MW off-centre beam. Stress components by the constrained face and displacement of the free face

Figure 3.3.34
21mm diameter cantilevered Be rod, 0.7MW off-centre beam. Stress components measured near the shower max

Figure 3.3.35
21 mm diameter cantilevered Be rod, 0.7 MW off-centre beam. Velocities components by the free face
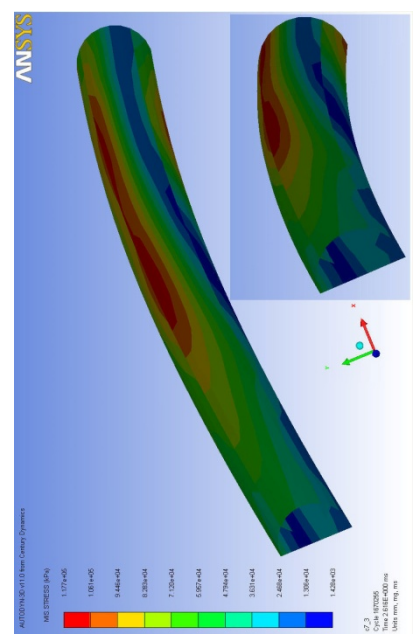
Figure 3.3.36
9mm diameter cantilevered Be rod, 0.7 MW off-centre beam. Real scale rod deformation. Note: the Figure does not show the max stresses

These examples highlight high deformations and high velocities unsuitable for final target design. The conditions express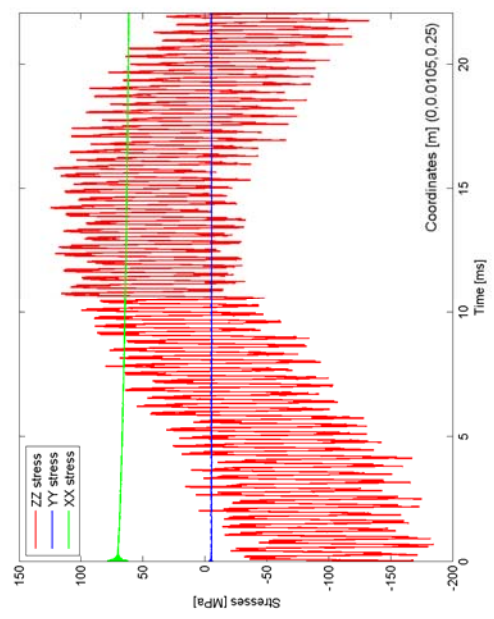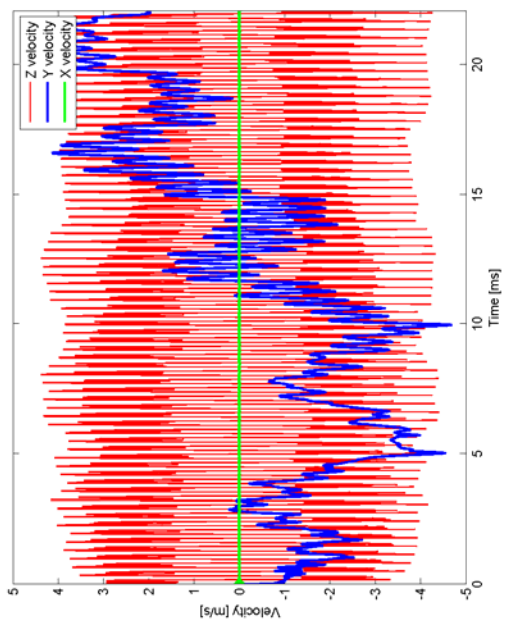ed in Figures 3.3.33 to 3.3.35 are strongly dependant amongst other things on the boundary conditions with which the target rod is constrained/supported. Figure 3.3.37 shows the simulated max Von Mises stresses of Be rods with different boundary conditions. As discussed later in this Section, note that the time averaged stresses depend on the resonant frequencies of the rods which in turn are a function of the boundary conditions. The simply-supported configuration (i.e. cantilever + cart) is probably the most realistic from an engineering point of view and so the results presented later in this section were simulated using this boundary condition. In this configuration one end of the rod is fixed while the other is held concentric and free to move axially.

Effect of boundary constraints on max dynamic Von Mises stresses
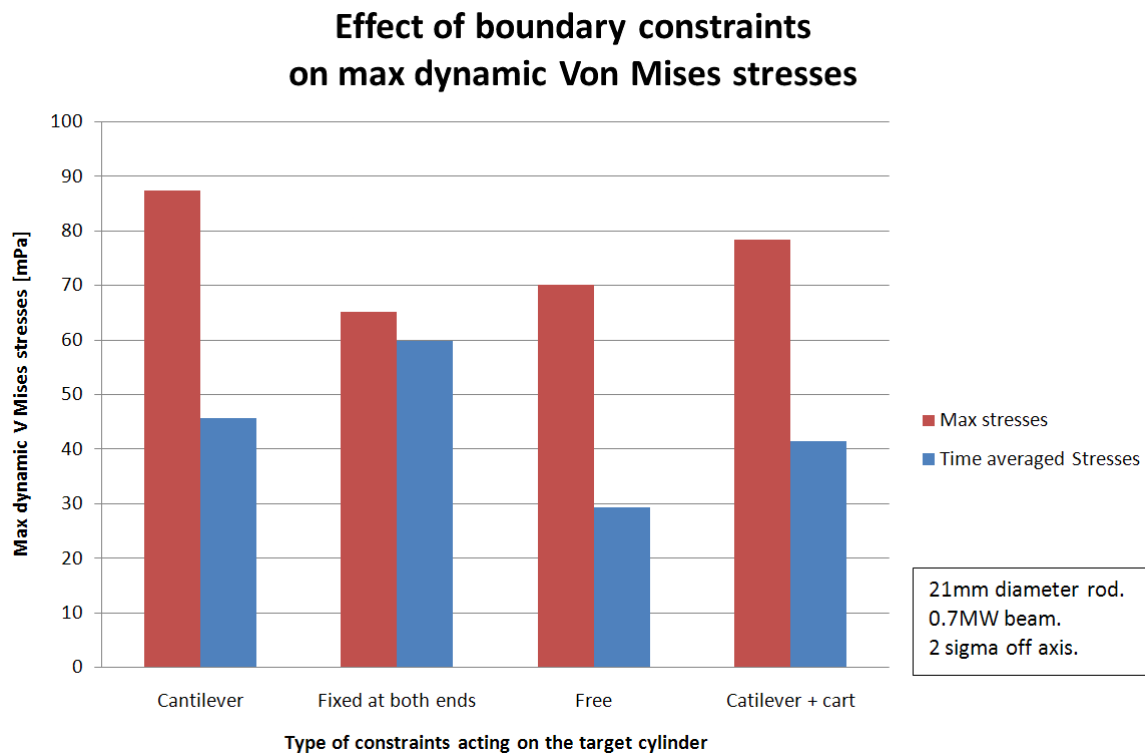
Figure 3.3.37 Effect of the boundary conditions on the peak stress in a cylindrical target for 0.7MW beam and 2sigma off axis

The complicated stress field developing in the target rod when excited by an off-centre beam can be discretized using frequency analysis. Figure 3.3.38 shows the single sided (i.e. absolute) amplitude spectrum up to 10 kHz of Von Mises stresses gauged throughout the target. The plot highlights the major dynamic stress components which are respectively due to the longitudinal resonance (i.e. the target stretching and compressing over the length) around 3 kHz and the transversal resonance (i.e. the bowing of the rod around the middle length) around 165 Hz. These frequencies are related to the geometrical characteristics of the rod as well as to the speed of sound in the material and can be validated analytically with reasonable accuracy for a simple rod. Figure 3.3.39 highlights on a logarithmic scale the less significant effect of the radial resonance frequency (i.e. thinning and swelling of the rod) around 300kHz. Note that these resonance frequencies are associated with real straining of the rod (e.g. bowing exemplified in Figure 3.3.37). In spite of the fact that the material may be more resistant at very high strain rates, [Schierloh et al], it should also be noted that the lower frequencies (e.g. the transversal bowing) could fatigue the rod. Figure 3.3.40 shows that whist resonating longitudinally at around 3 kHz the target material experiences significant velocities.
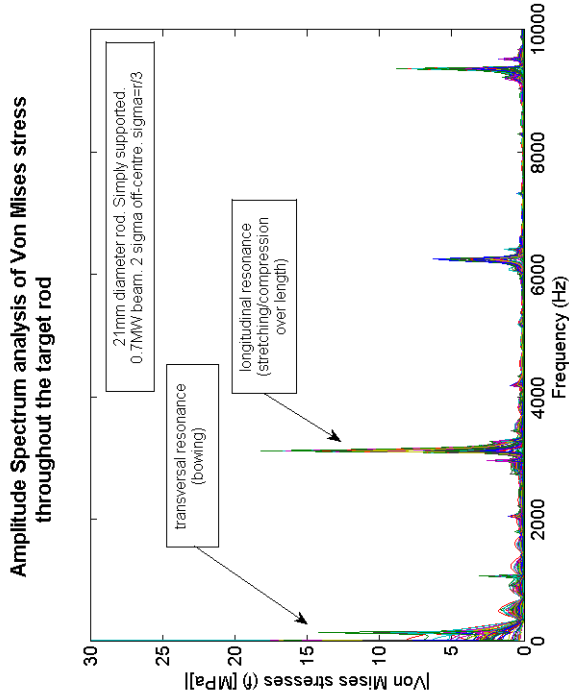
Figure 3.3.38
Single sided amplitude frequency analysis (up to 10 kHz) of Von Mises stresses
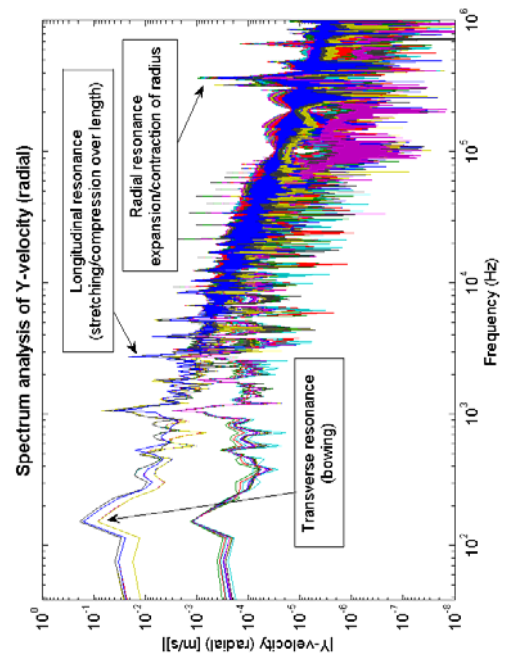
Figure 3.3.39
Single sided frequency analysis of radial velocities
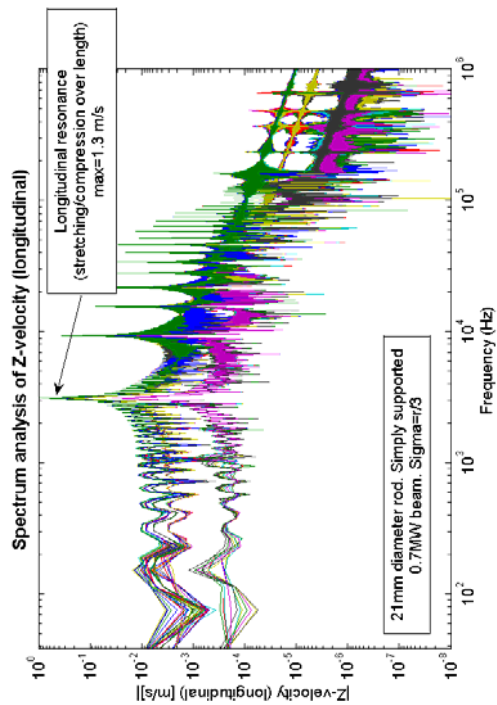
Figure 3.3.40
Single sided frequency analysis of longitudinal velocities
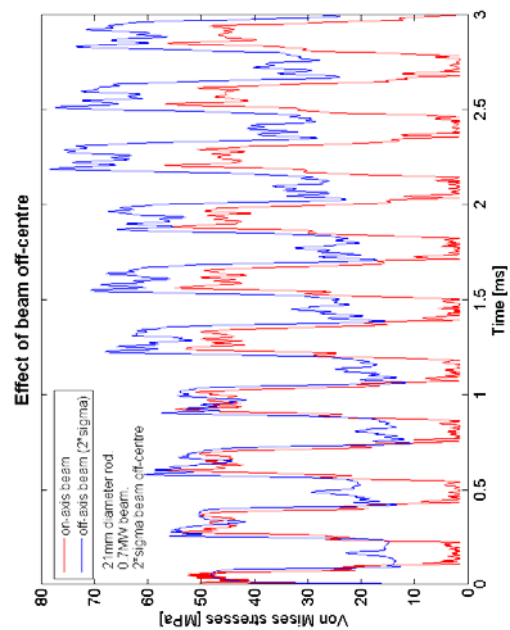
Figure 3.3.41
Effect of the beam off-centre on the dynamic stresses.

Figure 3.3.41 shows the superposition of the stress patterns generated by an on-centre and off-centre beams. The regular vertical peaks are due to the longitudinal resonance of the stresses. When the beam is off-centre there is a residual stress (base of the blue line) due to the thermal gradient, which as discussed in the previous Section, can be considered quasi-static on the millisecond time scale (the thermal gradient dissipates with thermal conduction which is slow compared with the other inertial stress waves described in this chapter). The variation in the oscillation of the blue line is due to the transverse resonance (i.e. bowing of the rod), a complete period of oscillation is not seen in the timescale of the graph.

In conclusion the highest stresses in the target rod are mostly due to a combination of the quasi-static thermal gradient stresses, the longitudinal stress wave resonance and the transverse stress resonance (bowing). Simulations suggested that an effective way to reduce each of these three components is to segment the target longitudinally.

Segmented Targets

One possible solution would be to have a series of finned segments (suitable for gas cooling) supported by an outer tube. A preliminary FLUKA-AUTODYN model was developed to evaluate the stresses in a 20 mm long, 9 mm diameter beryllium pellet with 10 mm cooling fins subjected to a 0.7 MW off-centre proton beam. As in Figure 3.3.42 the model highlights two main problems. Firstly the fins show signs of buckling as a result of the beam induced thermal expansion and considering the radial restraint due to the outer tube. Secondly, as expected, the simplified model shows stress concentrations focusing at the base of the fins. Both issues could be overcome with appropriate engineering of the target segments. The process of redesigning the segments to reduce stress concentrations whilst stiffening the fins is expressed in Figures 3.3.43 to 3.3.45. This however does not solve the problem as having stiffer fins would then transmit the stresses to the outer tube. Furthermore, this configuration is likely to be detrimental to the Figure of Merit as it adds material around the beam interaction region. If this configuration is selected for future studies, it should be noted that in this case engineering and physics yield are contradictory so that a mechanically viable design may provide low yield.
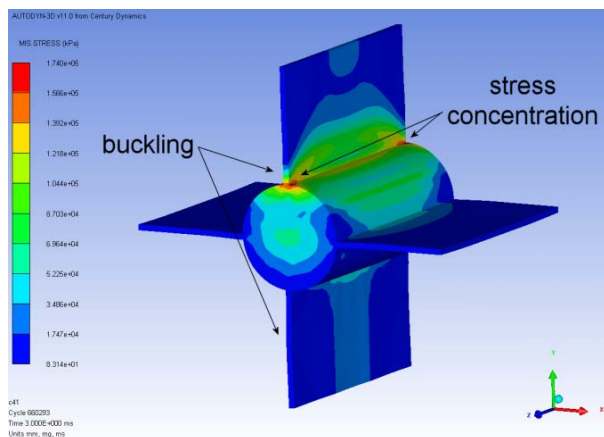
Figure 3.3.42
Stresses and deformations in a finned target segment
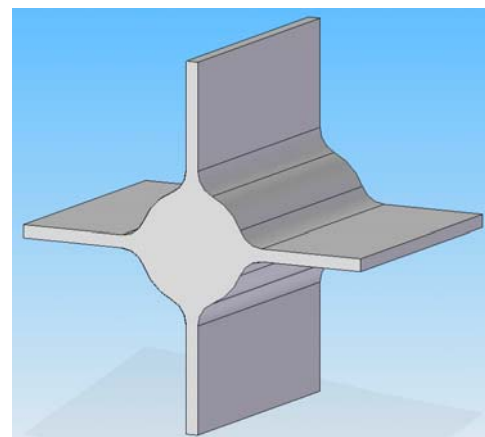
Figure 3.3.43
Target segment with rounded fin joints
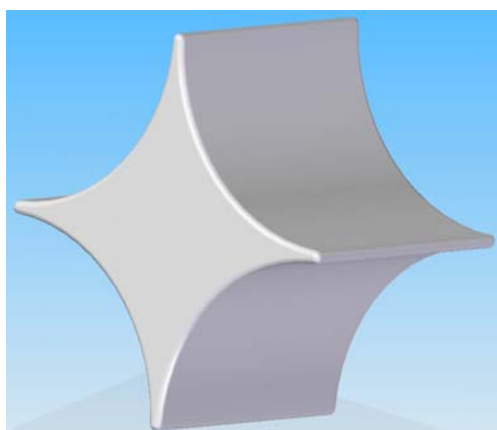
Figure 3.3.44
Target segment with stiffened fins

Figure 3.3.45
Target segment in the container tube

An alternative segmenting approach that has also been considered is to shrink fit a series of cylindrical beryllium segments inside a tube. Figure 3.3.46 shows the geometry of such a layout. Stress calculations for the 2.3 MW beam on 21 mm diameter segments indicate that the stress levels in the segments are reasonable (Figure 3.3.47). However with the off-centre beam the simulation indicates the presence of stress concentrations in the supporting tube at the gaps between the segments (Figures 3.3.48 and 3.3.49). The magnitude of stress in these regions is hard to resolve, but the result does highlight the physical presence of a stress concentration which would need further investigation if this concept was to be taken forward. The assembly was fixed at one end with a cart at the other end. Peak Deflection was found to be of the order of 1 mm with a beryllium outer tube, but several mm with an aluminium outer tube which has less stiffness and greater energy deposition and thermal expansion.
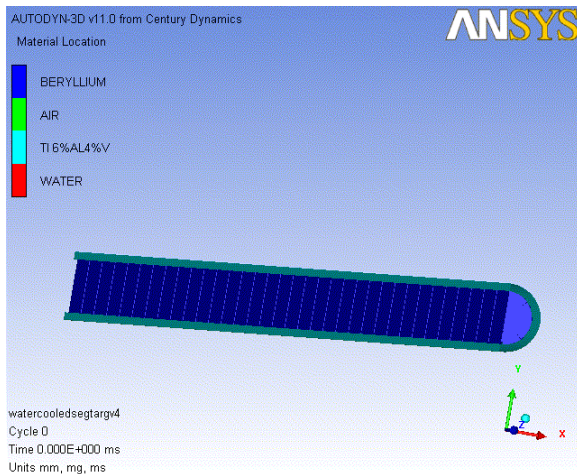
Figure 3.3.46
AUTODYN model of beryllium segments shrunk fit inside a titanium water jacket
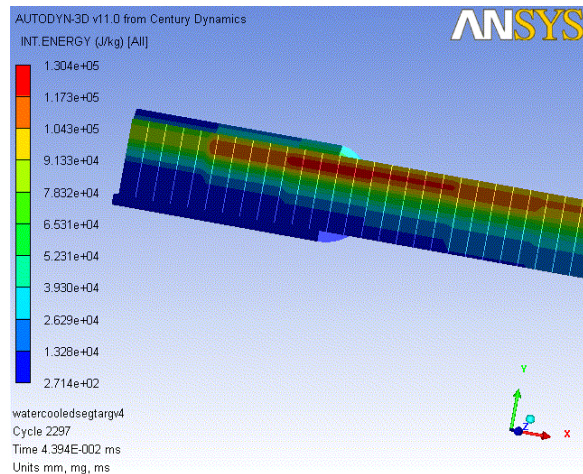
Figure 3.3.47
Energy deposition in the segments and tube as a result of off centre beam
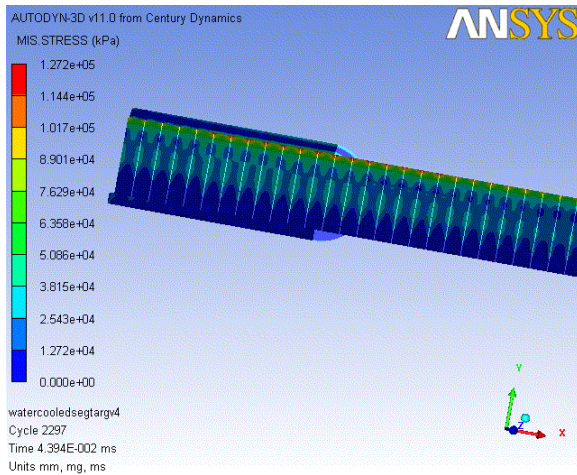
Figure 3.3.48
Stress in the segments ~130 MPa
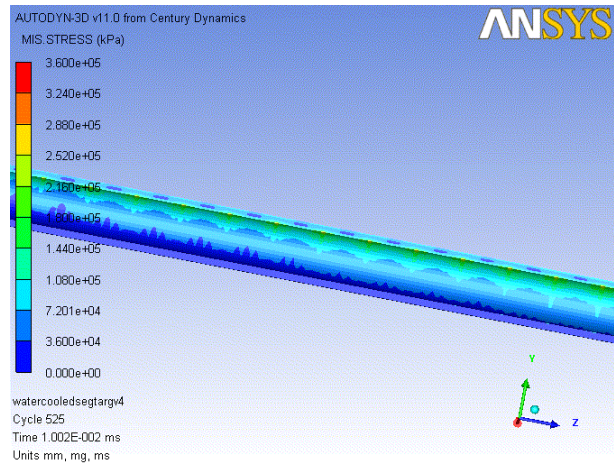
Figure 3.3.49
Stress concentrations in the tube predicted stress greater than 360 MPa (NB need to introduce curved surfaces to avoid stress concentrations)

It is standard engineering practice to avoid sharp edges as a method to prevent stress focusing. This naturally leads to a spherical design as this is the geometry which offers the most homogeneous stress field: the lack of corners and flat surfaces prevents focusing (or constructive interference) of the stress waves. Furthermore spheres have no structural weak point.

In order to evaluate the maximum dynamic stresses a set of FLUKA and AUTODYN models were developed simulating the effect of an off-centre beam interacting with an array of spheres. Figure 3.3.50 shows the energy deposited in some of the spheres at the ends of the target and near the shower max (beam direction right to left) while Figure 3.3.51 shows a typical stress contour plot in a section of a sphere.
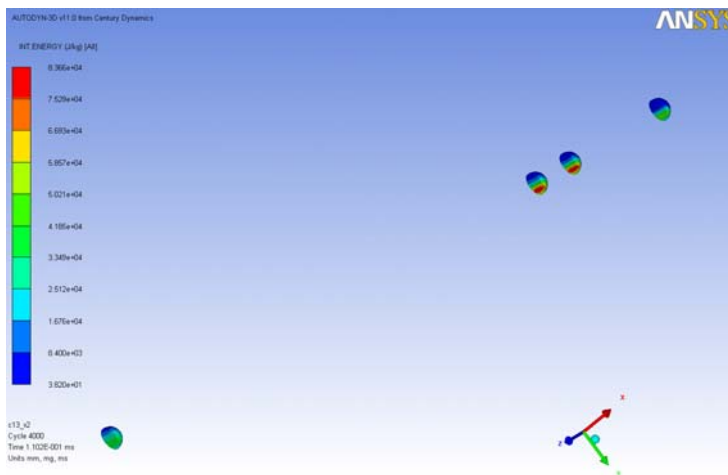
Figure 3.3.50
Segmentation of the target rod into spheres. Simulation of first, last and other spheres near or at the shower max subject to an off-centre beam.
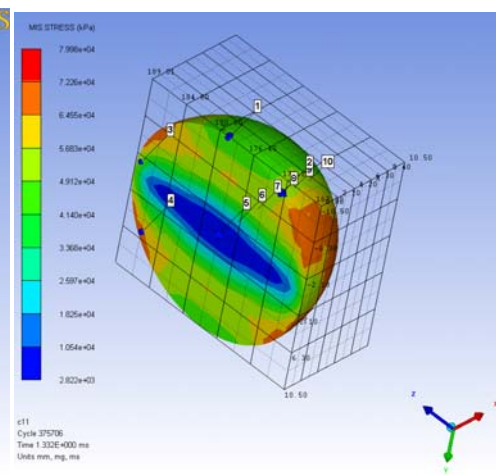
Figure 3.3.51
Von Mises stresses (not max) in a single beryllium sphere subject to an on-centre beam

Figure 3.3.52 highlights the difference in the stress pattern as well as in the stress intensity of a 17 mm beryllium rod compared to a beryllium sphere of equal diameter when subject to a 2.3 MW off-centre beam. As shown in the figure, the rod is predicted to experience spiralling stresses growing beyond the yield strength of the material. On the other hand the sphere faces a transient of inertial stress waves which is short and of relatively small intensity. The slow decline of the stress in the sphere (blue line sloping down) is due to the conduction of heat through the sphere.
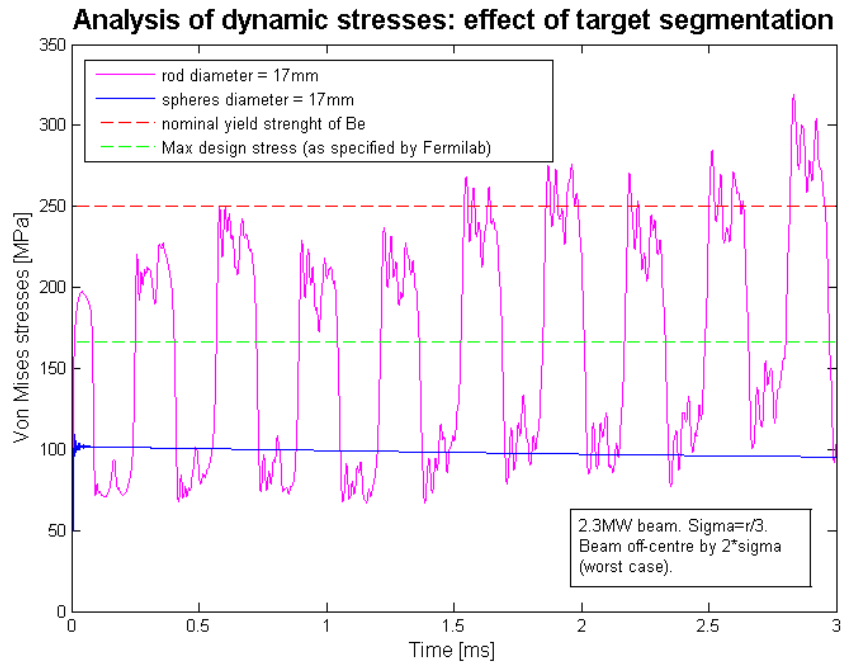
Figure 3.3.52 Comparison of stress patterns in a cylindrical rod and sphere both of the same diameter

So spheres of smaller diameter can be used to improve the pion yield whist remaining within a safe engineering envelope.

As in the previous example, the array of spheres (or pseudo-spheres) needs external support for example in the form of a thin titanium tube (low Z and high strength). The outer tube would provide structural integrity and so it should be kept away from the beam to minimise secondary heating induced stresses. Further, low density (to prevent pion re-absorption) non-structural elements are required to hold the spheres concentric in the outer tube whilst allowing room for the coolant. Figure 3.3.53 shows a simplified example of spheres based target layout. A preliminary FLUKA-AUTODYN model indicated however that the integrity of straight tubular titanium spacers could be compromised by the stresses resulting from secondary beam induced heating (see Figure 3.3.54). A variation of the model (see Figure 3.3.55) investigated a helical support showing that the stresses would in this configuration be well within the yield strength of the material. Note also that a target with tubular helical spacers could survive some degree of deformation of the spacers without overloading or compromising the structural integrity of the target array (e.g. the spacer could squash axially or radially to make room for the thermal expansion of the components). Figure 3.3.56 shows a concept design mock-up of an array of spheres with triple-helix concentric spacers and a Perspex outer casing.
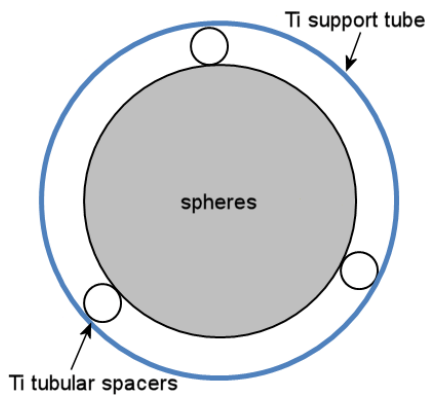
Figure 3.3.53
Simplified spheres based target layout
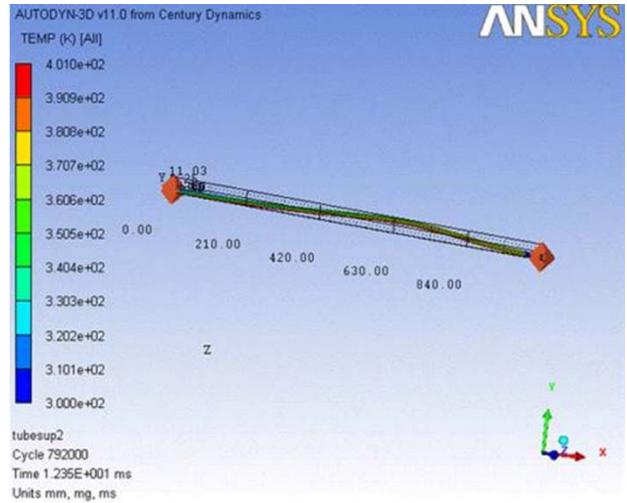
Figure 3.3.54
Array of spheres in a helical support
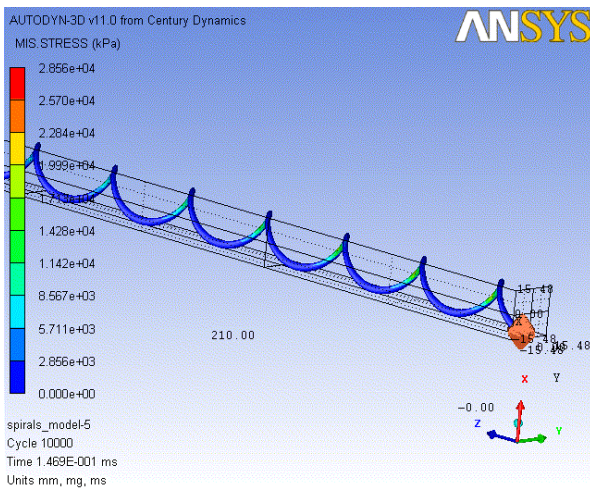
Figure 3.3.55
Beam secondary heating induced stresses in a Ti spiral support

Figure 3.3.56
Concept design of an array of spheres with triple helix spacers and Perspex outer casing

As further discussed in Section 4.9, the helical spacers could be optimised to guide and even inject coolant around the spheres.

3.4 Summary

Proton beam target interactions have been simulated using energy deposition results from FLUKA as an input for ANSYS and AUTODYN. Beryllium, AlBeMET and aluminium have been considered as target materials. Keeping to the rule of radius equalling three times the beam sigma, cylindrical target rods of varying diameter have been investigated. Both beam powers of 700 kW and 2.3 MW have been used as inputs to the stress calculations. Thermal stresses and inertial stresses are considered separately and in combination so as to identify their individual contributions. In addition to an on-centre beam, less than ideal but potentially realistic off-centre beam cases are considered. The parameter space defined in Task A in terms of target size and material has been covered and additionally some consideration has been given towards segmented target geometries (such as a series of spheres) as a way of reducing inertial stresses. Figure 3.5.1 shows the peak Von Mises stress (including thermal stress and all inertial effects) for simply supported beryllium cylindrical rods and spheres with a two sigma off-centre beam (worst stress case) across the range of diameters and power levels defined in Task A. Also shown on the figure is a design stress taken as two thirds of the nominal yield stress.
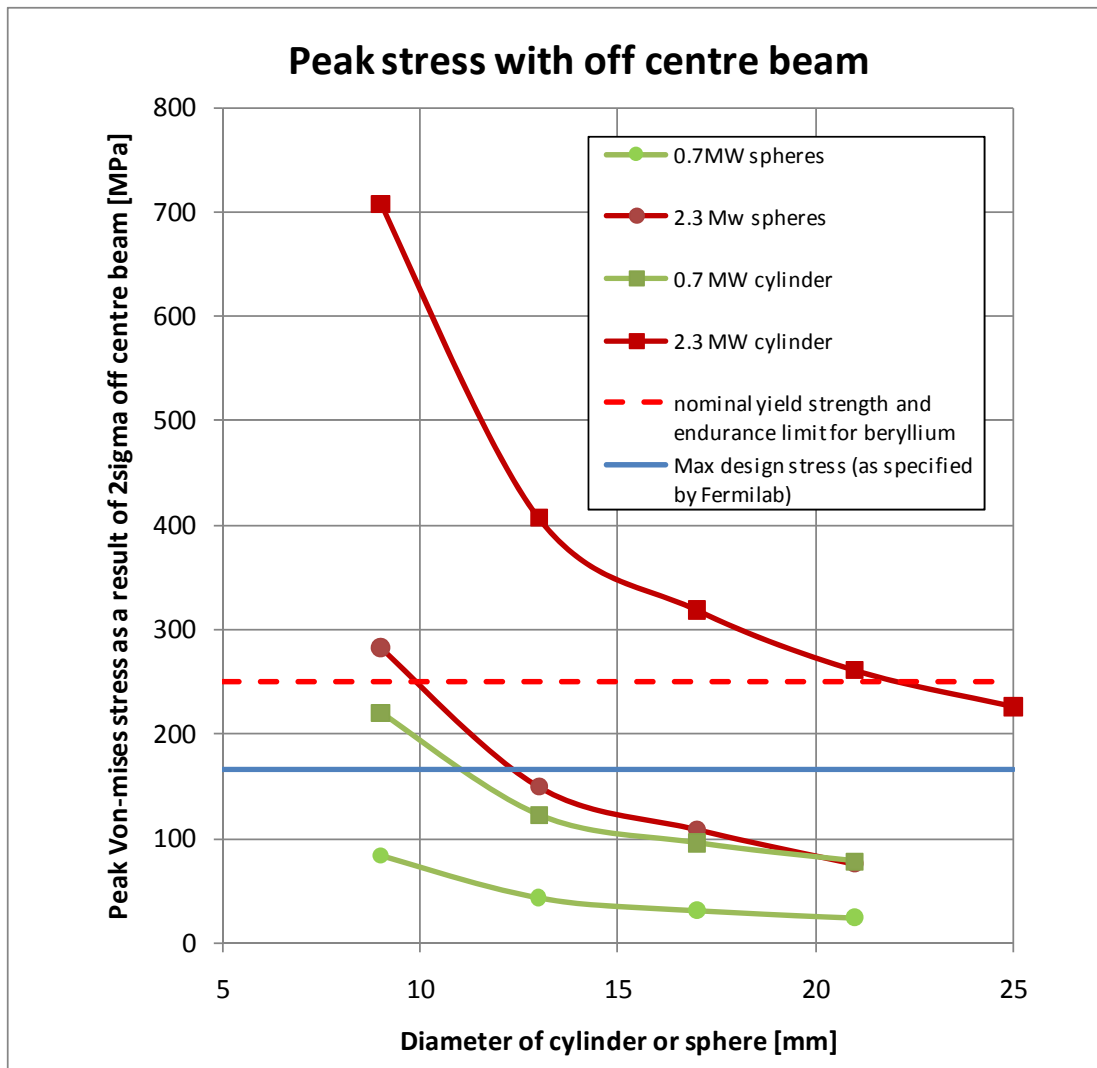
Figure 3.5.1 Peak stress across Task A parameter space for a 2 sigma off centre beam (worst case design point)

Table 3.5.1 Summary of peak Von Mises Stress

diameter [mm]	9	13	17	21
0.7 MW spheres [MPa]	84	44	32	25
2.3 Mw spheres [MPa]	283	150	109	76
0.7 MW cylinder [MPa]	221	123	96	78
2.3 MW cylinder [MPa]	708	407	319	261

700 kW Beam Power Target Summary

For 700 kW operation a 13 mm diameter 1 m long beryllium cylinder fixed at one end and constrained radially at the other end with a 2.16 mm beam sigma falls inside the chosen design point stress. The maximum deflection for this case has been calculated as 0.6 mm near the centre of the target. A series of spheres could be significantly smaller at the 700 kW power level.

2.3 MW Beam Power target summary

For 2.3 MW operation, a cylindrical rod beryllium target would have to be well above 21 mm in diameter (maximum size of interest in the Task A specification) in order to bring the peak dynamic stresses below the yield stress. The stress levels in the 2.3 MW cylinder are dominated by inertial effects in the form of both longitudinally stress waves and bending stresses induced by an off centre beam. Figure 3.5.1 shows that the stress in a series of spheres with the 2.3 MW beam can be kept below the design point with spheres of 13 mm diameter. This result indicates the advantage of longitudinally segmenting the target.

3.5   References

"Tensile properties of beryllium at high strain rates and temperatures"
F.Schierloh and S.Babcock
Technical Report AFML-TR-69-273 Air Force Materials Lab Ohio Oct 1969

"Effect of the Strain rate on the mechanical properties and failure mode of high strength steel"
A.P. Vashchenko, A.S.Dubhovnyi, G.V.Stepanov, V.M Tokarev and V.A.Chumachenko
Institute of Strength Problems, Academy of Sciences of the Ukranian SSR, Kiev, Leningrad.
Translated from Problemy Prochnosti, No 3 March 1987 Original article June 1985.

"Elastic Stress Waves in matter due to rapid heating by an intense high-energy particle beam"
P.Sievers
CERN Lab II/BT/74-2 26 June 1974

"FOM for pion Production"
Private note: March 23, 2010   Bob Zwaska Fermi Lab

National Institute of Standards and Technology online materials database
http://webbook.nist.gov/

Appendix 3.1 AUTODYN material properties for Beryllium

Material name	Beryllium
Equation of State	**Shock**
Reference density	1.85100E+00 (g/cm3)
Gruneisen coefficient	1.16000E+00 (none)
Parameter C1	7.99800E+03 (m/s)
Parameter S1	1.12400E+00 (none)
Parameter Quadratic S2	0.00000E+00 (s/m)
Relative volume, VE/V0	0.00000E+00 (none)
Relative volume, VB/V0	0.00000E+00 (none)
Parameter C2	0.00000E+00 (m/s)
Parameter S2	0.00000E+00 (none)
Reference Temperature	3.00000E+02 (K)
Specific Heat	1.85000E+03 (J/kgK)
Thermal Conductivity	1.83000E+02 (J/mKs)
Strength	**von Mises**
Shear Modulus	1.32000E+08 (kPa)
Yield Stress	2.80000E+05 (kPa)

Appendix 3.2 AUTODYN mesh validation

It was found that the thermal trace of the Gaussian beam on the target could be defined with sufficient accuracy using 10 energy bins over the radius of the rods. This was a compromise which provided a reasonable fit to the Gaussian particle distribution without requiring prohibitive FLUKA computations.

However it was found that a mesh with 10 cells across the radius would be computationally onerous when used for the AUTODYN dynamic stress simulations. It was then decided that 7 cells across the radius were to be used to reduce the computational times. Further this allowed extending the AUTODYN simulations to a period of several milliseconds which was necessary to stretch the analysis to low frequency phenomena. Compromising on the number of mesh cells reduced the accuracy of the temperature gradient simulated in the AUTODYN models as the energy deposition was averaged over a larger volume of material. More specifically the averaging effect resulted in lower peak temperatures at the core of the energy trace.

A set of AUTODYN models with a larger number of cells was then developed to validate the stress and temperature results. Figures a1 to a2 compare the temperature distribution in models with 7 and 12 mesh cells across the radius after the energy deposition (with reference temperature set to 300 K).

The expected analytical temperature rise for the two test cases can be compared with the results obtained from the simulations in the following Table and in Figures a1 to a4.

Diameter [mm]	Expected analytical dT [K]	Simulated dT [K] (7 mesh cells)	Simulated dT [K] (12 mesh cells)
21	68	62	64
9	243	212	227
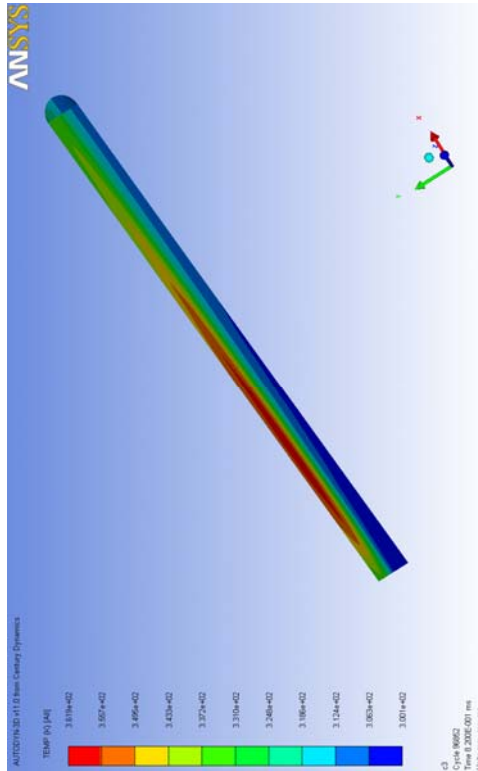
Figure a1. Temperature distribution in a 21 mm diameter Be rod. 2.3 MW beam. 2*sigma beam off-centre. 7 mesh cells across the radius
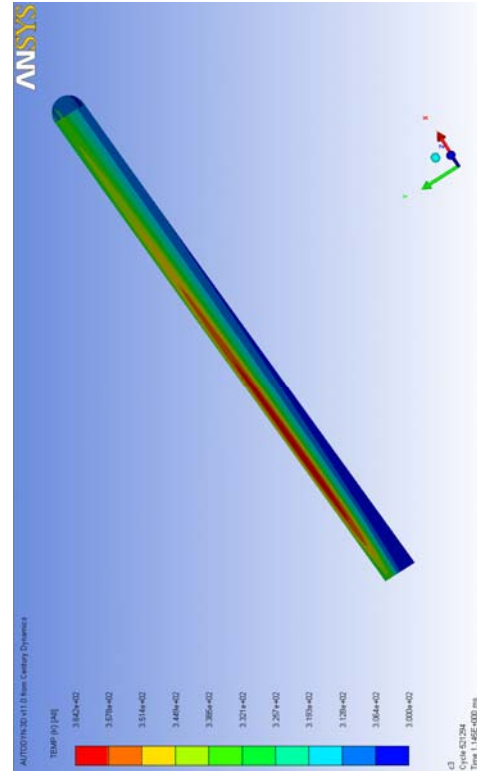
Figure a2. Temperature distribution in a 21 mm diameter Be rod. 2.3 MW beam. 2*sigma beam off-centre. 12 mesh cells across the radius.
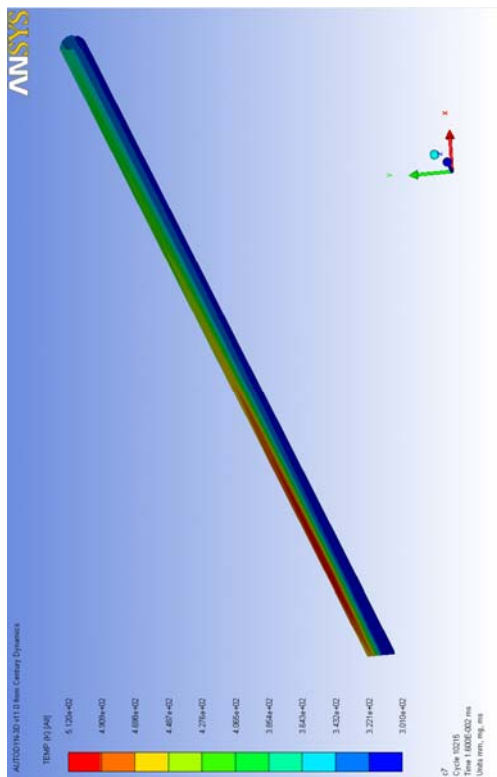
Figure a3. Temperature distribution in a 9 mm diameter Be rod. 2.3 MW beam. 2*sigma beam off-centre. 7 mesh cells across the radius.
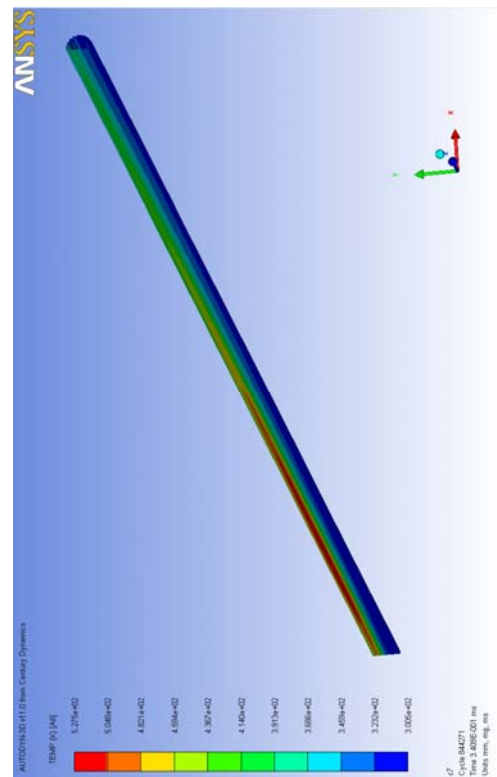
Figure a4. Temperature distribution in a 9mm diameter Be rod. 2.3 MW beam. 2*sigma beam off-centre. 12 mesh cells across the radius.

Despite the difference in the peak temperature rise, when looking at the stresses the difference between models with higher/lower mesh resolution appears marginal. A comparison of the maximum Von Mises stresses simulated in 21 mm beryllium rods (excited by a 2.3 MW off-centre beam) with different number of mesh cells is reported in Figure a5.
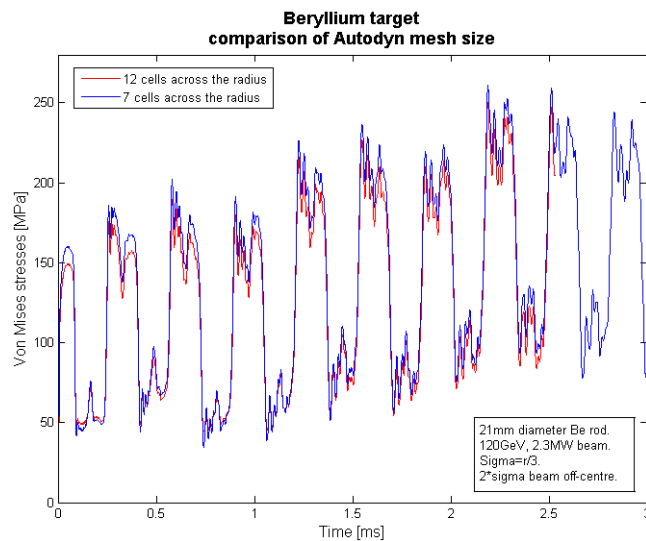
Figure a5. Comparison of the stresses obtained modelling a 9 mm diameter Be rod with different mesh sizes.

Similarly the Von Mises stresses simulated in 9 mm beryllium rods (excited by a 2.3 MW off-centre beam) are compared in Figure a6.
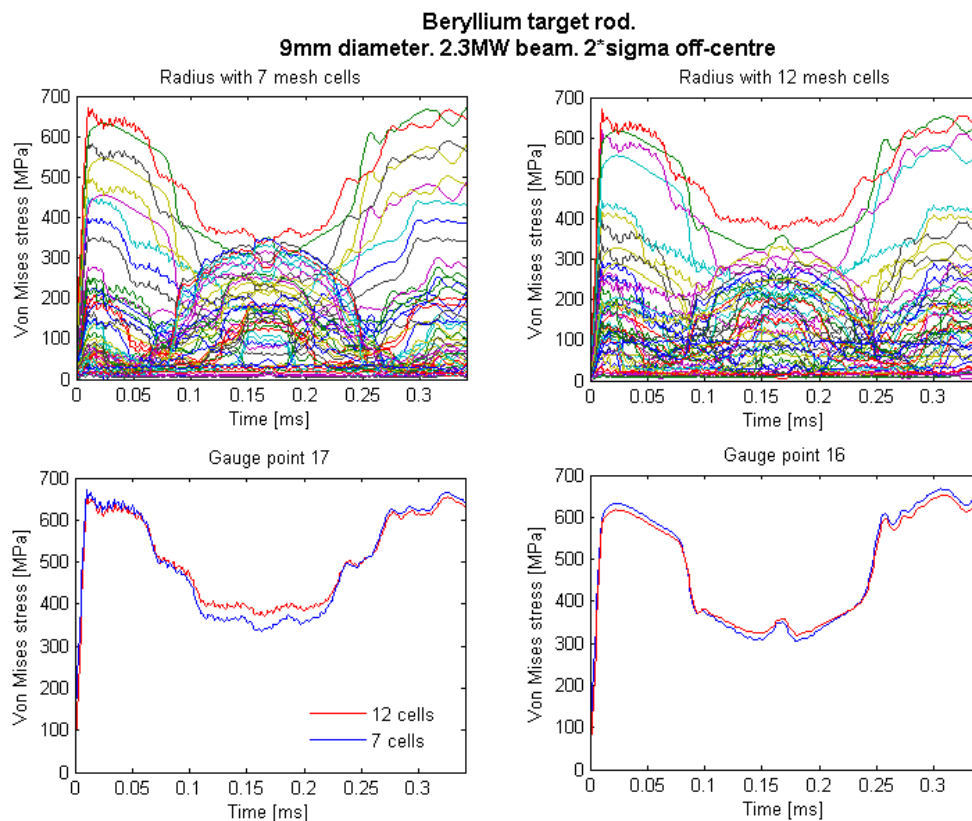
Figure a6. Result comparison with fine and coarse mesh

4. Report on Task B: Target Cooling Options

4.1 Introduction

In this section the steady-state cooling of the target is considered. Most of the study covers forced convection cooling by annular flow, but an assessment is also made of water spray cooling around an empirical Heat Transfer Coefficient figure and also heat transfer over a series of contained spheres. Calculations of Heat Transfer Coefficient (HTC), pressure drop and the steady state peak target temperature have been carried out. The fluids studied were helium, water and air. A summary of the time averaged power deposited in the target for each case is shown in Table 4.1.

Table 4.1 Summary of the time averaged power deposited in the target

Beam Energy (GeV)	Beam Power (MW)	Beam Sigma (mm)	Time Averaged Power (kW)		
			Beryllium	AlBeMet 162	Aluminium
120	0.7	1.5	3.2	4.8	9.5
		3.5	7.1	12.2	26.4
60	0.7	1.5	3.9	5.1	8.2
		3.5	7.9	11.7	12.4
120	2.3	1.5	10.8	16.0	31.6
		3.5	23.8	40.6	88.1
60	2	1.5	11.3	14.8	23.9
		3.5	22.9	33.9	36.2

For forced convection cooling the target is considered a simple cylinder 1 metre in length and the cooling fluid passes through an annular duct around the target as shown in Figure 4.1 The proton beam heating is modelled as internal heat generation within the cylinder.

Cold fluid inlet

Hot fluid outlet
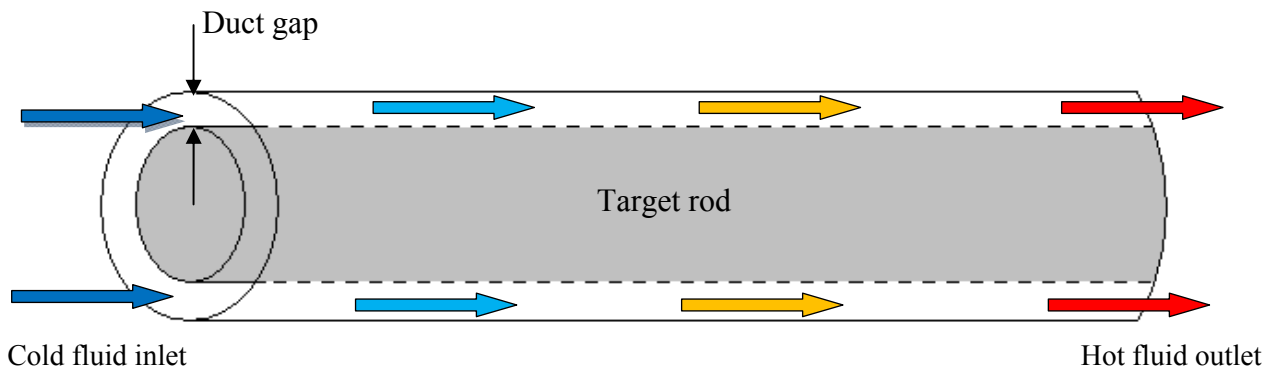
Figure 4.1 Annular duct cooling of target

Depending on design, it may be required that the cooling system has the inlet and outlet at the same end of the horn. In this case a double annular concentric duct would be required to cool the target. This will significantly increase the target pressure drop and diameter. If we consider that the current horn design has a bore radius of 20mm then there is only 9.5-15.5mm radial space for the cooling channels depending on the size of the target. This does not include any clearance between the target and horn which will be required.

When designing the target cooling system the following parameters must be taken into account:

- The required operating temperature of the target (Heat Transfer Coefficient and fluid temperature)

- The pressure drop of the system

- Pump/compressor requirements (Volume flow rate)

- The temperature difference of the fluid through the cooling process

Some of these parameters such as heat transfer coefficient and pressure drop have conflicting requirements. For example reducing the duct gap will increase the heat transfer coefficient but also increase the system pressure drop. Therefore a study of the parameter space is required to select a suitable cooling design. In addition to the fundamental cooling requirements other important considerations are:

- Cost of system

- Reliability/maintenance

- Radioactivity/activation of cooling system

- Interaction of secondary particles with cooling fluid

4.2 Forced convection empirical calculations

Nusselt number calculations

To calculate the heat transfer coefficient for water the Sieder-Tate[1] equation for Nusselt number in a smooth circular duct was found to give a good correlation with CFX results.

$$\frac{hD_e}{k} = 0.023 \left(\frac{\rho V D_e}{\mu}\right)^{0.8} \left(\frac{c_p \mu}{k}\right)^{\frac{1}{3}} \left(\frac{\mu}{\mu_w}\right)^{0.14}$$

Where

ρ = Density
V = Velocity

$D_e = Outer\ Diameter - Inner\ Diameter$

C_p = Specific heat capacity at constant pressure

μ = Dynamic viscosity

μ_w = Dynamic viscosity at wall temperature

k = Thermal conductivity

For helium cooling the empirical equations from Dwyer[2] were found to correlate well with CFX. This equation is valid for a concentric annular duct with the inner wall heated.

$$N_u = A + B(\beta Pe)^n$$

Where

$$r^* = \frac{inner\ radius}{outer\ radius}$$

$$A = 4.63 + \frac{0.686}{r^*}$$

$$B = 0.02154 - \frac{0.000043}{r^*}$$

$$n = 0.752 + \frac{0.01657}{r^*} - \frac{0.000883}{r^{*2}}$$

$$\left(\frac{\varepsilon_m}{\nu}\right)_{max,c} = 0.037 Re\sqrt{f}$$

$$\left(\frac{\varepsilon_m}{\nu}\right)_{max} = \frac{1}{2}\left(\frac{\varepsilon_m}{\nu}\right)_{max,c}$$

$$\beta = 1 - \frac{1.82}{Pr\ (\varepsilon_m/\nu)_{max}^{1.4}}$$

Pe = Peclet number

Re = Reynolds number

Pr = Prandlt number

f = friction factor

Pressure drop calculations

For all cases the cooling fluids are treated as having constant properties and incompressible. In the case of gasses the properties are evaluated at the system pressure and temperature using the ideal gas equation.

The equation used to calculate the pressure drop is shown below (Blevins [3]). It is valid for turbulent flow with Reynolds greater than 4000.

$$\Delta p = \frac{fL}{D}\frac{\rho U^2}{2}$$

The fanning friction factor, f for the duct is calculated from the Darcy-Weisach friction factor using the Haaland[4] equation.

$$f = \frac{f_{DW}}{4}$$

where

$$\frac{1}{\sqrt{f_{DW}}} = -1.8log_{10}\left[\left(\frac{\varepsilon/_D}{3.7}\right)^{1.11} + \frac{6.9}{Re}\right]$$

$$\varepsilon/_D = Relative\ roughness\ of\ duct$$

Steady-state peak target temperature estimation

The steady-state peak temperature of the target is estimated by using the equation for conduction in a cylinder with internal heat generation as shown below [5]. In reality the target temperature will oscillate around this value by the temperature rise per beam spill.

$$T_0 - T_w = \frac{\dot{q}R^2}{4k}$$

where

T_0 = Temperature at the centre of the cylinder
T_w = Wall temperature
$\dot{q}$ = Heat generation
R = Radius of cylinder
k = Thermal conductivity of cylinder

The wall temperature is estimated by calculating the fluid temperature at the position of peak energy deposition along the target length. This is calculated assuming that the fluid temperature rises uniformly along the target length. The average temperature difference between the target wall and bulk fluid is then added to the local fluid temperature to estimate the local wall temperature.

The heat generation rate used in this equation is the peak energy deposition from Fluka simulations which has been averaged over several bins. The thermal conductivity of Beryllium is highly non-linear in the temperature range of 300-700K. Therefore the peak temperature is found by iterating between the peak temperature and thermal conductivity.

Some of the assumptions in this estimation are:

1. The heat transfer to the fluid is constant along the target length
2. The fluid properties are constant along the target length
3. Temperature distribution in fluid is uniform across duct gap

4.3 Forced convection validation case (CFX)

To validate the empirical calculations a study of the Beryllium target was carried out using the Computational Fluid Dynamics (CFD) code CFX. This model incorporates beam heating data from Fluka simulations which varies the heat generation rate with the position in the target. This model includes Conjugate Heat Transfer (CHT) effects which improves the analysis in a number of ways:

1. The properties of the fluid are calculated along the target length. With gas cooling the temperature rise of the gas can be significant which will affect the pressure drop and heat transfer.
2. The complete energy deposition from Fluka is used
3. The fluid boundary layer and turbulence are evaluated along the target length
4. Compressible effects of gasses are captured
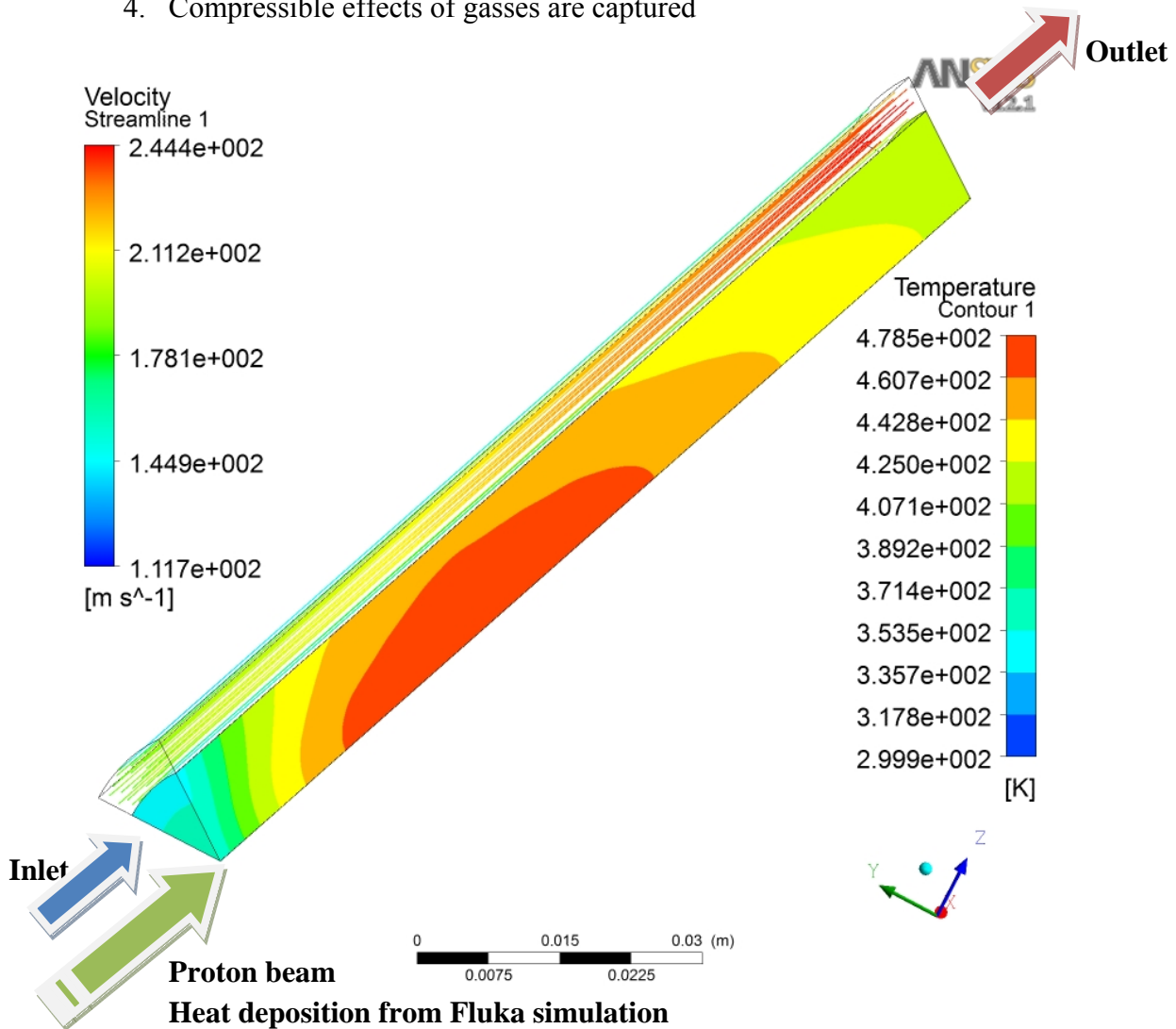
Figure 4.2 Example of Conjugate Heat Transfer (CHT) model showing target temperature contours and fluid velocity streamlines with heat load from FLUKA simulation.

To reduce the solution time a 36° slice (1/10) of the target and annular cooling duct were modelled as shown in the example Figure 4.2. Symmetry boundary conditions were applied to both the target and fluid region. The turbulence model used for this analysis was Shear Stress Transport (SST) which is generally regarded as superior to the k-epsilon method. The SST model used by CFX has very low grid sensitivity for near wall boundary layer calculations which is desirable for calculating heat transfer coefficient [6].

The boundary conditions were defined by a mass flow rate at inlet and a constant pressure at the outlet. Table 4.2 give a summary of the cases analysed and compared with empirical calculations. The inlet temperature of the fluid in all cases is assumed to be 300K.

Table 4.2 Summary of validation cases modelled using CFX

Fluid	Mass flow rate (kg/s)	Outlet Pressure (bar)	Target diameter (mm)	Annular duct gap (mm)	Energy deposition	Beam Power (MW)
Helium	0.05, 0.075, 0.1, 0.125, 0.15	10	9 (1.5 sigma beam), 21 (3.5 sigma beam)	3, 4, 5	60GeV (2MW), 120GeV (2.3MW)	2-2.3
Water	0.25, 0.50, 0.75, 0.10, 1.25	2	9 (1.5 sigma beam), 21 (3.5 sigma beam)	3, 4, 5	60GeV (2MW), 120GeV (2.3MW)	2-2.3
Air	0.1, 0.125, 0.15, 0.175, 0.2	2	9 (1.5 sigma beam), 21 (3.5 sigma beam)	4, 5	60GeV (0.7MW), 120GeV (0.7MW)	0.7

4.4 Forced convection results

Heat Transfer Coefficient and pressure drop

Figures 4.3 to 4.14 show the results from the analysis for Heat Transfer Coefficient (HTC) and pressure drop. They compare the results from empirical calculations and CFX simulations for the cases shown in Table 4.2.

The heat transfer coefficient values quoted are calculated using a bulk fluid temperature of 300K and are averaged over the complete target surface.

For the cases analysed the difference in the heat deposition between 60GeV and 120GeV seemed to have negligible effect on the Heat Transfer Coefficient and pressure drops. Therefore these calculations are valid for either the 60GeV or 120GeV case.

Helium cooled target – 9mm target diameter (10bar at outlet)
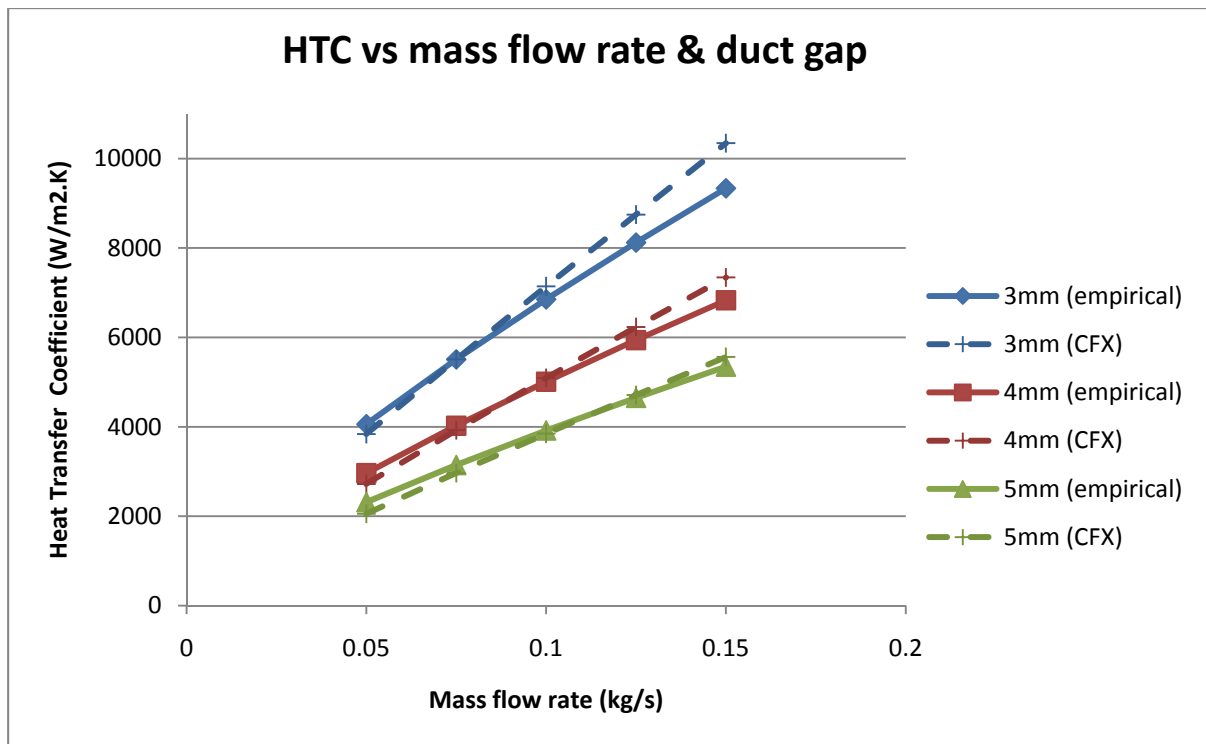
Figure 4.3 HTC vs. mass flow rate and duct gap for helium cooled 9mm diameter target
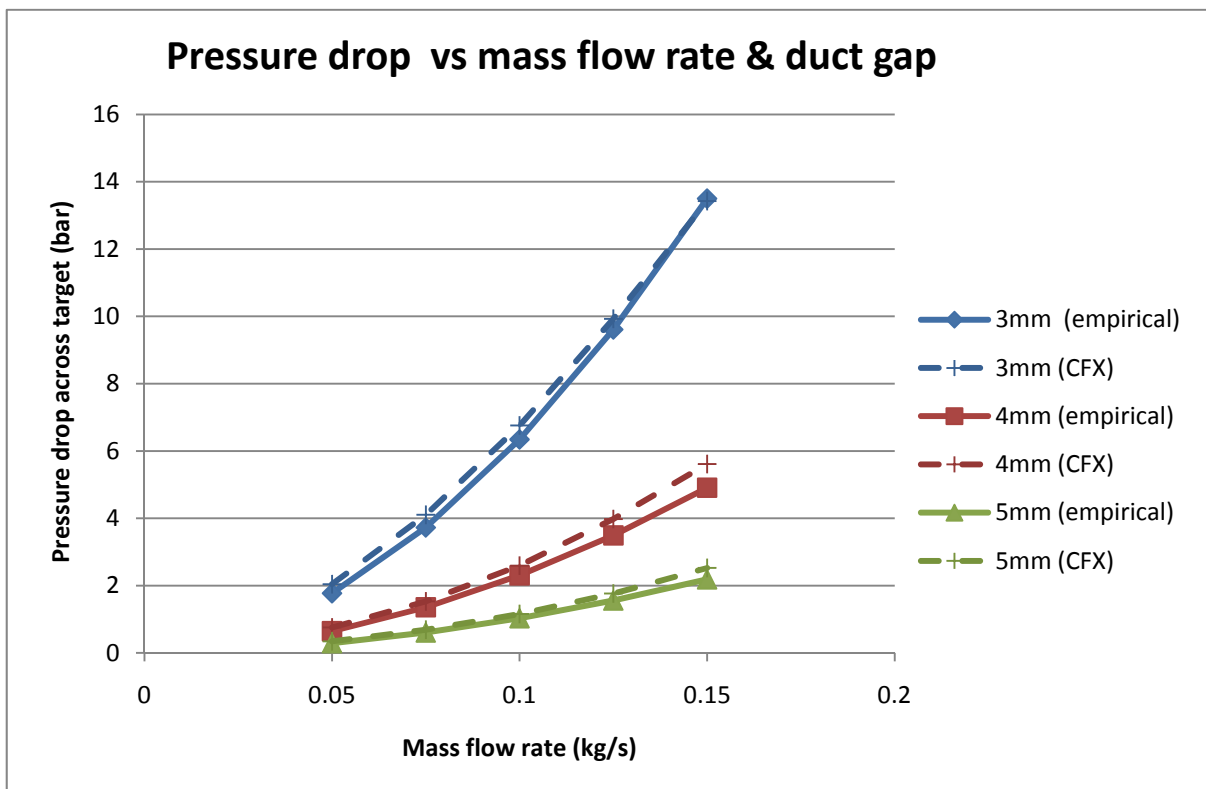
Figure 4.4 Pressure drop vs. mass flow rate and duct gap for helium cooled 9mm diameter target
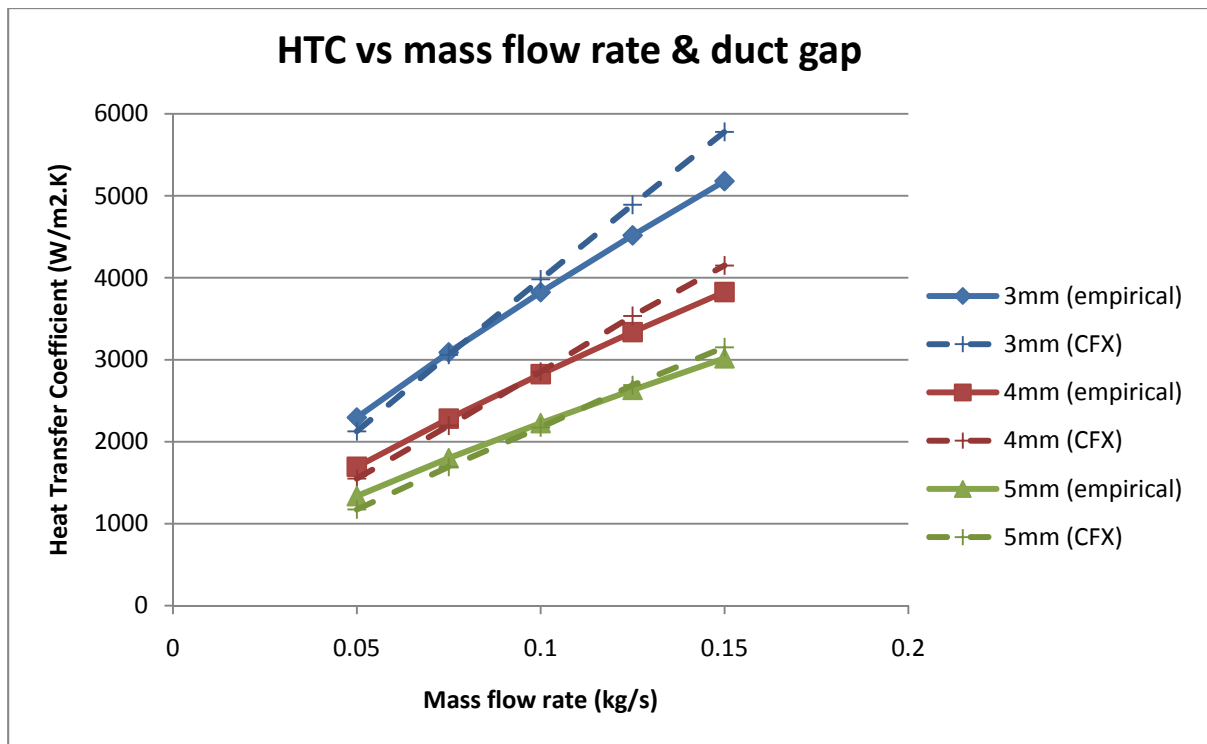
Figure 4.5 HTC vs. mass flow rate and duct gap for helium cooled 21mm diameter target
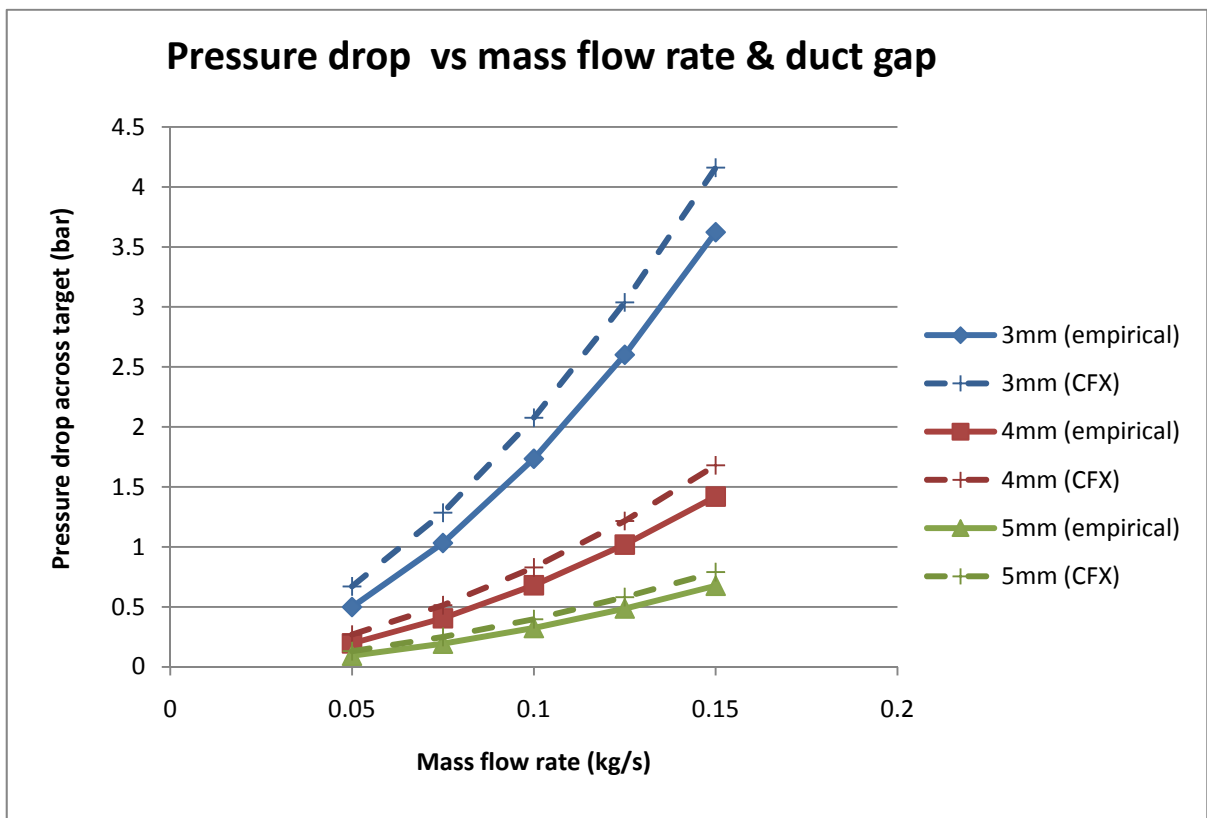
Figure 4.6 Pressure drop vs. mass flow rate and duct gap for helium cooled 21mm diameter target

<u>Water cooled target – 9mm target diameter</u>
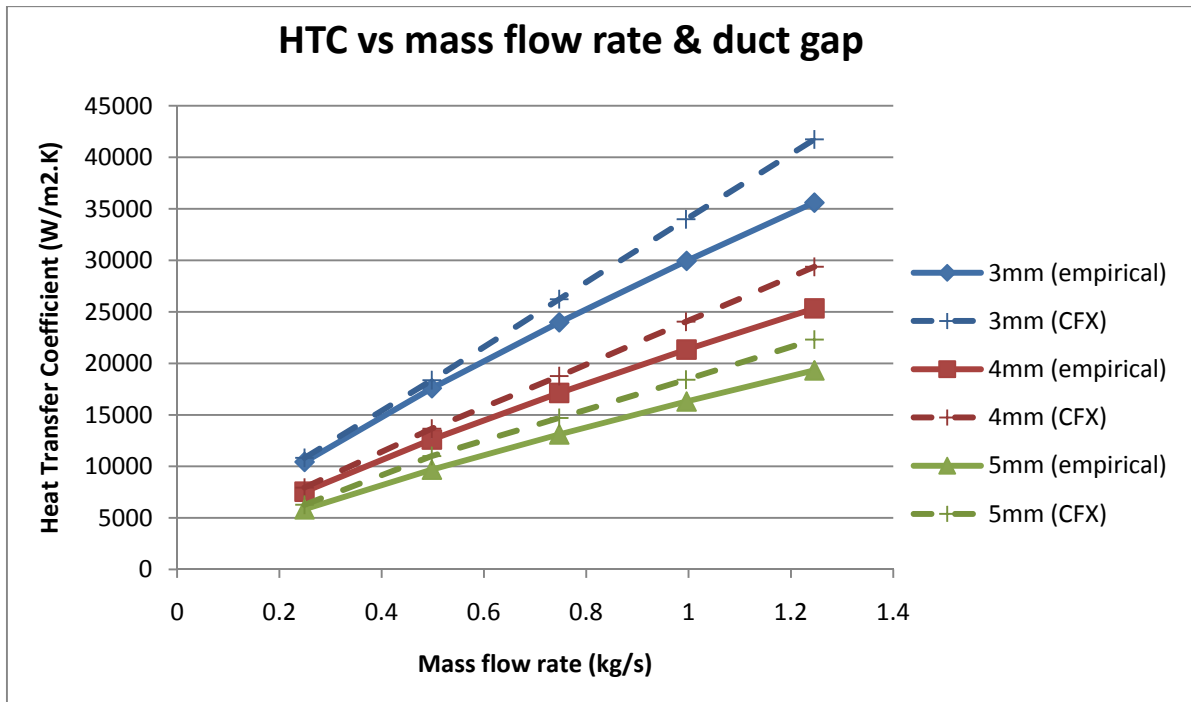
Figure 4.7 HTC vs. mass flow rate and duct gap for water cooled 9mm diameter target
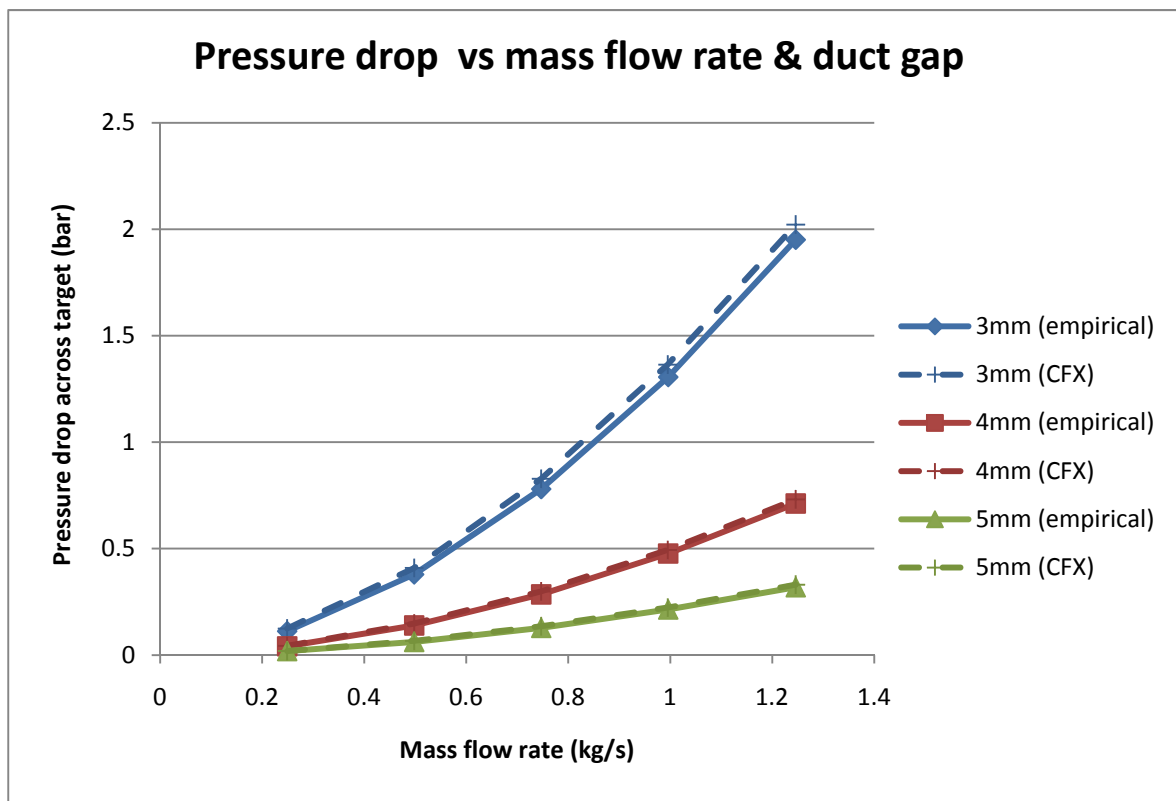
Figure 4.8 Pressure drop vs. mass flow rate and duct gap for water cooled 9mm diameter target
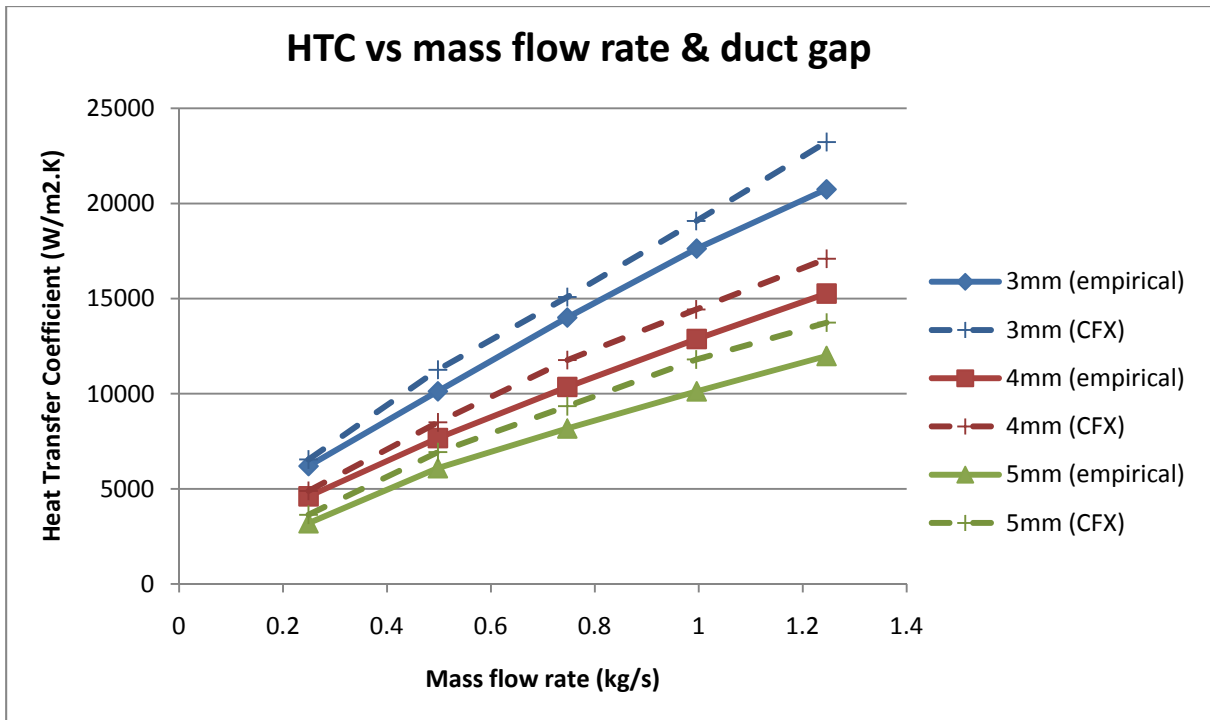
Figure 4.9 HTC vs. mass flow rate and duct gap for water cooled 21mm diameter target
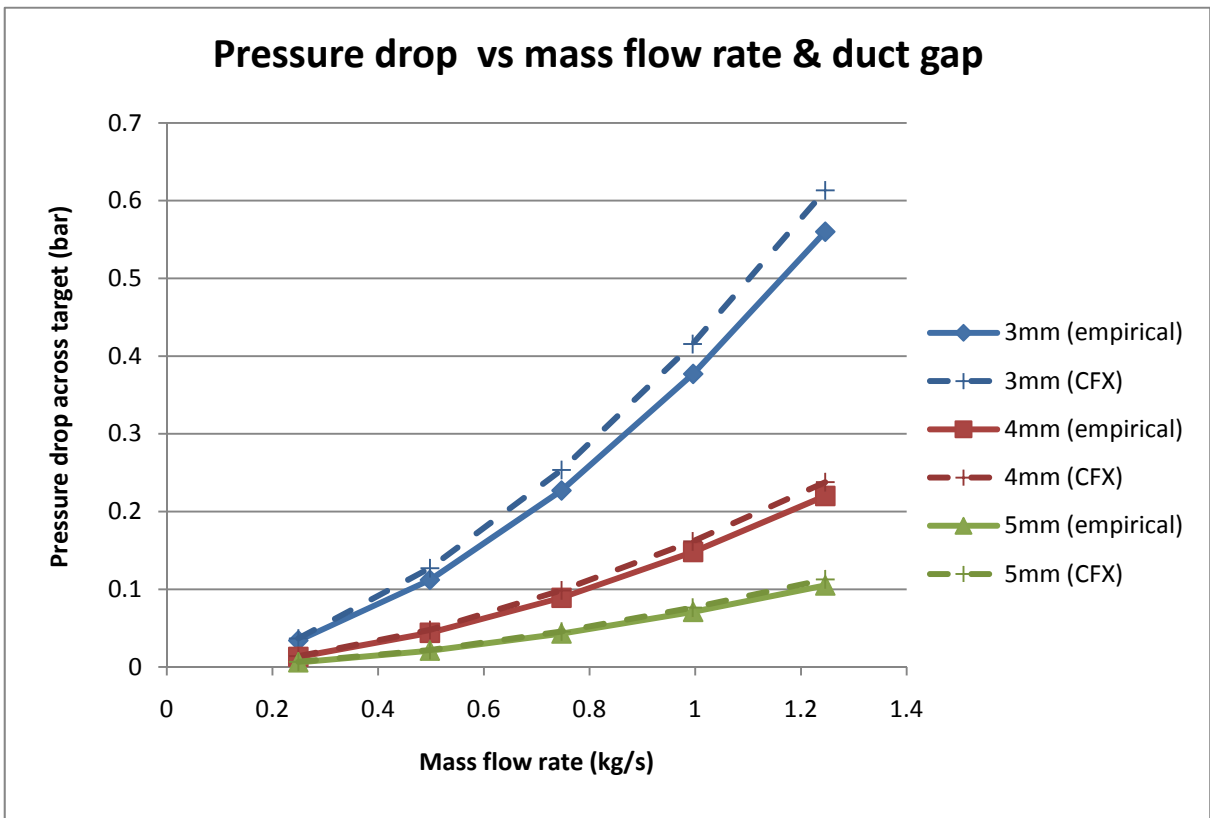
Figure 4.10 Pressure drop vs. mass flow rate and duct gap for water cooled 21mm diameter target
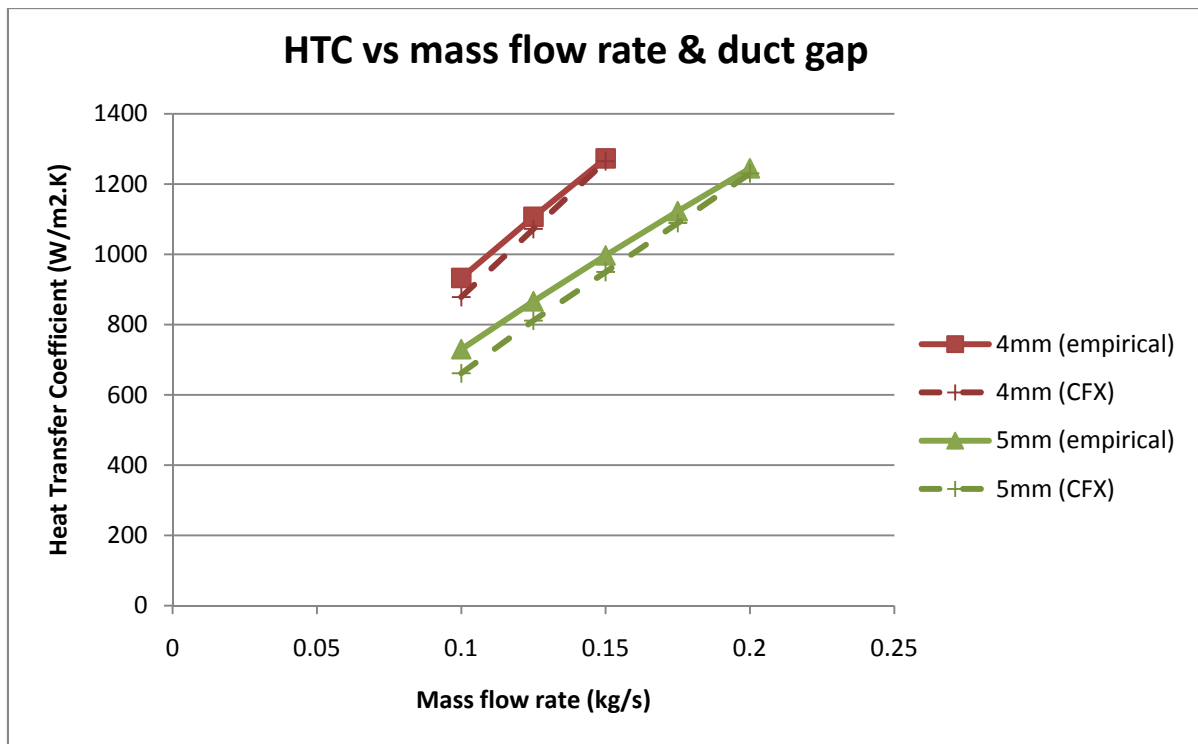
Figure 4.11 HTC vs. mass flow rate and duct gap for an air cooled 9mm diameter target
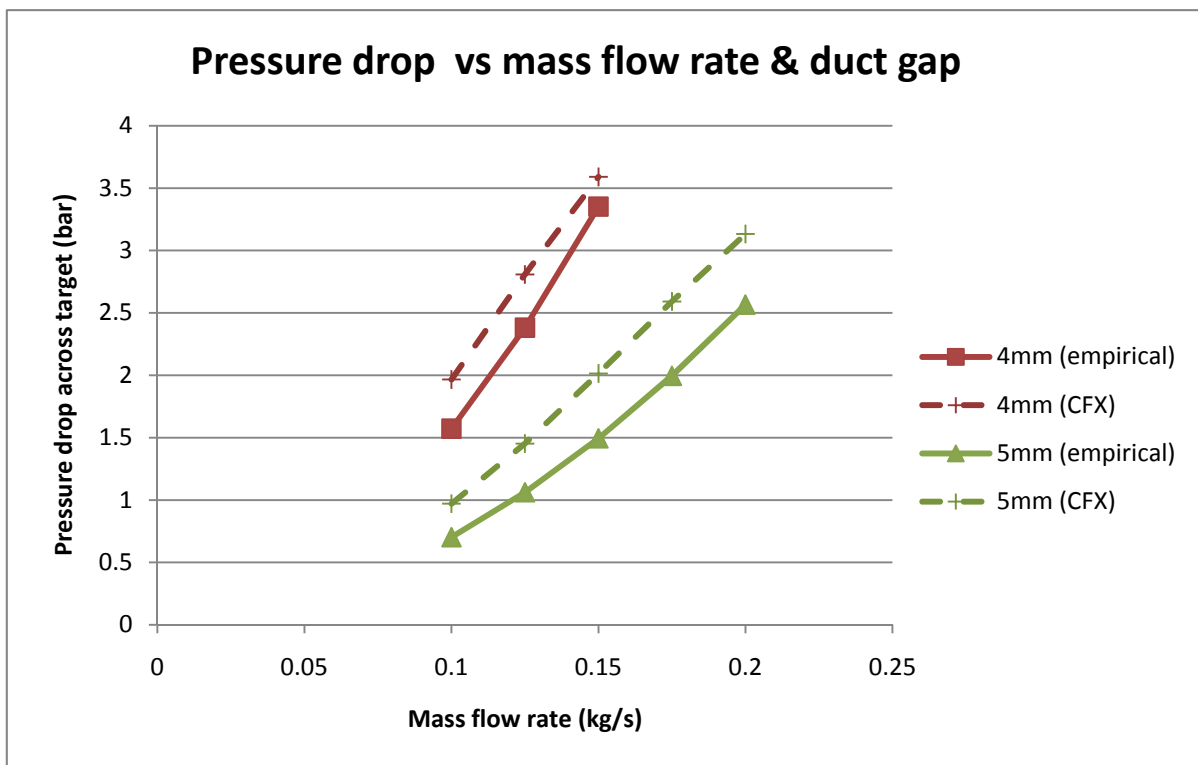
Figure 4.12 Pressure drop vs. mass flow rate and duct gap for an air cooled 9mm diameter target
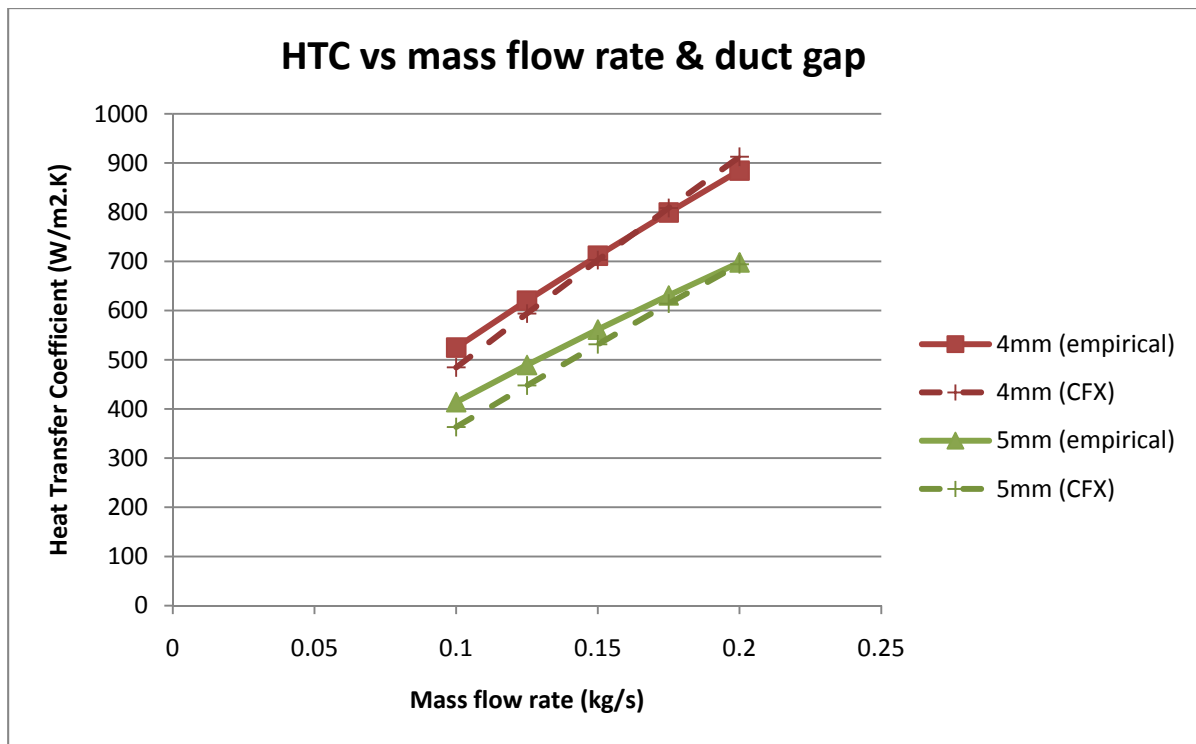
Figure 4.13 HTC vs. mass flow rate and duct gap for an air cooled 21mm diameter target
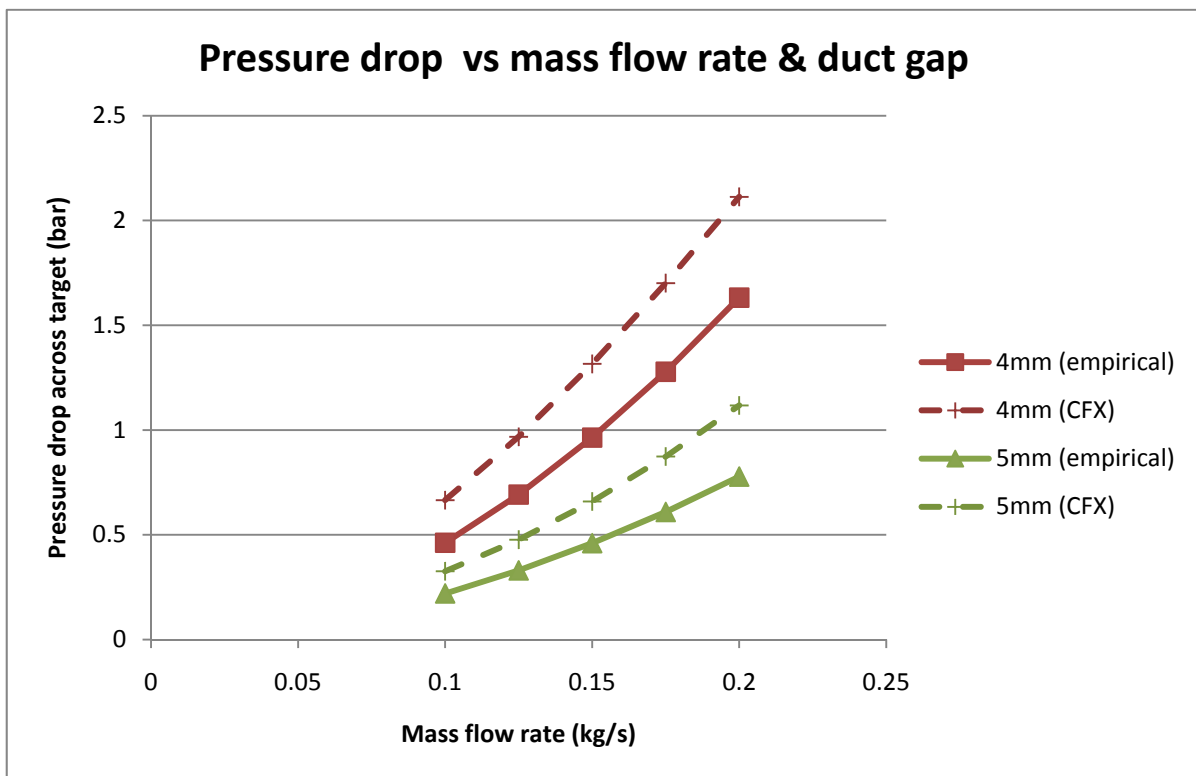
Figure 4.14 Pressure drop vs. mass flow rate and duct gap for an air cooled 9mm diameter target

From these results it can be seen that there is good agreement between empirical calculations and CFX for all fluids. In general empirical calculations tend to slightly underestimate the heat transfer coefficient. For Helium cooling at the lowest flow rates the empirical calculations overestimate the heat transfer coefficient.

The results for system pressure drop are as expected from an incompressible analysis. For water, an incompressible fluid there is excellent agreement with CFX. However for Helium and air the incompressible equations underestimate the pressure drop and the error increases with flow rate because they neglect the compressible effects. Empirical calculations will also underestimate the pressure drop as the heating of the cooling fluid is neglected. This is most significant for gases where the temperature rise is large and therefore the change in density of the gas becomes important.

Target peak steady-state operating temperature

Figures 4.16 to 4.27 show the peak steady-state target temperature of Beryllium targets. These figures compare the results from the empirical calculations for HTC and simple conduction to the Conjugate Heat Transfer (CHT) analysis using CFX and Fluka. As previously mentioned the actual target peak temperature will oscillate around the steady-state value as shown in Figure 4.15
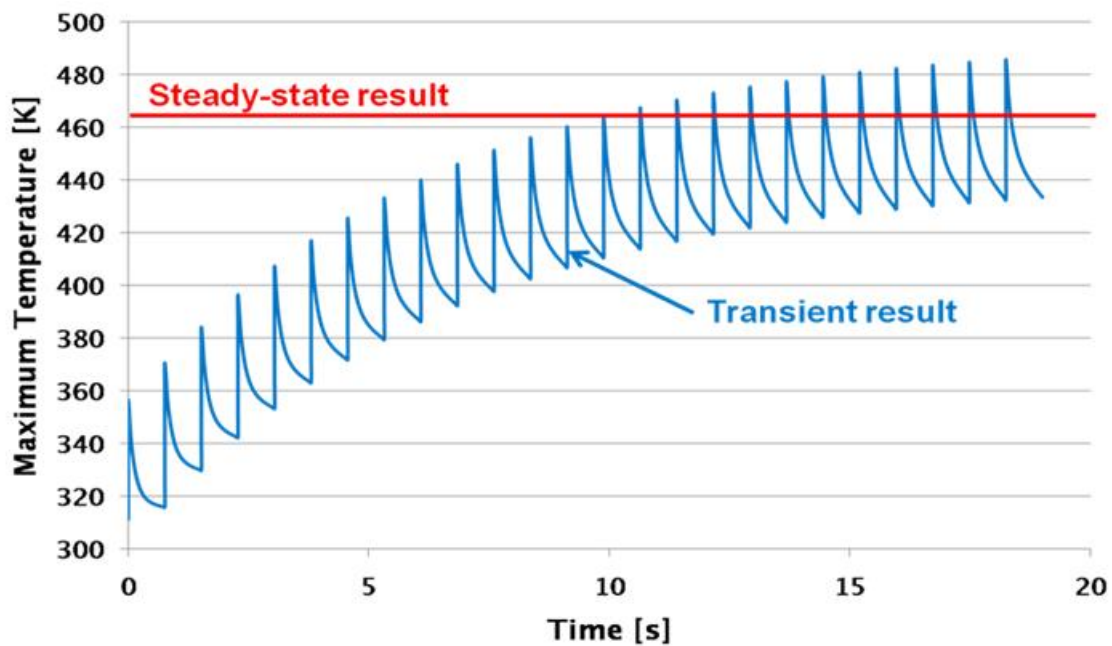
Figure 4.15 Comparison of steady-state and transient thermal results.
Water cooled Beryllium target (21mm) – 60GeV, 2MW, 3.5mmm sigma beam
5mm annular gap, mass flow rate = 0.4kg/s

The thermal conductivity of Beryllium is highly non linear in the range of 300-700K which is 185-110 W/m.K [7]. This has a significant effect on the target operation temperature so the following equation was used in CFX and empirical equations to calculate the thermal conductivity.

$$\text{Thermal Conductivity} = -8.2563\text{E}+01\ln(T) + 6.5383\text{E}+02$$
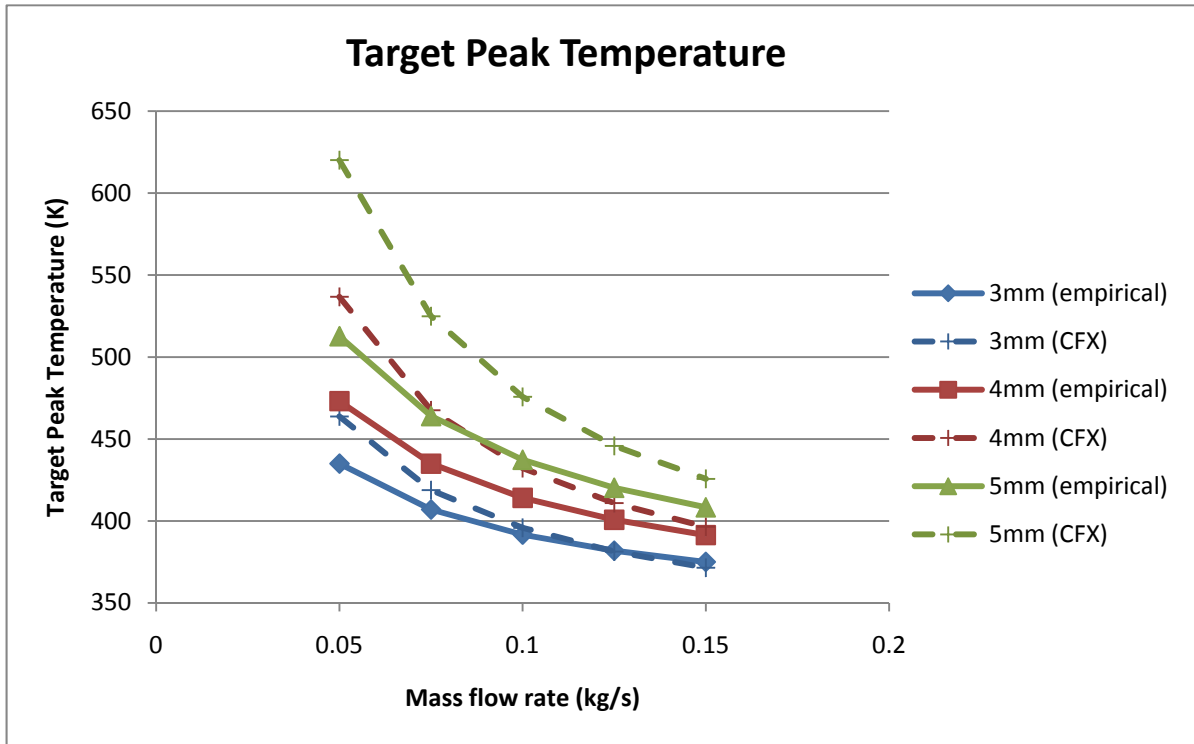
Figure 4.16 Helium cooled Beryllium target (9mm) – 60GeV, 2MW, 1.5mmm sigma beam
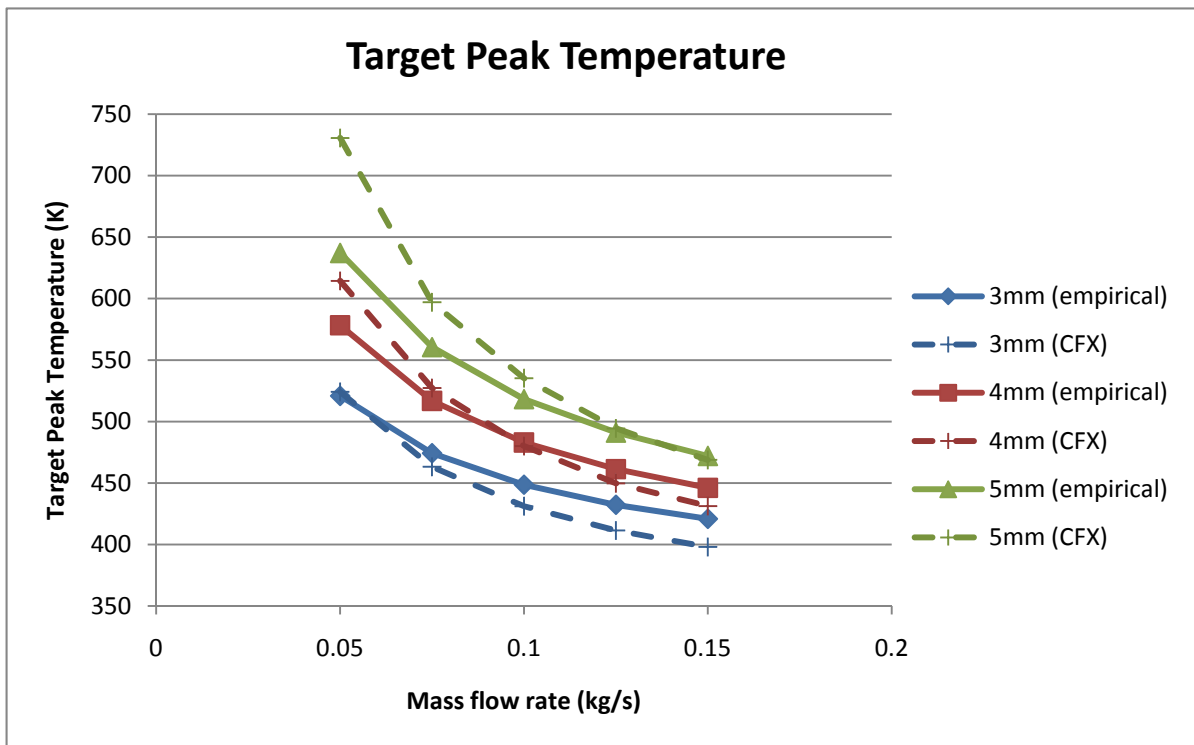
Figure 4.17 Helium cooled Beryllium target (21mm) – 60GeV, 2MW, 3.5mmm sigma beam
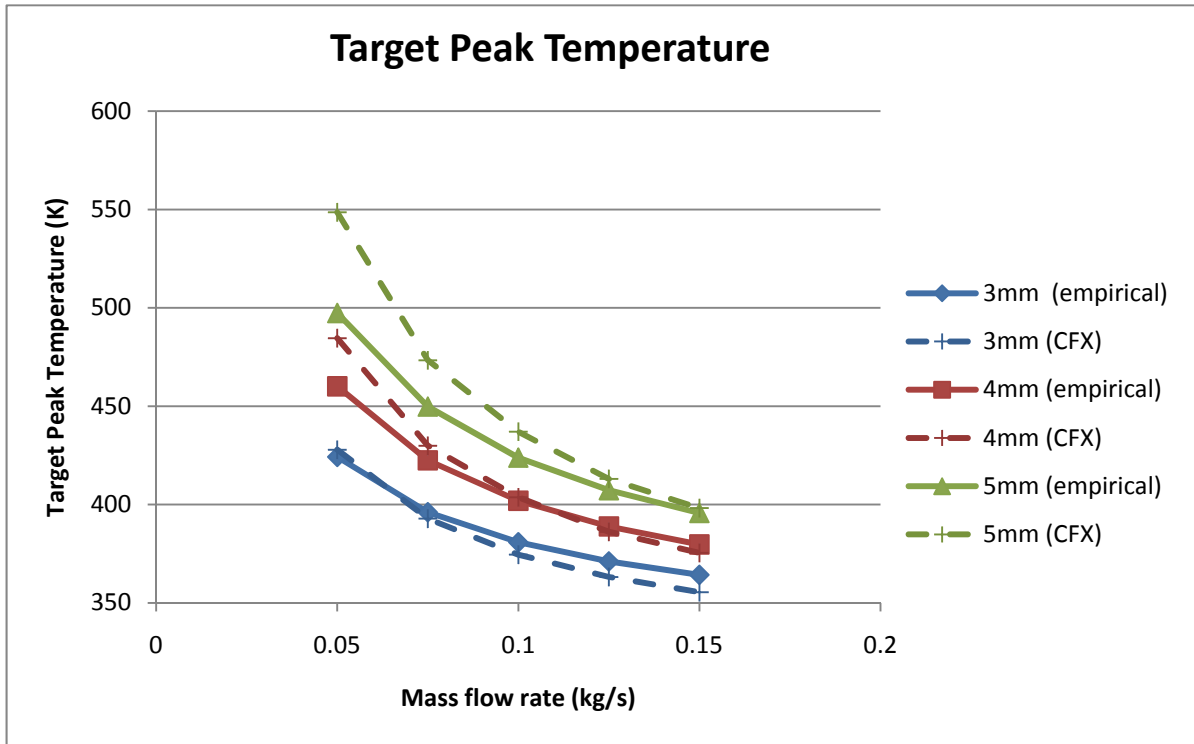
Figure 4.18 Helium cooled Beryllium target (9mm) – 120GeV, 2.3MW, 1.5mmm sigma beam
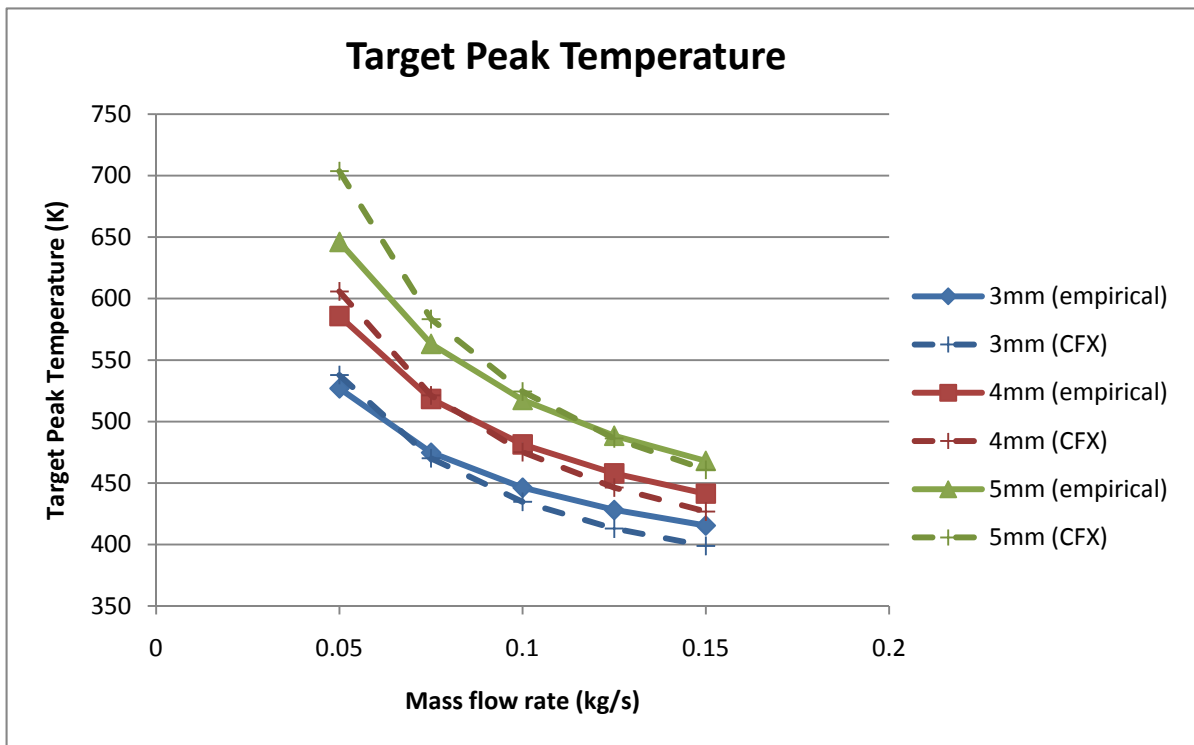
Figure 4.19 Helium cooled Beryllium target (21mm) – 120GeV, 2.3MW, 3.5mmm sigma beam
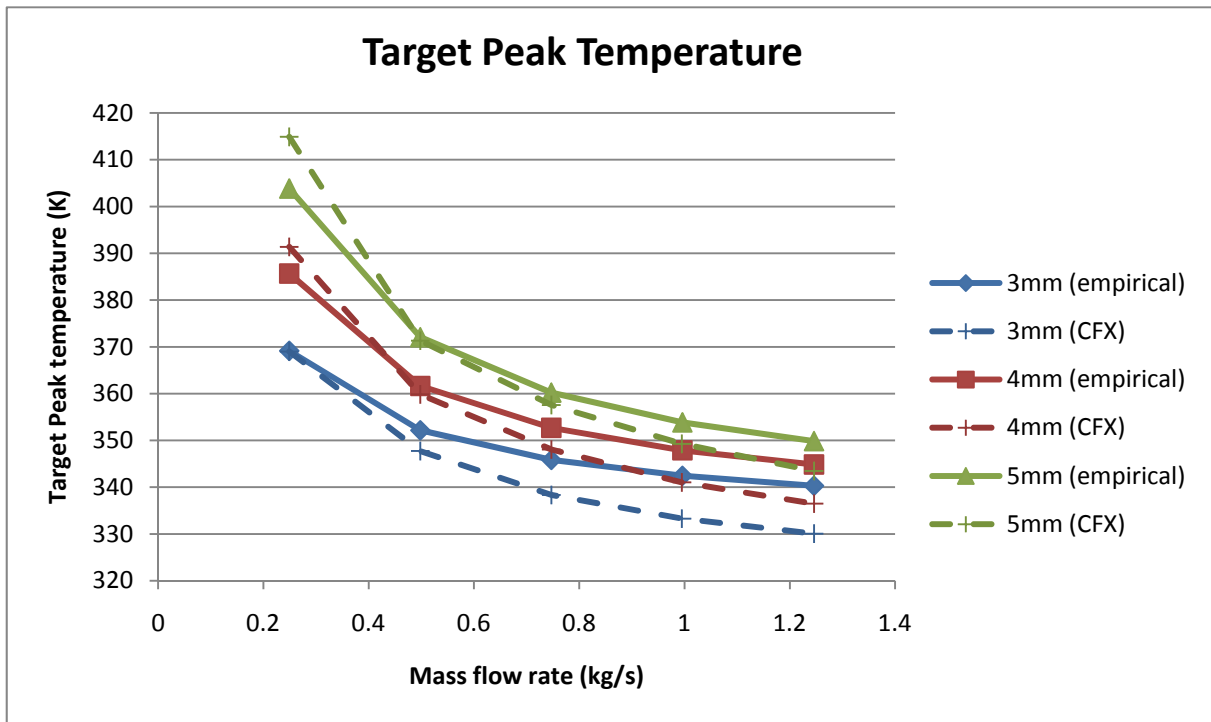
Figure 4.20 Water cooled Beryllium target (9mm) – 60GeV, 2MW, 1.5mmm sigma beam
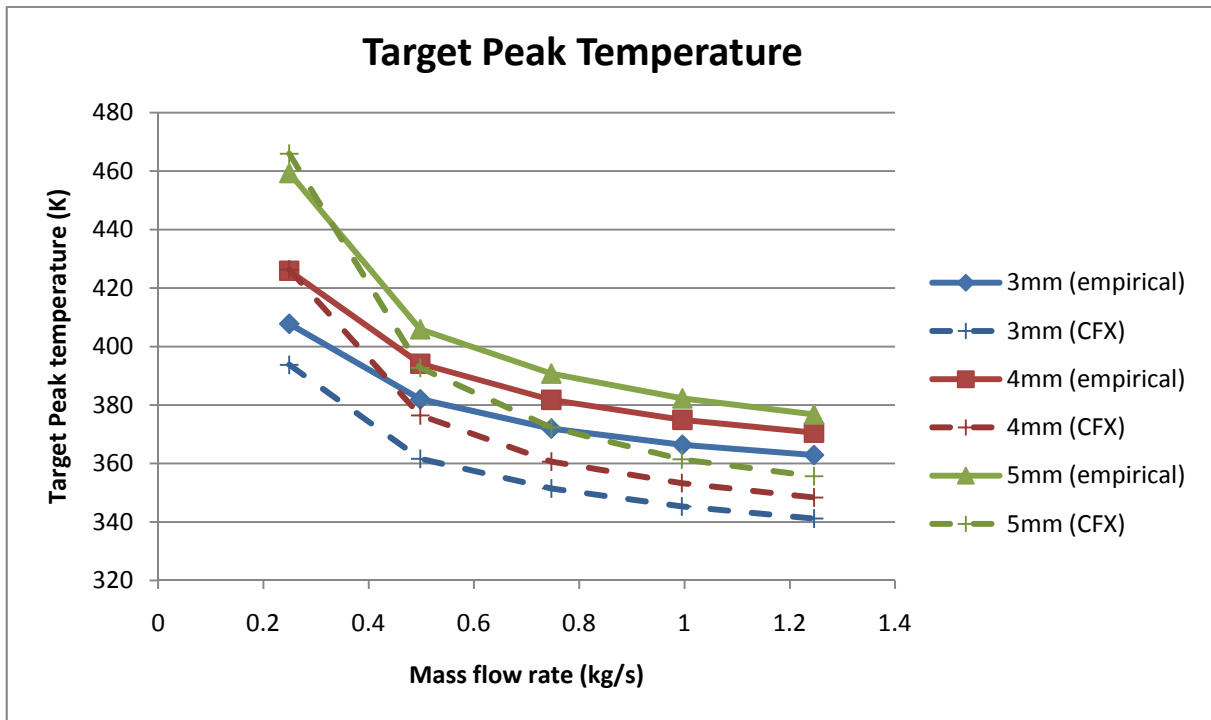
Figure 4.21 Water cooled Beryllium target (21mm) – 60GeV, 2MW, 3.5mmm sigma beam
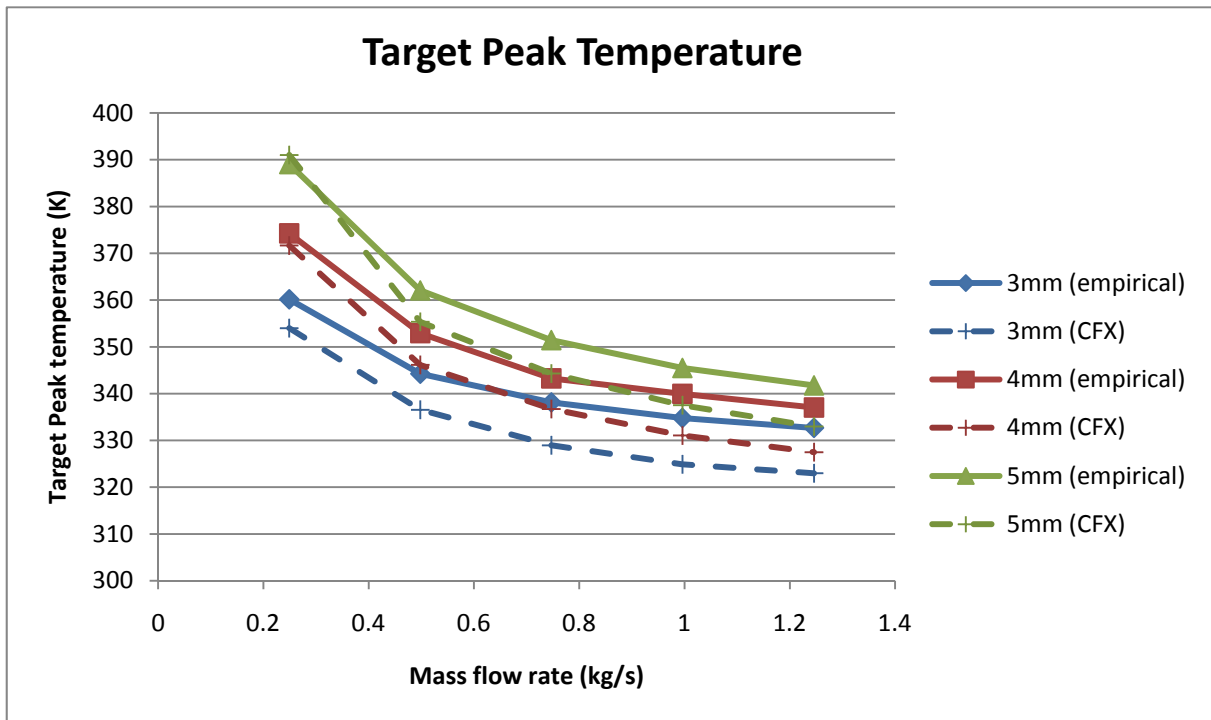
Figure 4.22 Water cooled Beryllium target (9mm) – 120GeV, 2.3MW, 1.5mmm sigma beam
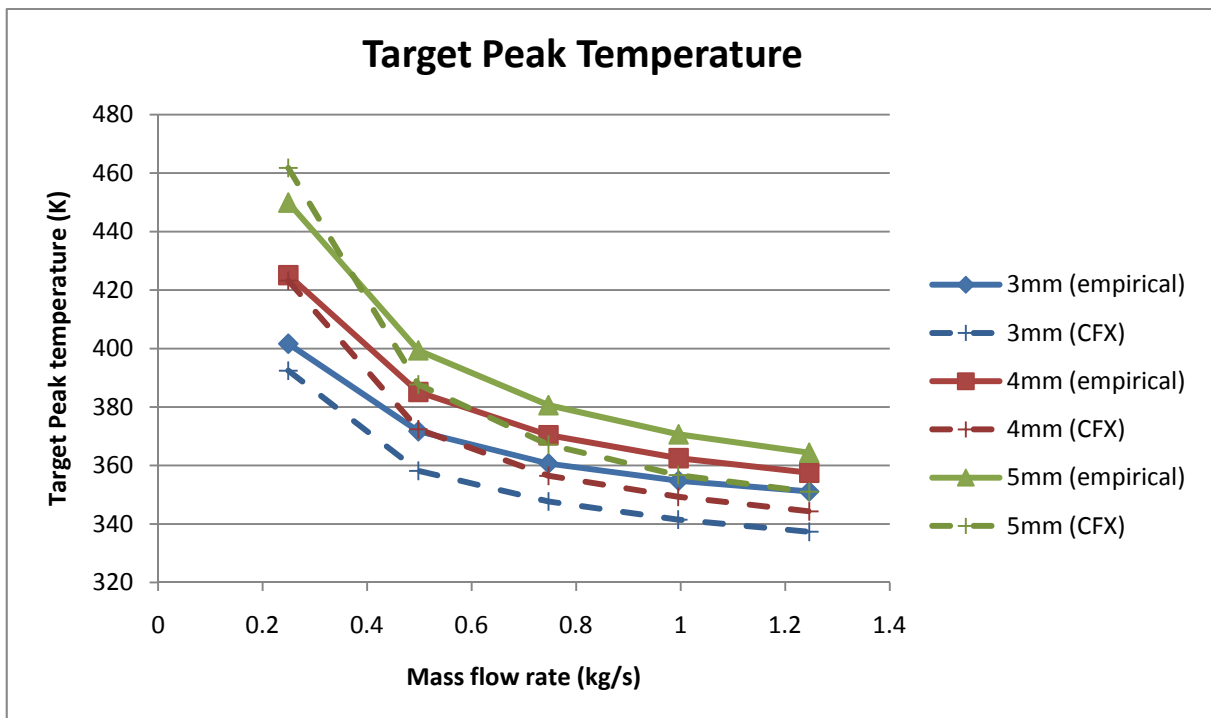
Figure 4.23 Water cooled Beryllium target (21mm) – 120GeV, 2.3MW, 3.5mmm sigma beam
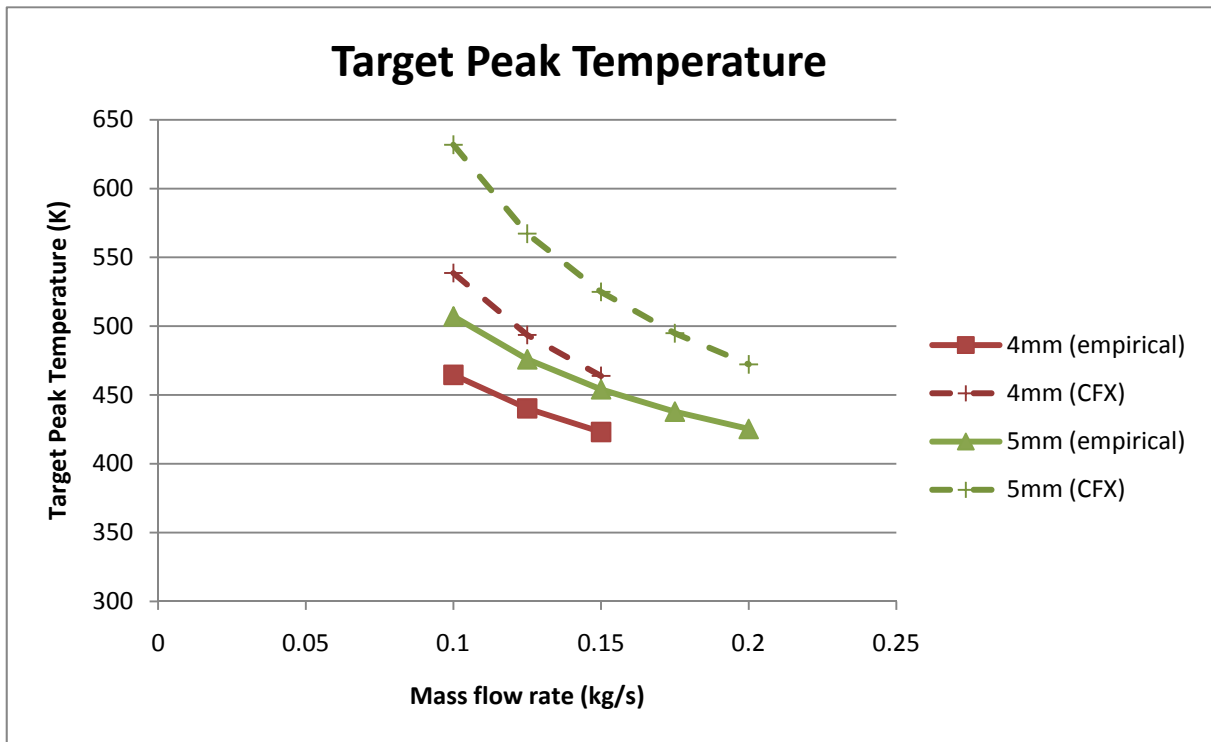
Figure 4.24 Air cooled Beryllium target (9mm) – 60GeV, 700kW, 1.5mmm sigma beam
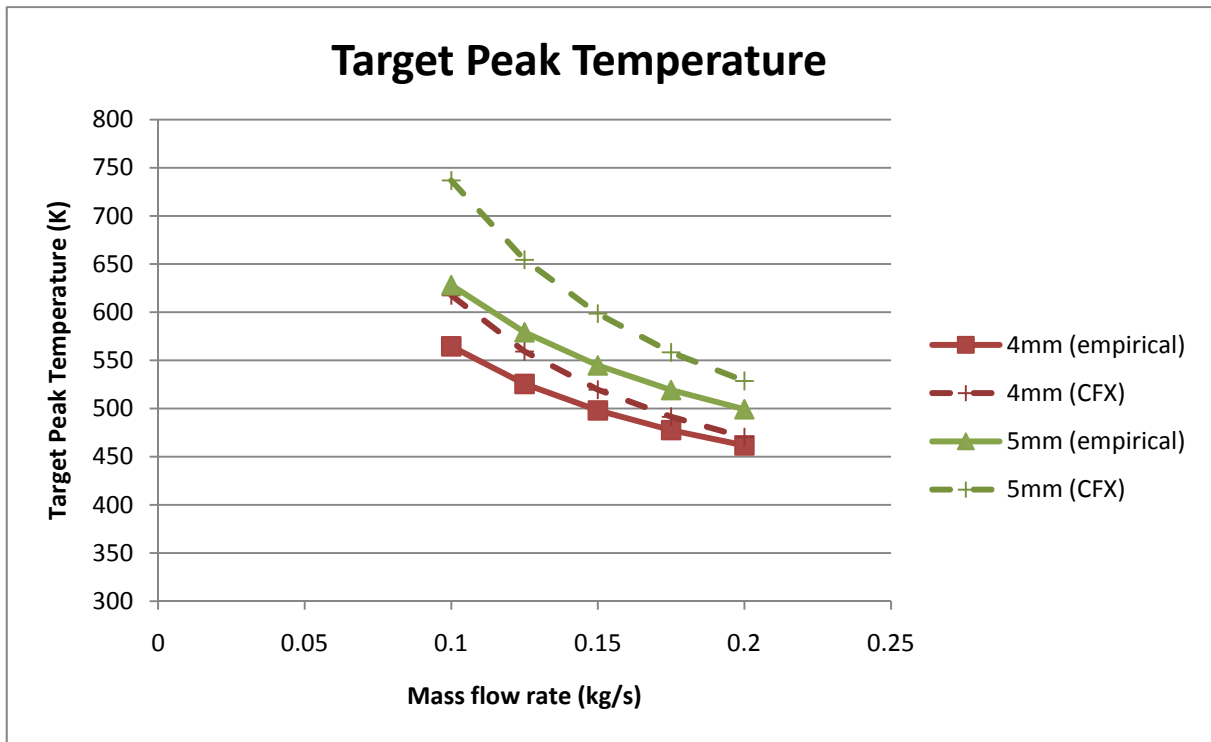
Figure 4.25 Air cooled Beryllium target (21mm) – 60GeV, 700kW, 3.5mmm sigma beam
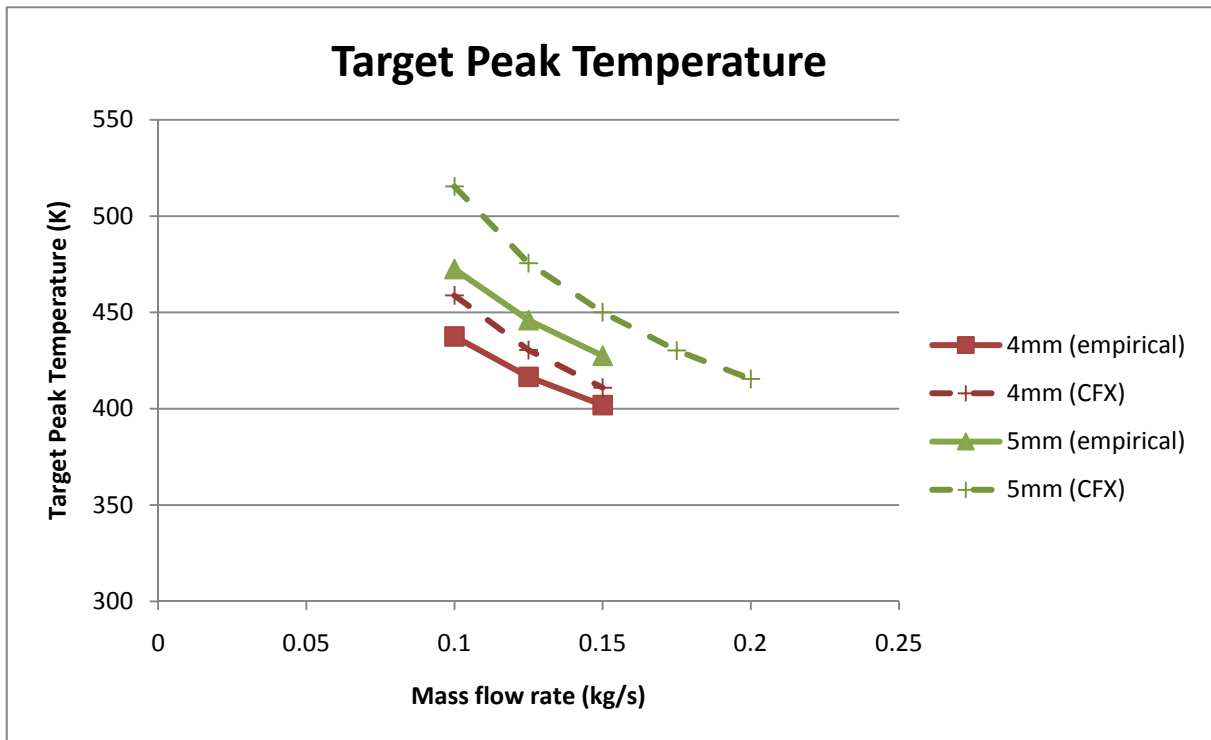
Figure 4.26 Air cooled Beryllium target (9mm) – 120GeV, 700kW, 1.5mmm sigma beam
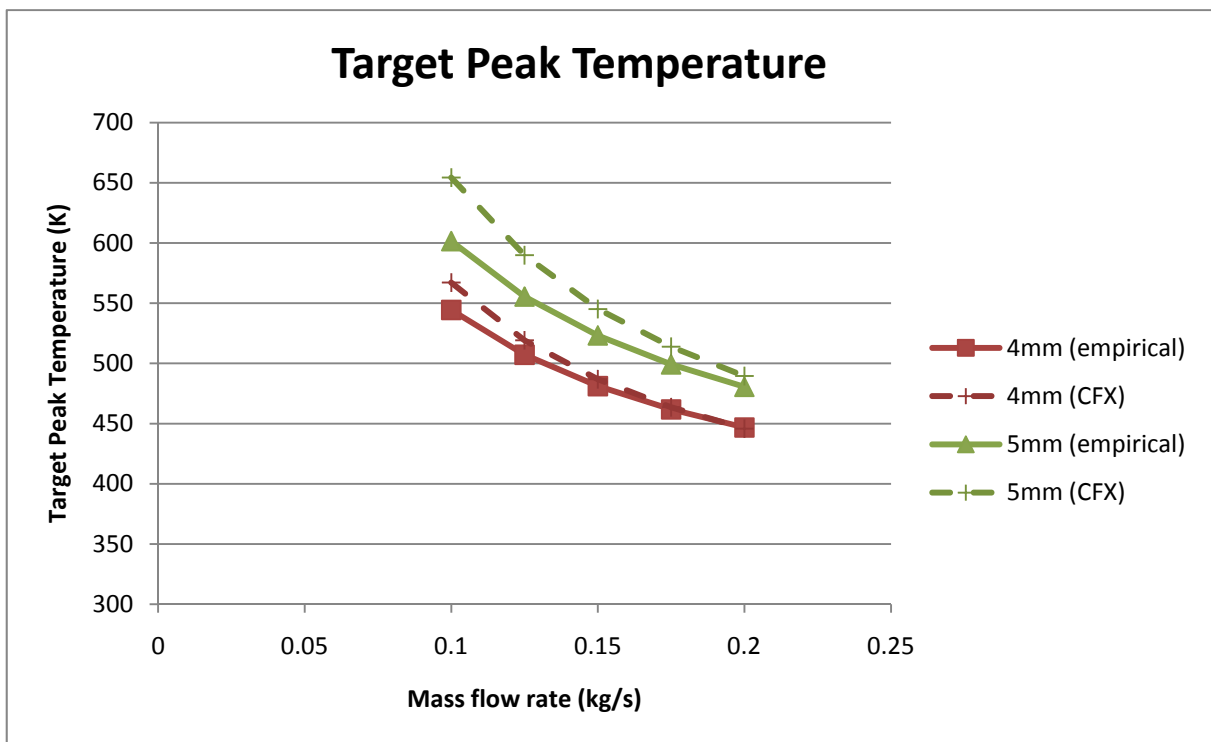
Figure 4.27 Air cooled Beryllium target (21mm) – 120GeV, 700kW, 3.5mmm sigma beam

From the results for peak target temperature it can be seen that the temperature estimation from a simple conduction calculation are reasonable for water cooled targets. This estimation also gives good agreement with gas cooled targets at high flow rates. However the peak temperature of gas cooled targets at low flow rates with a large duct gap are generally underestimated.

To investigate this discrepancy an Ansys model was used to study one of the worst cases with the heat transfer coefficient from both empirical calculations and CFX simulations. The heat deposition in the Ansys model was imported from a Fluka output file. An example for a Helium cooled, 21mm diameter Beryllium target with a 60GeV, 2MW beam is shown in Figure 4.28.
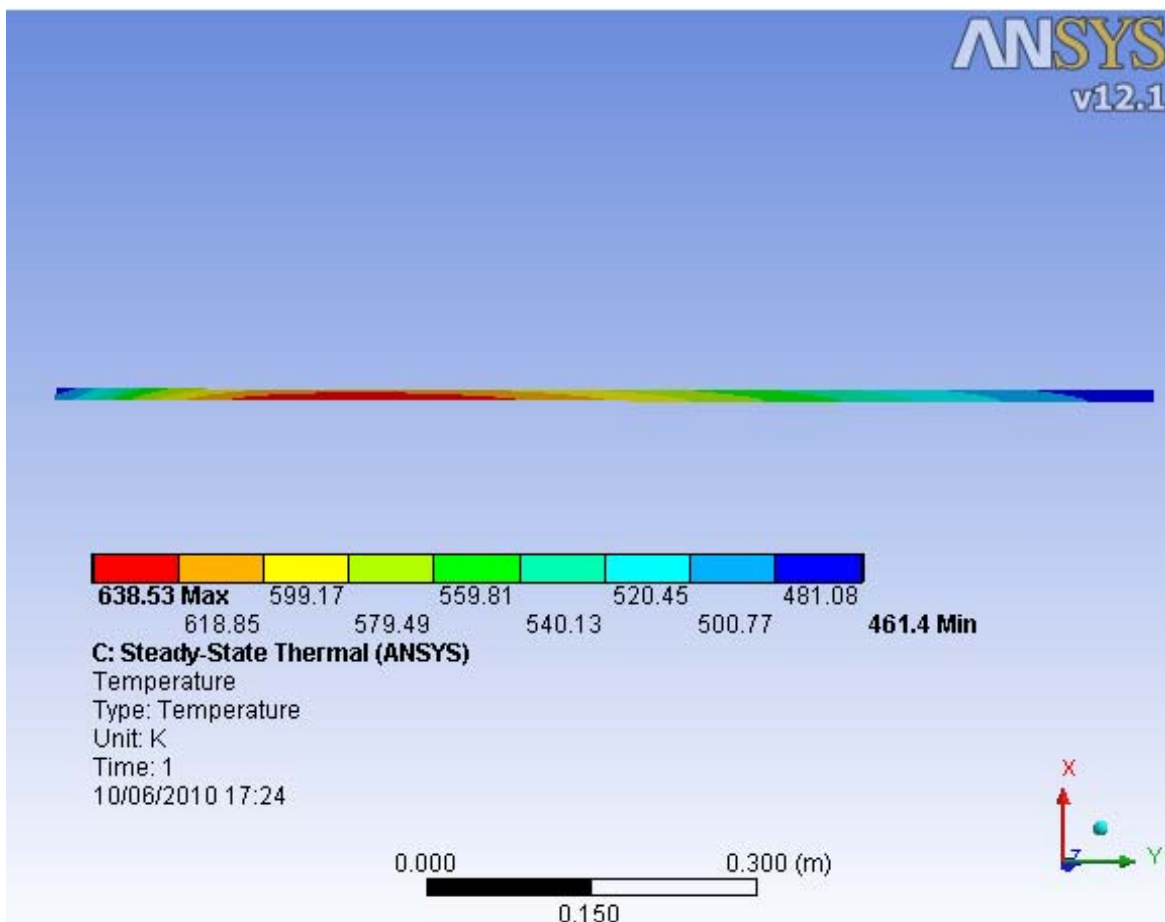
Figure 4.28 Ansys simulation showing steady-state target temperature for 21mm Beryllium rod. Heat deposition from a 60GeV, 3.5mm sigma, 2MW beam (Heat Transfer coefficient = 1335 W/m²·K)

Table 4.3 shows a comparison of peak target temperatures using different methods for a case with a large discrepancy.

Table 4.3 Comparison of peak target temperature calculation using different methods. Helium cooled (50g/s with 5mm duct gap), 21mm diameter Beryllium target with a 60GeV, 2MW beam.

Analysis method	Heat Transfer coefficient (W/m^2.K)	Target Peak temperature (K)
Empirical HTC + Simple conduction	1335	637.2
Empirical HTC + Ansys (full Fluka input)	1335	638.5
CFX HTC + Ansys (full Fluka input)	1173	682.6
CFX CHT (using full Fluka input)	1173	730.6

From this study it can be seen that a conjugate heat transfer analysis is important to correctly estimate the target temperature if the flow rate is low and/or the duct gap is large. Reasons for this are:

1. Heating of fluid is underestimated by uniform distribution. This is significant at low flow rates and/or large duct gaps where the change in the local fluid temperature are high
2. CFX calculates the heat transfer coefficient and near wall temperature along the length of the target
3. Heat transfer coefficient is overestimated by the empirical calculations used in this study for gases at low flow rates

4.5 Additional considerations for pressure drop

In the above analysis we have only considered the pressure drop from a single pass of the cooling fluid (e.g. an annular duct over 1 metre). To minimize material downstream of the target and for practical issues of integration with the horn, it is preferable for both coolant supply and return pipes to be at the upstream end of the target, requiring a 180 degree turn of the coolant at the downstream end. This will significantly increase the pressure drop due to the extra length of the cooling circuit and the losses that occur by turning the fluid 180° in a restricted volume. Figure 4.29 shows an example of this for 100g/s of Helium at 10bar pressure. In this analysis the target diameter is 21mm and the inner duct gap is 4mm. The space between the inner and outer ducts is 0.5mm and the gap in the outer flow duct is 3.05mm to give a uniform cross-section. For a horn with a bore of 39mm this design would only leave a 1.5mm clearance gap between the target and horn.
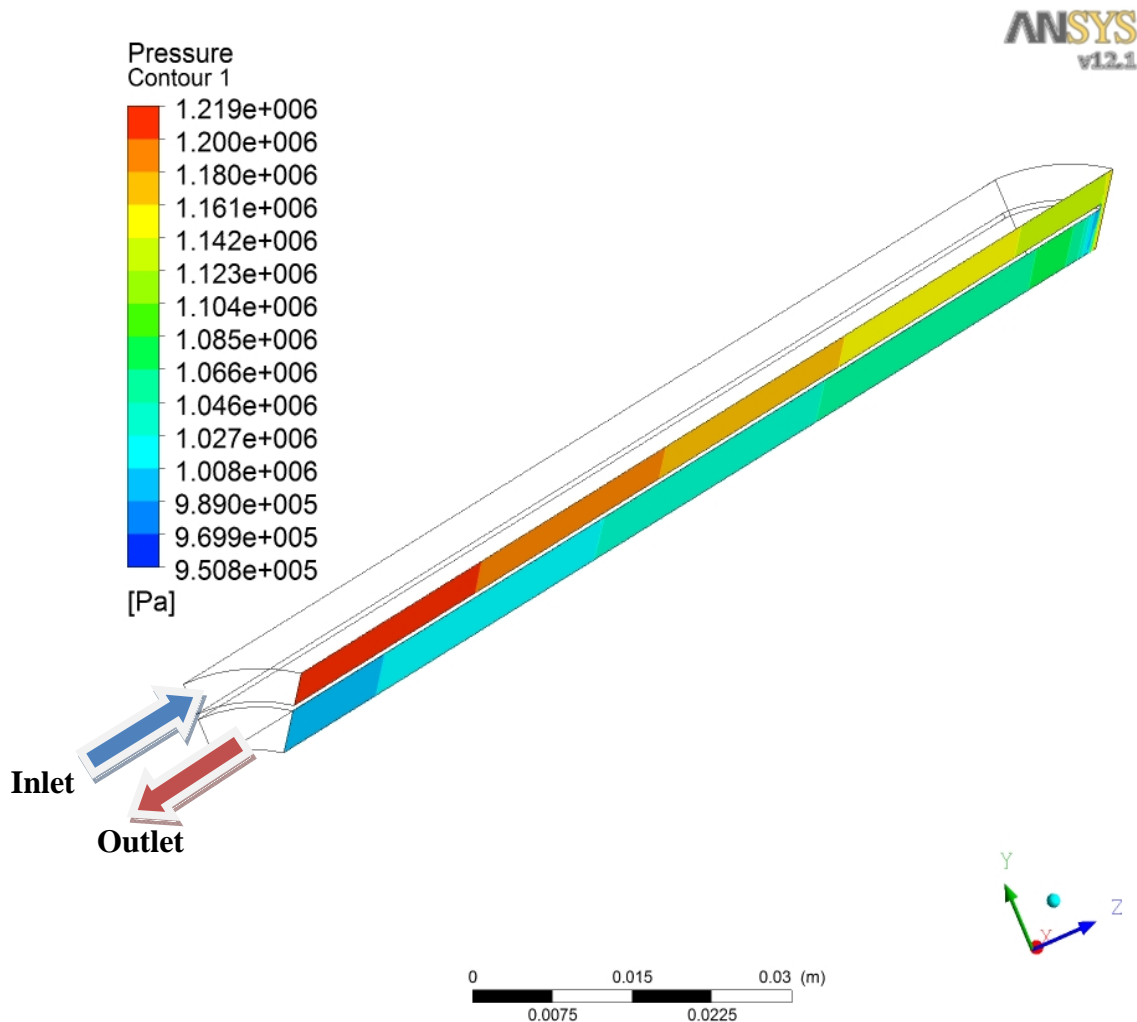
Figure 4.29 Example of annular duct cooling with 180° turn and return channel

Figure 4.30 shows a plot of the velocity contours at the 180° bend. It can be seen that the effective cross section of the outlet duct is reduced due to the momentum of the fluid. This effect gives rise to the additional pressure drop.
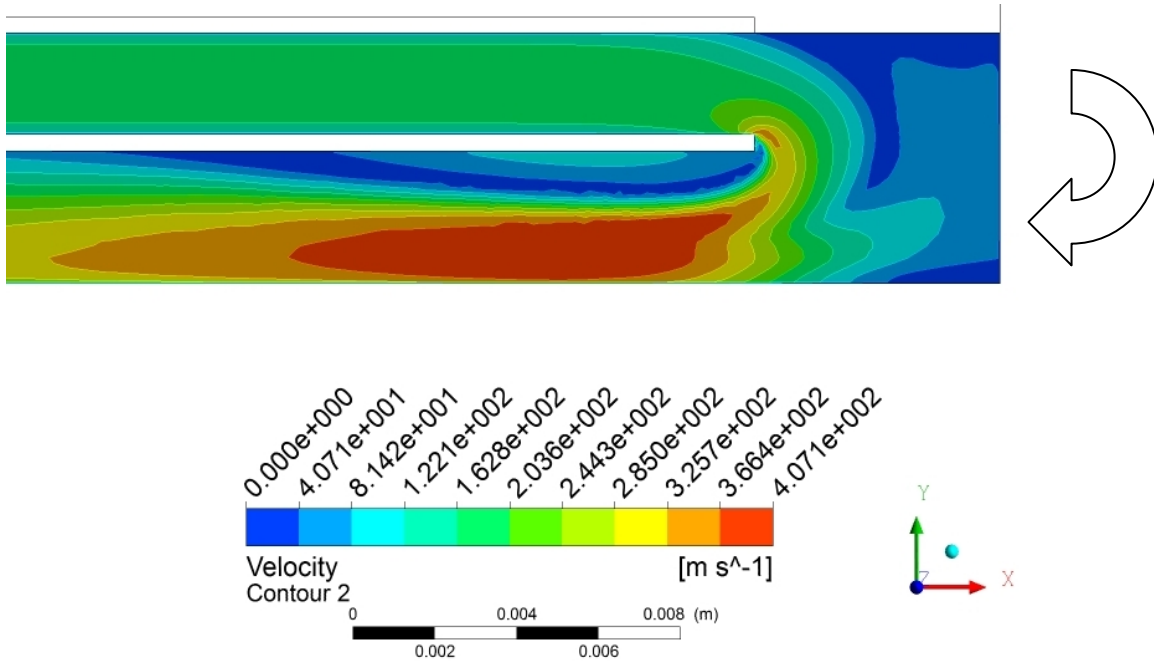
Figure 4.30 Velocity contours of helium gas at 180° bend

Figure 4.31 shows a comparison of the pressure drop from a single pass annular cooling channel and a return flow double concentric cooling system. From these results it can be seen that the pressure drop is approximately 2.6 times higher for the double annular duct.
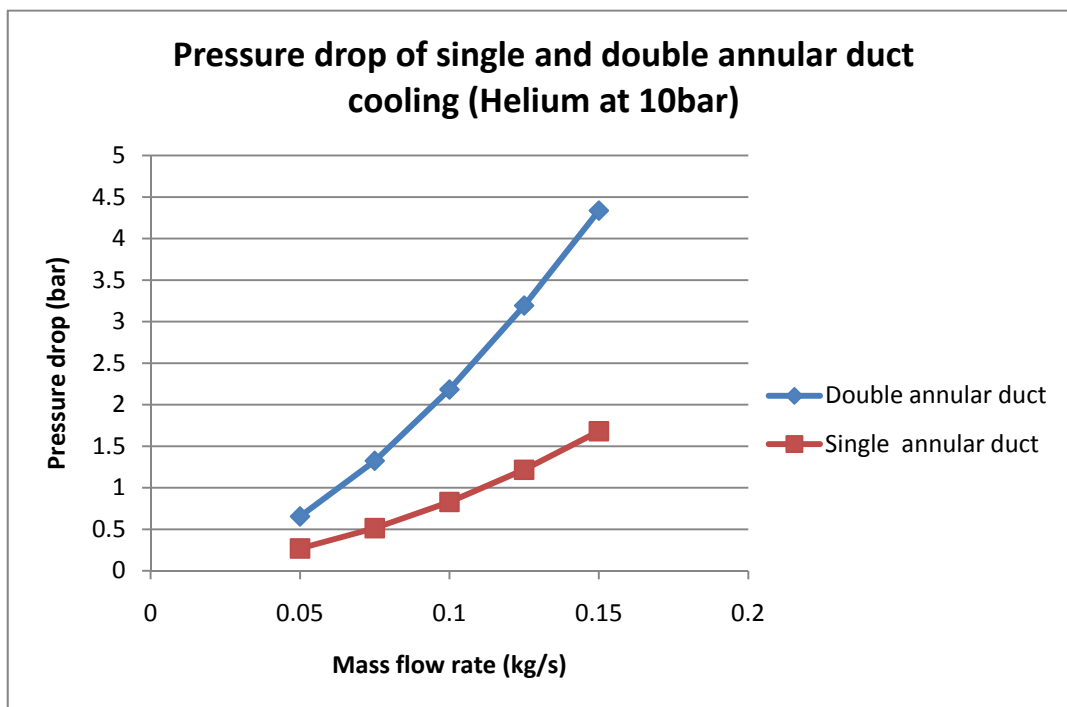
Figure 4.31 Comparison of the pressure drop between single and double annular ducts

The pressure drop of the 180° bend can be reduced by careful optimisation of the geometry. The aim of this optimisation is to create a more gradual direction change and to locally increase the duct cross-sectional area.

In addition to the pressure drop from the target a significant margin must be allowed for heat exchangers and pipe work when specifying compressor or pump requirements. It is possible that the total system pressure drop could be between 2-3 times that of the target alone. This is an important consideration when selecting the target cooling method.

For compressible gases the pressure drop of the target cooling system can be reduced by increasing the system pressure as shown in Figure 4.32. Increasing the system pressure decreases the pressure drop by reducing the flow velocity and therefore the frictional losses.
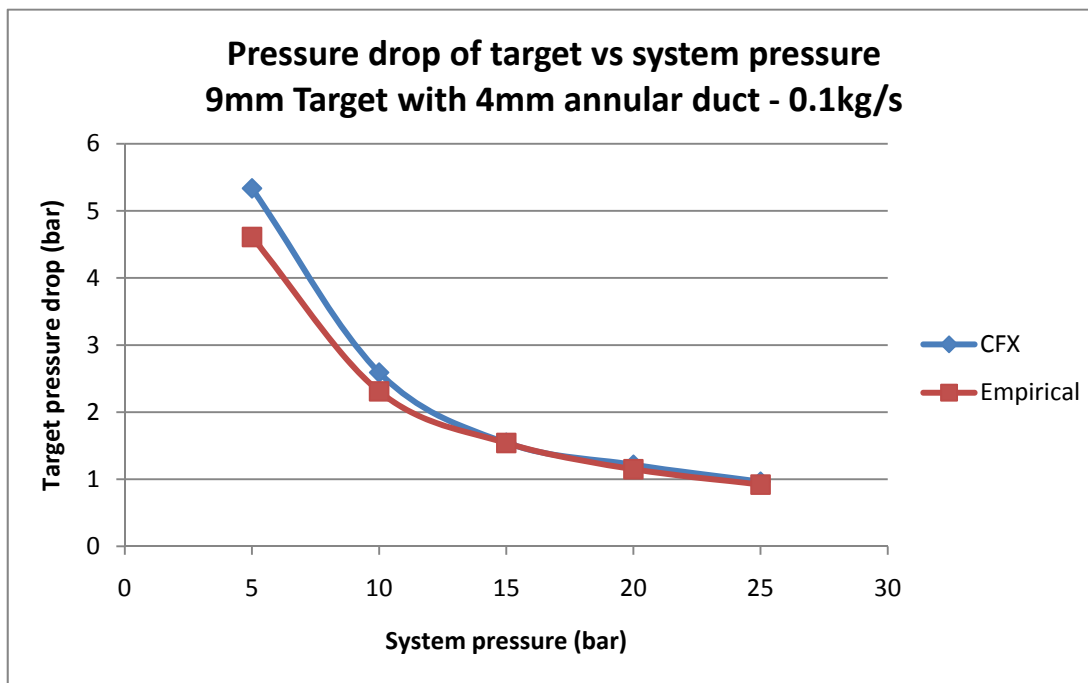
Figure 4.32 Pressure drop vs. System pressure

Increasing the system pressure reduces the fluid velocity and increases the fluid density. These changes cancel out in the Reynolds number calculation for a given mass flow rate. Therefore the heat transfer coefficient is not dependant on system pressure and the HTC results in this study are reasonably valid regardless of system pressure.

4.6 Energy deposition in water and associated pressure jump

Energy deposition in helium or air is not thought to be significant however, the energy deposition in water must be considered. In this analysis we consider the annular channel of flowing water around the target as shown in Figure 4.1. As a result of the beam interaction with the target particles leave the target and enter the water jacket depositing energy in the water as they interact with the water molecules. FLUKA is used to obtain the energy deposition in the water, an example of the energy deposition in the target and water is shown in Figure 4.33. Energy deposition in the water is calculated for both 700kW and 2.3MW with both 9 and 21mm diameter beryllium targets (Results summary in table 4.4). Beam sigma is taken as one third of the target radius. The annular water duct is 4.5mm wide for the 21mm diameter target and 3.5mm for the 9mm diameter target.
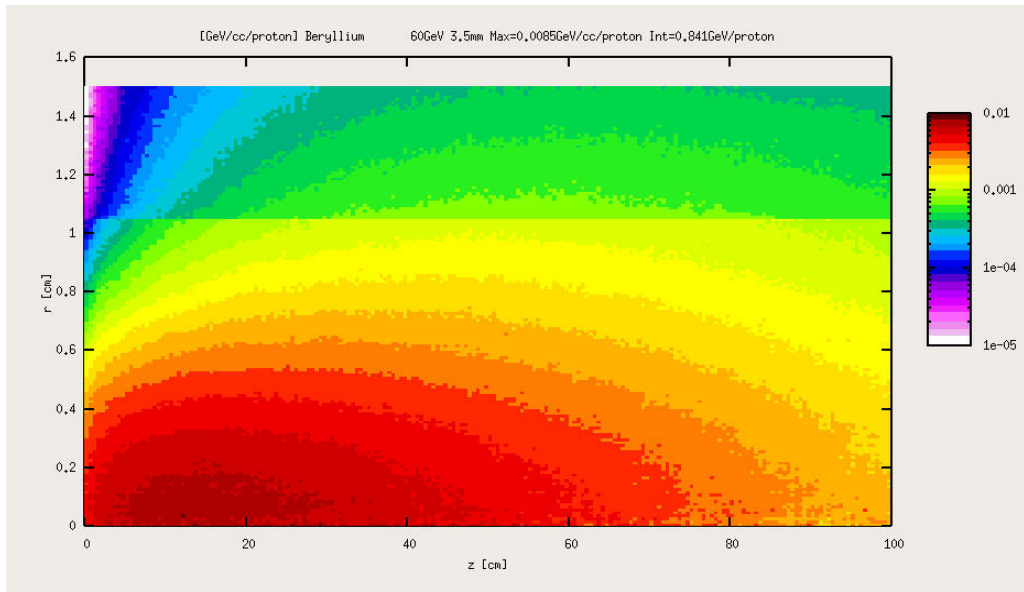
Figure 4.33 Energy deposition in beryllium target and annular water jacket, 60GeV 3.5mm sigma beam

The pressure jump in the water can be estimated using the following expression for pressure rise as a result of a constant volume temperature jump.

$$\propto_v = \frac{1}{V} \frac{dV}{dT}$$

$$K = V \frac{dP}{dV}$$

$$dP = K \propto_v dT$$

The first thing to note is that the Bulk modulus and the volumetric thermal expansion coefficient for water change significantly with temperature. Figure 4.34 shows how the two parameters vary in the temperature range of interest (NIST).
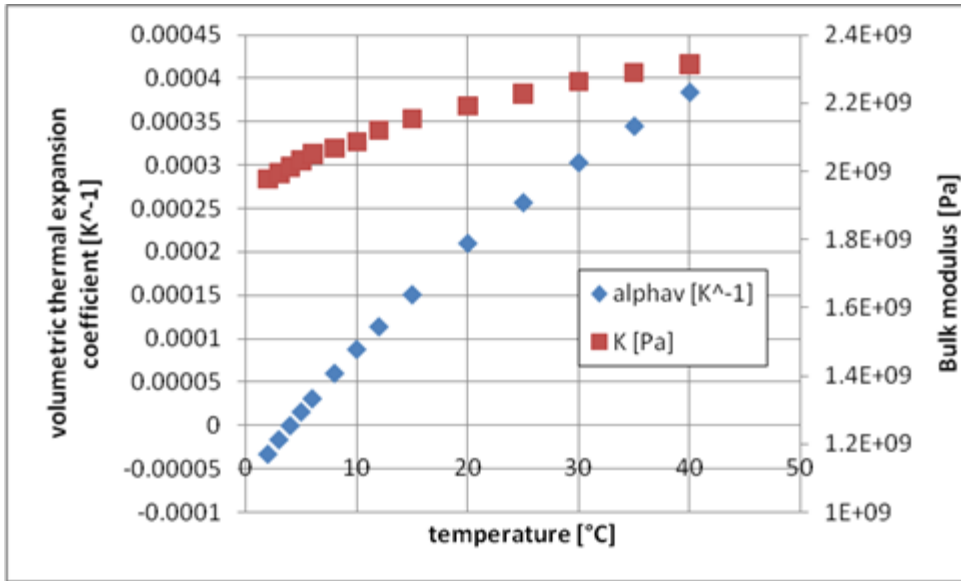
Figure 4.34 Variation in water properties with temperature

Based on the maximum temperature rise in the water per pulse the maximum pressure rise can be calculated using the temperature dependant properties. To obtain the max pressure rise as a function of temperature a simple average temperature has been taken such that if the water starts at 5K then the properties at 5K+ 0.5*temperature jump are used. Clearly from this it can be seen that cold water is beneficial in terms of the pressure jump (Figure 4.35).
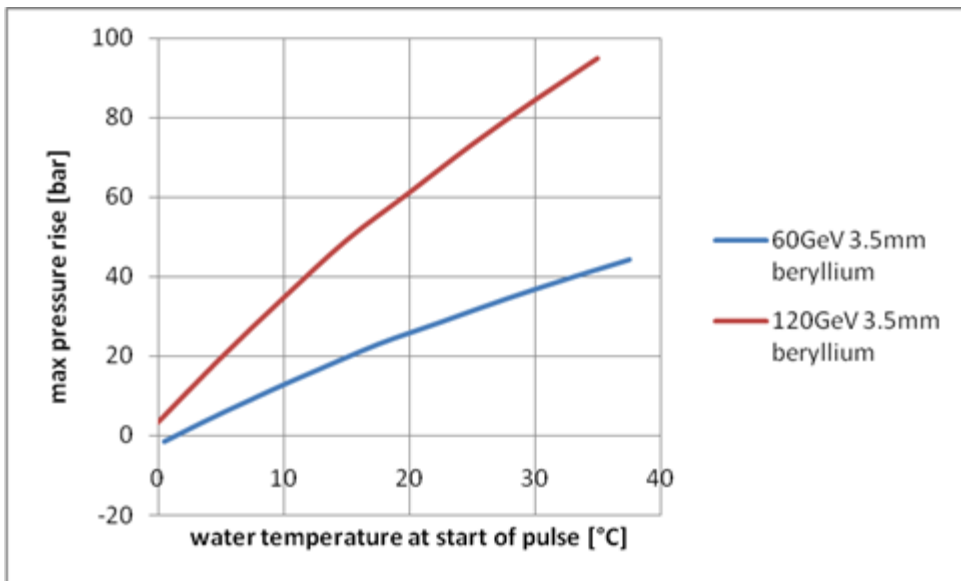
Figure 4.35 Pressure rise as a function of water temperature at start of the spill for beryllium targets with 60 and 120GeV 3.5mm sigma beams

Table 4.4 shows the peak and integrated energy deposition in a water jacket for all the beryllium target cases that we are considering. The maximum pressure rise is calculated based on the average water temperature before the pulse being 20°C.

Table 4.4 Water energy deposition summary for beryllium targets

Beam Energy (GeV)	Beam Power (MW)	Beam sigma (mm)	Maximum energy deposited in water per pulse [J/cc]	Maximum temperature jump per pulse [K]	Maximum pressure rise based on KαΔT, water starts at 20°C [bar]	Integrated energy deposition per pulse [kJ/pulse]	Time averaged power deposited in the water [kW]
120	0.7	1.5	32	7.6	41	2.0	1.6
		3.5	14	3.3	16	2.5	1.9
60	0.7	1.5	21	5.0	26	1.2	1.6
		3.5	7	1.8	9	1.5	2.0
120	2.3	1.5	105	25.1	185	6.7	5.1
		3.5	45	10.7	61	8.2	6.2
60	2	1.5	59	14.1	88	3.4	4.5
		3.5	21	5.0	26	4.4	5.8

The IHEP report [8] stated a maximum temperature jump of 20K for the case of 120 GeV 2MW with a 1.5 mm beam sigma. It is interesting to note that they assume a water inlet temperature of 37°C which gives them 150 bar pressure jump for the 20K temperature rise. They also estimated a 30 kW heat load on the water system with 25 kW of that being heat transferred from the target and presumably the rest coming from direct energy deposition in the water. These calculations also indicate a significant additional heat load on the cooling system resulting from energy deposition in the water (Table 4.4).

Other factors that effect water pressure jump

The simple calculation used to obtain Figure 4.35, i.e. $\Delta P = \propto_v K \Delta T$ can only be used to give a worse case indication. The simple calculation does not account for spreading of the pressure waves during the pulse duration, nor does it account for flexibility of the water containment vessel. Using the FLUKA data as an input for an autodyn model where the boundaries of the water volume are rigid (i.e. no room for expansion) the peak pressure is not as high as the "$\Delta P = \propto K \Delta T$ estimate" due to spreading of pressure waves during the pulse (Figure 4.36). The plot of several gauge points in the water jacket indicates that the peak pressure is about 40 bar as opposed to 46 bar obtained from the constant volume approximation using the same values for the water properties. The plot also shows an oscillation in the water pressure which is as a result of longitudinal pressure waves travelling through the water.
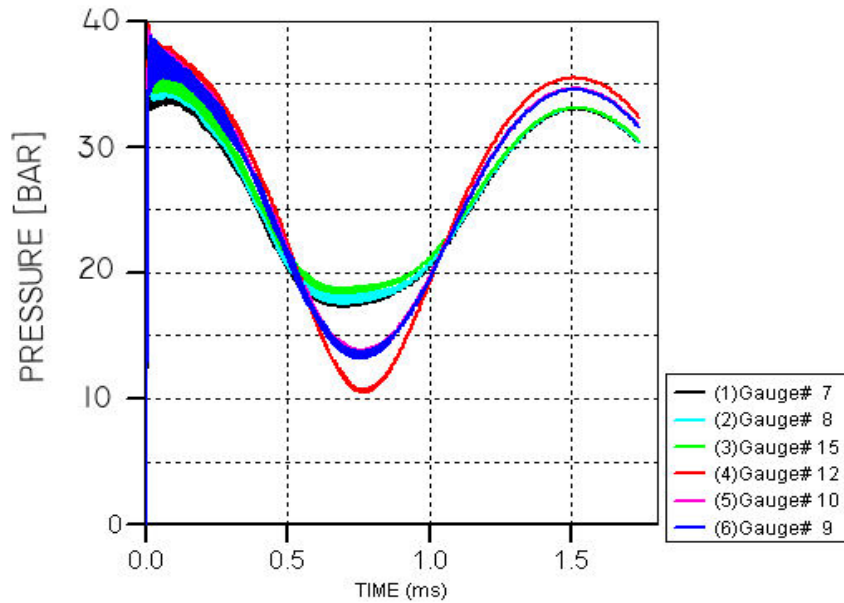
Figure 4.36 Pressure rise at several points in the water, water properties taken at 20°C, result accounts for spreading of pressure waves during the spill but assumes rigid boundary conditions to the water volume,. Maximum pressure = 40bar.

If the water is contained by a beryllium tube which is sufficiently thin to flex as the pressure of the water acts on it, as indicated in Figure 4.37, then the peak pressure reduces with respect to the rigid boundary condition. Figure 4.38 shows the pressure peak in water contained in a 2 mm thick tube is reduced to around 30 bar. A small amount of expansion as the waves from each bunch reach the inner surface of the water jacket can have a significant effect on the peak pressure. It is worth noting that heating and subsequent expansion of the water containment due to secondary particle interaction may also reduce the water pressure however this effect has not been analysed here.
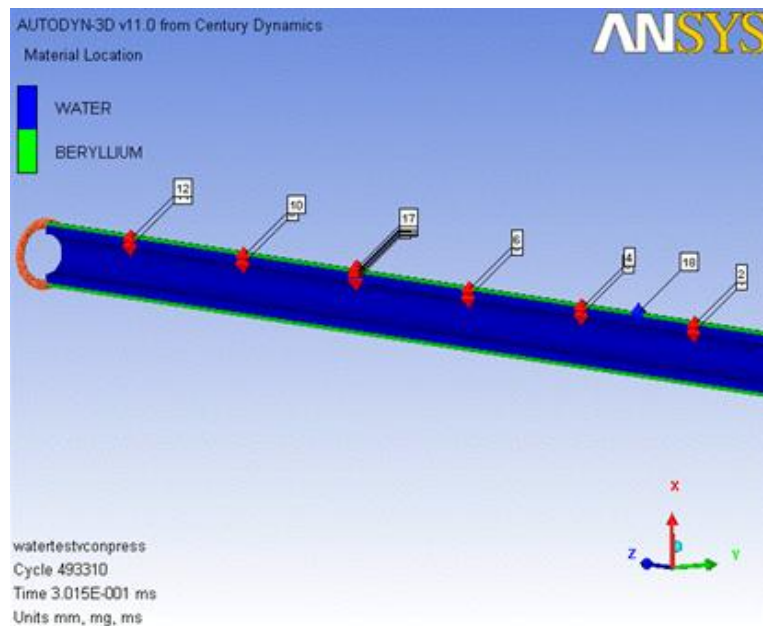
Figure 4.37 Graphical image of the Autodyn model of a water jacket contained by a beryllium tube
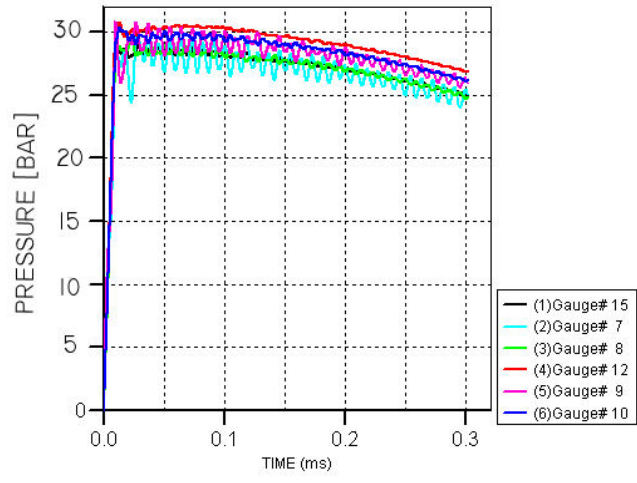
Figure 4.38 Maximum pressure rise with allowance for expansion of water jacket

One method that has been proposed to reduce the pulsed beam induced pressure waves generated and transmitted in a contained liquid is to inject a sufficient population of gas bubbles into the flowing liquid [9]. The purpose of the compressible bubbles is to attenuate the pressure wave. Indeed, the scattering or attenuation of acoustic waves may be used to measure the bubble population [10].

Another important consideration when selecting a cooling method is that a water jacket could absorb a significant number of the pions emerging from the target. This would not be a problem with gas cooling which is relatively transparent to the pions. To evaluate this the FoM from a simple cylindrical beryllium target is compared with the FoM based on pions emerging from the surface of an annular water jacket and from the end of the target which is not covered by water. A reduction in FoM of around 4% is expected as a result of the water jacket, (Figure 4.39). This calculation does not include the addition of a metallic tube to contain the water which will further absorb pions.
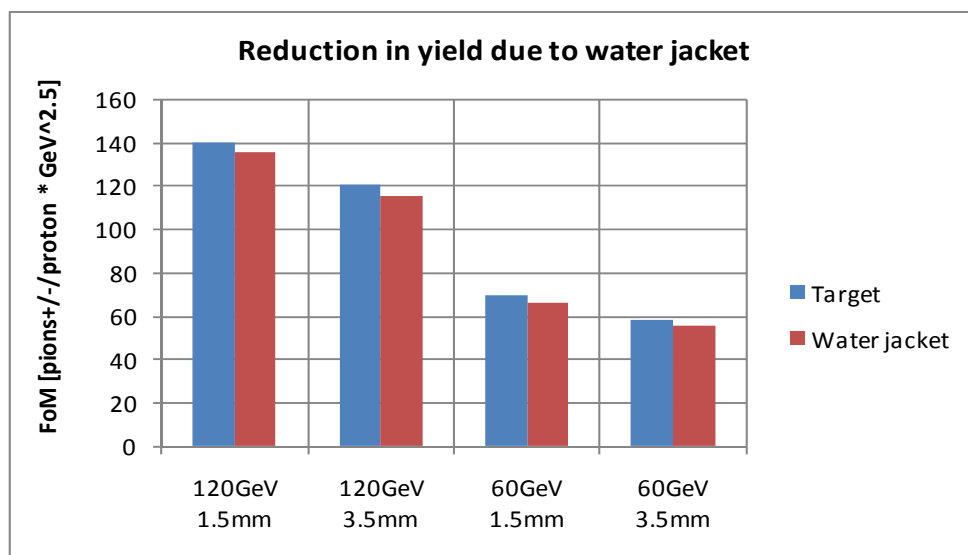
Figure 4.39 Reduction in pion yield as a result of an annular water jacket for beryllium targets

4.7 Water spray cooling

A preliminary study of water spray cooling was carried out to investigate the effects of non-uniform heat transfer. Due to the space required, water spray cooling is only an option for the integrated target and horn inner conductor concepts studied in Section 5. The model shown in the following case was for a 21mm Beryllium target with steady-state 2MW heat deposition from Fluka for the 60GeV, 3.5mm sigma case. It should be noted that this model only includes beam heating and does not include the resistive heating from the horn current. A quarter symmetry was used and the spray jets were applied by 6 coordinate systems normal to the target surface as shown in Figure 4.40.
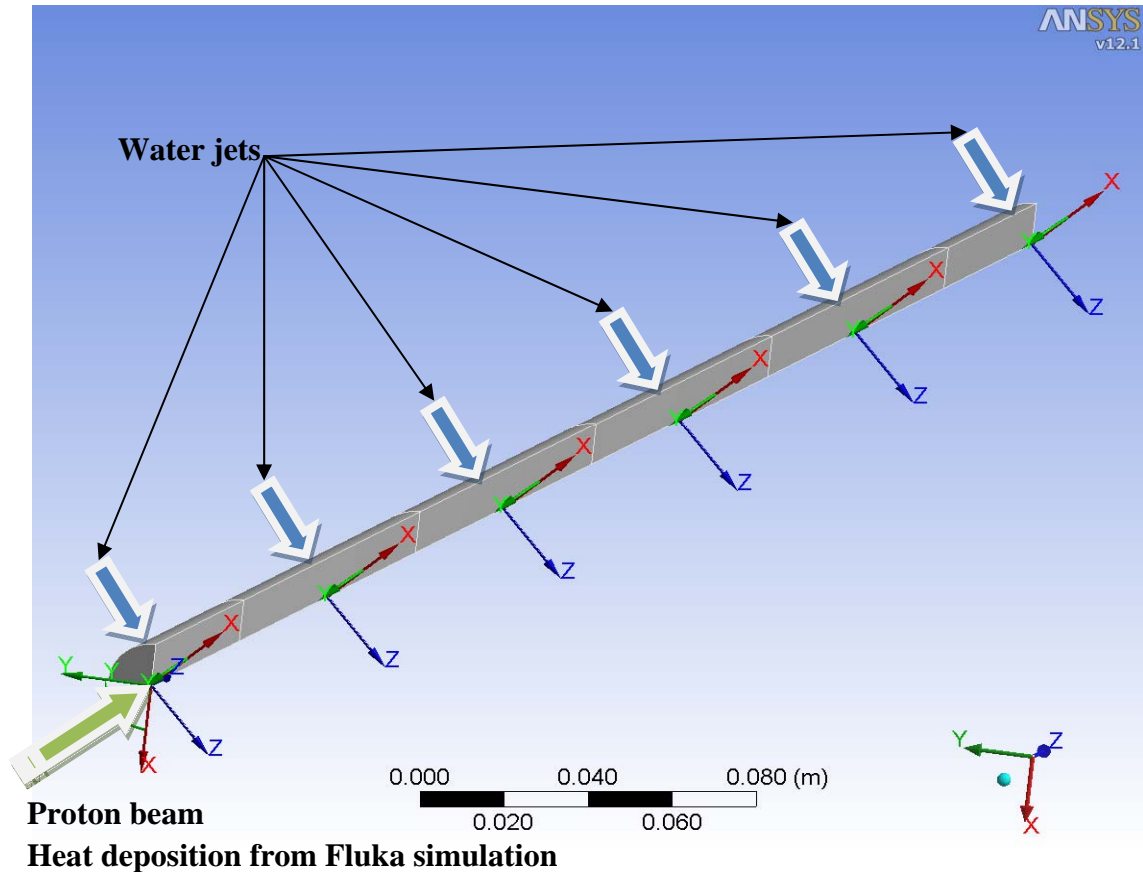
Figure 4.40 Ansys water spray cooling model

In all cases an approximate average heat transfer coefficient of 12,000 $W/m^2.K$ was applied to the target surface. The distribution of the heat transfer was initially uniform and then modified to simulate an increasingly focused water jets as shown in Figure 4.41
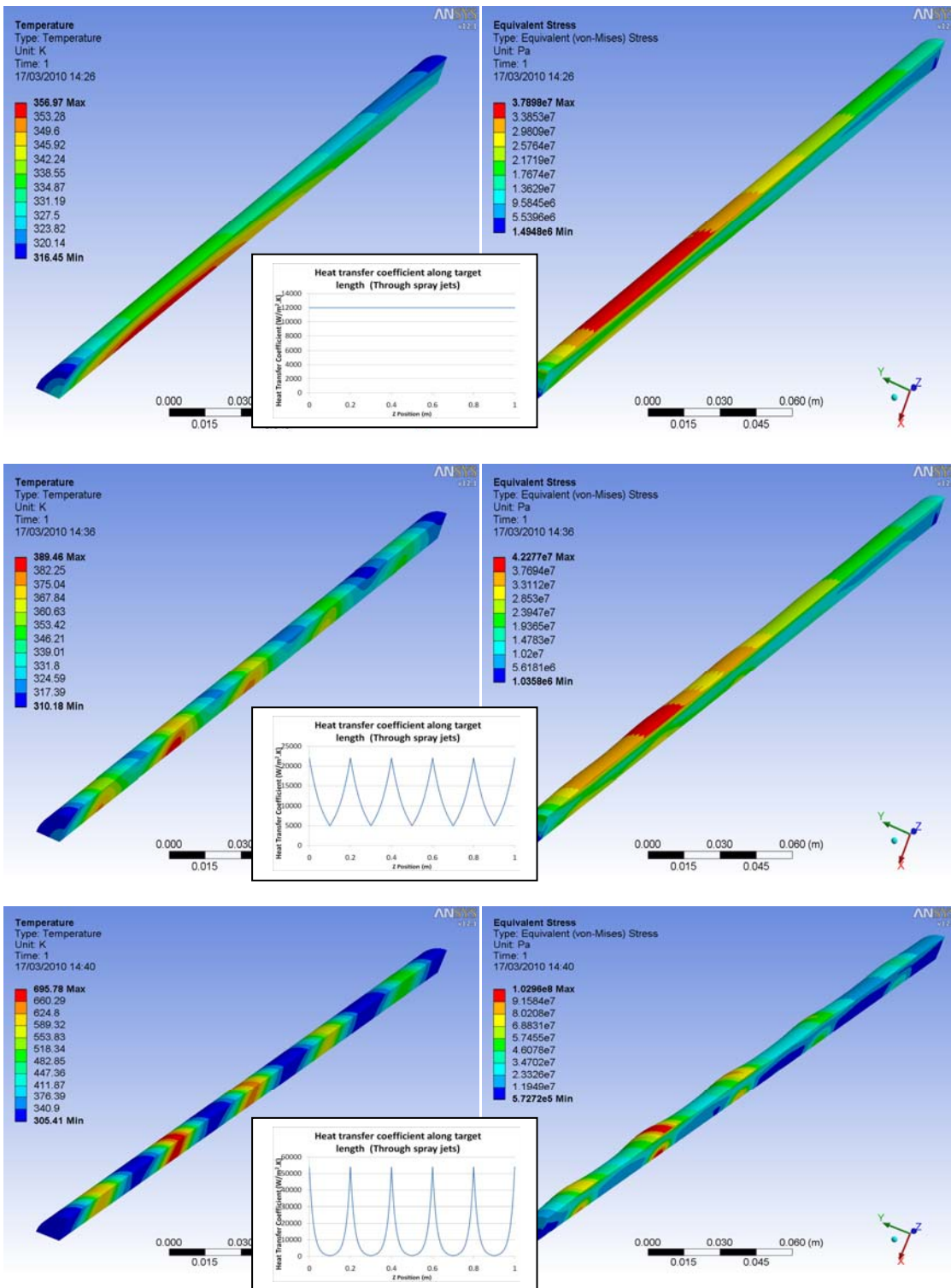
Figure 4.41 Effect of heat transfer coefficient uniformity on target temperature and stress distribution (Top results are uniform HTC and results below for non-uniform water spray jets)

From these results it is clear that a non-uniform heat transfer on the target surface could significantly increase the maximum target temperature and stress. However this result is for a time averaged beam and the effect should be studied to include transient effects.

4.8 Study of a proposed single layer water cooled design

As it was shown in section 4.6 that the cooling water surrounding the target can contribute significantly to pion absorption, a concept design was studied which minimises the thickness of water surrounding the target. A design with a single annular duct split into four channels as shown in Figure 4.42 is proposed.
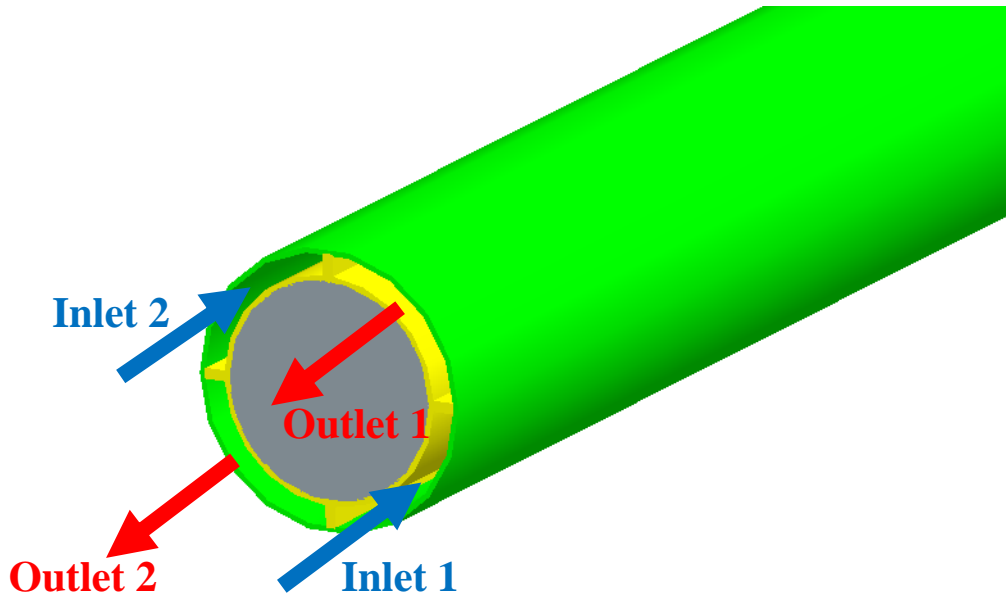
Figure 4.42 Inlets and outlets of concept design

Two different designs were considered for returning the flow at the downstream end. The first design consisted of two completely independent channels and the second design allowed flow between channels to combine. Figure 4.43 shows a flat representation of the cooling channels around the target.
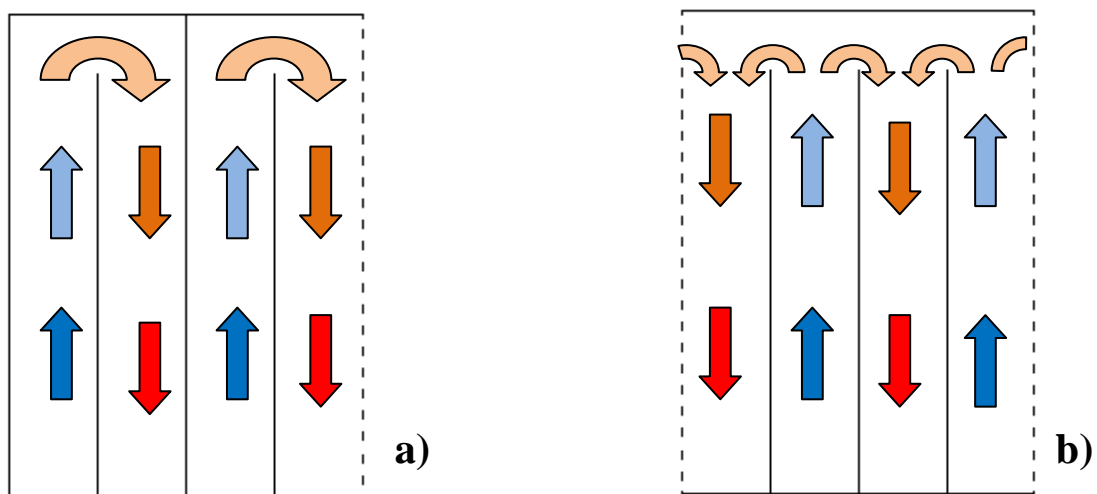
Figure 4.43 a) Two independent channels, b) Combined outlet channels

Using a CFD analysis it was found that the design with combined outlet channels was preferable. This design resulted in a lower pressure drop and a more uniform flow and heat transfer in the outlet channel. This is shown from a plot of streamlines in Figure 4.44
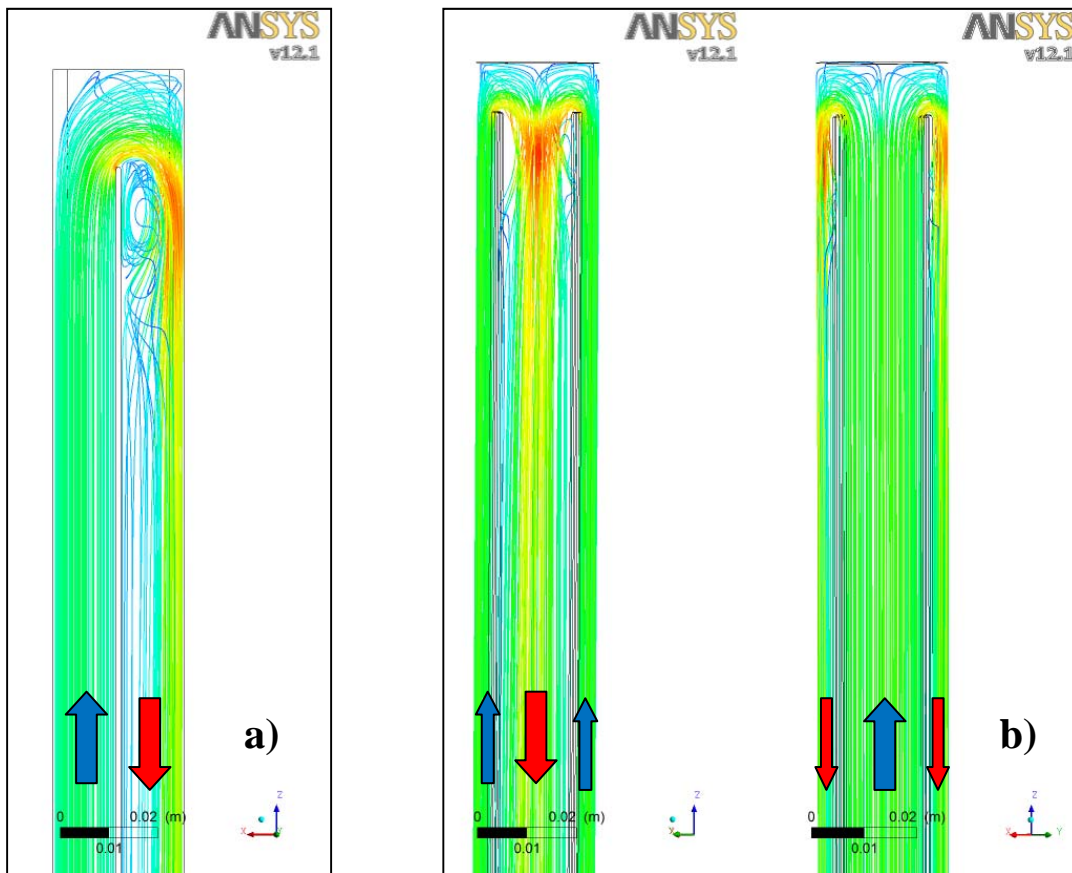
Figure 4.44 CFD plots showing velocity streamlines for two different designs. a) Two independent channels, b) Combined outlet channels

The cooling of the proposed concept with combined outlet channels was studied to check the pressure drop and the steady state target operating temperature. This was completed for a range of flow rates and duct gaps using a conjugate heat transfer analysis with Ansys CFX. In this study the target is treated as a simple Beryllium rod (diameters 21mm and 9mm) with an energy density applied from Fluka. The beam energy was 120GeV and the beam power was 2.3MW for all cases. This equates to approximately 24kW of heat for the 21mm target and 11kW of heat for the 9mm target. The distance between the end of the flow guides and the end of the target in this study is maintained at a constant gap of 10mm (Figure 4.45).
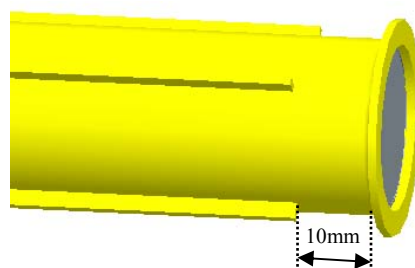
Figure 4.45 Flow return gap size

The fluid region was modelled to be in direct contact with the target rod and coupled using a General Grid Interface (GGI). The fluid was modelled as water with constant properties and the Shear Stress Transport (SST) turbulence model was used. The inlets to the model were defined by the mass flow rate in each of the inlet channels and at a temperature of 300K. The outlet boundary condition was an outlet with a constant absolute pressure of 2bar.

A simulation was carried out which modelled the solid fins to check the effects of increased surface area and conduction through the fins. This was found to make little difference to the operating temperature of the target due to the low number and height of the fins. Therefore they were neglected from this study to improve the efficiency of the simulations. Figure 4.46 shows the steady-state target core operating temperature for a range of mass flow rates and duct gaps. In this figure any of the cases shown would be acceptable in terms of maximum steady-state temperature for Beryllium.
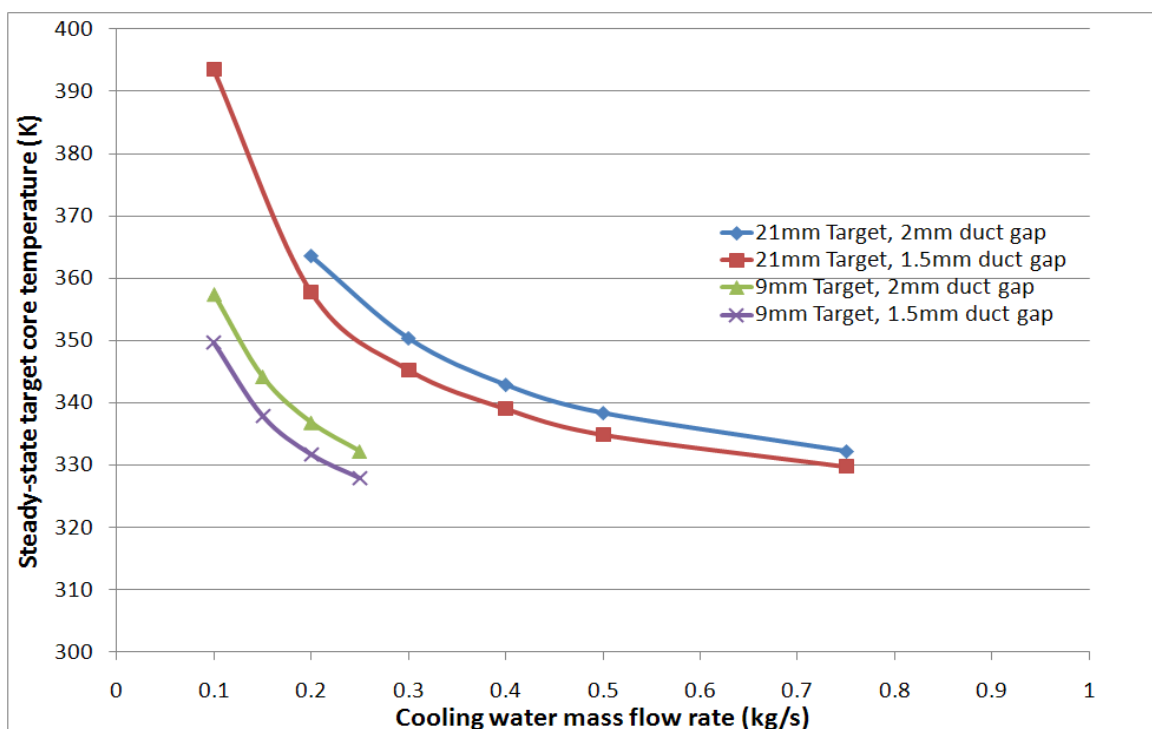
Figure 4.46 Steady-state target core temperature for a range of flow rates and duct gaps

The pressure drop of this design was also studied as it was expected to be considerably higher than the single annular duct analysis. By splitting the single cooling layer into inlets and outlets the flow cross section has been halved, doubling the flow velocity (U) and the duct length (L). If we consider the equation below which is used to calculate the pressure drop than we can see that this will increase the pressure drop by a factor of 8. However this neglects the extra losses that will arise from turning the fluid 180° so the actual increase in pressure drop will be higher.

$$\Delta p = \frac{f L}{D} \frac{\rho U^2}{2}$$

The pressure drops for this design with duct gaps of 1.5mm and 2mm are shown in Figure 4.47. With this design the pressure drop of the target becomes significant with water. Pressure drops are higher for the 9mm target due to the lower cross sectional area, but lower flow rates are acceptable as the power deposited in smaller targets is less.

The pressure drop is also sensitive to the gap between the end of the flow guides and the end of the target (described in Figure 4.45). Larger gaps result in a lower pressure drop but can reduce the cooling performance at the end of the target.
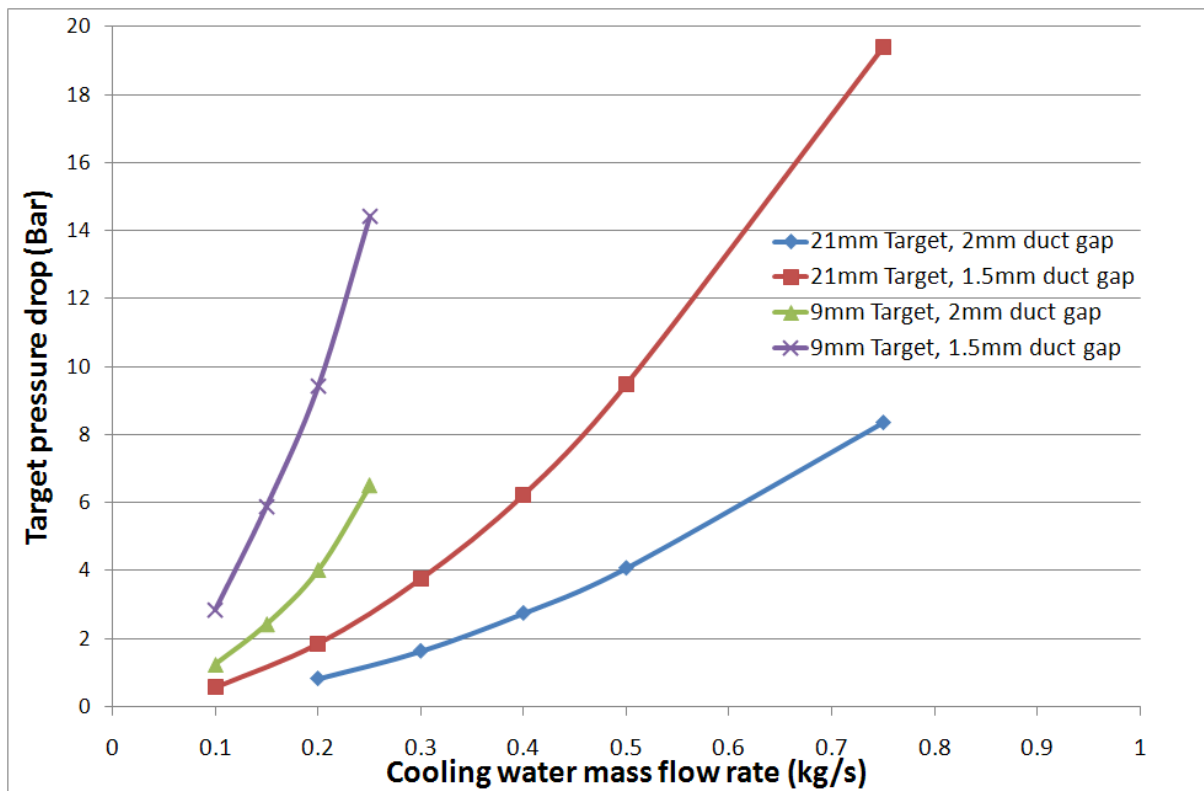
Figure 4.47 Target pressure drop for a range of flow rates and duct gaps

Figure 4.48 shows the temperature rise of the water between the inlet and outlet of the target based on the energy deposition in the target alone. For the actual target design there will also be energy deposited in the target cooling structure and directly in the cooling water. In all of the cases analysed the water stays well below 100°C. However there are advantages to limiting the temperature increase of the water to a low level. As shown in section 4.6, the volumetric expansion of water increase with temperature. This means higher transient pressures will be expected in higher temperature water. Higher temperature cooling water will also accelerate the erosion/corrosion of pipes and the target container.
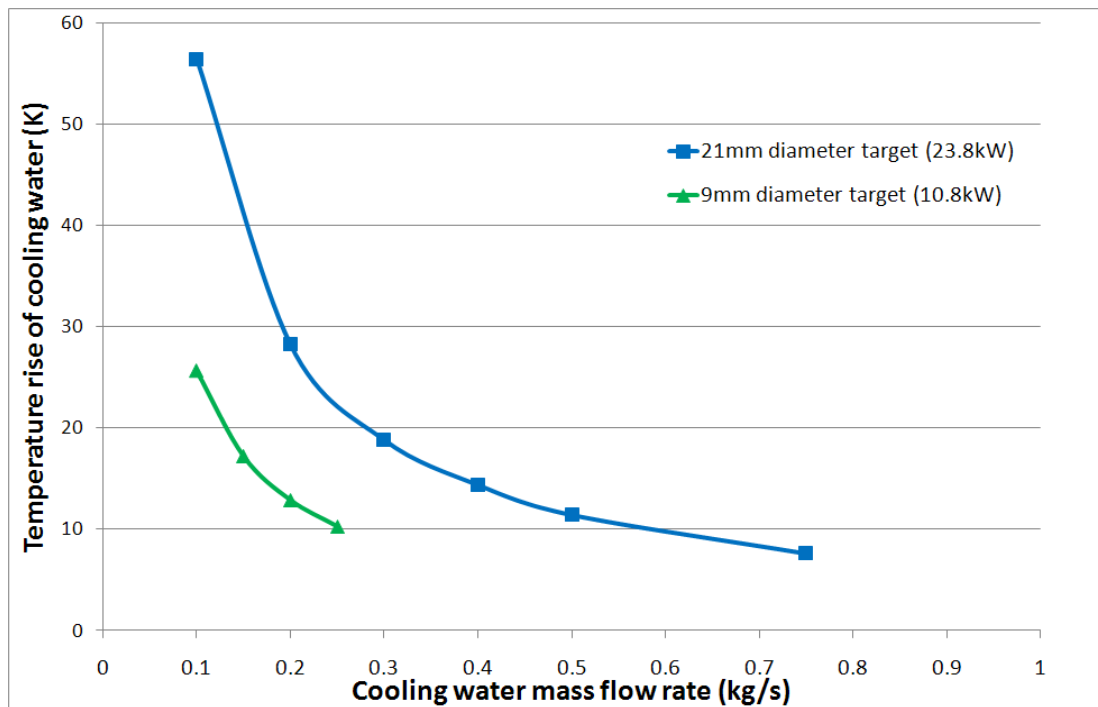
Figure 4.48 Mean temperature rise of cooling water

Another effect of a large temperature rise of the cooling water will be a non-uniform temperature distribution in the target. This is most significant at the upstream end of the target where the cool water enters and the hot water exits as shown in Figure 4.49. Higher flow rates result in less thermal gradient between the inlet and outlets channels and therefore will experience less stress.
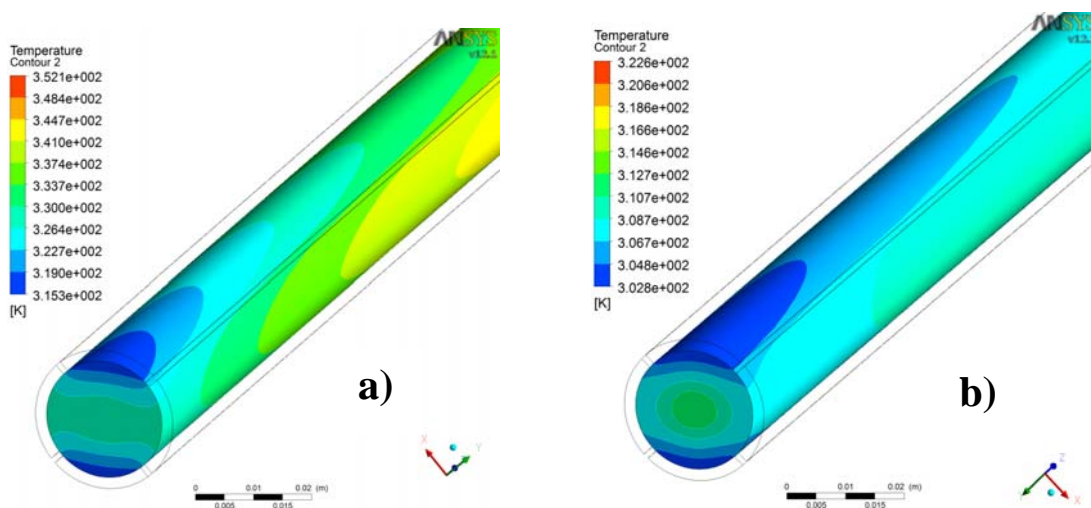
Figure 4.49 Surface temperature of 21mm target with 2.3MW beam.
a)Mass flow rate = 0.2kg/s, b) Mass flow rate = 1kg/s

Erosion-corrosion

High cooling water flow velocities can lead to premature failure of materials by a mechanism known as erosion-corrosion. The protective oxide layer of many metals can be damaged by high velocity flow which then allows the metal to corrode. This process then repeats until failure of the pipe occurs. Some of the factors that determine erosion-corrosion rate are the flow velocity, impingement angle and material selection. Materials with a weak oxide layer are particularly susceptible. Copper and aluminium are such materials and guides for heat exchangers quote maximum flow velocities for cold water of around 2m/s for aluminium and 3m/s for copper to avoid this type of damage [11]. Harder materials and materials with a strong oxide layer such as stainless steel and nickel alloys are much more resistance to this type of damage.

Values for maximum flow velocities for stainless steel have been found in the range of 5-20 m/s [11][12]. The mean flow velocities for the concept design are shown in Figure 4.50. Whilst the effects of erosion-corrosion are probably small, they should be considered as the target design is likely to include thin walls to reduce heat deposition.
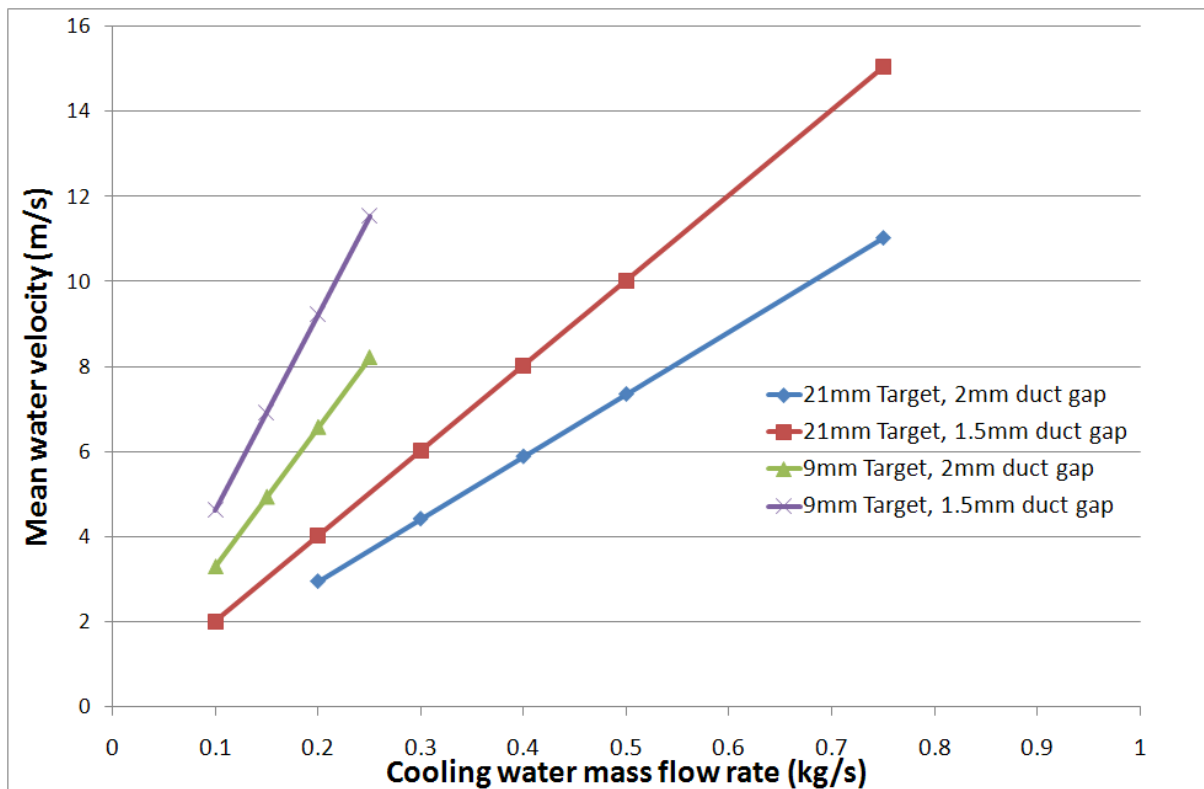
Figure 4.50 Mean velocity of cooling water

Summary of water-cooled target design

This study has shown that a single layer water cooling design concept is viable for 2.3MW. The final cooling parameters must be selected by evaluating the desired operating pressure and temperature of the target. Thinner water channels will give rise to a higher operating pressure and increase the sensitivity of the heat transfer coefficient to a variation in the duct gap. A uniform heat transfer coefficient is required to maintain the straightness of the target during operation. Larger duct gaps will increase pion absorption but make the pumping requirements and target manufacture less demanding.

The design of the downstream end of the target where the cooling water makes a 180° turn should be refined when the final operating parameters have been selected. The aim of this refinement would be to ensure the end of the target is cooled whilst minimising the pressure drop. This requires the optimisation of the gap between the end of the flow guides and the end of the target. Additional optimisation could be achieved by refining the shape of the end of the flow guides and locally reducing the water velocity by increasing the flow cross sectional area.

To check for erosion-corrosion and cavitation damage a flow mock-up of the final design should be tested. This can be run at higher than design flow rates to accelerate any damage which might occur.

4.9 Single pass air cooling

An air cooled target design favours a single pass annular duct where the hot air is exhausted out of the horn at atmospheric pressure into the target station. This has the advantage that the system and compressors will be low cost and not get activated. The heat would then be removed by the target station air circulation system. For the smaller 9mm diameter target this heat load is only 3.2kW for Beryllium. A schematic of a possible air cooled target and horn design is shown in Figure 4.51.
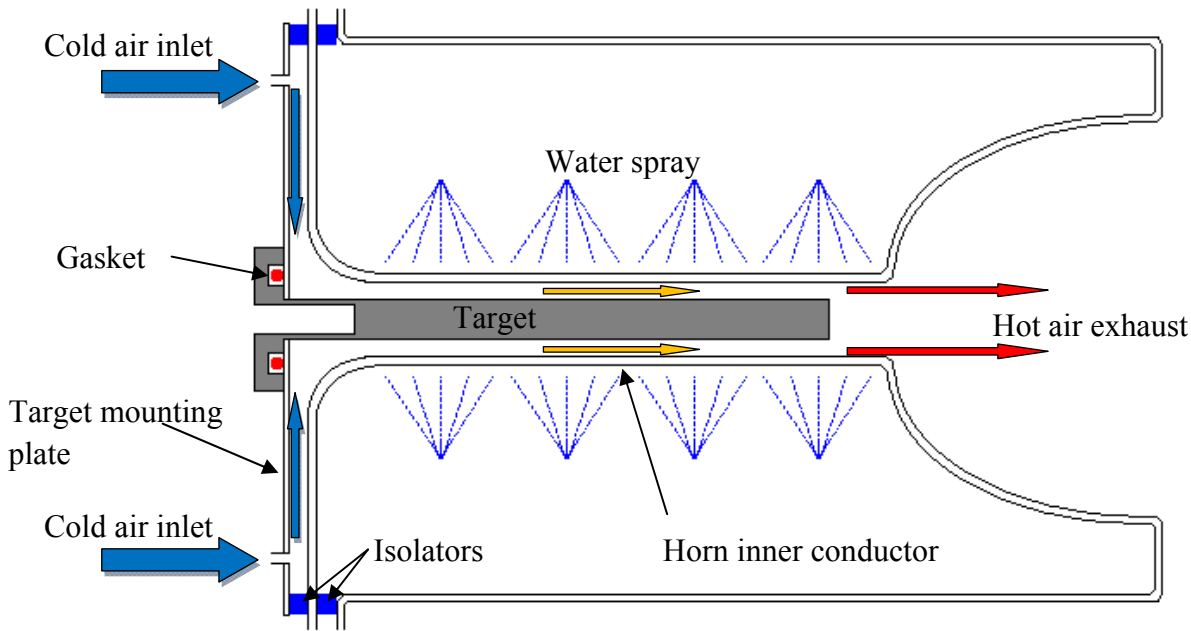
Figure 4.51 Schematic of single pass air cooled target and horn design

Table 4.5 gives details of the required operating parameters for a 120GeV, Beryllium air cooled target with the following constraints:

1. The steady-state temperature should not exceed 500K,
2. The temperature rise of the air should not exceed 80K
3. The air velocity should not exceed Mach 0.8

Using these constraints the mass flow rate, duct gap and target operating pressure have been estimated from empirical calculations.

Table 4.5 Example operating parameters for air cooled target

Target diameter	Duct gap	Power deposition	Mass flow	Vol. flow	Outlet P	Inlet P	Air temp rise	Target core temp	Mach no
mm	mm	kW (beam)	kg/s	Nm3/hr	bar	bar	K	K	
9	3	3.2 (700kW)	0.041	114	1.2	2.6	78.68	498	0.75
9	2.1	10.8 (2.3MW)	0.14	390	6	15.3	76.80	497	0.79
21	2.9	7.1 (700kW)	0.09	237	1.3	3.0	79.15	486	0.79
21	1.8	23.8 (2.3MW)	0.30	835	7.4	19.5	79.15	495	0.72
Example design limits							80	500	0.8

This table shows that a high mass flow rate and target operating pressure are required for a 2.3MW beam. The high mass flow rates required result in the need to run the target at high pressure to keep the air velocity subsonic. Using the equation below the ideal isentropic compression power has been calculated to give an indication of the compressor requirements for each case.

$$W = \dot{m}CpT_1\left(\left(\frac{P_2}{P_1}\right)^{\gamma-1/\gamma} - 1\right)$$

Where

$\dot{m}$ = mass flow rate
Cp = Specific heat at constant pressure
T_1 = Inlet temperature
P_1 = Inlet Pressure
P_2 = Outlet Pressure
g = Ratio of specific heats (1.4 for air)

The results from these calculations are shown in table 4.6. From this table it is clear that the compressor requirements for a 2.3MW air cooled target are demanding. However, air cooling could be an attractive solution for the lower 700kW beam power as suitable compressors are readily available.

Table 4.6 Ideal compressor power for air cooled targets

Diameter & Power	Mass flow [kg/s]	Outlet pressure [bar]	Ideal power [kW]
9mm (700kW)	0.04	2.6	3.6
9mm (2.3MW)	0.14	15.3	47.6
21mm (700kW)	0.09	3	9.6
21mm (2.3MW)	0.3	19.5	115.5

If a closed cooling system is used then it is clear that Helium is the obvious choice over air due to its superior thermal properties. This reduces the mass flow rate requirement which leads to less demanding compressor requirements.

4.10 Study of gas cooled sphere target

As was shown in section 3, segmenting the target can all but eliminate the stresses that result from inertial effects. A potential method of achieving a segmented target is to have a series of spheres inside supporting helical springs as shown in section 3.3.4. The helical spring keeps the spheres located centrally within a tube but provides channels for gas to flow around the outside of the spheres. Here we present a CFX conjugate heat transfer model of the spheres supported by three helical springs contained within a tube. A FLUKA model is used to calculate the energy deposition in the spheres and we consider the most challenging case of the 2.3MW beam. We have modelled 13mm diameter spheres as it was shown in section 3 that the stress levels are comfortably below the design stress with the 2.3MW beam. The model results presented below are for helium with an absolute exhaust pressure of 10bar. The helium circuit would need to be pressurised in order to obtain adequate mass flow without too large a pressure drop as shown earlier in section 4. Figure 4.52 shows streamlines swirling through the geometry. The pressure drop is predicted to be 1.1bar for a helium mass flow of 17grams/s. The inlet velocity is around 40m/s and the maximum velocity reached is 185m/s, the maximum Mach number 0.16. The gas accelerates in the spirals but also as it heats up towards the outlet of the geometry. The power deposited in the spheres and removed in the helium in this steady state simulation is 9.4kW. Figure 4.53 shows temperature on a plane through the middle of the model indicating the maximum sphere temperature as 178°C and the exit gas temperature as 116°C.
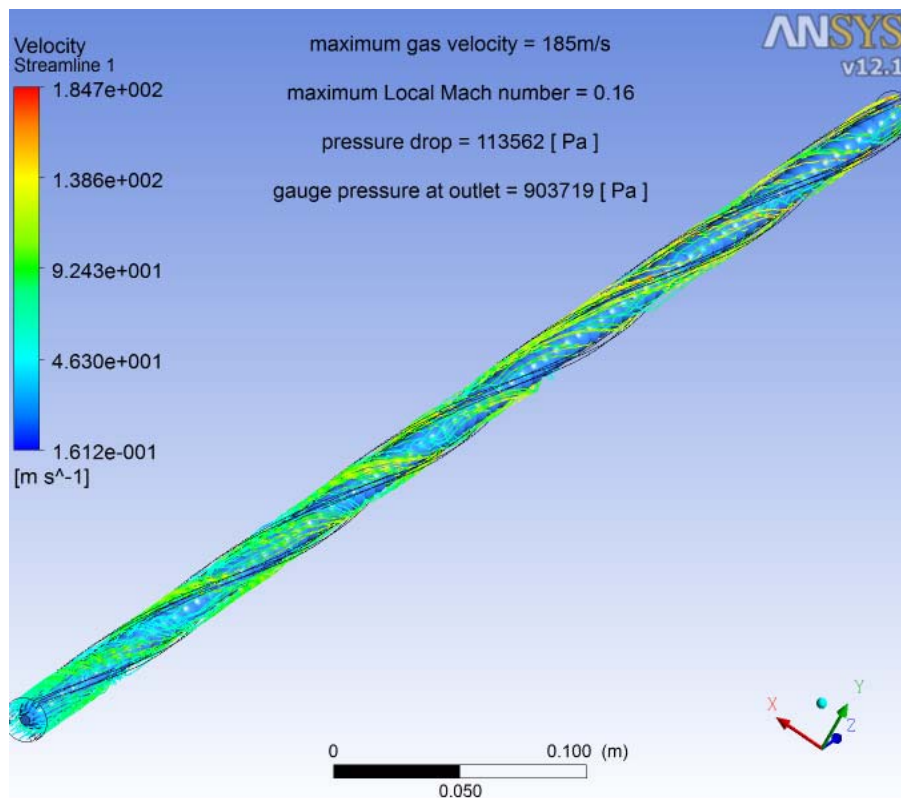
Figure 4.52 Streamlines in the sphere target
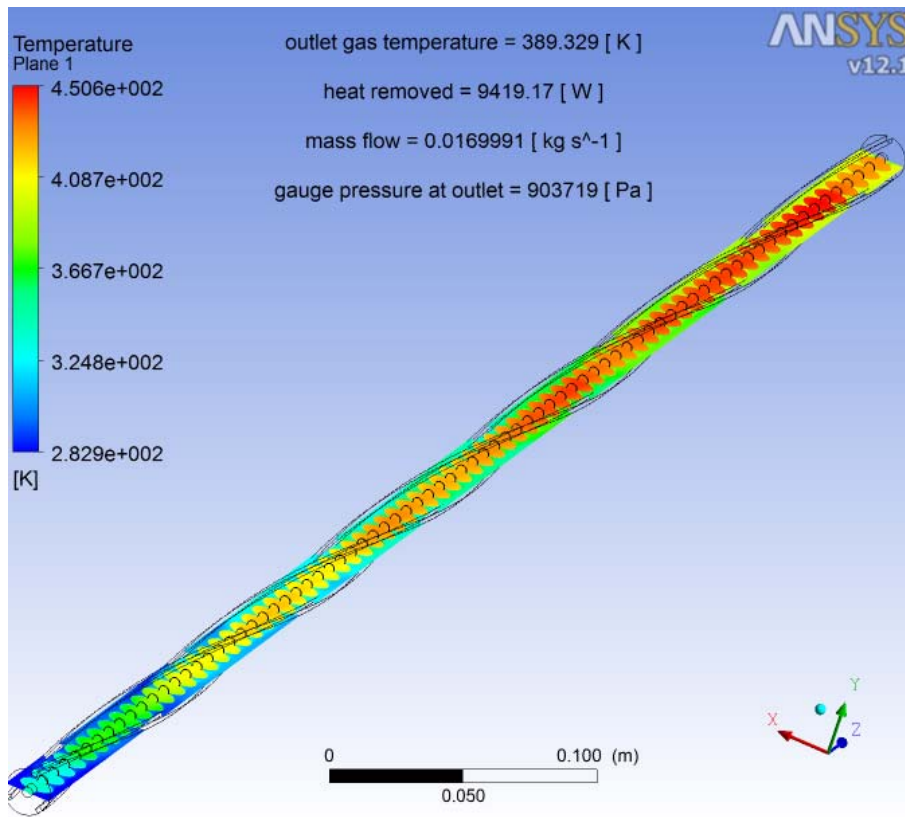
Figure 4.53 Temperature plane through the centre of the sphere target
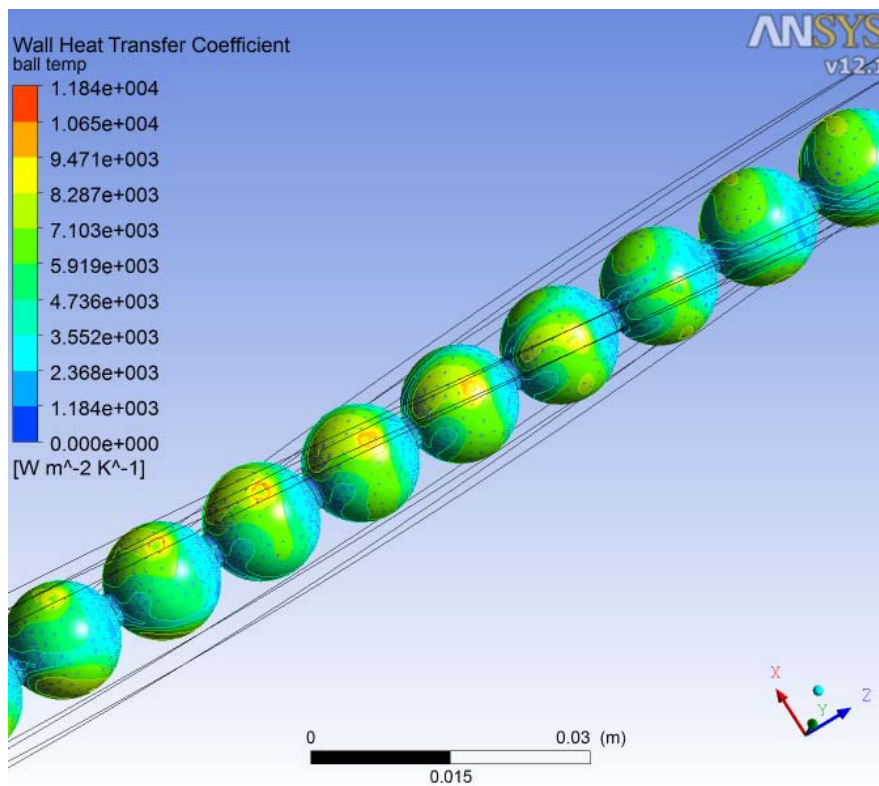
Figure 4.54 Heat Transfer Coefficient on surface of the spheres

At this stage none of the inputs to this model have been optimised, much work could be done to optimise annular gap thickness, helix pitch and even flow path, however the results do indicate that such a scheme is feasible from a heat transfer perspective. If a little more pressure would be acceptable, then pressurised air cooling is also possible although results for this are not presented here. While air has lower thermal conductivity and heat capacity its larger density for a given pressure means that for the same flow velocity the heat transfer is not too far behind helium. The speed of sound being much lower in air limits the flow velocity but the maximum velocity in this helium model is well below the speed of sound of air.

An advantage of the spheres is that you can select fairly small spheres without worrying about stress levels and as such the heat loads are lower than they would be if we were forced to go to a larger diameter target. Also the spheres having less material than a rod have a lower energy deposition for the same diameter too. Additionally the core temperature of the spheres may be kept lower than the core temperature of a rod due to the larger surface area for heat transfer and the fact that gas gets near to the core of the beam. Good heat transfer is achieved over the whole front face of the sphere and not so good on the rear face as shown in Figure 4.54. Note that for the heat transfer plot, the heat transfer coefficient is calculated using the wall adjacent temperature and not a bulk fluid temperature, so these values have to be read with care and not compared to typical values which are usually based on the bulk fluid temperature. The wake region behind the sphere contains some flow instabilities which maybe improved along with the rear face heat transfer coefficient by introducing some alternative flow paths or flow guides to the design.

Potential issues with gas cooled sphere targets

There are a number of issues regarding gas cooled sphere targets which either may be causes for concern or may need further study:

i.   Any direct gas cooled target of the type discussed in this section would require at least one beam window. The pressures such windows would be subjected to are significantly greater than those considered in the vacuum-to-air beam window section, however the stresses resulting from the pressure component are relatively low and so this issue is not expected to offer a significantly greater technical challenge.

ii. Potentially serious failure scenarios resulting in beryllium 'projectiles' being propelled through the horn by the gas pressure.

iii. Configuration not compatible with water cooling since the beam would directly interact with the water – gas cooling only.

4.11 Summary of Task B

Each cooling method is discussed below and then the advantages and disadvantages are summarised in Table 4.7

Forced convection Helium cooling

Cooling a 2MW Beryllium target with helium has been shown to be possible for both cylindrical and contained sphere concepts. However a large mass flow rate is required to achieve a sufficient heat transfer coefficient and to keep the temperature difference of the gas within acceptable limits. A closed loop helium re-circulating system could operate at an elevated pressure to achieve sufficient mass flow rate with a practical flow velocity and pressure drop of the complete circuit. The circuit should be optimised to minimise the operating pressure in order to control the risk and consequences of a target container/window failure.

Forced convection water cooling

Water cooling is by far the most effective cooling method. The target temperature and temperature rise of the cooling water are low. The flow rates required are easily achievable and the pressure drop of the system are generally low. Water cooling does have some significant disadvantages such as energy deposition directly in the water. This causes an additional heat load to the system, pion absorption and pressure transients from the rapid heating. A single layer concept cooling design is described in section 4.8 which minimises the thickness of the cooling water, consequently reducing pion absorption. In any design the pressure waves must be studied to ensure they do not cause premature failure of the cooling system by excessive stress or cavitation damage.

A water cooling system will become highly activated from production of Be^7 and tritium. This will require a primary and secondary cooling circuit, ion exchange units and heat exchangers although much experience exists in this field at Fermilab.

Water spray cooling

Water spray cooling is only an option for a combined target and horn due to the restricted space between the horn inner conductor and a separate target. Considerable experience in this technique exists at Fermilab for horn cooling. Initial studies have shown that patchy or non-uniform heat transfer coefficient will increase the temperature and stresses in the target. If any areas of the target rod are missed by the spray coverage then the increase in stresses is significant.

Forced convection air cooling

An air cooled target design favours a single pass annular duct where the hot air is exhausted out of the horn at atmospheric pressure into the target station. This has the advantage that the system and compressors will be low cost and not get activated. The heat would then be removed by the target station air circulation system. For the smaller 9mm diameter target this heat load is only 3.2kW for Beryllium.

The practical power limit for a single pass air cooled target has not been fully explored. It is simpler to implement than a contained helium circuit, but as the heat load is increased the pressure required to drive a sufficient mass flow rate while discharging at atmospheric pressure is also increased.

Table 4.7 Advantages & disadvantages of different cooling methods

	Advantages	Disadvantages
Water spray cooling	• High heat transfer • No shock issues • Experience for horn cooling	• Patchy/non uniform cooling • Reliability of nozzles • Tritium production • Dissociation of water
Water forced convection cooling	• Uniform cooling • High heat transfer • Simple hardware requirements • Low temperature rise of water	• Shock/water hammer issues • Heat deposition in water • Tritium production • Dissociation of water
Helium forced convection cooling	• Uniform cooling • No shock issues • Low radiation	• Lower heat transfer • High pressures require to reduce pressure drop and obtain sufficient mass flow • Leaks
Forced convection air cooling	• Simple hardware requirements • Uniform cooling • Low cost • Can exhaust cooling air into target station • Non re-circulating system, no activation of compressor	• Low specific heat requires high flow rates • Lower heat transfer • Most attractive for low beam powers • Consequences of NO_x production and other radiochemistry effects

700kW cooling preference

At 700kW beam power we can see that air cooling is an attractive option for a separate target and horn system. Helium or water are also options and both have superior cooling performance but will add significant cost and complexity to the system. Either may become more desirable for an increase in beam power beyond 700 kW.

For a combined target and horn, water spray cooling should pose no significant problem at this power. The heat load on beryllium from a 700kW beam is lower than the joule heating from the horn current.

2MW cooling preference

From this study it is shown that helium or water cooling are viable options for cooling a 2MW separate beryllium target. If we assume a maximum desirable steady-state operating temperature of 500K then this is easily achievable with water. This is also achievable with helium although it is slightly more challenging due to the pressure drops and demanding compressor requirements. In terms of target reliability, pion production and energy deposition in the coolant then helium cooling would seem to have a slight advantage over water. However for lower target temperatures a water cooled system would have an advantage. A concept design has been demonstrated which minimises the thickness of the water surrounding the target. An alternative concept of gas cooled spheres contained in a tube also appears to have significant potential.

For a combined target and horn, water spray cooling would seem to be an attractive option. However the uniformity and coverage of the spray nozzles must be studied and optimised to avoid high stresses and temperature.

4.12 References

[1] Rohsenow, Hartnett & Cho (1998), Handbook of Heat Transfer, 3rd edition. McGraw-Hill, Page 5.26

[2] Rohsenow, Hartnett & Cho (1998), Handbook of Heat Transfer, 3rd edition. McGraw-Hill, Page 5.55

[3] Blevins, R.D. (1984), Applied Fluid Dynamics Handbook, Van Nostrand Reinhold Company Inc, Page 49

[4] Haaland, SE (1983). "Simple and Explicit Formulas for the Friction Factor in Turbulent Flow". Journal of Fluids Engineering (ASME) 103 (5): 89–90

[5] Olson, A.T and Shelstad, K. A. (1987), Introduction to Fluid Flow and the Transfer of Heat and Mass, Prentice-Hall Inc, Page 118-119

[6] Innovative Turbulence Modelling: SST Model in ANSYS® CFX (Dec 2006), http://www.ansys.com/assets/tech-briefs/cfx-sst.pdf

[7] Iter Material Properties Handbook, (1997), http://fusionnet.seas.ucla.edu/fusionnetwork/iter_properties.php?mid=MU-%23101&tid=0104P-0700

[8] Design Study of the NuMI Target for 2 MW Upgrades, V.Garkusha, A.Mikheyev, I.Ponimash, A.Ryabov,T.Ryabova, F.Novoskoltsev and V.Zarucheisky, INSTITUTE FOR HIGH ENERGY PHYSICS, STATE RESEARCH CENTER OF RUSSIA Protvino, Moscow region_ Russia

[9] Knud Thomsen, "Mitigation of cavitation effects by means of gas bubbles on a surface", Journal of Nuclear Materials, Volume 356, Issues 1-3, 15 September 2006, Pages 321-324, Proceedings of the Seventh International Workshop on Spallation Materials Technology, Proceedings of the Seventh International Workshop on Spallation Materials Technology

[10] T. G. Leighton, P. R. White, C. L. Morfey, J. W. L. Clarke, G. J. Heald, H.A. Dumbrell, and K. R. Holland, "The effect of reverberation on the damping of bubbles," J. Acoust. Soc. Am. **112**, 1366–1376 _2002

[11] Erosion-Corrosion in Cooling Systems (accessed September 2010) http://www.lytron.com/tools-technical/notes/cooling-systems-erosion-corrosion.aspx

[12] Tip 4 - Forms of Corrosion (accessed September 2010) http://midlandcorrosion.co.uk/corrosion-tips/page/2/

5. Report on Task C: Combined Target and Horn IC Study

5.1 Introduction

In this section we consider the concept of a combined target and horn inner-conductor, illustrated schematically in Figure 5.1. In this scenario a portion of the horn inner-conductor takes the form of a solid cylindrical rod which is cooled by a peripheral water spray. The solid portion of the inner-conductor doubles as the primary proton beam target, and must withstand both the horn current pulses and the particle beam interactions. The water-spray cooling must be sufficient to remove the heat generated by both resistive heating and by particle interactions in the combined target / conductor.
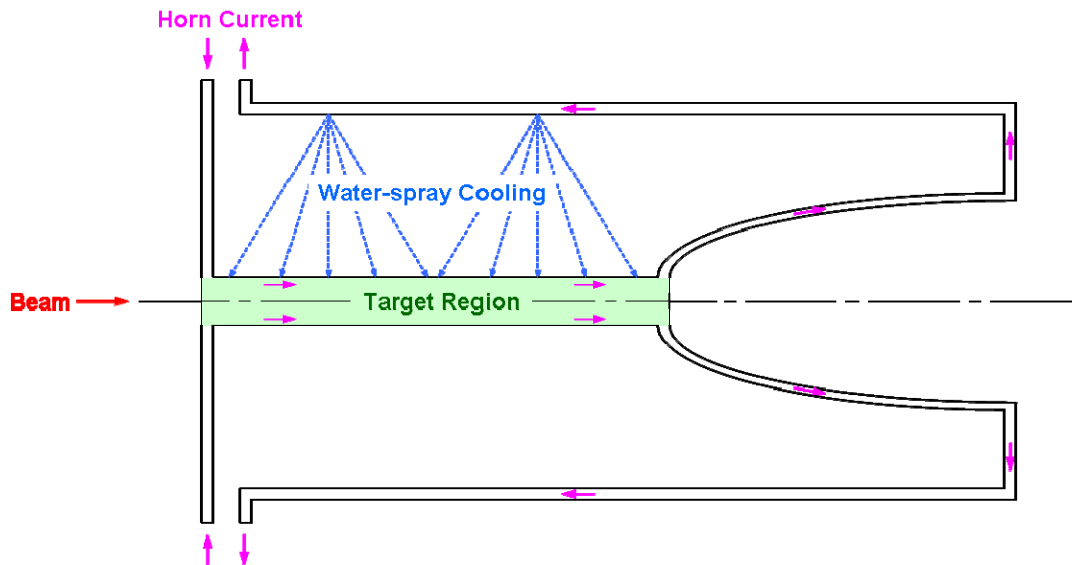
Figure 5.1 Schematic of a magnetic horn with a combined target and inner-conductor

The following physical effects acting on the combined target / conductor region were investigated using the finite element code ANSYS:

1. *Beam Heating* (see section 3). When the primary proton beam interacts with the target material, energy is deposited in the form of heat. Temperature gradients in the target give rise to transient thermal stresses.

2. *Resistive Heating*. When a horn current pulse passes through the combined target / inner conductor, energy is deposited by resistive heating in the conductor material. Skin effects arising from the short duration of the current pulse lead to non-uniform heating of the conductor. The resulting temperature gradients generate transient thermal stresses.

3. *Magnetic Force*. In the magnetic horn, electromagnetic forces are generated by the action of the pulsed current passing through its own magnetic field. These magnetic forces will be referred to as "Lorentz" forces. The resulting effect on the horn inner conductor is a radial "pinch", while the upstream and downstream horn end plates tend to repel one-another.

The analysis was tackled in a number of stages. First-of-all the resistive heating and Lorentz force effects in a long cylindrical conductor were investigated (section 5.2). The simulation was then extended to include the magnetic horn end effects (section 5.3). Finally, the beam heat loads were added to the simulation to allow the combination of beam and current effects to be studied (section 5.4).

5.2 ANSYS Models: Pulsed Current in a Long Cylindrical Conductor

Outline

We consider the case of a 1 milli-second duration, half sine-wave current pulse flowing in a long cylindrical conductor. The objective is to calculate the following for a range of conductor materials and diameters:

- The temperature rise from resistive heating of the conductor material, and the associated transient thermal stress both during and after the current pulse.
- The radial Lorentz force distribution and the corresponding Lorentz stress during the current pulse.

As for the separate beam heating case considered in section 3, in order to explore the entire parameter-space in a quick and efficient way while keeping the results as generic as possible, a number of simplifications were made. These included limiting the simulation to a single current pulse, applying linear rather than temperature dependent material properties, and ignoring the method of cooling by specifying an adiabatic surface boundary condition. Magnetic horn end effects which introduce additional longitudinal Lorentz forces are not captured because the conductor is assumed to be infinitely long. Magnetic horn end effects are discussed in section 5.3.

By way of illustration, contour plots and other specific results are shown for the particular case of a 21 mm diameter beryllium conductor. Results for other material and diameter combinations are summarised in table 5.2 at the end of this section.

Analysis Procedure

An ANSYS simulation was performed following the multi-stage process illustrated in Figure 5.2. Three consecutively solved stand-alone physics environments were solved in order to describe each of the necessary phenomena. This multi-stage approach is computationally less expensive than a fully coupled "multiphysics" methodology, while at the same time it is still able to capture all of the relevant effects.
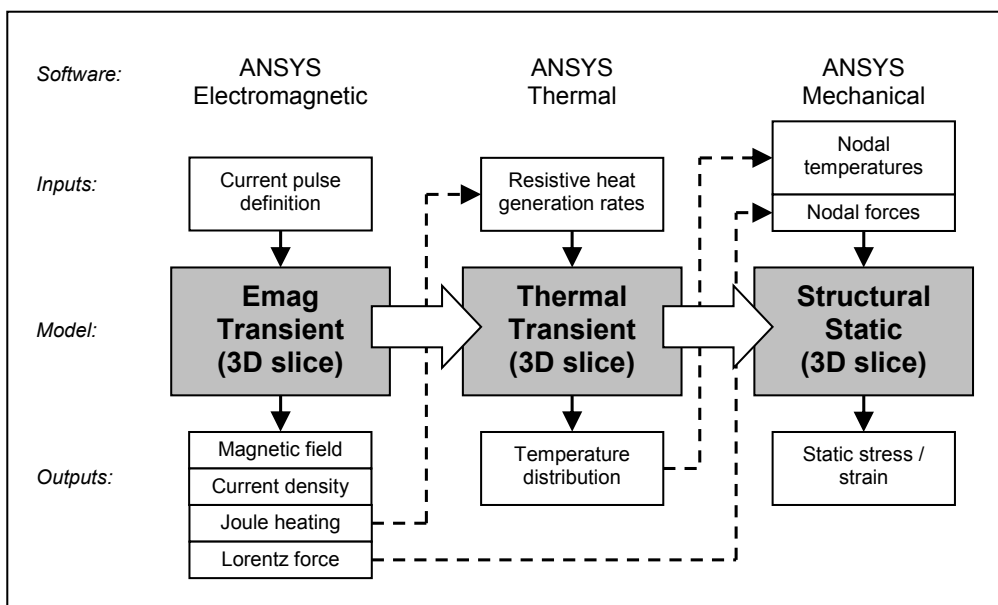
Figure 5.2 Analysis procedure, pulsed current effects

Firstly, the horn current pulse was modelled in the ANSYS electromagnetics environment, where the transient evolution of current density and magnetic field in the conductor was simulated. A "Bulk conductor" element formulation was used so that skin effects would be fully described. The Lorentz force distribution, calculated from the vector cross product of the current density and magnetic field was recorded, and the resistive (Joule) heat generation rates were stored for each element.

Secondly, the resistive (Joule) heat generation rates were used in a transient thermal simulation. The temperature distribution was calculated both during and between current pulses, taking account of thermal conduction within the solid conductor material.

Finally, a series of structural static runs were performed, using the temperature profiles at each time step of the transient thermal analysis, and the Lorentz force distribution from the transient electromagnetics analysis as inputs. The transient stresses generated by the combined action of the temperature gradients and radial magnetic forces were calculated

Model Description

Although the problem is essentially axisymmetric in nature, a 3D model was needed to allow current to flow in the plane of the model, rather than normal to it as is required in all of the ANSYS 2D electromagnetics formulations. A suitable "quasi-axisymmetric" mesh, representing a 1 meter long cylinder, was created using 3D elements rotated through a small angle about the conductor axis to form a wedge shaped model space (Figure 5.3). Both the solid conductor region (green) and the surrounding air volume (purple) were included in the model. The purpose of including the air region was to capture the surrounding magnetic field generated by the pulsed horn current.

A regular mapped mesh consisting of 100 axial divisions, 50 radial divisions, and a single azimuthal division was generated in the solid region. The choice of mesh density was informed through a mesh refinement study. In the air region the radial element size was increased with distance from the solid / air boundary, leaving a fine mesh near the conductor surface where the rate of change of field with radial position is highest. 8-node brick elements of type SOLID97 for the electromagnetic, SOLID70 for the thermal, and SOLID45 for the structural environments were used. In each case an identical mesh was used in order to facilitate the smooth transfer of nodal and element results between physics environments. The air region was solved only in the electromagnetics environment and then ignored in the subsequent thermal and structural models.
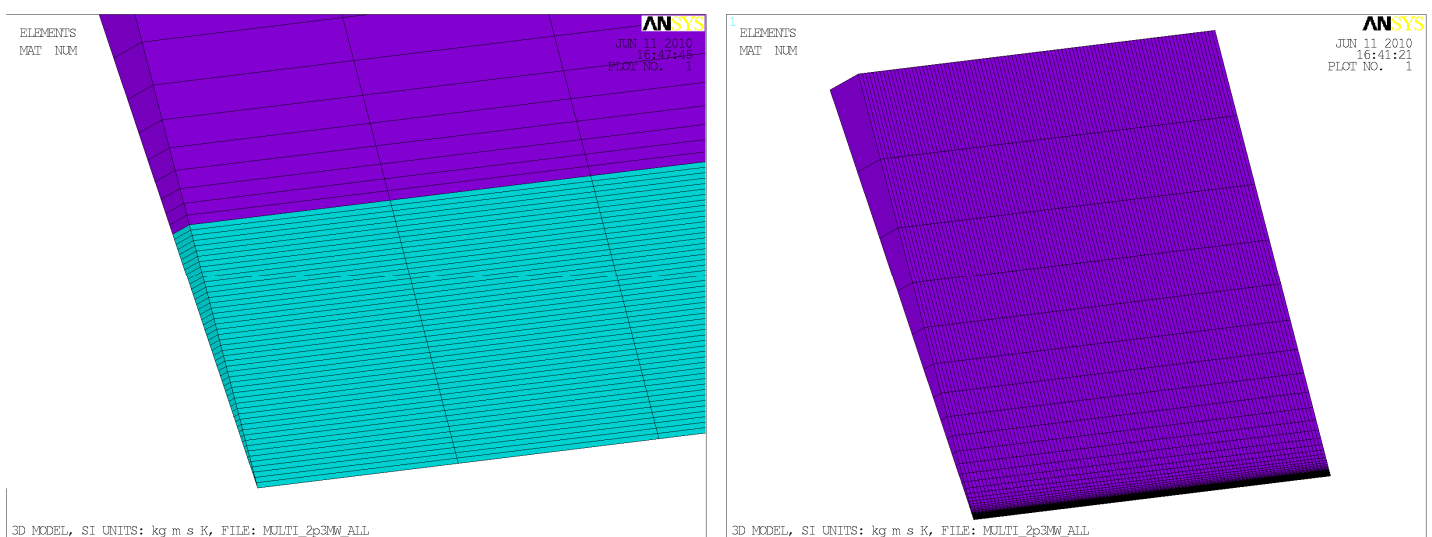
Figure 5.3 ANSYS finite element mesh

In the transient electromagnetic simulation electrical excitation boundary conditions were applied to the conductor end faces. The voltage degree of freedom of all the upstream end nodes was coupled,

and at the downstream end the voltage was set to zero (ground). The net current, which varied according to a 300 kA peak, half-sine function, was applied to a single node in the coupled set at the upstream end. The distribution of current with time was calculated by ANSYS during the solution. To take advantage of assumed symmetry in the magnetic field, flux-normal and flux-parallel conditions were applied to the conductor and air regions. Flux-parallel at the end faces and at the outer boundary of the air volume, and flux-normal at the symmetry cut-planes.

In the transient thermal simulation an initial uniform temperature of 300K was applied throughout the model. The resistive heat generation rates were then read-in from the previous electromagnetic results and applied as a load history.

In the static structural simulation the conductor was fixed at the upstream end and allowed to expand axially at the downstream end. Structural symmetry boundary conditions were applied to the cut planes. The effect of gravity was not included. Static (rather than transient) structural analyses were performed in order to simplify the solution by deliberately ignoring inertia effects. This means that the code will not try to resolve stress-wave propagation or bulk "violin-mode" oscillations of the conductor, allowing the solution to converge more quickly and using fewer time-steps.

The model time structure included both the 1 msec current pulse during which the resistive heating and magnetic loads are applied, and the interval between pulses in which thermal conduction took place. The half sine-wave current pulse shape was simulated by dividing the pulse time into 24 linear ramps as illustrated in Figure 5.4. No damping was included in the sine-wave pulse shape.
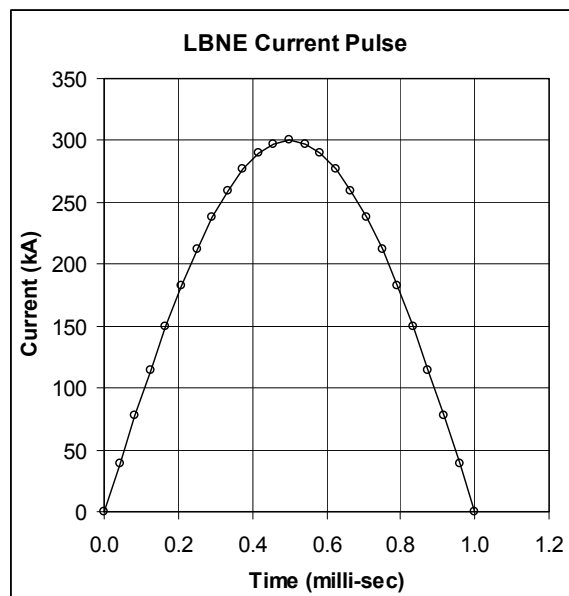
Figure 5.4 The LBNE pulse shape: an undamped 300 kA peak, half sine-wave current pulse

Skin Effect

Both the resistive heating and Lorentz force effects depend strongly on the distribution of current within the conductor cross-section. If the current was continuous (d.c.) then the current density would be uniform throughout the conductor cross-section. With an a.c. or pulsed current, however, the current density will tend to concentrate on the conductor surface. With an a.c. current, as the frequency increases the effect becomes more pronounced until the current flow is confined to a very thin surface layer. This phenomena, known as the skin effect, is important in defining the apparent resistance of the conductor.

For an a.c. current in a cylindrical conductor the current density can be assumed to decrease exponentially from the surface. The skin depth δ is then defined as the depth below the conductor surface at which the current density has reduced to $1/e$ of its maximum intensity at the surface. Assuming the absence of any ferromagnetic materials we have

$$\delta = \sqrt{\frac{2\rho}{\omega\mu_0}} \qquad [m]$$

Where: ω is the angular frequency *[rad/s]*
              μ_0 is the permeability of free space *[H/m]*
              ρ is the electrical resistivity of the conducting material *[Ω.m]*

Substituting in the time for a half sine-wave period

$$\tau = \omega/\pi \qquad [sec]$$

leads to an equation we can use to estimate the skin depth δ associated with the half sine-wave current pulse of the LBNE horn:

$$\delta = \sqrt{\frac{2\tau\rho}{\pi\mu_0}} \qquad [m]$$

Table 5.1 lists the skin depth calculated in this way for each of the conductor materials of interest. In all cases the skin depth is found to be similar in magnitude to the dimension of the conductor radii in this study. This means that we cannot assume that the current will be either uniformly distributed (large skin depth compared to conductor size), or confined to a small region near the conductor surface (small skin depth compared to conductor size). That is, we should expect the current distribution to be somewhere in between those two extreme cases. For this reason it was decided to use the ANSYS simulation to calculate the particular current distribution relating to each conductor material and diameter combination of interest.

Table 5.1 Estimated skin depth for a 1 msec duration, half sine-wave current pulse in various materials

Material	Skin Depth (mm)
Pure Aluminium	3.7
Beryllium	4.8
AlBeMET	4.2
Aluminium alloy 6082	4.4

The ANSYS simulation was designed to capture the transient evolution of current density and magnetic field in the model space. Figure 5.5 shows how the current density varied as a function of radial position in the conductor, at four points in time during the pulse. By way of example the case of a 21 mm diameter beryllium conductor is illustrated, but results from other combinations of material and diameter follow a similar trend. In the first part of the pulse (t=0.25 msec) the bulk of the current is flowing near the conductor surface. At the peak (t=0.5 msec) a significant portion of the current has penetrated to the conductor centre, and at t=0.75 msec the current is quite uniformly distributed. At t=1.0 msec there is zero net current flowing, but a remnant eddy current remains, with some reverse flow at the outer radius that is counter-balanced by a forward flow near to the conductor centre.
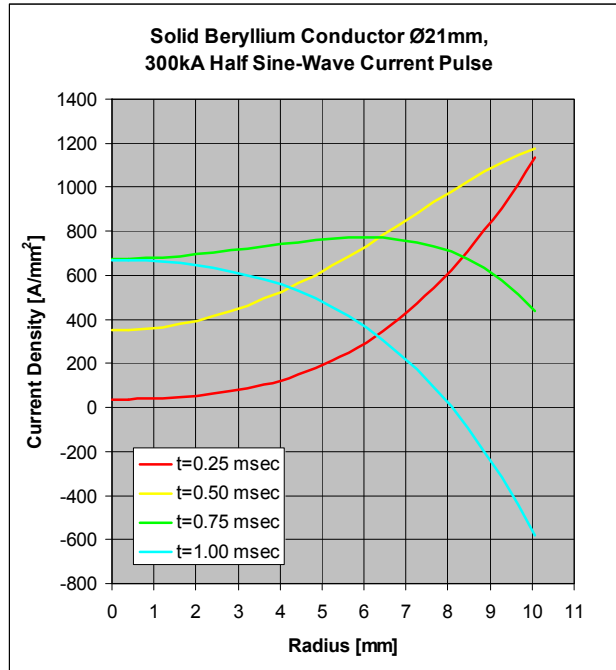
Figure 5.5 Current density evolution in a long cylindrical conductor
Example case: 21 mm diameter, beryllium conductor

Magnetic Field

Figure 5.6 shows the magnetic field both inside and outside of the conductor at the peak of the current pulse according to the ANSYS simulation. The dotted vertical line indicates the outer radius of the conductor. The magnetic field outside of the conductor (but inside the coaxial return in a magnetic horn) reduces with the inverse of its radial position according to

$$B = \frac{\mu_0 I}{2\pi R} \qquad [T]$$

while the field inside the solid cylindrical conductor varies according to whatever distribution of current density is present. For example, a uniformly distributed (d.c.) current would yield a magnetic field inside the conductor that rises linearly, i.e. is proportional to radius. In the other extreme, if the current was confined to a thin surface layer then the field deep inside the conductor would be zero, rising quickly to a maximum at the surface.
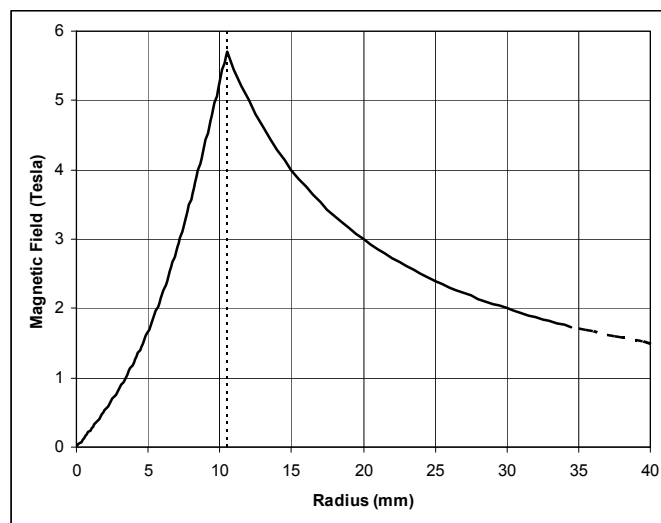
Figure 5.6 Radial Distribution of magnetic field at the peak of the 300 kA, 1 msec, current pulse
Example case: 21 mm diameter, beryllium conductor

Radial Lorentz Stress

In a long cylindrical conductor a magnetic "pinch effect" arises from the self attraction of parallel lines of electric current flowing in the same direction. In essence, as the current flows through its own magnetic field, an inward radial force is generated, where the force density comes from the vector cross product of the current density and the magnetic field, J×B (Figure 5.7). This effect leads to a radial compressive "Lorentz stress" in the horn inner conductor.
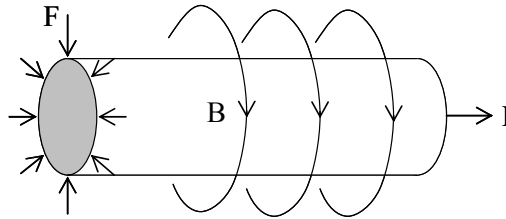
Figure 5.7 Magnetic pinch effect

Figure 5.8 shows the evolution of Lorentz stress in the conductor during the 1 msec current pulse as calculated in the ANSYS model. The magnetic force distribution that generates this stress depends on the evolution of current density and magnetic field inside the conductor (see skin-effect above). The maximum Von-Mises Stress occurs at the conductor centre, soon after the pulse peak (t=0.5 msec). Remnant eddy currents that live on after the net current has reduced to zero (t=1.0 msec) mean that the Lorentz stress does not fully decay until a short time after the end of the pulse.

Note that only radial (and not longitudinal) Lorentz forces are captured in this "long cylinder" simulation. Axial Lorentz stresses that arise due to the horn end effects are discussed in section 5.3..
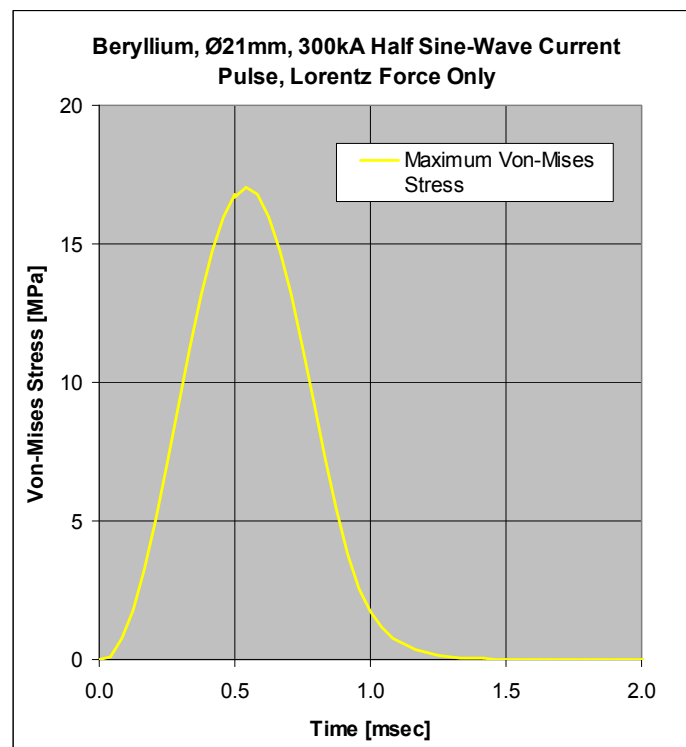
Figure 5.8 Stress due to radial Lorentz forces on a long cylindrical conductor
Example case: 21 mm diameter, beryllium conductor

The Von-Mises stress distribution, due to radial Lorentz forces at the peak of the current pulse, is illustrated in Figure 5.9, for the example case of a long, diameter 21mm beryllium conductor.
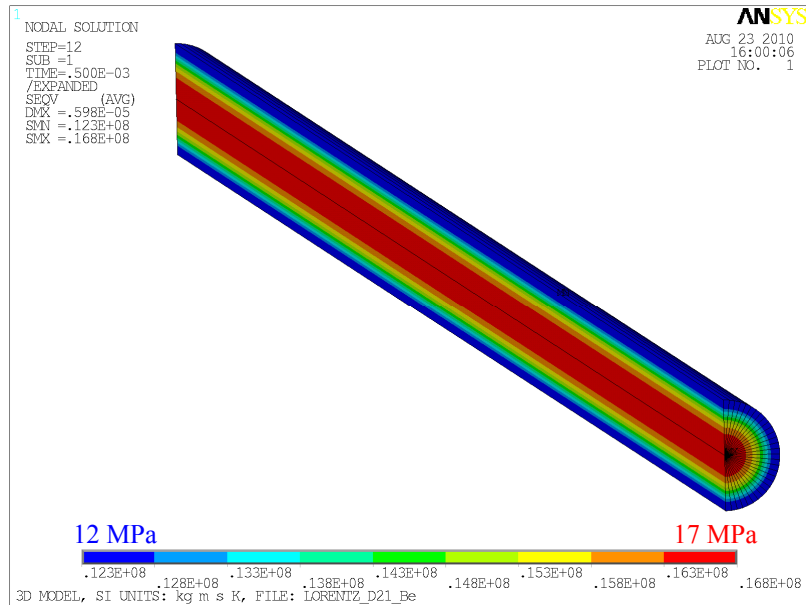
*Figure 5.9 Stress due to radial Lorentz forces on a long cylindrical conductor at the peak of the current pulse
Example case: 21 mm diameter, beryllium conductor*

Resistive Heating

Resistive heating, also known as Joule heating, is the process by which the passage of an electric current through a conducting material generates heat. Joule's first law states that the heat Q generated by a uniform current flowing through a conductor is given by

$$Q = I^2 R \qquad [W]$$

Where: I is the current flowing through the conductor *[A]*
          R is the electrical resistance of the conductor *[Ω]*

The electrical resistance R of a conductor of uniform cross-section may be computed from

$$R = \frac{\rho l}{A} \qquad [Ω]$$

Where: ρ is the electrical resistivity of the conducting material *[Ω.m]*
          l is the conductor length *[m]*
          A is the cross-section area of the conductor *[m²]*

The resistive power density, Q' deposited in the conducting material is then

$$Q' = J^2 \rho \qquad [W/m^3]$$

Where: J is the current density *[A/m²]*

In a long cylindrical conductor a d.c. current would uniformly distribute the current density throughout the cross-section, leading to uniform resistive heating and zero thermal stress. A pulsed current, however, can generate non-uniform heating of the conductor, the amount of heat deposited in a particular region being proportional to the local current density squared. Radial temperature gradients set up by the non uniform heating then generate a transient thermal stress in the conductor (see skin effect above).

Figure 5.10 shows how the maximum and minimum temperature due to resistive heating in the model, and the maximum Von-Mises thermal stress vary with time. The two plots show the same data-set displayed over different timescales, milliseconds on the left, and seconds on the right. The maximum temperature in the model rises during the current pulse (first 1 msec) as the resistive

137

heating takes place. Note that the 1 milli-second LBNE pulse length is short enough that little thermal conduction takes place during the pulse itself. The model then runs on in time for a further ~1 second during which thermal conduction takes effect, tending to equalise the temperature throughout the conductor. As a result we see the maximum and minimum temperatures converge, and the thermal stress, which is driven by the temperature gradient in the conductor, drops to zero.
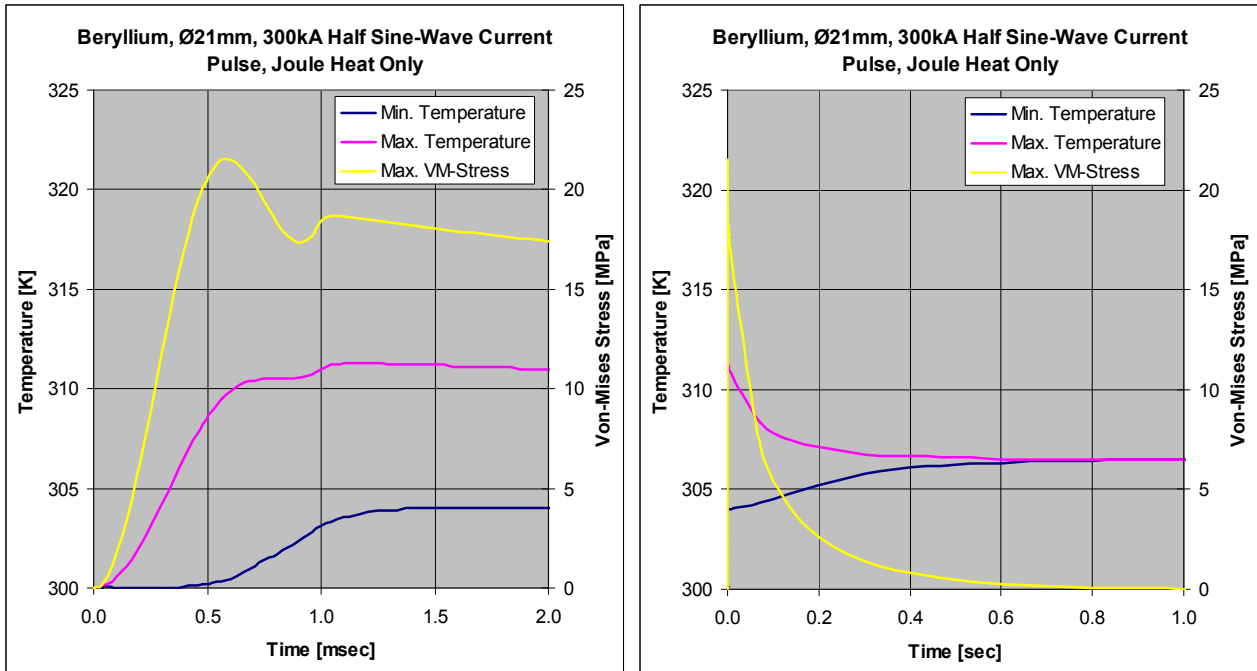
Figure 5.10 Thermal stress results summary
Example case: 21 mm diameter, beryllium conductor

Figure 5.11 shows the temperature distribution at the end of a single 1 msec, 300 kA peak, half sine-wave current pulse. We see that the conductor centre has increased in temperature by 3 degrees, and the conductor outer surface by 11 degrees, compared to the uniform initial temperature of 300 K.
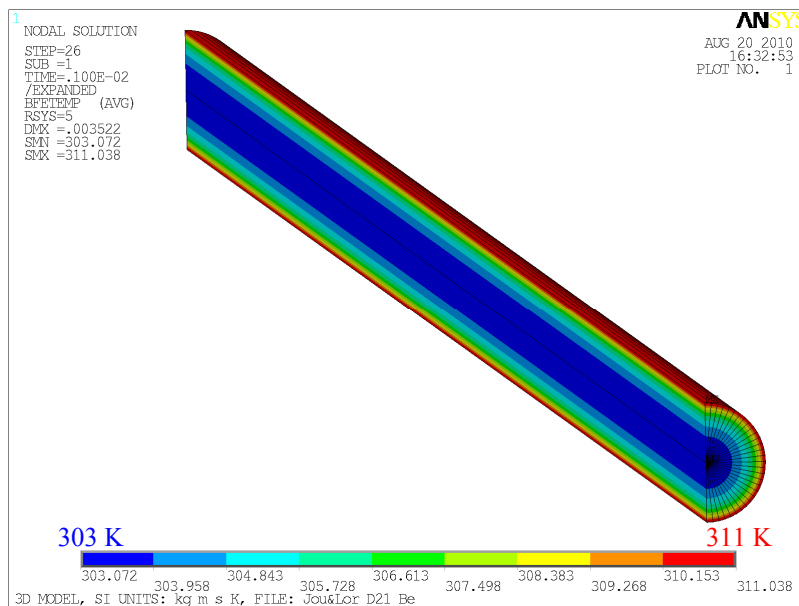
Figure 5.11 Temperature distribution at the end of the current pulse in a long cylinder
Example case: 21 mm diameter, beryllium conductor

Parameter Study Results

The model was run several times with varying input parameters to sweep the required design parameter space. Four separate materials were investigated, aluminium, beryllium, AlBeMET (an alloy of aluminium and beryllium), and a common structural aluminium alloy (6082). The material properties used are listed in section 1. The aluminium alloy properties used were identical to pure aluminium, with the exception of thermal conductivity which was reduced by 15% in the case of the alloy. A range of conductor diameters between 21mm and 9 mm were considered.

Initially the individual effects of the thermal and magnetic loads were isolated and analysed separately in order to understand their importance within the design parameter space. A summary of these individual results is given in table 5.2. Included in the table are the resistive heat energy deposited by a single pulse in a 1m long conductor, the maximum temperature increase due to resistive heating at any point in the conductor, the maximum thermal stress due to temperature gradients generated in the conductor, and the maximum Lorentz stress due to the radial Lorentz forces. We see that in all cases, the level of stress generated by these two mechanisms is of similar magnitude. Both the thermal and Lorentz stresses can be significantly reduced by increasing the conductor diameter.

Table 5.2 Current pulse parameter study results, individual effects of thermal and magnetic loads

Conductor Material	Conductor Diameter (mm)	Deposited Resistive Heat (kJ/pulse)	Max. ΔT per pulse (K)	Max. Thermal Stress (MPa)	Max. Lorentz Stress (MPa)
Beryllium	9	33.0	161	85.7	103
	21	7.5	11.3	21.5	17.0
Aluminium	9	19.6	139	75.8	87.6
	21	5.1	13.5	18.4	14.6
AlBeMET	9	25.3	129	75.6	97.8
	21	6.1	10.7	18.7	16.0
Al-Alloy	9	27.4	186	73.1	88.1
	21	6.5	14.6	18.3	15.0

The thermal and magnetic loads were then combined (applied simultaneously in the model). The conductor diameter was varied and the results obtained are summarised in Figure 5.12. The deposited resistive heat energy, the maximum temperature rise, and the maximum combined thermal and radial Lorentz stress were all seen to reduce as the conductor diameter was increased. The horizontal dashed line in the stress plot indicates a nominal design stress limit of 2/3 yield stress in beryllium. All of the cases considered fall below this nominal material limit. However, given the pulsed nature of the loading, a lower practical limit would be sensible to account for other effects, for example: lateral oscillations (violin-modes) which are not included in this analysis, and issues of fatigue.

The current pulse is not expected to generate significant acoustic stress waves because its duration is long when compared to the characteristic dimensions and speed-of-sound in the conductor. This is in contrast to the case of beam induced heating which is effectively instantaneous due to the short duration of the beam spill (see section 3). Note that the 1 milli-second duration of the current pulse is much longer than the 10 micro-second duration of the beam spill.
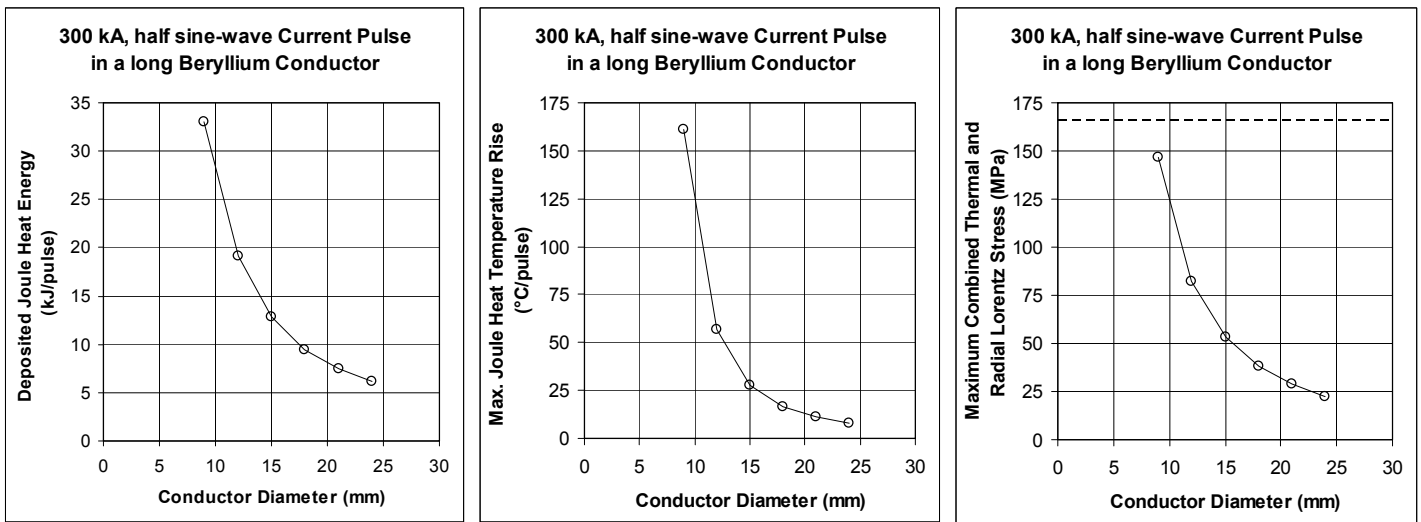
Figure 5.12 Results for combined radial Lorentz force and resistive heat load in a long beryllium conductor subjected to a 1 msec duration half sine-wave current pulse

Summary, Pulsed Current in a Long Cylindrical Conductor

The thermal and mechanical effects of a 300 kA peak, 1 milli-second duration, half sine-wave current pulse in a long cylindrical conductor were simulated using ANSYS. Skin effects arising from the short duration of the current pulse were included. For the range of design parameters considered the thermal stress (driven by non-uniform heating of the conductor) and radial Lorentz stress (generated by the electromagnetic pinch effect) were of similar magnitude. The results showed that increasing the conductor diameter was an effective way of reducing each of the following results:

- The maximum thermal stress
- The maximum Lorentz stress
- The total resistive heat energy deposited by each pulse
- The maximum temperature rise in the conductor

For any conductor diameter greater than 9 mm the maximum combined thermal and radial Lorentz stress from a single current pulse was within the nominal design stress limit of 2/3 yield in beryllium.

In order to apply these results to the case of a horn inner conductor one must also include longitudinal Lorentz forces that arise due to end effects in the magnetic horn. This is the subject of the following section.

5.3 ANSYS Models: Magnetic Horn End Effects

Axial Lorentz Force

In general terms the Lorentz body force F comes from the cross product of the current density J and magnetic field B

$$F = J \times B$$

The direction of the magnetic forces acting on various parts of the horn structure can be determined using Fleming's left-hand rule, where the vectors *F*, *J*, and *B* are perpendicular to one another. We saw previously that this leads to a radial compressive "pinch" force in a long cylindrical conductor. This type of radial pinch effect is experienced by the horn inner conductor.

At both ends of a magnetic horn the electric current flows in a radial direction to traverse the space between the inner and outer conductors (Figure 5.13). This radial flow of current "I" interacts with the azimuthally oriented magnetic field "B" to yield a force "F" in the axial direction. The end plates repel one another with an equal but opposite force, and the resulting longitudinal tensile load is shared by the inner and outer conductors. Since the outer conductor thickness can be made as large as is needed, the problem becomes one of ensuring that the inner conductor cross-section is sufficient to carry it's share of the total tensile load.

The axial magnetic body force acting on the horn end connections is not uniformly distributed. Rather, it is at a maximum at the inner radius of the end plate, reducing quickly with increased radial position. This has the unfortunate consequence that the inner conductor tends to bear a larger portion of the total axial force than the outer conductor.
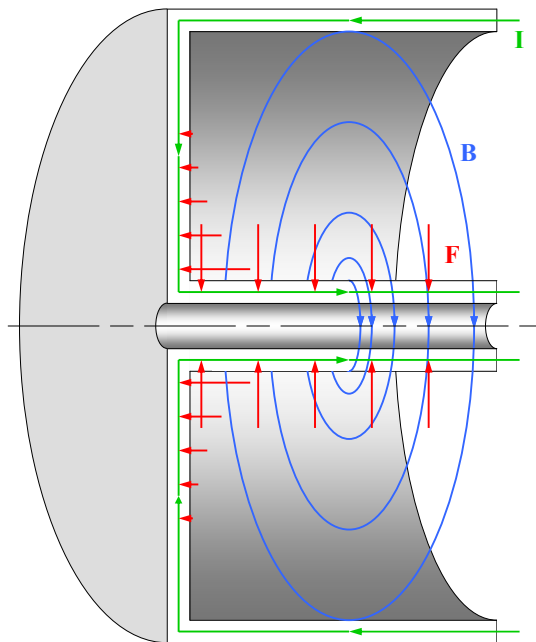
Figure 5.13 Horn end loads

From simple geometry we can infer that the radial current density J_r in one of these end connections varies according to the inverse of the radial position according to

$$J_r = \frac{I}{2\pi R t} \qquad [A/m^2]$$

Where: *R* is radial position
               t is the current depth (in the axial direction) in the end plate

And the magnetic field inside the magnetic volume also reduces according to the inverse of the radial position according to

$$B = \frac{\mu_0 I}{2\pi R} \qquad [T]$$

It's mean value in t is half that amount. From which the force density is

$$F' = \frac{\mu_0 I^2}{8\pi^2 R^2 t} \qquad [N/m^3]$$

That is, the force density acting on the horn end plate reduces according to $1/R^2$. The total force acting on the end plate between the inner radius R_1 and outer Radius R_2 is found from

$$F_{long} = \int_{R=R_1}^{R=R_2} \frac{\mu_0 I^2}{8\pi^2 R^2 t} 2\pi R t dR \qquad [N]$$

And solution of the integral gives

$$F_{long} = \frac{\mu_0 I^2}{4\pi} \ln\left(\frac{R_2}{R_1}\right) \qquad [N]$$

From this we see that the total axial force is proportional to the current squared, and that it is much more sensitive to small changes in the inner radius (where the current density and field are high), than it is to small changes in the outer radius (where the current density and field are low). We note that the longitudinal force is independent of the horn length.

Horn with a Hollow Inner Conductor

The ANSYS finite element model outlined in section 5.2 above was extended to include the horn outer conductor and connecting end plate in order to capture the horn end forces. The same multi-stage process, comprising linked electromagnetic, thermal, and mechanical simulations was used.
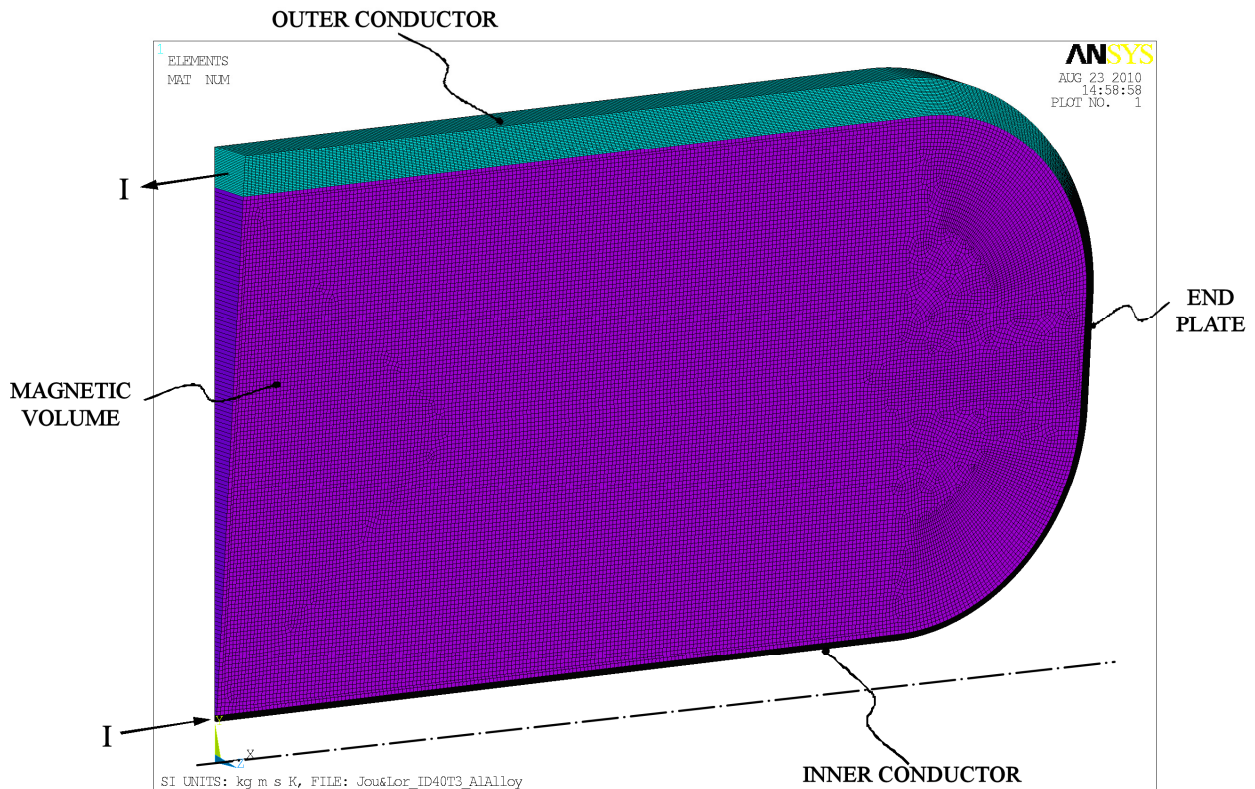
Figure 5.14 Finite element mesh: horn with a hollow cylindrical inner conductor

The model geometry (Figure 5.14) comprises an inner conductor, co-axial outer conductor, and connecting end-plate. Boundary conditions were applied such that the model represents an infinite current loop, with current entering and exiting the model space as it crosses a central symmetry plane. Aluminium alloy 6082 was chosen as the horn conductor material. The air-filled magnetic volume was also included in the model so that the magnetic field distribution would be captured. The horn geometry was kept as generic as possible, but was based loosely on the specified LBNE horn dimensions. The geometry is summarised in table 5.3.

To avoid a stress concentration, fillet radii were added in the corners where the inner and outer conductors join onto the end plate. To obtain sensible results a first level of optimisation was carried out whereby the fillet radii were increased in size until the peak stress moved from the corner onto the straight section.

Table 5.3 Model geometry parameters: horn with a hollow inner conductor

Inner radius of inner conductor	20 mm
Outer radius of outer conductor	300 mm
Horn overall length	2 x 500 = 1000 mm
Inner conductor wall-thickness	3 mm
Outer conductor wall-thickness	20 mm
End plate wall-thickness	4 mm
Fillet radius	100 mm

Results plots corresponding to the peak of the 300 kA current pulse are included in Figure 5.15. The current density plot confirms that the maximum occurs in the inner conductor, which is where the conductor cross-section is smallest. The magnetic field plot shows how the field inside the magnetic volume reduces with radius according to 1/R. The Von-Mises stress plot shows that the peak stress occurs in the inner conductor. The stress is dominated by a tensile component that comes from axial Lorentz forces on the end plates being transmitted by the inner conductor. The temperature plot indicates a temperature rise of 5 degrees in the inner conductor at the end of the 1 milli-second current pulse.

The two graphs in Figure 5.16 show how the maximum and minimum temperature, the maximum Von-Mises thermal stress, and the axial load carried by the inner and outer conductors vary with time during the current pulse. The maximum axial loads occur at the peak of the current pulse, with the inner conductor taking a larger share of the total load than the outer conductor. As previously discussed, the axial load varies with the current squared. This means that while the net current varies with time according to a $\sin\theta$ function, the axial load varies according to a $\sin^2\theta$ function.

The inside diameter of the hollow inner conductor was then varied while keeping the wall thickness constant at 3 mm. Figure 5.17 shows how the axial force carried by the inner conductor increases as the inside diameter is reduced. This happens because in reducing the diameter we are adding an additional length of radial conductor to the end plate in a region where both the current density and magnetic field are high, resulting in a significant additional magnetic force. The axial tensile stress in the hollow inner conductor then depends on its cross-sectional area, which decreases as the inner radius is reduced. The result is a rapid increase in tensile stress as the conductor inner diameter is reduced.
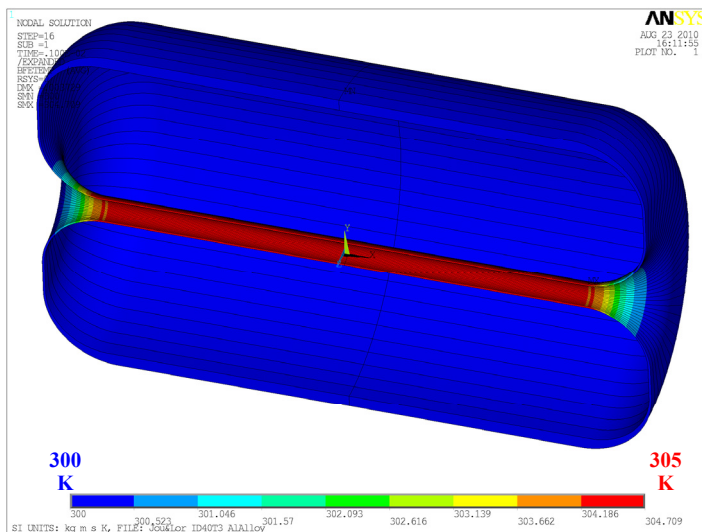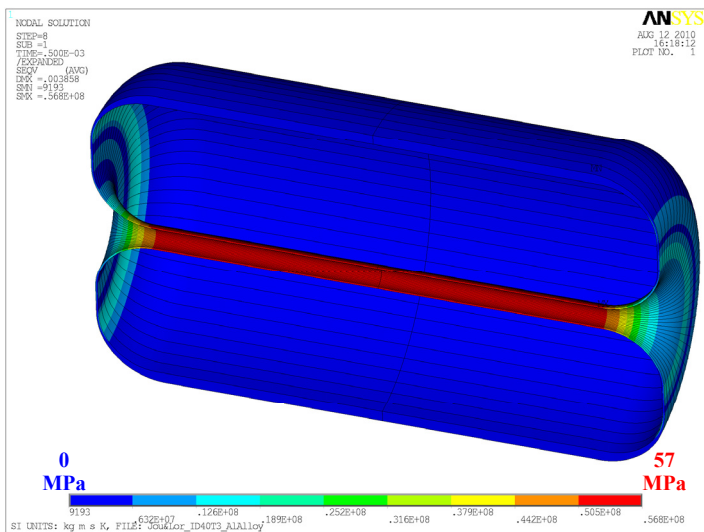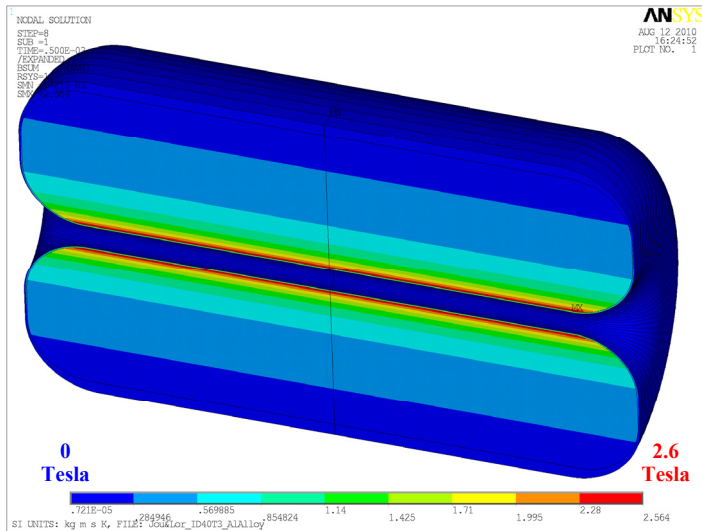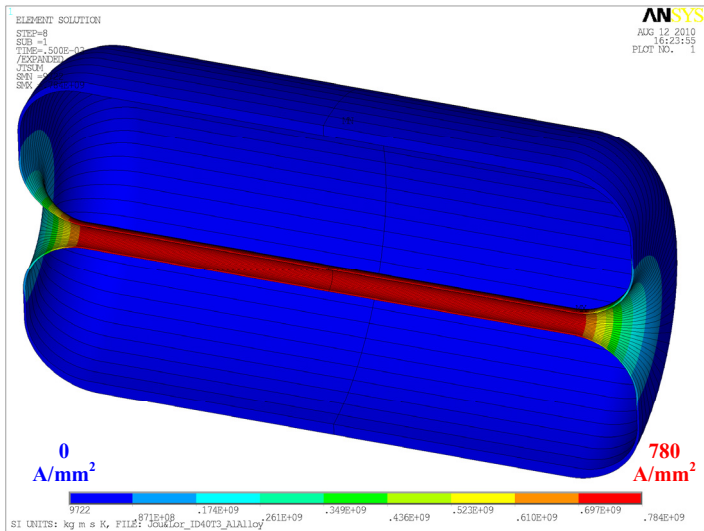
Figure 5.15 Example result plots, hollow aluminium alloy inner conductor, inside diameter=40mm, thickness=3mm

Top-left:	*Current density at the peak of the current pulse*
Top-right:	*Magnetic field at the peak of the current pulse*
Bottom-left:	*Von-Mises stress at the peak of the current pulse*
Bottom-right:	*Temperature at the end of the current pulse*
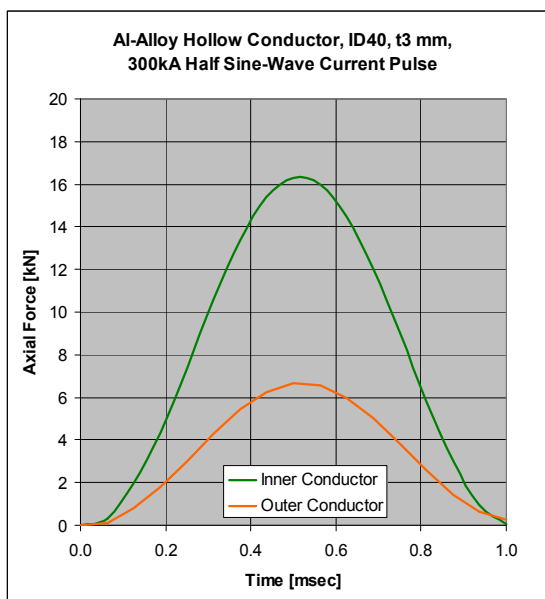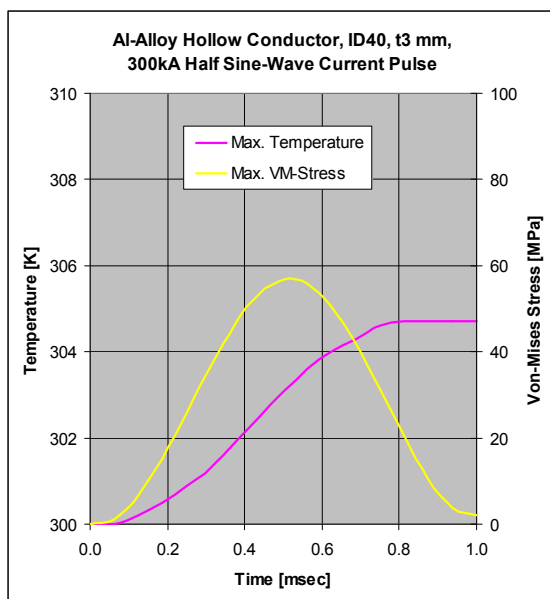
Figure 5.16 Results summary: diameter 40mm,wall- thickness 3mm, hollow cylindrical inner conductor
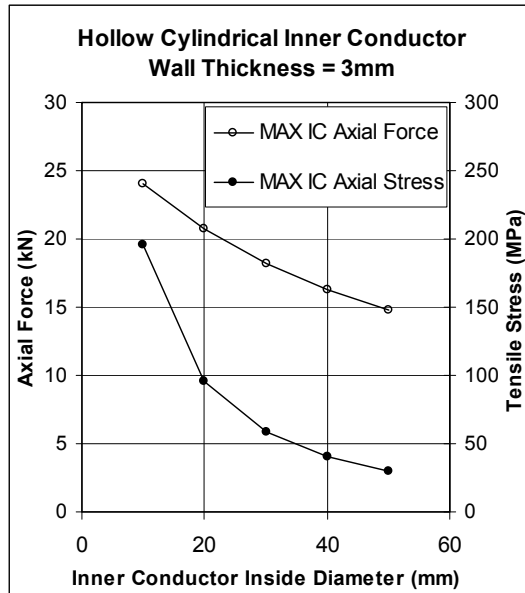
Figure 5.17 Effects of changing the conductor inside diameter

Horn with a Solid Inner Conductor

The horn model was modified to have a solid (rather than hollow) inner conductor as illustrated in Figure 5.18. In this case the full current flows down the solid inner conductor, spreads radially outwards in the end plates, and returns in the co-axial outer conductor.
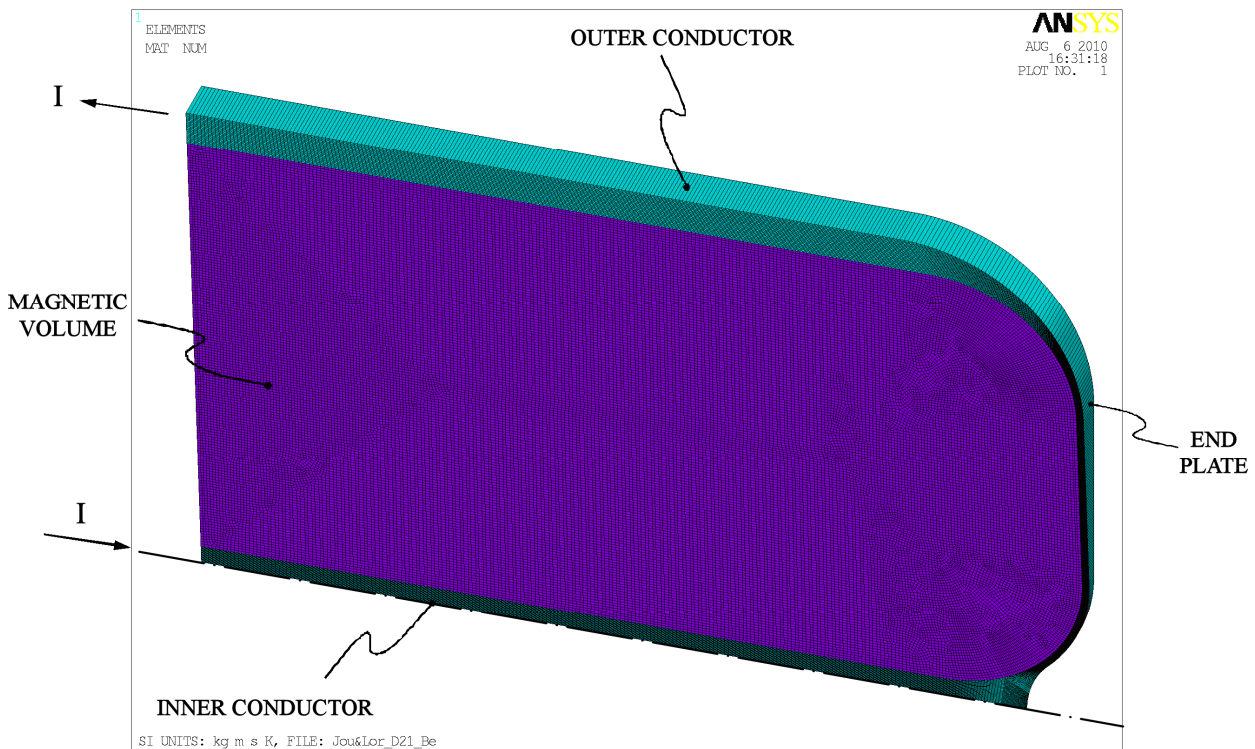
Figure 5.18 Finite element mesh: horn with a solid cylindrical inner conductor

Results plots corresponding to the peak of the 300 kA current pulse are included in Figure 5.19. The skin-effect is clearly visible in the current density plot where the maximum occurs at the inner conductor surface. The magnetic field plot shows the field inside the magnetic volume reducing with 1/R. In a similar way to the hollow conductor results the Von-Mises stress plot indicates a

uniformly distributed stress in the inner conductor. Again, the inner conductor stress is dominated by a tensile component that comes from Lorentz forces on the end plate. The temperature plot indicates a maximum temperature rise at the surface of the inner conductor of 11 degrees at the end of the 1 milli-second current pulse.
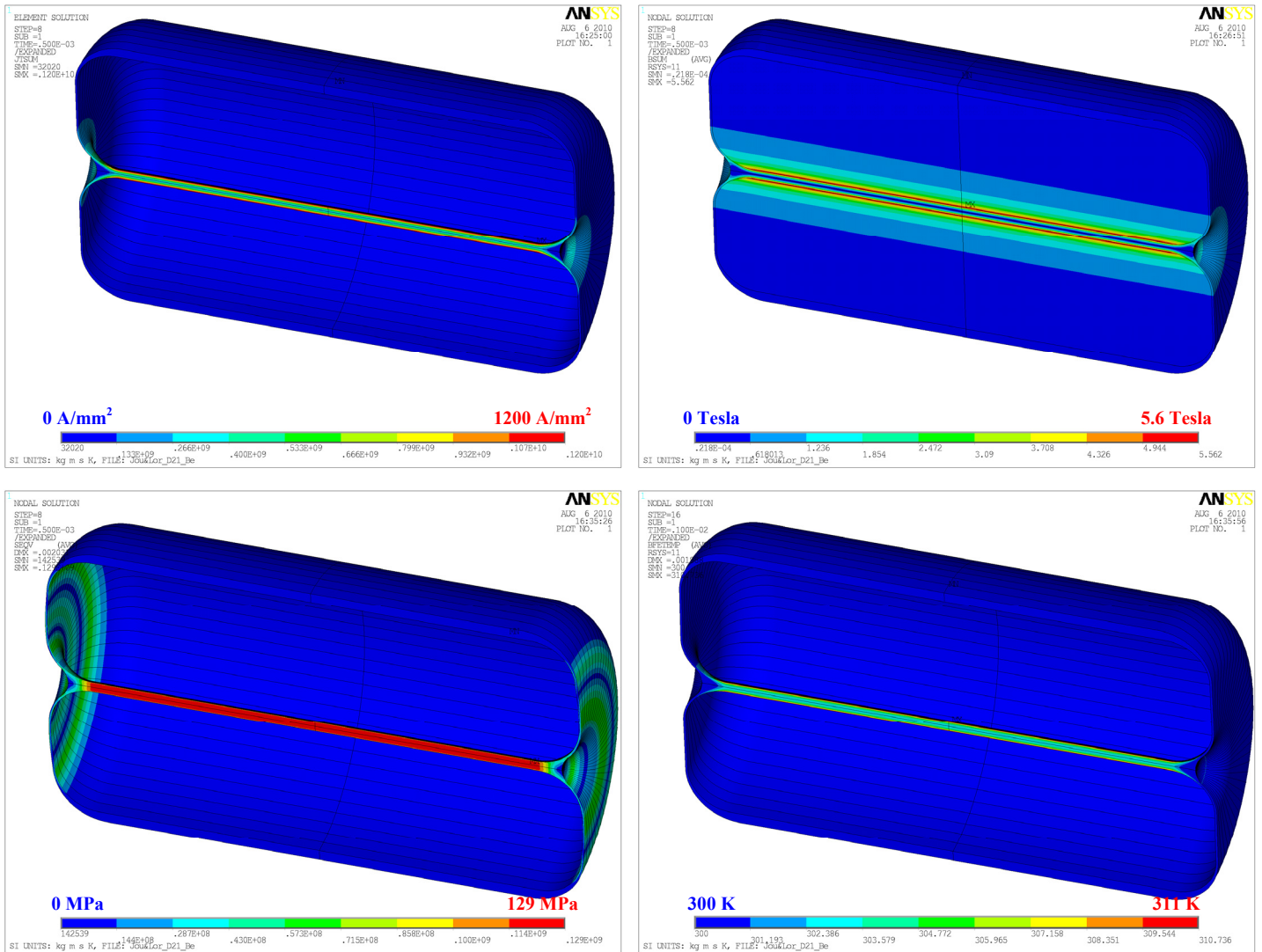
Figure 5.19 Example result contour plots, solid beryllium conductor, diameter=21mm
Top-left: Current density at the peak of the current pulse
Top-right: Magnetic field at the peak of the current pulse
Bottom-left: Lorentz stress at the peak of the current pulse
Bottom-right: Temperature at the end of the current pulse

The two graphs in Figure 5.20 show how the maximum and minimum temperature, the maximum Von-Mises thermal stress, and the axial load carried by the inner and outer conductors vary with time. Significantly larger axial forces were generated in the model with a solid inner conductor, compared to the model with a hollow inner conductor.
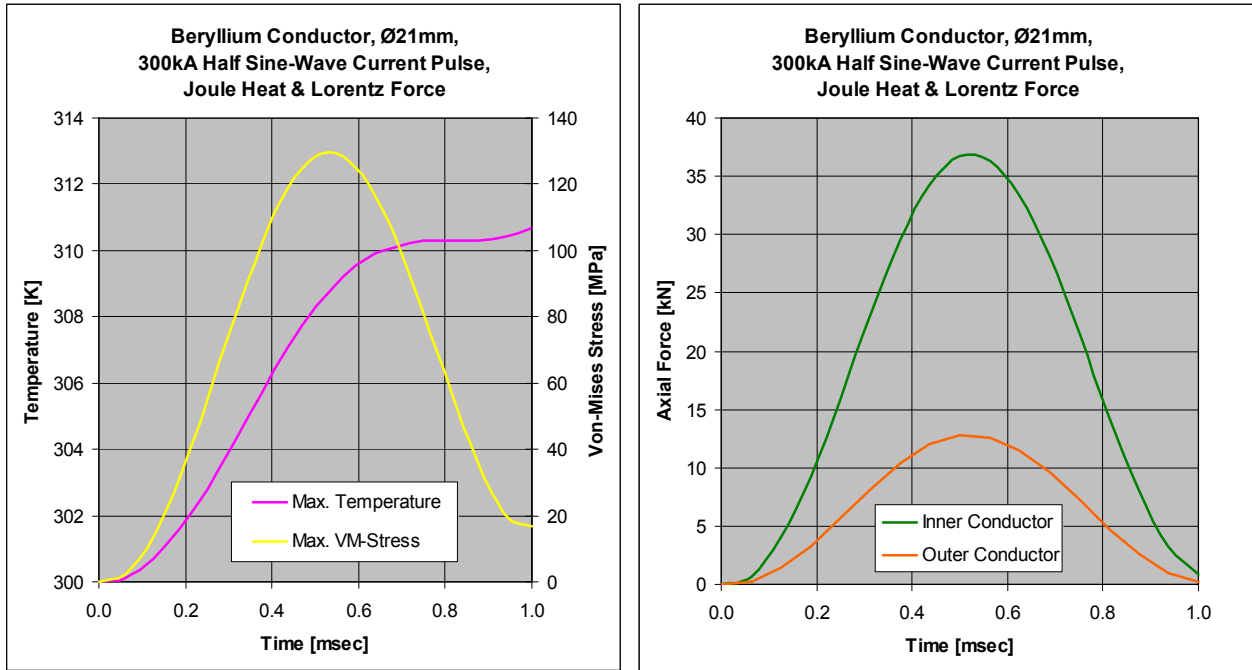
Figure 5.20 Results summary, diameter 21mm solid beryllium inner conductor

The model was run many times with varying input parameters to cover the design parameter space. A results summary covering a range of materials and inner conductor diameters is included in table 5.4. The Von-Mises stress results in the table are a combination of a thermal stress (driven by temperature gradients in the horn) and a Lorentz stress (dominated by the axial Lorentz force). The thermal stress depends on the electrical resistivity and heat capacity of the conducting material, while the Lorentz stress depends on geometry and on the net current applied. The Lorentz stress dominates, and as a result the maximum Von-Mises stress is more-or-less independent of material choice. A solid inner conductor diameter of at least 21mm is required in order to bring the maximum Von-Mises stress within the nominal design stress limit of 2/3 yield stress in Beryllium.

Table 5.4 Results summary, pulsed current effects in a solid inner conductor

Conductor Material	Inner Conductor Diameter (mm)	Max. ΔT per pulse (K)	Max. Axial Lorentz Force (kN)	Max. Von-Mises Stress (MPa)
Beryllium	9	160.9	41.6	799
	15	27.4	39.8	275
	21	10.7	36.7	129
	27	5.8	34.0	72
Al Alloy 6082	9	185.2	41.6	778
	15	33.8	39.5	266
	21	13.9	36.4	125
	27	7.6	33.7	70
AlBeMet	9	128.5	41.9	792
	15	24.2	39.6	269
	21	10.1	36.4	125
	27	5.5	33.7	70

The tensile axial force transmitted by solid inner conductors of various diameters is illustrated in Figure 5.21. The results show that reducing the diameter of the solid inner-conductor leads to an increased axial force. This is again explained by recalling that the magnetic pressure acting on the end plate is largest at the inner radius. The problem is made worse by the fact that a smaller diameter conductor also has a reduced cross-sectional area in which to distribute that axial force. For each conductor size studied a 6th order polynomial fit was made to the axial force vs time results data. The polynomial function could then be used as a force input in subsequent structural analyses.
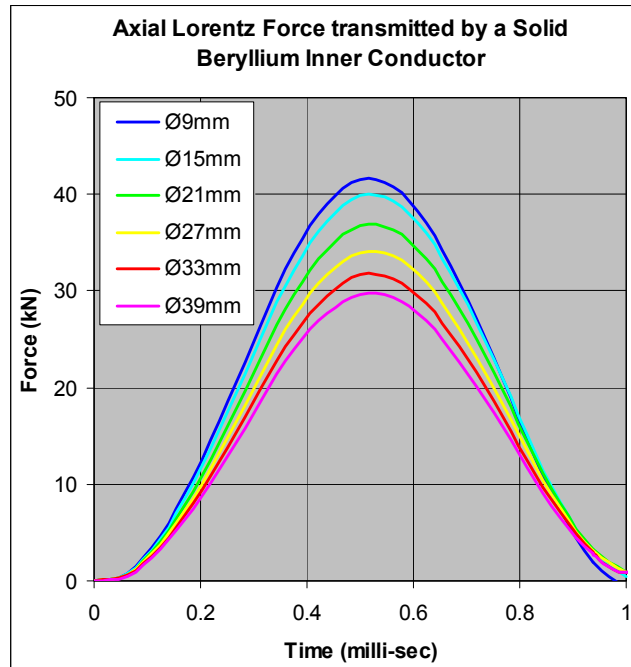
Figure 5.21 The Axial Lorentz Force as a function of solid inner-conductor diameter

Another key difference between the solid and hollow inner conductor options is in the strength of the focussing magnetic field in the region of the target. Figure 5.22 illustrates the magnetic field as a function of radius in a slice through the centre of the two magnetic horn concepts. The vertical dotted lines indicate the extremities of the magnetic volume (air region).
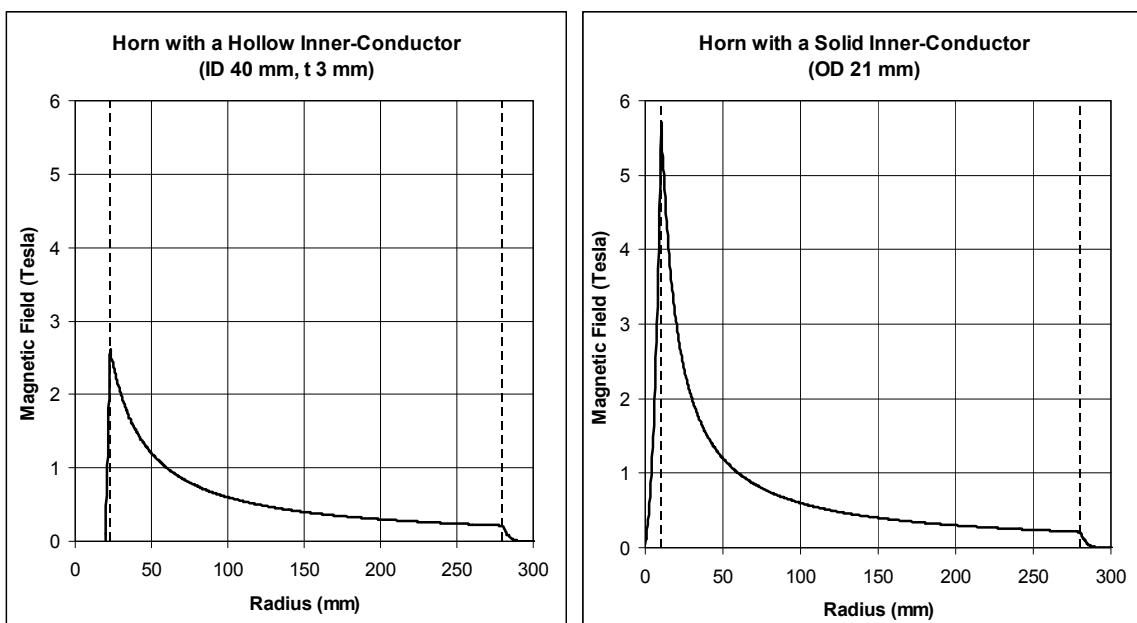
Figure 5.22 Magnetic field as a function of radius for two different horn concepts

148

In the case of a solid inner conductor the field rises from zero on the target/conductor axis to a maximum at the surface. Figure 5.22 shows that peak field in the horn is significantly greater in the case of a solid inner conductor. This is simply because the peak field is defined by the outer radius of the inner-conductor, which is smaller in the case of a solid inner conductor. We note that at any radial position inside the magnetic volume the field is identical in either case.

In terms of particle focussing there is a clear distinction between the concept of placing a target inside the bore of a hollow inner conductor, and the concept of incorporating a solid "combined" target and horn inner conductor. In the former case there is zero magnetic field in the target region, whereas in the latter case the magnetic field penetrates into the target itself. Studying the effects of this additional focussing field on the particle capture system is beyond the scope of this study.

Summary of Magnetic Horn End Effects

The "magnetic pressure" acting on the horn end plates results in a tensile axial force that must be shared between the inner and outer conductors. The force magnitude depends on the net current squared, and on horn geometry parameters. It is sensitive to small changes in the inner conductor diameter but relatively insensitive to changes in the outer conductor diameter. It is independent of the horn length and the conductor material.

For the range of geometry parameters considered in this study, the stresses generated in the inner conductor by axial Lorentz forces were far more significant than those generated by radial Lorentz forces. The problem therefore becomes one of ensuring that the inner conductor has sufficient cross-sectional area to carry the required tensile load.

Changing from a hollow inner conductor to a solid inner conductor has the double negative effect of increasing the total axial load, while at the same time reducing the cross-sectional area. This leads to significantly increased stress levels in a solid inner conductor.

5.4 ANSYS Models: Combined Beam heating and Current Pulse Effects

Outline

We consider the combination of beam spill and horn current effects for a solid cylindrical combined target and horn inner conductor. The objective is to simultaneously apply beam heating, resistive heating, and Lorentz force loads in the simulation in order to study their combined effect.

Analysis Procedure

An analysis was performed following the multi-stage process illustrated in Figure 5.23, comprising both FLUKA and ANSYS simulations.

Firstly, the beam/target interaction was modelled using FLUKA in order to determine the energy density distribution in the target. The energy deposition data was output from FLUKA in a table in a suitable format to be interfaced with ANSYS. Then, following the same procedure used in the previous analyses above, three consecutive ANSYS physics environments were solved, capturing the relevant electromagnetic, thermal, and mechanical effects.
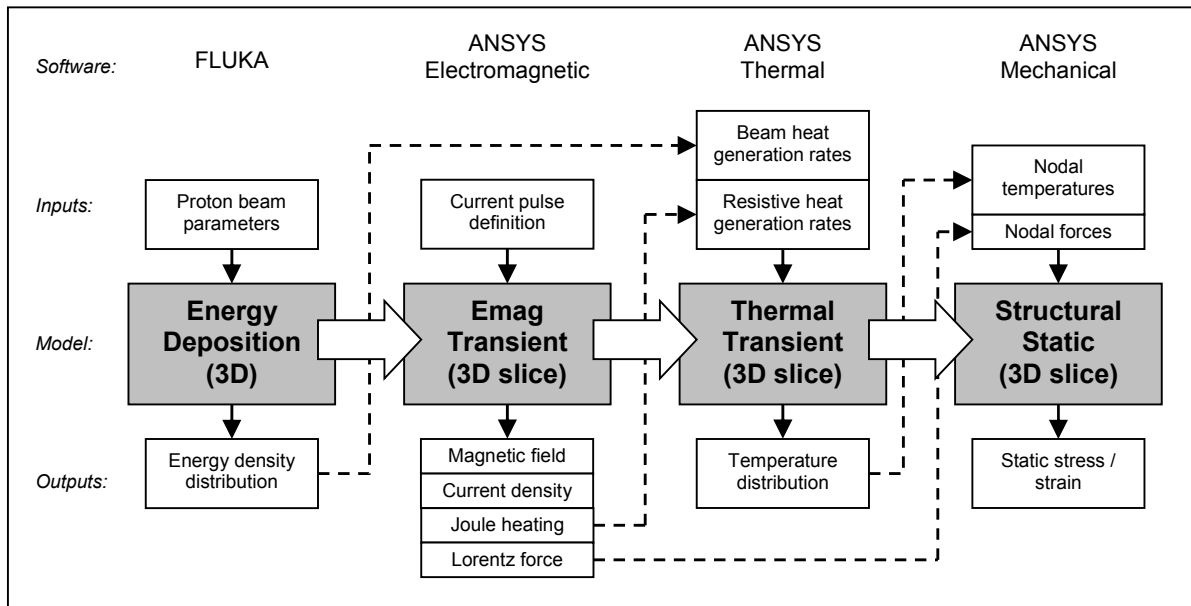
Figure 5.23 Analysis process, combined beam and horn current effects

Model Description

In this model the target / conductor region was simplified to a 1m long solid cylinder. The same type of quasi-axisymmetric mesh that was employed in the previous "long cylindrical conductor" analysis was used (recall Figure 5.3).

The transient electromagnetic simulation was performed using the same current loads and symmetry boundary conditions discussed previously. Skin-effects were fully described. In the transient thermal simulation two heat sources were included:

1. Joule heating based on the current distribution calculated in the previous electromagnetic steps. The intensity and spatial distribution of the Joule heat load varied during the 1 milli-second current pulse time according to the ANSYS electromagnetic solution.

2. Beam heating based on the distribution defined in the FLUKA output file. The intensity and spatial distribution of the beam heat load was constant during the (short) 10 micro-second spill time.

In the static structural simulation the target / conductor was again fixed at the upstream end and allowed to expand axially at the downstream end. Time-varying temperature distributions and radial Lorentz forces were applied according to the previous thermal and electromagnetic solutions. In addition, a time varying tensile axial force was applied to simulate the magnetic horn end loading (discussed in the previous section, recall Figure 5.21). This additional tensile load was applied using a 6th order polynomial function defined by fitting the results data from the previous parameterised "end effects" models.

The model time structure is illustrated in Figure 5.24. It includes the current pulse time during which heat energy is added to the model, and the interval between pulses in which thermal conduction takes place. In the thermal transient analysis the resistive (Joule) heat generation rates were ramped, while the beam heat generation, applied at the peak of the current pulse, was stepped on and then off. To allow the beam and current heat generation rates to be applied one at a time, the beam heating was applied over a shorter timescale than the physical spill time so that the simulated time gap in the resistive heat input was reduced to a negligible level. This is appropriate because the beam heating occurs over a timescale which is effectively instantaneous with respect to thermal conduction taking place in any case. This method avoids the complication of needing to apply both beam heating and resistive heating in the model simultaneously.
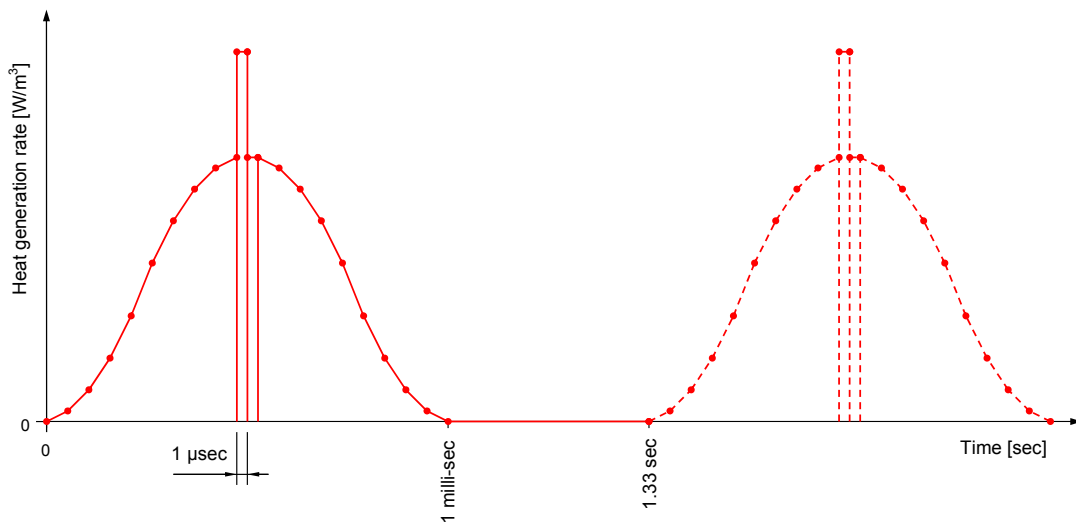
Figure 5.24 Model time structure

Results: Combined Beam heating and Current Pulse Effects

Results were obtained for a single target / conductor geometry, that of a 1m long, 21mm diameter, cylinder. Smaller target / conductor diameters were not considered due to excessive resistive heating from the horn current pulse and high tensile Lorentz stresses. Two different beam powers were studied, 0.7 MW and 2.3 MW. The model configurations are listed in table 5.5. The model was first run considering each effect separately, i.e. beam heating only, Joule heating only, and Lorentz force only. Finally all three effects were combined and solved simultaneously. The results for the 2.3 MW beam case are illustrated in Figure 5.25.

Table 5.5 Combined effects model configurations

Proton Beam Energy (GeV)	Proton Beam Power (MW)	Beam Sigma (mm)	Target Diameter (mm)
120	0.7	3.5	21
120	2.3	3.5	21
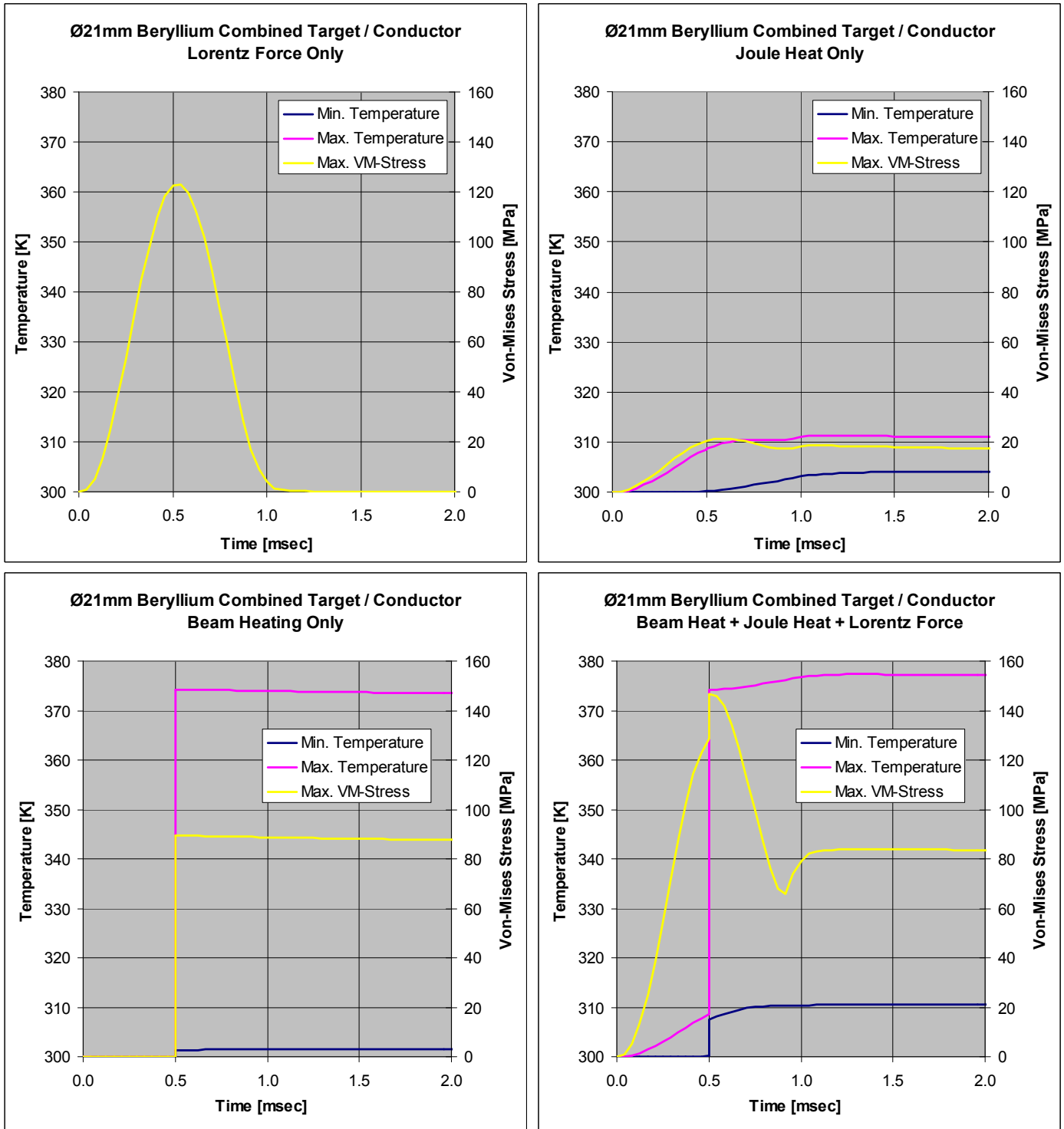
Figure 5.25 Breakdown of individual effects, 2.3 MW 120 GeV beam spill, 300 kA 1 msec Current pulse
top-left: Lorentz force only, top-right: joule heat only, bottom-left: beam heat only, bottom-right: combined effects

In the 2.3 MW combined case we see the maximum temperature slowly rising as the current is ramped from zero to 300 kA (0.0 msec to 0.5 msec). At 0.5 msec, which corresponds to the peak of the current pulse, the beam heating effect is visible as a large stepped increase in temperature. As the current is ramped from 300 kA back to zero (0.5 msec to 1.0 msec) the maximum temperature continues to rise slowly, and reaches a peak value soon after the end of the pulse (1.0 msec) when the remnant eddy currents from the current pulse have fully dissipated.

The maximum stress in the combined target / inner-conductor is dominated by the axial Lorentz force component. During the first half of the current pulse the maximum stress increases in proportion to the axial Lorentz force, which varies with the current squared. At the peak of the

current pulse (t=0.5 msec) the thermal stress component generated by beam induced heating is visible as a stepped increase in maximum stress. At the end of the current pulse a remnant thermal stress remains due to thermal gradients in the combined target / inner-conductor, which reduces over time as thermal conduction takes effect.

The effects of varying the combined target / inner-conductor diameter were also investigated. In all cases the beam sigma was scaled to be one-third of the target radius. A summary of results is included in table 5.6. Figure 5.26 illustrates how the total heat energy deposited in the combined target / inner-conductor depends on its diameter. The beam heating component increases (roughly linearly) with target diameter because there is more material volume available in which the particle shower can build up. At the same time, the resistive (Joule) heating component, driven by the current density in the conductor, reduces with increased conductor diameter. The result is that an optimum diameter range exists at which the steady-state power (the heating power that must be dealt with by the cooling system) is at a minimum. If the target / conductor diameter is too small then there is an excessively high resistive heat input, whereas if the target / conductor is too large then there is an excessively high beam heating input.
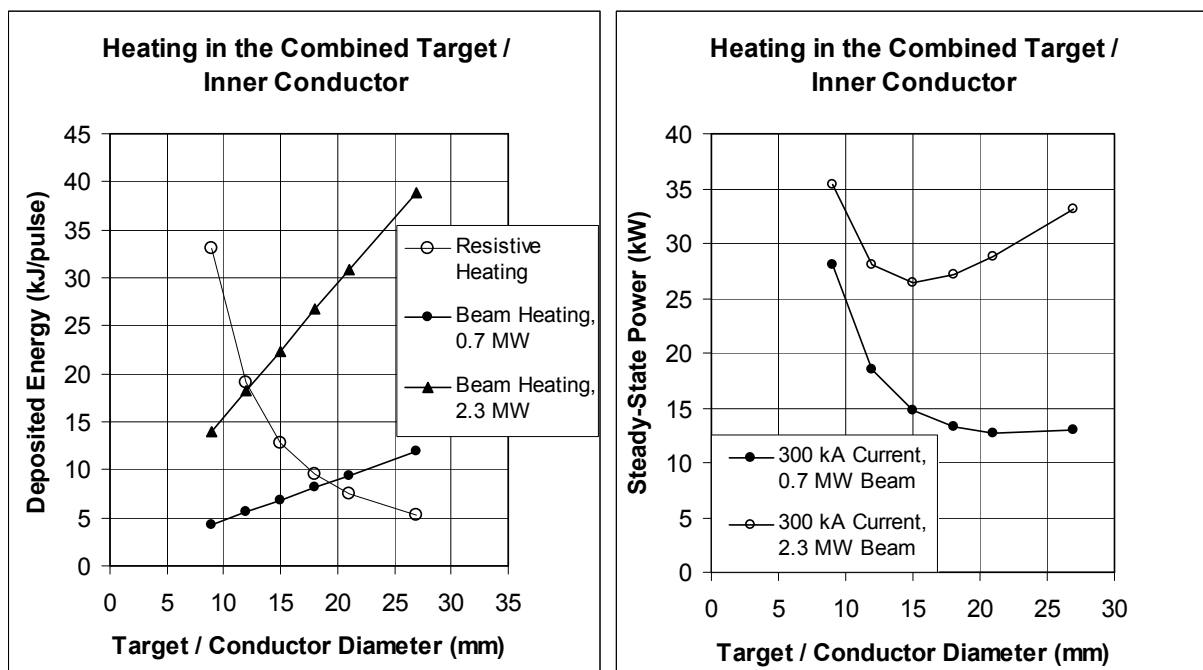
Figure 5.26 Heat energy deposited in a combined target / inner-conductor

Figure 5.27 illustrates how the maximum temperature rise and maximum stress in the model vary with changes to the target / conductor diameter. The temperature rise is driven by the deposited energy density from a combination of beam heating and resistive heating. A roughly three times higher energy density is predicted in the case of the 2.3 MW beam compared to the 0.7 MW beam, hence the larger temperature rise in the 2.3 MW case. The Von-Mises stress is derived from a combination of thermal and Lorentz stresses. The stress field is dominated by the longitudinal tensile Lorentz stress, and as a result there is little difference between the 2.3 MW and 0.7 MW cases. The horizontal dashed line indicates a nominal design stress limit of 2/3 yield stress in Beryllium. The results indicate that a target / conductor diameter greater than ~20 mm is needed to remain within this limit. However, a number of factors not included in this analysis can lead to much increased stresses. These factors, discussed elsewhere in this report, include:

1. Longitudinal elastic stress waves generated by the instantaneous nature of the beam heating.
2. Off-centre beam interactions leading to asymmetric loads on the target.
3. Bulk oscillations ("violin-modes") of the target / conductor.
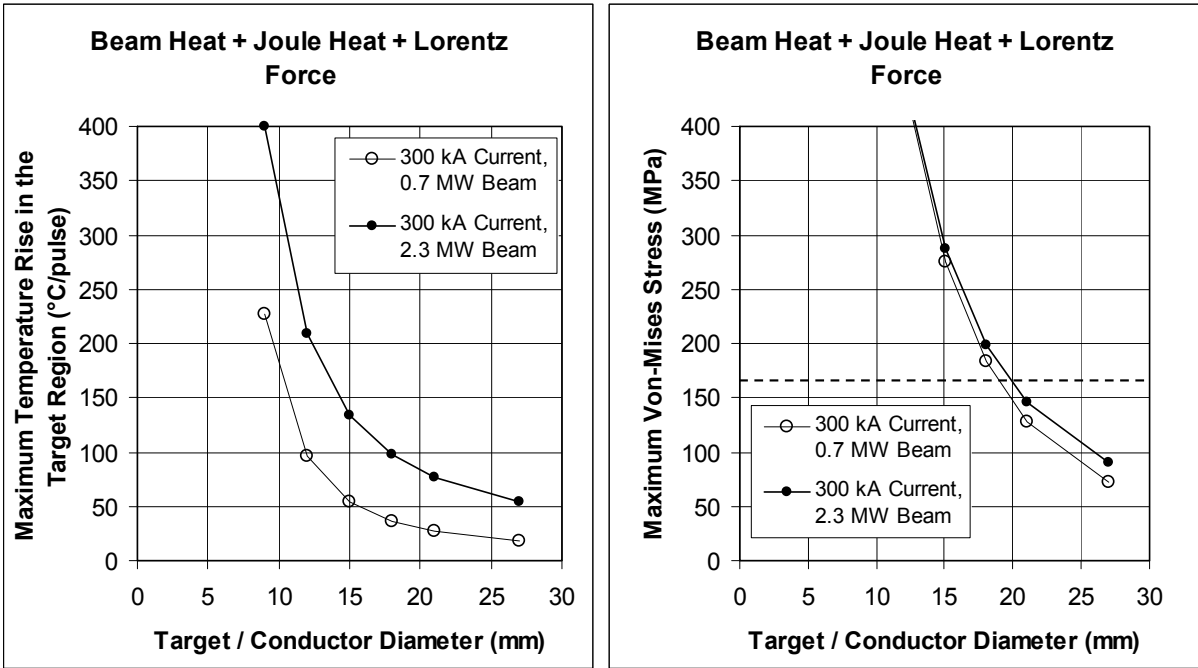
Figure 5.27 Maximum temperature and stress in a combined target / inner-conductor

Table 5.6 Results summary: combined target and horn inner-conductor

Target / Conductor Material	Beam Energy (GeV)	Beam Power (MW)	Beam Sigma (mm)	Conductor Diameter (mm)	Deposited Resistive Energy (kJ/pulse)	Deposited Beam Energy (kJ/spill)	Steady-state Power (kW)	Max. ΔT (∘C)	Max. Von-Mises Stress (MPa)	Max. IC Axial Force (kN)
Beryllium	120	0.7	1.5	9	33.0	4.3	28	228	799	42
			2.0	12	19.1	5.6	19	96	445	41
			2.5	15	12.8	6.9	15	54	275	40
			3.0	18	9.5	8.2	13	36	183	38
			3.5	21	7.5	9.4	13	26	129	37
			4.5	27	5.3	11.9	13	17	72	34
		2.3	1.5	9	33.0	14.0	35	401	799	42
			2.0	12	19.1	18.2	28	209	450	41
			2.5	15	12.8	22.4	26	135	287	40
			3.0	18	9.5	26.7	27	98	199	38
			3.5	21	7.5	30.8	29	77	147	37
			4.5	27	5.3	38.8	33	54	90	34

5.5 Summary of Task C

Two particular issues emerged as critical in the feasibility of a combined target / horn inner-conductor:

1. For the cross-section area of a combined target / conductor to be sufficient to carry the longitudinal Lorentz force generated by the horn current pulse. This issue was studied in some detail (see "magnetic horn end effects" in section 5.3). The results indicate the need for a large diameter solid inner conductor in excess of, say, 20 mm, purely to support the magnetic loads. However, simply increasing the diameter of the combined target / inner-conductor in order to mitigate the longitudinal Lorentz stress has unwanted side effects such as increasing the secondary beam heat load, and reducing the pion production efficiency (see figure of merit). In the 700 kW beam power scenario the longitudinal Lorentz forces were shown to be the dominant effect, i.e. the beam heating and Joule heating effects were less significant.

2. For the dynamic stress component, in particular the longitudinal stress waves, to be maintained within acceptable limits. This issue is discussed at length in section 3. The intensity of longitudinal stress waves generated by the instantaneous nature of the beam heat load increases with the pulsed power density. In the 2.3 MW beam power scenario the beam induced dynamic stress component was shown to be the dominant effect, i.e. the Joule heating and Lorentz force effects were less significant. Segmenting the target was introduced as a potential way of reducing the impact of longitudinal stress-waves, but unfortunately this method is inherently incompatible with the combined target / conductor concept where the target must be continuous in order to conduct the 300 kA horn current pulse.

700 kW Beam Power Target Summary

For the 700 kW beam scenario a 21mm diameter beryllium combined target / conductor does look feasible. At this beam power results from the dynamic simulations indicate that the effects of longitudinal stress waves and off-centre beam heating are relatively small. The target diameter is therefore driven largely by the need to support the longitudinal Lorentz force component. However, at beam powers in excess of 700 kW the beam induced dynamic stress component becomes more significant and a further increase in target diameter would be required in order to manage the combined stresses.

2 – 2.3 MW Beam Power Target Summary

The results suggest that a very large target diameter, perhaps in the region of ~40 mm, and a corresponding large beam sigma, could be required in order to reduce the combined beam and current related stresses to an acceptable level. However, moving outside of the design parameter range in this way would introduce a significant additional secondary heat load and a reduction in pion production efficiency that is deemed unacceptable. Thus, for the 2.3 MW scenario a combined target / inner conductor does not look feasible. The limiting factor is the dynamic stress magnitude which appears unfeasible in the case of a well centred beam, and even worse in the case of a mis-steered beam.

Appendix 5.1

Benchmarking: Capturing Skin Effects in ANSYS

The ANSYS finite element code was benchmarked against a derived analytical solution to verify that pulsed current skin effects were being correctly captured in the simulation.

Ref: A.J.Lennox, *Skin Effect in Electrically Pulsed Cylindrical Conductors Used as Focusing Devices*, $\bar{\text{p}}$ note #269, Fermilab, 28 Jan 1983.

The boundary conditions used in the analytical solution were replicated in the ANSYS model in order to make a fair comparison. The conductor diameter was adjusted to 19.3 mm so that the outer radius was equal to twice the nominal skin depth in beryllium. Note that this is close to the 21 mm target diameter that is of interest for LBNE. An un-damped half sine-wave current pulse shape was assumed in the analytical solution. This is also directly relevant in the LBNE study.
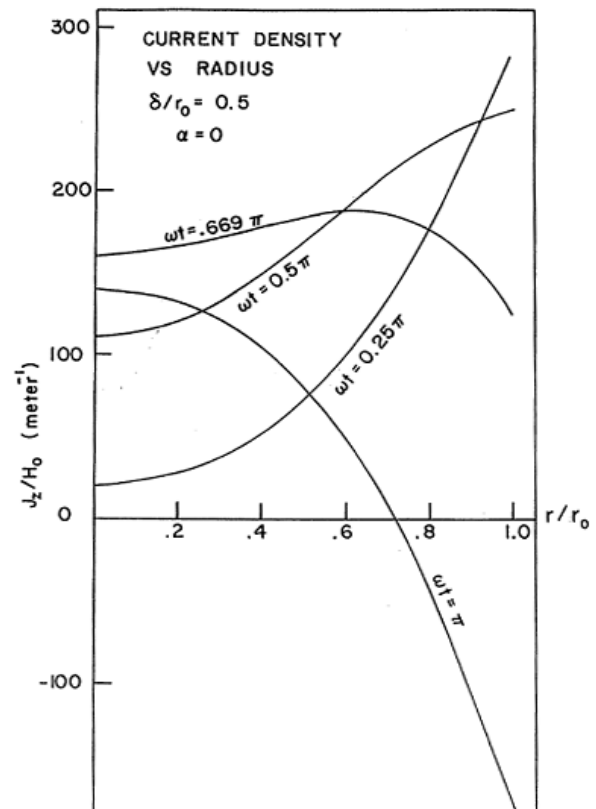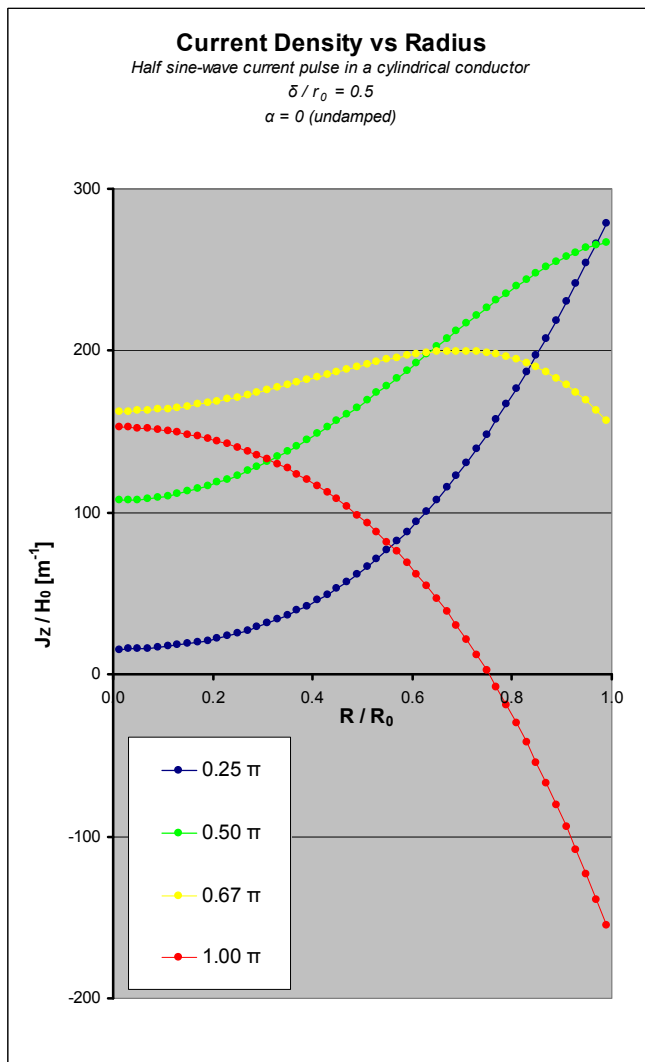
benchmark of skin-effect current distribution
Left: ANSYS model, right: analytical solution

The plots show how the current density varies as a function of radial position, at four points in time during the current pulse. Good agreement is seen between the ANSYS solution on the left, and the analytical solution on the right. In the plots, the current density is normalised to the peak field H_0, which is found from:

$$H_0 = \frac{I_{peak}}{2\pi R_0} \qquad [A/m]$$

Where: I_{peak} is the peak current $[A]$
R_0 is the conductor outer radius $[m]$

The plot describes how the current density evolves during the 1 msec pulse. At the start of the pulse there is assumed to be zero current density at all positions in the conductor cross-section. At t=0.25 msec the bulk of the current is flowing close to the conductor surface. At the peak of the current pulse, t=0.5 msec, the maximum current density still occurs at the conductor surface, but the distribution of current in the conductor cross-section is becoming more uniform. At t=0.67 msec the distribution of current density is at its most uniform. At the end of the current pulse, t=1msec, there is zero net current flowing in the conductor. However this zero net current is made up of local current densities that act in opposite directions. That is, a downstream current density is present at the conductor centre that is balanced by an upstream current density located near to the conductor surface.

The validation exercise demonstrates that ANSYS successfully captures these pulsed current skin effects. We conclude that modelling the current distribution in this level of detail will allow the correct resistive heating and Lorentz force loads to be identified and exploited.

Appendix 5.2

Example Input File: Combined Effects of Beam Spill and Horn Pulse

```
!----------------------------
!3D ELECTROMAGNETIC + THERMAL + STRUCTURAL ANALYSES
!USE ANSYS MULTIPHYSICS v11.0
!P.LOVERIDGE
!JULY 2010
!----------------------------
FINISH
/CLEAR
/FILENAME,Combi_D21_Be_2p3MW,1           !SET THIS TO THE INPUT DECK FILENAME
*GET,FNAME,ACTIVE,,JOBNAM
/TITLE,3D MODEL, SI UNITS: kg m s K, FILE: %FNAME%
/FILENAME,%FNAME%_EMAG,1                  !ADD A SUFFIX FOR EMAG FILENAMES
/PREP7

!--------------------------
!INPUT PARAMETERS
!--------------------------
*SET,R1,0.0105                           !INNER CONDUCTOR OUTER RADIUS [m]
*SET,R2,1.000                            !OUTER RADIUS OF AIR VOLUME   [m]
*SET,L,1.000                             !LENGTH = 1m                  [m]
*SET,PTIM,1E-3                           !CURRENT PULSE LENGTH         [sec]
*SET,BTIM,1E-6                           !BEAM SPILL LENGTH            [sec]
*SET,REP,0.76                            !PULSE REPETITION PERIOD      [sec]

!--------------------------
!MATERIAL 1: BERYLLIUM
!--------------------------
MP,DENS,1,1821                           !DENSITY                 [kg/m3]
MP,ALPX,1,11.5E-6                        !LINEAR EXPANSION        [/DEGREE]
MP,KXX,1,183                             !THERMAL CONDUCTIVITY    [W/m.K]
MP,C,1,1829                              !HEAT CAPACITY           [J/kg.K]
MP,MURX,1,1                              !RELATIVE PERMEABILITY   [-]
MP,RSVX,1,4.6E-8                         !ELECTRICAL RESISTIVITY  [Ohm.m]
MP,EX,1,309E9                            !ELASTIC MODULUS         [N/m2]
MP,PRXY,1,0.07                           !POISSON RATIO           [-]

!--------------------------
!MATERIAL 2: AIR
!--------------------------
MP,MURX,2,1                              !RELATIVE PERMEABILITY   [-]

!--------------------------
!GEOMETRY
!--------------------------
RECTNG,0,R1,0,L
RECTNG,R1,R2,0,L
NUMMRG,ALL

!--------------------------
!ELEMENT TYPES
!--------------------------
ET,1,SOLID97,1                           !3-D 8-NODE MAGNETIC BRICK
                                         !CONDUCTING ELEMENTS
ET,2,SOLID97,0                           !3-D 8-NODE MAGNETIC BRICK
                                         !NON-CONDUCTING ELEMENTS
ET,11,MESH200,6                          !NOT SOLVED
                                         !4-NODE QUAD

!--------------------------
!AREA MESH
!--------------------------
ASEL,S,,,1                               !DEFINE AREA ATTRIBUTES
AATT,1,,11
ASEL,S,,,2
AATT,2,,11

!CONDUCTOR MESH DIVISIONS
LSEL,S,LOC,X,0
LESIZE,ALL,,,100                         !SET AXIAL MESH DIVISIONS
LSEL,S,LOC,X,0,R1
LSEL,R,LOC,Y,0
LESIZE,ALL,,,50                          !SET RADIAL MESH DIVISIONS

!AIR MESH DIVISIONS
```

```
LSEL,S,LOC,Y,0
LSEL,R,LOC,X,R1,R2
LESIZE,ALL,,,30,500                        !SET RADIAL MESH DIVISIONS
LSEL,S,LOC,Y,L
LSEL,R,LOC,X,R1,R2
LESIZE,ALL,,,30,1/500                      !SET RADIAL MESH DIVISIONS

MSHAPE,0,2D
MSHKEY,1
ALLSEL
AMESH,ALL                                  !MESH ALL AREAS


!---------------------------
!VOLUME MESH
!---------------------------
EXTOPT,ESIZE,1                             !NO. AZIMUTHAL ELEMENT DIVISIONS
EXTOPT,ATTR,1                              !USE AREA MATERIAL LABELS

TYPE,1
ASEL,S,MAT,,1
VROTAT,ALL,,,,,,1,4,6,1                    !SWEEP CONDUCTING AREAS BY 6 DEGREES

TYPE,2
ASEL,S,MAT,,2
VROTAT,ALL,,,,,,1,4,6,1                    !SWEEP NON-CONDUCTING AREAS BY 6 DEGREES

NUMMRG,NODE,1E-6                           !MERGE COINCIDENT NODES

!---------------------------
!SYMMETRY BOUNDARY CONDITIONS
!---------------------------
ALLSEL
CSYS,5                                     !POLAR CYLINDRICAL COORDINATES
NROTAT,ALL                                 !ROTATE NODES TO CYLINDRICAL COORDINATE SYSTEM

!FLUX NORMAL TO R-Z PLANE EVERYWHERE
NSEL,ALL
D,ALL,AY,0

!FLUX PARALLEL TO THETA-Z PLANE ON OD SURFACE
NSEL,S,LOC,X,R2
D,ALL,,,,,,AY,AZ

!FLUX PARALLEL TO THETA-R PLANE ON END SURFACES
NSEL,S,LOC,Z,0
NSEL,A,LOC,Z,L
D,ALL,,,,,,AY,AX

CSYS,0                                     !CARTESIAN COORDINATES
ALLSEL

!---------------------------
!VOLTAGE IN
!---------------------------
ASEL,S,LOC,Y,0,0
ASEL,R,LOC,X,0,R1                          !SELECT THE INPUT AREA
NSLA,S,1                                   !SELECT NODES ATTACHED TO THE AREA
CP,1,VOLT,ALL                             !COUPLE VOLTAGES AT INPUT NODES

!---------------------------
!VOLTAGE OUT
!---------------------------
ASEL,S,LOC,Y,L,L
ASEL,R,LOC,X,0,R1                          !SELECT THE OUTPUT AREA
NSLA,S,1                                   !SELECT NODES ATTACHED TO THE AREA
D,ALL,VOLT,0                              !GROUND VOLTAGE AT OUTPUT NODES

!---------------------------
!ANALYSIS OPTIONS
!---------------------------
/SOLU                                      !ENTER SOLUTION PROCESSOR
ANTYPE,TRAN                                !TRANSIENT ANALYSIS
TIMINT,ON,ALL                             !INCLUDE TRANSIENT EFFECTS
AUTOTS,OFF                                 !TURN OFF AUTO TIME-STEPPING
OUTPR,ALL,ALL                             !OUTPUT ALL QUANTITIES AT EVERY SUBSTEP
OUTRES,ALL,ALL                            !WRITE SOLUTION DATA AT EVERY SUBSTREP
KBC,0                                      !LOADS ARE TO BE RAMPED

NLST=24                                    !DIVIDE 1/2 SINE-WAVE INTO 24 LOADSTEPS
AINC=180/NLST                             !ANGLE INCREMENT [DEGREES]
TINC=PTIM/NLST                            !TIME INCREMENT [SEC]
```

```
!---------------------------
!PART A. STEPS 1 - 12
!       RISING PART OF HALF SINE-WAVE CURRENT PULSE
!---------------------------
*DO,COUNT,1,12,1
        *AFUN,DEG                        !EVALUATE ANGULAR FUNCTIONS IN DEGREES
        FACT=SIN(COUNT*AINC)             !FACTOR FOR J ACCORDING TO SINE FUNCTION
        ASEL,S,LOC,Y,0,0
        ASEL,R,LOC,X,0,R1                !SELECT THE INPUT AREA
        NSLA,S,1                         !SELECT THE INPUT NODES
        F,NDNEXT(0),AMPS,FACT*300E3*6/360  !APPLY THE NET CURRENT TO THE SLICE
        ALLSEL

        TIME,COUNT*TINC                  !TIME AT RAMP END [SEC]
        NSUB,1                           !RAMP IN 1 SUBSTEP
        LSWRITE,                         !INTEGER LOADSTEP NUMBER
*ENDDO                                   !END TIMESTEP LOOP


!---------------------------
!PART B. STEPS 13 - 14
!       TWO "VERY SHORT" TIME STEPS AT CURRENT PEAK WHERE BEAM HEAT MAY BE ADDED LATER
!---------------------------
        TIME,PTIM/2+BTIM                 !TIME AT RAMP END [SEC]
        NSUB,1                           !RAMP IN 1 SUBSTEP
        LSWRITE,                         !INTEGER LOADSTEP NUMBER

        TIME,PTIM/2+2*BTIM               !TIME AT RAMP END [SEC]
        NSUB,1                           !RAMP IN 1 SUBSTEP
        LSWRITE,                         !INTEGER LOADSTEP NUMBER


!---------------------------
!PART C. STEPS 15 - 26
!       FALLING PART OF HALF SINE-WAVE CURRENT PULSE
!---------------------------
*DO,COUNT,15,26,1
        *AFUN,DEG                        !EVALUATE ANGULAR FUNCTIONS IN DEGREES
        FACT=SIN((COUNT-2)*AINC)         !FACTOR FOR J ACCORDING TO SINE FUNCTION
        ASEL,S,LOC,Y,0,0
        ASEL,R,LOC,X,0,R1                !SELECT THE INPUT AREA
        NSLA,S,1                         !SELECT THE INPUT NODES
        F,NDNEXT(0),AMPS,FACT*300E3*6/360  !APPLY THE NET CURRENT TO THE SLICE
        ALLSEL

        TIME,(COUNT-2)*TINC              !TIME AT RAMP END [SEC]
        NSUB,1                           !RAMP IN 1 SUBSTEP
        LSWRITE,                         !INTEGER LOADSTEP NUMBER
*ENDDO                                   !END TIMESTEP LOOP


!---------------------------
!PART D. STEPS 27 - 50
!       2ND HALF SINE-PERIOD, ZERO NET CURRENT THROUGHOUT
!---------------------------
*DO,COUNT,27,50,1
        ASEL,S,LOC,Y,0,0
        ASEL,R,LOC,X,0,R1                !SELECT THE INPUT AREA
        NSLA,S,1                         !SELECT NODES ATTACHED TO THE AREA
        F,NDNEXT(0),AMPS,0               !ZERO NET CURRENT
        ALLSEL

        TIME,(COUNT-2)*TINC              !TIME AT RAMP END [SEC]
        NSUB,1                           !RAMP IN 1 SUBSTEP
        LSWRITE,                         !INTEGER LOADSTEP NUMBER
*ENDDO                                   !END TIMESTEP LOOP


!---------------------------
!PART E. STEP 51
!PAUSE BETWEEN PULSES, ZERO NET CURRENT THROUGHOUT
!---------------------------
        ASEL,S,LOC,Y,0,0
        ASEL,R,LOC,X,0,R1                !SELECT THE INPUT AREA
        NSLA,S,1                         !SELECT NODES ATTACHED TO THE AREA
        F,NDNEXT(0),AMPS,0               !ZERO NET CURRENT
        ALLSEL

        TIME,REP
        NSUB,20                          !RAMP IN 20 SUBSTEPs
        LSWRITE,                         !INTEGER LOADSTEP NUMBER

!---------------------------
!CARRY OUT EMAG SOLUTION
!---------------------------
ALLSEL                                   !SELECT EVERYTHING
```

```
FINISH
/CONFIG,NRES,10000                          !MAX NUMBER OF SUBSTEPS
/SOLU                                       !ENTER THE SOLUTION PROCESSOR
LSSOLVE,01,51                               !NOTE: 51 STEPS IN 1 PERIOD
SAVE


!--------------------------------------------------------------------------------
!TRANSIENT THERMAL ANALYSIS STARTS HERE
!--------------------------------------------------------------------------------
FINISH
ALLSEL

/POST1
*GET,NSET,ACTIVE,,SET,NSET                  !GET NO. RESULTS SETS ON FILE
*DIM,TEMAG,ARRAY,NSET,1                     !DIMENSION AN ARRAY WITH 1 COLUMN

*DO,I,1,NSET,1                              !LOOP THROUGH EACH RESULTS SET
      SET,,,,,,,I                           !READ SET NUMBER I
      *GET,TIME,ACTIVE,,SET,TIME            !TIME AT THIS RESULTS SET
      TEMAG(I,1)=TIME                       !STORE IN 1ST COLUMN
*ENDDO                                      !END OF LOOP

FINISH
/FILENAME,%FNAME%_THERM,1                   !ADD A SUFFIX FOR THERMAL FILENAMES

!---------------------------
!CLEAR THE EMAG LOADS
!---------------------------
/PREP7
LSCLEAR,ALL

!---------------------------
!CHANGE ELEMENT TYPES FROM EMAG TO THERMAL
!---------------------------
/PREP7
ET,1,SOLID70                                !8-NODE BRICK THERMAL SOLID
ET,2,0                                      !NOT SOLVED

!---------------------------
!THERMAL BOUNDARY CONDITIONS
!---------------------------
TREF,300                                    !REFERENCE TEMP FOR THERMAL SRAIN CALCS
TUNIF,300                                   !INITIAL UNIFORM TEMPERATURE DISTRIBUTION

!---------------------------
!ANALYSIS OPTIONS
!---------------------------
/SOLU                                       !ENTER SOLUTION PROCESSOR
ANTYPE,TRAN                                 !TRANSIENT ANALYSIS
TIMINT,ON,ALL                              !INCLUDE TRANSIENT EFFECTS
AUTOTS,OFF                                  !TURN OFF AUTO TIME-STEPPING
OUTPR,ALL,ALL                              !OUTPUT ALL QUANTITIES AT EVERY SUBSTEP
OUTRES,ALL,ALL                             !WRITE SOLUTION DATA AT EVERY SUBSTREP
KBC,0                                       !LOADS ARE TO BE RAMPED
NSUB,1                                      !SOLVE EACH STEP IN 1 SUBSTEP

!---------------------------
!SOLVE
!---------------------------
/SOLU                                       !ENTER SOLUTION PROCESSOR
ALLSEL                                      !SELECT EVERYTHING
ESEL,U,MAT,,2                               !UNSELECT THE AIR ELEMENTS
NSLE,S                                      !SELECT NODES ATTACHED TO ELEMENTS

      !---------------------------
      !PART A. STEPS 1 - 12
      !       RISING PART OF HALF SINE-WAVE CURRENT PULSE
      !---------------------------
      *DO,I,1,12,1                          !LOOP THROUGH EACH THERMAL LOAD STEP
            TIME,TEMAG(I,1)                 !SET THE TIME
            LDREAD,HGEN,,,TEMAG(I,1),,%FNAME%_EMAG,RST   !READ IN THE ELEMENT HEAT GEN RATES
            LSWRITE,I                       !WRITE THE LOADSTEP FILE
      *ENDDO                                !END OF LOOP

      !---------------------------
      !PART B. STEPS 13 - 14
      !       BEAM SPILL
      !---------------------------
      KBC,1                                 !LOADS ARE TO BE STEPPED

      CLOCAL,100,CART,   0,0,0,   0,-90,0
      BINX=21
```

161

```
        BINY=21
        BINZ=40
        *DIM,BHEAT,TABLE,BINX,BINY,BINZ,X,Y,Z,100          !DEFINE A TABLE FOR THE RAW FLUKA DATA
        *DIM,BHEATFAC,TABLE,BINX,BINY,BINZ,X,Y,Z,100       !DEFINE A TABLE FOR SI UNITS CONVERSION

        F1=1.60217646E-10                                  !CONVERT J/GeV
        F2=1E6                                             !CONVERT cc/m3
        F3=1.6e14                                          !PROTONS PER SPILL

        *TREAD,BHEAT,Be120GeV_Sig3p5,CSV                   !READ FLUKA DATA IN GeV/cc/PROTON
        *TOPER,BHEATFAC,BHEAT,ADD,BHEAT,F1*F2*F3/BTIM,0,0,  !CONVERT TO W/m3

        BFE,ALL,HGEN,,%BHEATFAC%                           !APPLY THE HEAT LOADS
        TIME,TEMAG(13,1)
        LSWRITE,13

        BFE,ALL,HGEN,,0                                    !CLEAR THE BEAM HEAT LOADS
        TIME,TEMAG(14,1)                                   !SET THE TIME
        LDREAD,HGEN,,,TEMAG(14,1),,%FNAME%_EMAG,RST        !READ IN THE ELEMENT HEAT GEN RATES
        LSWRITE,14                                         !WRITE THE LOADSTEP FILE

        !--------------------------
        !PART C. STEPS 15 - 26
        !        FALLING PART OF HALF SINE-WAVE CURRENT PULSE
        !--------------------------
        KBC,0                                              !LOADS ARE TO BE RAMPED
        *DO,I,15,26,1                                      !LOOP THROUGH EACH THERMAL LOAD STEP
            TIME,TEMAG(I,1)                                !SET THE TIME
            LDREAD,HGEN,,,TEMAG(I,1),,%FNAME%_EMAG,RST     !READ IN THE ELEMENT HEAT GEN RATES
            LSWRITE,I                                      !WRITE THE LOADSTEP FILE
        *ENDDO                                             !END OF LOOP

        !--------------------------
        !PART D. STEPS 27 - 50
        !      2ND HALF SINE-PERIOD, ZERO NET CURRENT THROUGHOUT
        !--------------------------
        *DO,I,27,50,1                                      !LOOP THROUGH EACH THERMAL LOAD STEP
            TIME,TEMAG(I,1)                                !SET THE TIME
            LDREAD,HGEN,,,TEMAG(I,1),,%FNAME%_EMAG,RST     !READ IN THE ELEMENT HEAT GEN RATES
            LSWRITE,I                                      !WRITE THE LOADSTEP FILE
        *ENDDO                                             !END OF LOOP

        !--------------------------
        !PART E. STEP 51
        !PAUSE BETWEEN PULSES, ZERO NET CURRENT THROUGHOUT
        !--------------------------
        BFEDELE,ALL,HGEN
        TIME,REP
        KBC,1                                              !LOADS ARE TO BE STEPPED
        NSUB,20                                            !SOLVE IN 20 SUBSTEPS
        LSWRITE,51

!--------------------------
!CARRY OUT THERMAL SOLUTION
!--------------------------
ALLSEL                                          !SELECT EVERYTHING
FINISH
/CONFIG,NRES,10000                              !MAX NUMBER OF SUBSTEPS
/SOLU                                           !ENTER THE SOLUTION PROCESSOR
LSSOLVE,01,51                                   !NOTE: 50 STEPS IN 1 PERIOD
SAVE

!--------------------------------------------------------------------------
!STRUCTURAL ANALYSIS STARTS HERE
!--------------------------------------------------------------------------
FINISH
ALLSEL

/POST1
*GET,NSET,ACTIVE,,SET,NSET                      !GET NO. RESULTS SETS ON FILE
*DIM,TTHERM,ARRAY,NSET,1                        !DIMENSION AN ARRAY WITH 1 COLUMN

*DO,I,1,NSET,1                                  !LOOP THROUGH EACH RESULTS SET
    SET,,,,,,,,I                                !READ SET NUMBER I
    *GET,TIME,ACTIVE,,SET,TIME                  !TIME AT THIS RESULTS SET
    TTHERM(I,1)=TIME                            !STORE IN 1ST COLUMN
*ENDDO                                          !END OF LOOP

FINISH
/FILENAME,%FNAME%_STRUC,1                       !ADD A SUFFIX FOR STRUCTURAL FILENAMES

!--------------------------
```

```
!CLEAR THE THERMAL LOADS
!---------------------------
/PREP7
LSCLEAR,ALL


!---------------------------
!CHANGE ELEMENT TYPE THERM TO STRUCT
!---------------------------
/PREP7
ET,1,SOLID45                              !8-NODE BRICK STUCTURAL SOLID
ET,2,0                                    !NOT SOLVED


!---------------------------
!STRUCTURAL SYMMETRY BOUNDARY CONDITIONS
!---------------------------
!UPSTREAM END
DA,3,UZ,0                                 !END FIXED

!DOWNSTREAM END - ALLOW AXIAL EXPANSION
ASEL,S,,,5
NSLA,S,1
CP,11,UZ,ALL                             !COUPLE NODES IN AXIAL DIRECTION

!CUT FACES
DA,1,UY,0                                !ZERO THETA DISPLACEMENT
DA,6,UY,0                                !ZERO THETA DISPLACEMENT

!ON-AXIS NODES
LSEL,S,LOC,X,0
NSLL,S,1
D,ALL,UX,0                               !ZERO RADIAL DISPLACEMENT
ALLSEL


!---------------------------
!SOLVE
!---------------------------
/SOLU                                    !ENTER SOLUTION PROCESSOR
ALLSEL
ESEL,U,MAT,,2                            !UNSELECT THE AIR ELEMENTS
NSLE,S                                   !SELECT NODES ATTACHED TO ELEMENTS

        !FACTORS FOR 6TH ORDER POLYNOMIAL FIT
        C0=  0
        C1= -5.835978E6
        C2=  2.469840E11
        C3=  7.571829E14
        C4= -3.271504E18
        C5=  3.336333E21
        C6= -1.062301E24

ANTYPE,STATIC                            !STATIC ANALYSIS
NSUB,1                                   !SOLVE EACH STEP IN 1 SUBSTEP

*DO,I,1,NSET,1                                                    !LOOP THROUGH EACH STRUCTURAL LOADSTEP
        TIME,TTHERM(I,1)                                 !SET THE TIME
        LDREAD,FORC,,,TEMAG(I,1),,%FNAME%_EMAG,RST       !READ IN THE NODAL LORENTZ FORCES
        LDREAD,TEMP,,,TTHERM(I,1),,%FNAME%_THERM,RTH     !READ IN THE NODAL TEMPERATURES
SFA,5,1,PRES,0                                           !ZERO TENSILE LORENTZ FORCE

*IF,TTHERM(I,1),LE,PTIM,THEN
        TF=TTHERM(I,1)
        F0=C0*TF**0
        F1=C1*TF**1
        F2=C2*TF**2
        F3=C3*TF**3
        F4=C4*TF**4
        F5=C5*TF**5
        F6=C6*TF**6
        F=F0+F1+F2+F3+F4+F5+F6
        A=3.14159*R1**2
        P=-1*F/A
        SFA,5,1,PRES,P                  !TENSILE LORENTZ FORCE
*ENDIF

LSWRITE,I                               !WRITE THE LOADSTEP FILE
*ENDDO                                  !END OF LOOP

LSSOLVE,01,NSET                         !SOLVE THE STRUCTURAL LOADSTEPS
SAVE
```

6. Report on Task D: Beam Window

6.0 Results summary

The LBNE primary beam window must be able to withstand the thermal stresses caused by passage of a 120 GeV pulsed proton beam, in addition to a likely differential pressure of 1 bar. The main candidate materials for the window are beryllium (circumferentially water cooled) and titanium alloy (Ti-6Al-4V, double-skinned with direct helium cooling). The baseline shape for both is a partial hemisphere, 0.25 mm thick.

An extensive study has been completed to determine the limits of these materials in terms of minimum spot size and cooling requirements. Figures 6.1 and 6.2 summarise the results of ANSYS simulations (see Section 6.3) to estimate the maximum stress in beryllium and titanium alloy windows due to a single beam pulse. The graphs show the increase in stress as the beam becomes more tightly focussed (which increases the temperature rise per pulse). The red line is the design stress limit for beam windows used by Fermilab [1], which is half the ultimate tensile stress. Section 6.8 discusses whether this design stress is too conservative and Appendix 6.2 discusses the design stress in relation to pressure vessel codes.
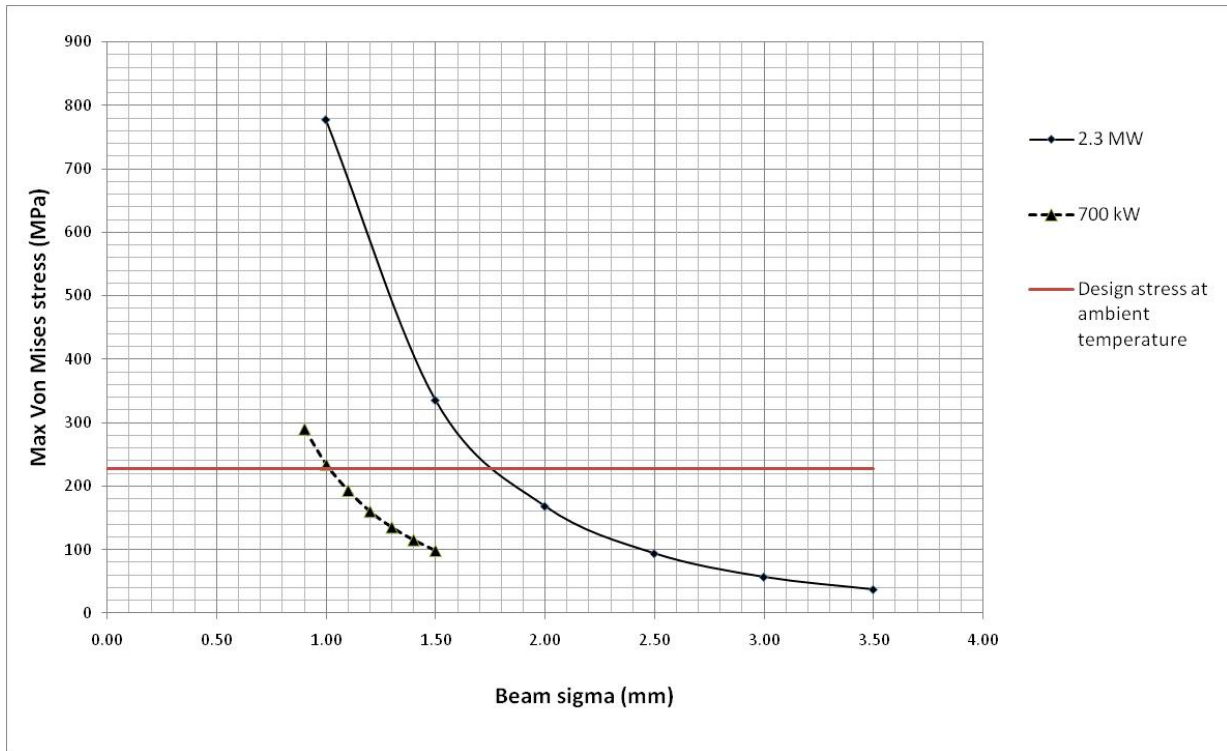

Figure 6.1 Summary of simulated stress in a 0.25 mm thick beryllium window subjected to a 120 GeV pulsed proton beam of varying size

From Figure 6.1 it can be seen that, according to the stated Fermilab criterion, the minimum tolerable beam sigma size for a beryllium window at 700 kW is around 1.1 mm, whilst for 2.3 MW it is about 1.8 mm. The temperature jump per pulse in beryllium for these cases is of the order of 100°C, and the material returns to ambient temperature between pulses, so temperature

164

dependent properties are no so significant. Due to the high thermal conductivity of beryllium, circumferential water cooling is sufficient in all cases.
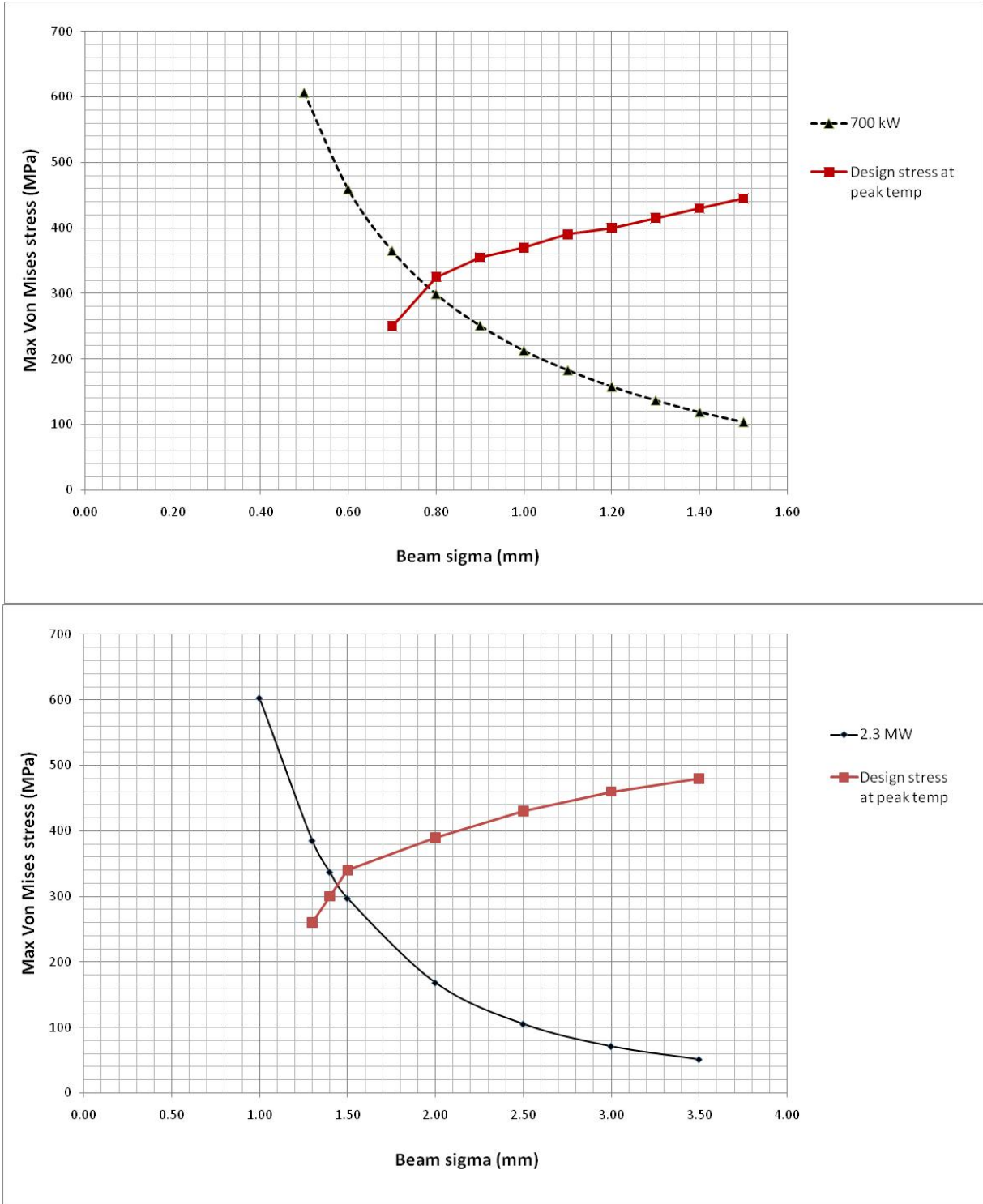

Figure 6.2 Summary of simulated stress in a 0.25 mm thick titanium alloy window subjected to a 120 GeV pulsed proton beam of varying size (2.3 MW and 700 kW cases)

The temperature rise per pulse for titanium is much greater, and the thermal conductivity much worse, so the design strength must take temperature effects into account [2]. Figure 6.2 shows how the maximum stress in a titanium alloy window increases with a decreasing spot size. For 700 kW the absolute minimum beam sigma is 0.8 mm, whilst for 2.3 MW it is 1.5 mm. The temperature jump per pulse in these cases, however, is around 500 K and high velocity gaseous helium cooling (or equivalent) would be required to prevent such a window from melting.

Sections 6.1-6.6 outline the stress analysis of the LBNE beam window in more detail.

6.1 Overview and specification

Task D: *Conceptual design of a proton beam window for the same beam parameters as Task A, including time-averaged power removal, thermal stress and shock wave studies. Initial window "clear" aperture diameter shall be 50 mm. In addition to the ideal case of incident beam centered on the window, the case of accidental, off-axis incident proton beam (limited to 1-5 pulses) anywhere in the "clear" aperture area that presents the greatest threat to window survivability shall be evaluated.*

Given that beryllium windows have already been successfully used in the NuMI facility at Fermilab, this is an obvious starting point for investigation. However, the titanium alloy Ti-6Al-4V offers certain advantages over beryllium, particular in relation to its ability to withstand thermal shock, so will also be a candidate. It was the intention to study the beryllium alloy AlBeMet, but initial simulations suggest it offers little advantage over beryllium (see Section 6.4 for details). The material properties of the two materials are similar and the stress and temperature results for beryllium can be assumed to be of a comparable magnitude for AlBeMet. A decision to use AlBeMet would be influenced by other factors. However, this beryllium alloy has had less exposure to the radiation environment of a proton accelerator compared with pure beryllium. So AlBeMet may be more of a risky choice until comprehensive radiation damage data has been gathered.

Table 6.1: LBNE beam parameters for use with the design study

Proton Beam Energy (GeV)	Protons per Pulse	Repetition Period (sec)	Proton Beam Power (MW)	Beam sigma, radius (mm)
120	4.9e13	1.33	0.7	1.2-1.5
120	1.6e14	1.33	2.3	1.5-3.5
Bunch length (nano-sec)	Bunch spacing (nano-sec)	Bunches per Pulse	Protons per Bunch	Pulse length (micro-sec)
2-5	18.8	519	1.1e11 (3.1e11 for 2.3 MW)	9.78

Table 6.1 shows the likely beam parameters for LBNE. FLUKA simulations have been carried out to obtain the energy deposited.

Taking beryllium as a baseline, the conceptual design study of the beam window is divided into the following tasks.

1. Separate analysis of the pressure stresses – ignoring beam heating – to determine viable shapes and thickness for the window (see Appendix 6.1).
2. Determine the minimum permissible beam size for 700 kW and 2.3 MW operation.
3. A study of the stress waves generated in the window due to one pulse, including an investigation of the effect of pulse structure to determine if there is a potential for elevated stress in the window due to resonance effects.
4. Combined pressure and transient thermal simulations over multiple pulses.
5. Required cooling.
6. Effect of an off-centre beam.
7. Titanium alloy and AlBeMet as alternative beam window materials.

NOTE: This analysis has focussed on the 120 GeV beam as this is seen as the most likely option. For 60 GeV the stress and temperature rise per pulse is slightly less (around 10%) [3], but the average power deposited is almost double due to increase beam frequency thus making cooling requirements slightly more challenging.

6.2 Beam parameters and associated heat loads

The particle deposition code FLUKA has been used to determine energy deposition in a 1 mm thick beryllium window [3]. A Gaussian approximation of the FLUKA data has been used for simplicity in ANSYS and in all simulations the energy deposition in the z (though-thickness) direction has been assumed constant. For titanium alloy and AlBeMet simulations the energy deposition is assumed to scale by density. The FLUKA simulations were run for 2.3 MW and the energy deposition for 700 kW is obtained by scaling by the number of protons per pulse. Bunch spacing, length and beam frequency are assumed to be the same.

For a thin beam window or foil the lack of a shower build up means that energy deposition for a variety of beam sigmas can be estimated by a manipulation of the Gaussian function, assuming that the total energy deposited is constant. This is outlined in the following derivation and has been verified by a comparison with FLUKA results for a variety of beam sigmas, as shown in Figure 6.3.

Assume a Gaussian energy deposition profile where A is the peak energy deposition:

$$E = Ae^{-r^2/2\sigma^2}$$

Total energy deposited within a radius, *rmax* per unit depth through the window is:

$$A \int_0^{2\pi} \int_0^{rmax} \theta r e^{-r^2/2\sigma^2} dr d\theta \quad = \quad -2A\pi\sigma^2(e^{-rmax^2/2\sigma^2} - 1)$$

If we assume that the total energy deposited is independent of beam sigma, approximately correct for a thin beam window then:

$$A\sigma^2(e^{-rmax^2/2\sigma^2} - 1) = \text{constant}$$

If *rmax* is large (rmax>3sigma) i.e. want the total energy absorbed in the thin window then the above simplifies to:

$$A\sigma^2 = constant$$

If for example we know that for a thin beryllium window with 120 GeV protons the peak energy deposition is 0.012 GeV/cc/primary when the beam sigma is 2 mm then we can calculate the constant as 4.8e-8. Using the constant you can then calculate the peak energy deposition as a function of beam sigma.
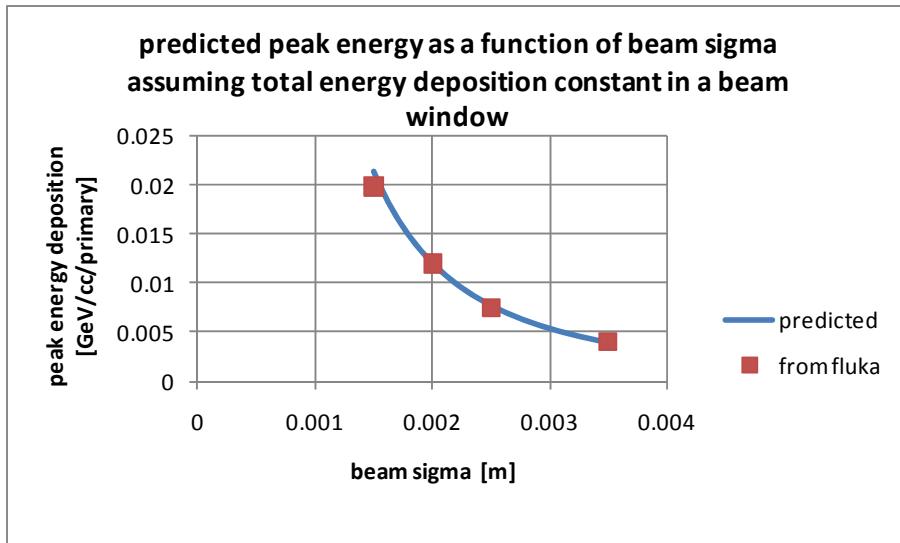
predicted peak energy as a function of beam sigma assuming total energy deposition constant in a beam window

Figure 6.3 Agreement between predicted energy depositions from FLUKA and interpolated by manipulation of the Gaussian function [3]

ANSYS Multiphysics V.11 has been used in all simulations. An axisymmetric approximation has been made in the first instance as the computing cost of a full 3D model would be excessive, especially for stress wave simulations. A full 3D model was required, however, to study the effect of an off-centre beam been (Section 6.3.6).

Figure 6.4 shows a typical model setup with various options for cooling.
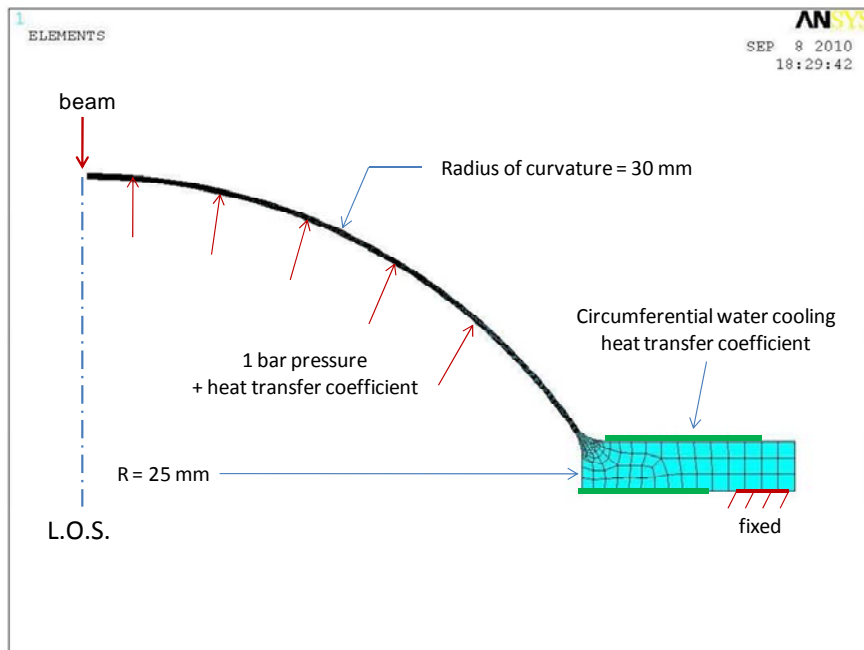
Figure 6.4 ANSYS model setup

6.3 Beryllium window

6.3.1 Overview of Results for beryllium window

The relationship between energy deposition and beam sigma derived in Section 6.2 has been used to produce the two curves in Figure 6.5, which show the peak energy deposition as a function of beam sigma for 2.3 MW and 700 kW beams.
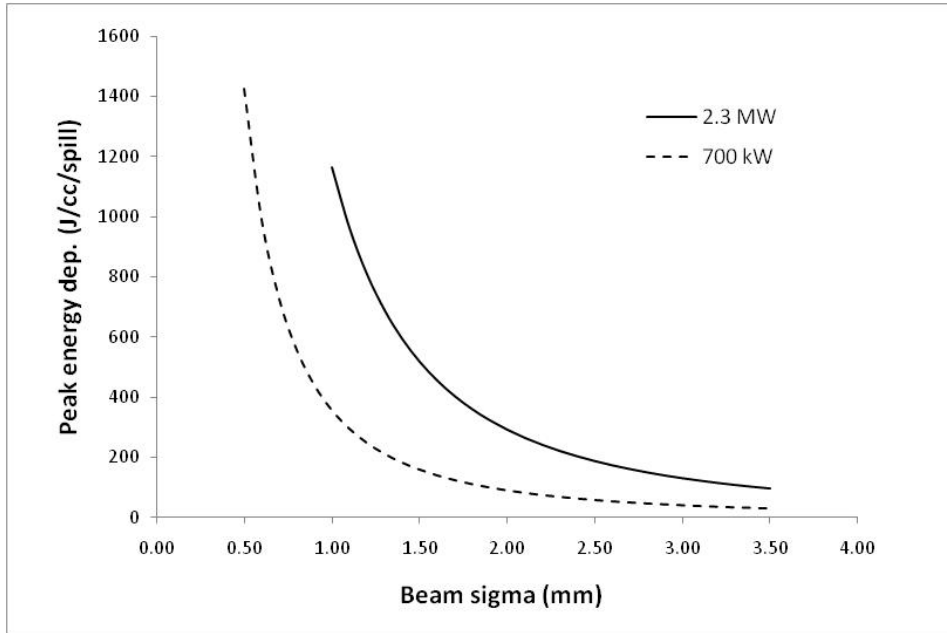

Figure 6.5 Peak energy deposition in beryllium windows for a 120 GeV beam with varying beam size

From this energy deposition data the approximate temperature rise per pulse (Figure 6.6) can be derived using the equation below. This graph, however, does not take into account temperature dependent properties and so will slightly overestimate the peak temperatures.

$$\Delta T = \frac{Peak\_energy\_density}{Material\_density \times specific\_heat\_capcity}$$
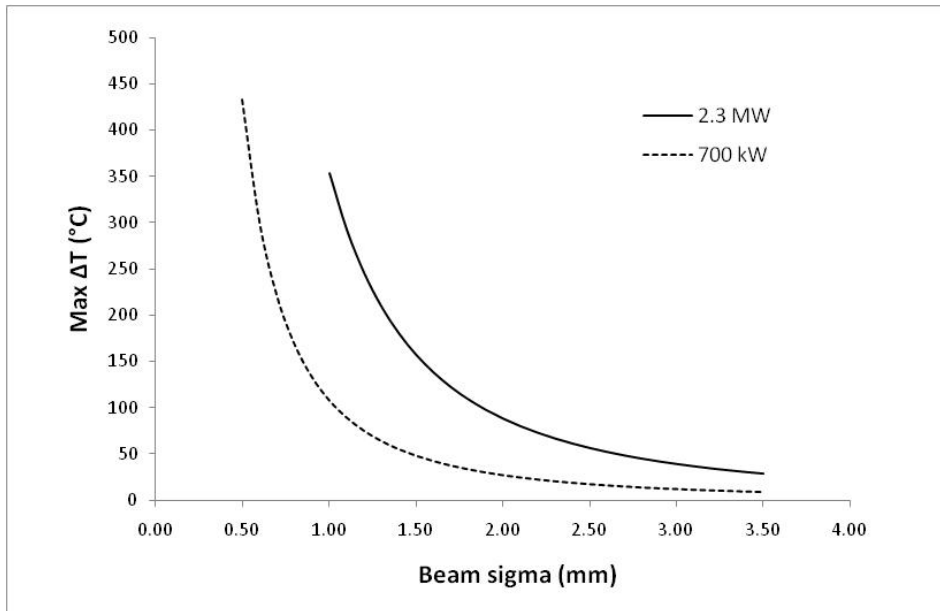
Figure 6.6 Temperature rise per pulse in beryllium windows for a 120 GeV beam as a function of beam size

A design stress criterion of half the Ultimate Tensile Stress (UTS) is used for beam windows in Fermilab [1]. This can be used to estimate a minimum permissible beam spot size for various combinations of beam power, energy, and window material. The ITER Material Properties Handbook [4] gives beryllium a room temperature UTS of 454 MPa, giving a design stress of 227 MPa.
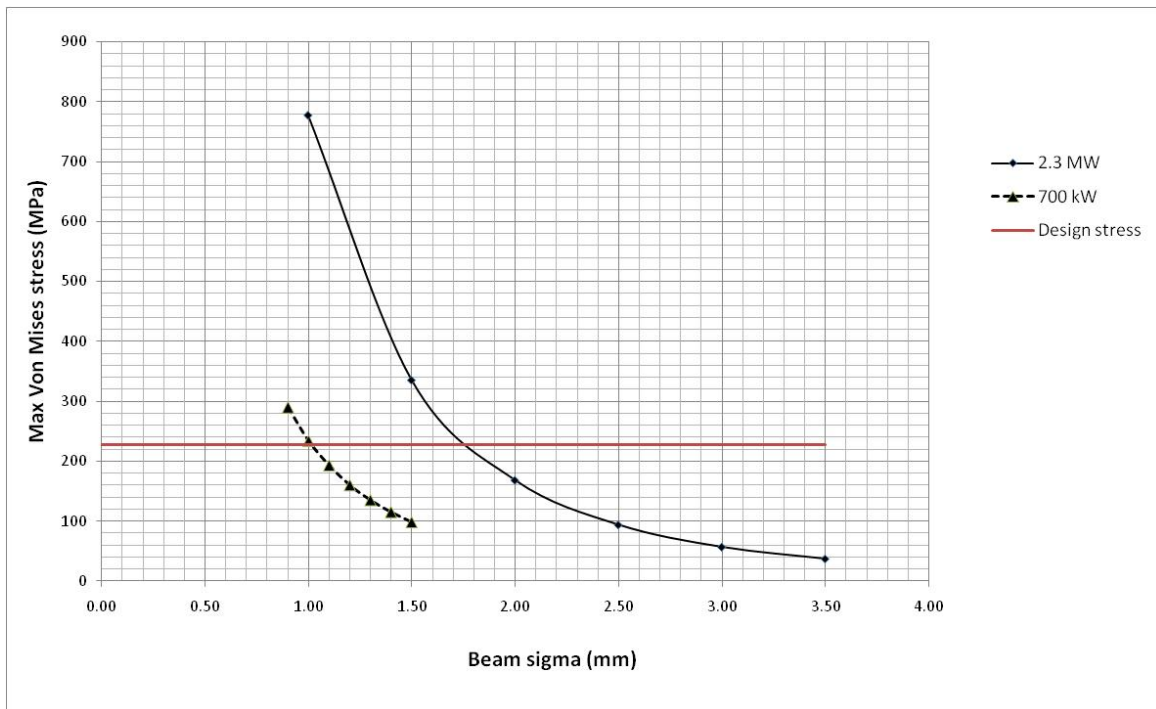

Figure 6.7 Relationship between spot size and maximum stress due to single 120 GeV beam pulse in a 0.25 mm thick half hemispherical window

Figure 6.7 shows ANSYS simulation results for peak stress due to a single pulse in a 0.25 mm thick beryllium window for a variety of beam profiles. This gives an indication of the minimum spot size in both the 2.3 MW and 700 kW cases.

If we also allow for a small reduction in strength of beryllium at the peak temperature of around 130°C, as shown in Figure 6.8, the minimum beam sigmas for 700 kW and 2.3 MW are 1.1 mm and 1.8 mm respectively.
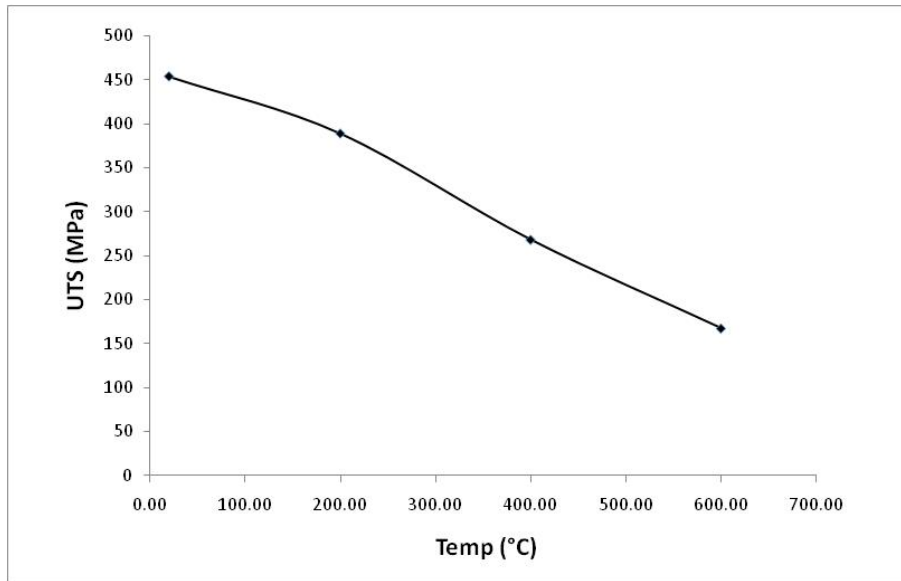

Figure 6.8 Reduction in the ultimate tensile strength of beryllium with increasing temperature [4]

6.3.2 Stress analysis overview

The LBNE beam window will have three types of stress to cope with, each of which operates on a different timescale. First of all, there is the constant background stress due to pressure, though this can be minimised by choosing the correct shape and thickness (see Appendix 6.1). Then there is the quasi-static stress caused by the initial compression of the window material, which is relieved between pulses as it is cooled and expands. Figure 6.9 shows how a hemispherical shaped window will deform upon beam heating following the initial compressive stress.
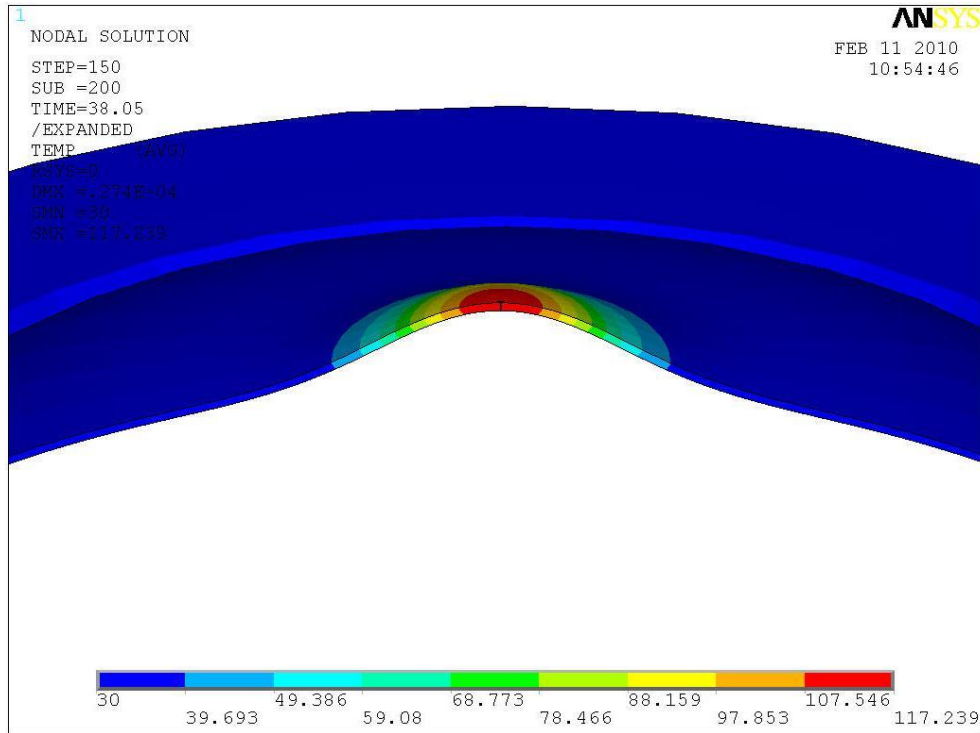

Figure 6.9 Slice through the centre of an ANSYS model showing heat rise and deformation due to the LBNE proton beam

The third type of stress experienced by the window is a dynamic component of stress that arises due to the short pulsed nature of the beam and is most significant on the timescale of microseconds. These elastic stress waves are an extra factor on top of the quasi-static stress and the magnitude of the stress waves will depend on the shortness of the beam pulse in relation to the beam spot size. If the pulse length is shorter than the time it takes a sound wave to traverse the beam spot then the dynamic stress will be maximal. If the pulse length is longer than this then the dynamic component will be reduced by some ratio between the two times [5].

Due to the different timescales involved, which makes it very difficult to study all phenomena together in ANSYS, the quasi-static thermal stress and elastic stress waves have been examined in separate simulations.

6.3.3 Elastic stress waves generated due to one pulse

Before looking at the magnitude of the stress waves generated in the window, this next section examines the effect of geometry on the generation of stress waves and how certain combinations of pulses structure and window thickness can result in an elevated stress.

A note on 'stress resonance':

The 9.78 µs LBNE beam pulse is made up of 519 micro-bunches. Certain combinations of material geometry and pulse structure can result in a type of 'stress resonance' occurring. This is when stress waves produced by individual bunches constructively interfere with one another. In beam windows this can give rise to larger through-thickness, longitudinal stress waves (those that reflect between inner and outer surfaces) than would otherwise occur.

Consider a flat window of thickness t. Upon interaction with a short proton pulse, tensile waves will initiate at either surface, travel to the opposite surface, and be reflected as compressive wave. And this continues until the stress waves dissipate. The worst case scenario then for stress resonance is when the bunch spacing is equal to two times the duration it takes a wave to travel from one surface to another, i.e. when:

Bunch spacing = 2t/c

Where c is the speed of sound in the material.

For beryllium the thickness to avoid is 0.124 mm (this is similar for AlBeMet, whilst the worst thickness for titanium alloy is 60 microns). Figure 6.10 shows how stress waves would develop over the first 20 (of the 519) bunches in a window of this thickness.
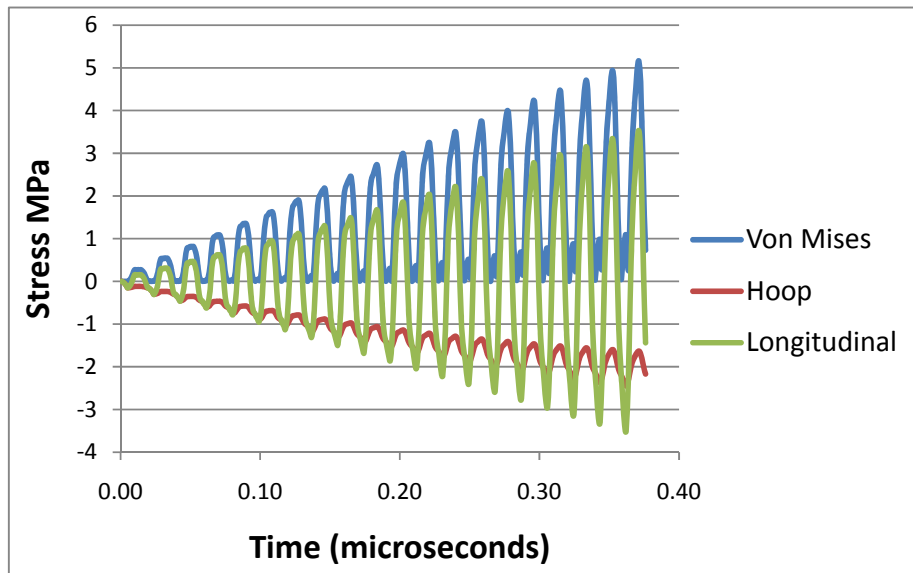

Figure 6.10 Stress resonance in a beryllium window of thickness 0.1244 mm

Whereas Figure 6.11 shows what happens if you double the thickness. The through thickness stress waves cancel out and become negligible and the equivalent Von Mises stress reduces accordingly. One must still worry about radial stresses, however.
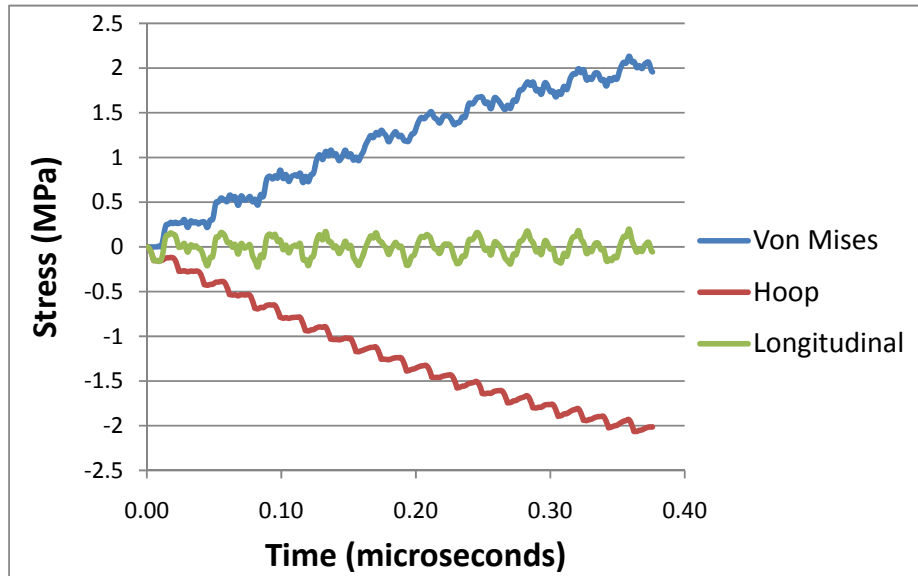

Figure 6.11 Stress waves developing in a 0.2488 mm thick beryllium window

Due to strength requirements to withstand the differential pressure, a beryllium window is likely to be thicker than 0.1244 mm anyway. Lesser resonant stress peaks will occur at thicknesses less than 0.124 mm, so as long as the window is thicker than, say, 0.15 mm, there are no concerns regarding stress peaks in the beryllium beam window. This calculation would need to be repeated if changes to the pulse structure are made.

A study of stress waves resulting due to one pulse:

Each one of the 519 bunches that comprise the LBNE proton pulse induces a small temperature rise and associated stress waves in the window material. However, the stress waves from each of these bunches are negligibly small and can be ignored unless they positively interfere with one another – as in the case of the 0.1244 mm window. For the purposes of these simulations then, it is reasonable to assume an averaged heat load over the 9.78 microsecond pulse and discount the fact that it is actually the result of 519 individual bunches. This has been verified by comparing simulation results in the case of averaged heat load with a simulation of the full 519 pulses and they produce identical results.

Figure 6.12 shows the maximum stress on the surfaces a 0.25 mm thick beryllium window following the passage of the LBNE proton beam (700 kW, 1.1 mm beam sigma case), whilst Figure 6.13 shows the component stresses at mid-plane. A temperature jump of 79°C causes a peak stress of 193 MPa. This would give a safety factor of 2 on the UTS of beryllium, taking temperature effects into account. Referring back to Figure 6.7, a larger beam will result in a lower peak stress.
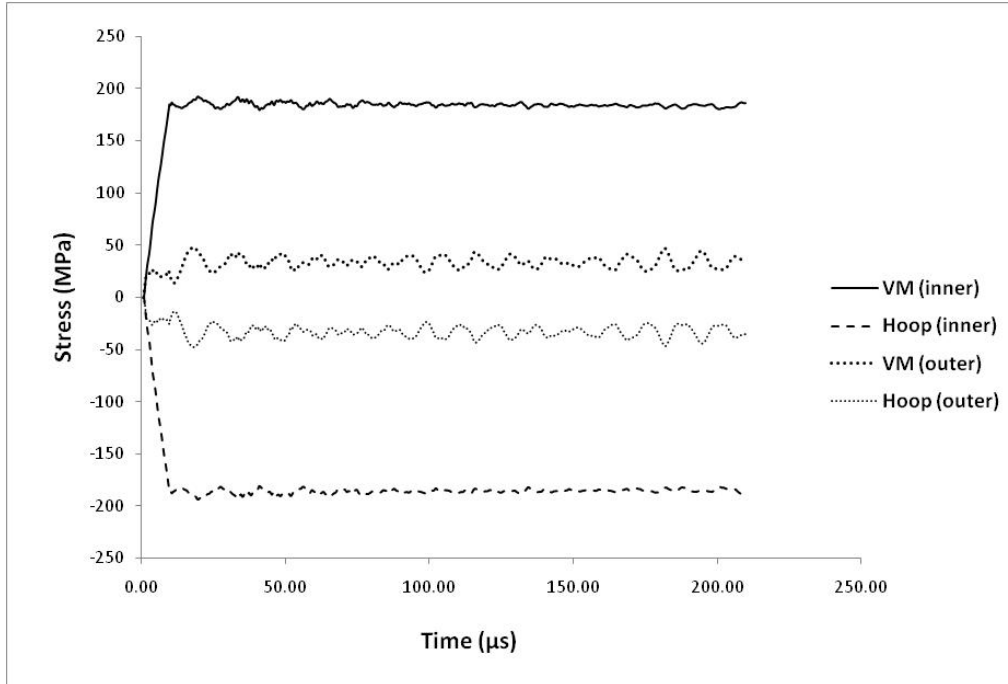
Figure 6.12 Component surface stresses in a 0.25 mm thick beryllium window subjected to a 120 GeV 700 kW beam (1.1 mm beam sigma)
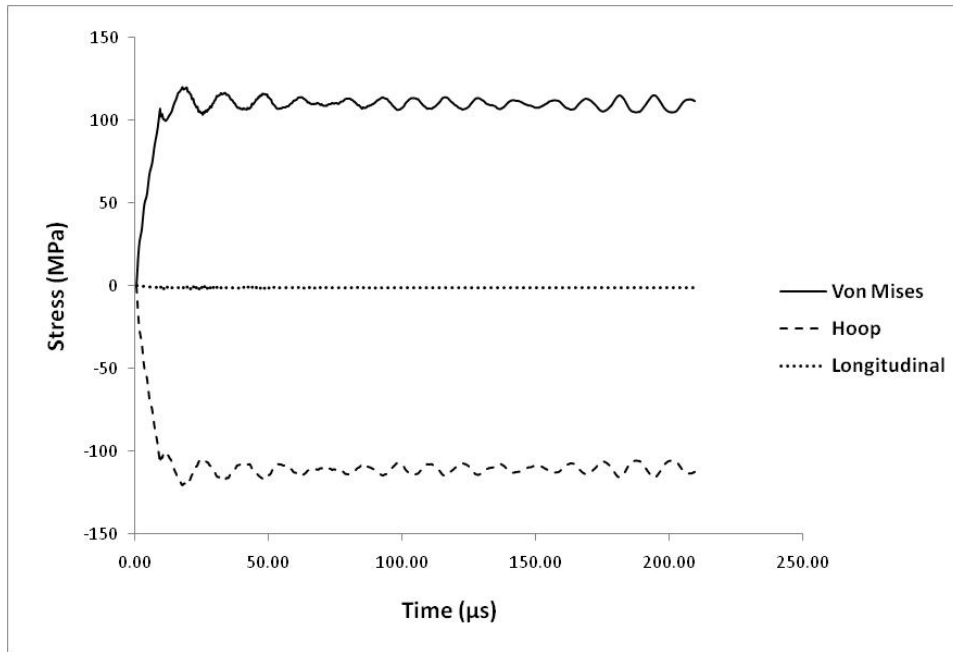

Figure 6.13 Component stresses at mid-plane of a 0.25 mm thick beryllium window subjected to a 120 GeV 700 kW beam (1.1 mm beam sigma)

The relatively long duration of the LBNE beam compared with the acoustic transit time means that the dynamic component of stress is quite small, perhaps on 5% of the total in this case

(though it will also depend on the spot size). The peak stress therefore is mainly due to pure compression upon heating. Figure 6.14 shows the surface displacement at beam centre during and after a single pulse.
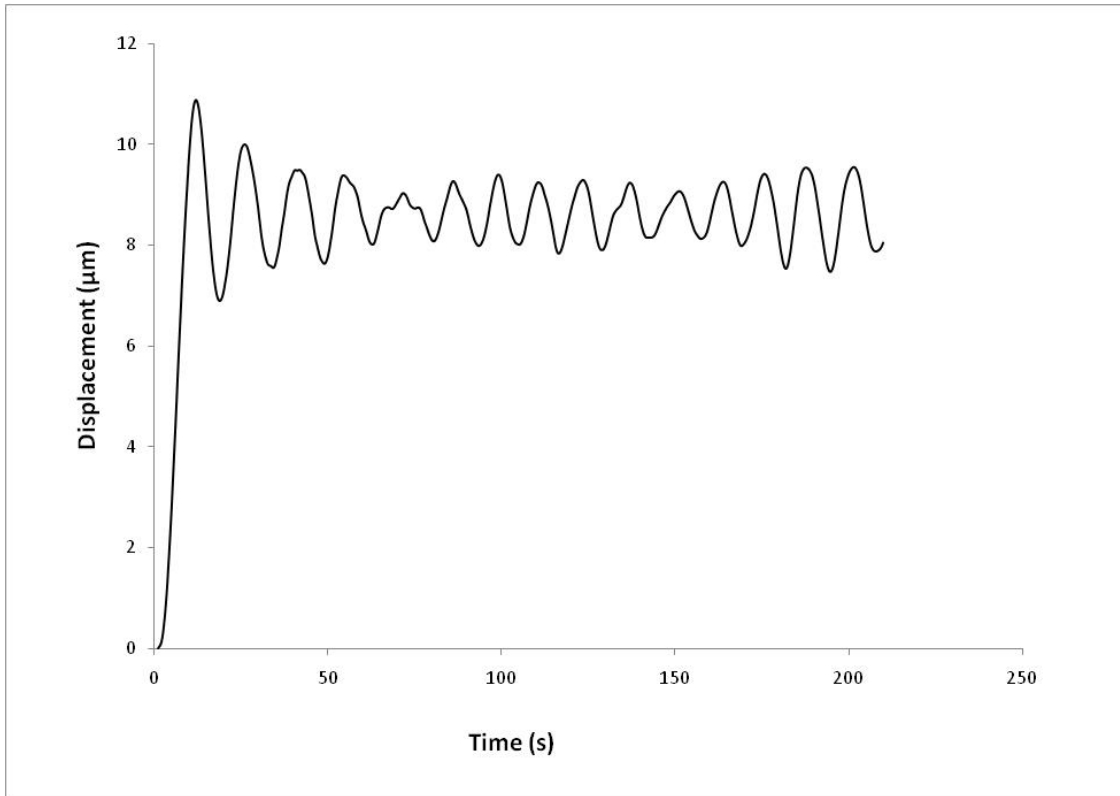

Figure 6.14 Surface displacement at beam centre due to a 700 kW beam (1.1 mm beam sigma)

6.3.4 Transient thermal stress over many pulses

Figure 6.15 shows the peak quasi-static stress in a 0.25 mm beryllium window over eight pulses, whilst Figure 6.16 shows the surface displacement. A peak compressive stress of 178 MPa occurs on the internal edge of the window.
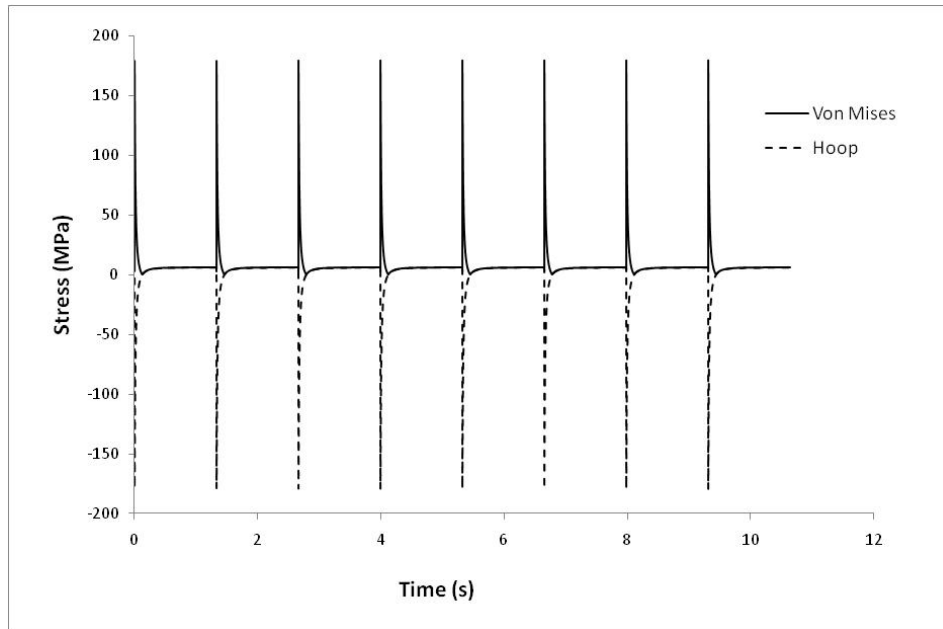

Figure 6.15 Transient thermal stress over on the internal surface of a 0.25 mm thick beryllium beam window interacting with a 700 kW beam (1.1 mm sigma)
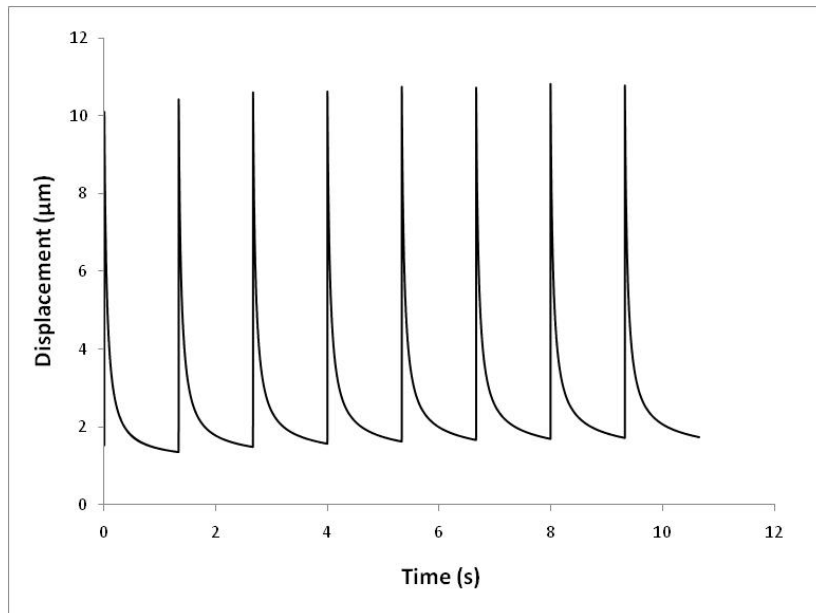

Figure 6.16 Displacement of the internal surface, at beam centre, of a 0.25 mm thick beryllium beam window interacting with a 700 kW beam (1.1 mm sigma)

Thinner domed beam windows can result in a lower peak quasi-static stress if they are optimised so that the beam pulse acts to partially relieve tension created by the pressure force. This effect, however, was found to be reduced for smaller, tighter beams. In fact, it was almost

negligible for the 1.5 mm case or smaller. Changing the window geometry for the smaller beams to give it a conical shape or a tighter radius of curvature may improve its ability to accommodate the large temperature fluctuations. A small reduction in stress occurs when the curvature of the beam window is reduced because it makes the shape more conducive to thermal expansion.

6.3.5 Cooling requirements

Beryllium has many properties that make it a desirable beam window material. Its low density means that energy absorption – and associated heat rise – is relatively small; whilst its high thermal conductivity allowed a NuMI window to operate without any forced convection or water cooling.

To test whether this would still be the case for LBNE beam parameters, a thermal transient simulation was run for a 0.25 mm thick beryllium window assuming only ambient air cooling on the internal edge (10 W/m^2.K). Figure 6.17 shows the temperature at beam centre over many pulses and this is shown to stabilise at a peak of 110°C, whilst the minimum between pulses is only 5°C above the starting temperature of 30°C. This suggests that a 0.25 mm beryllium window could be used for the 700 kW beam without any active cooling.
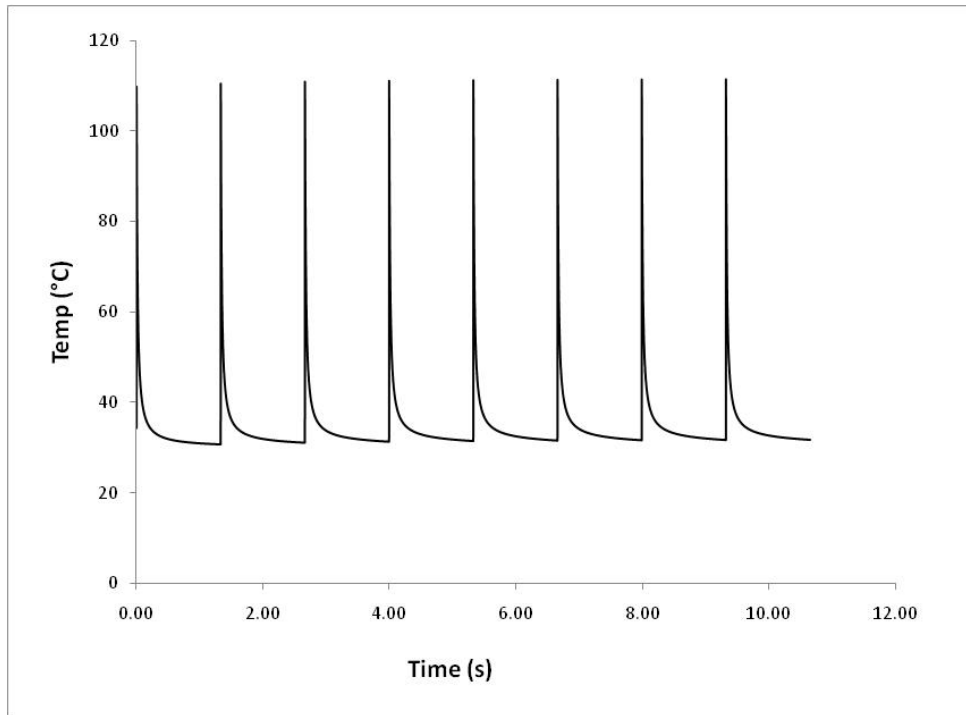

Figure 6.17 Temperature at centre of a 0.25 mm beryllium window with no active cooling (just air on internal side, 10 W/m^2.K) when interacting with a 700 kW beam with a beam sigma of 1.1 mm

However, simulations suggest cooling may be beneficial for a beryllium window for LBNE at 2.3 MW. Figure 6.18 shows the results of a combined static-transient thermal simulation (using plane77 axisymmetric elements). The first timestep simulates the average heat load, discounting beam pulsing, to find the equilibrium temperature; then 10 pulses have subsequently been simulated in the normal transient manner to find the ultimate peak temperature of 187°C. Water cooling around the circumference a beryllium window is an effective way to substantially reduce this peak temperature, as shown in Figure 6.19.
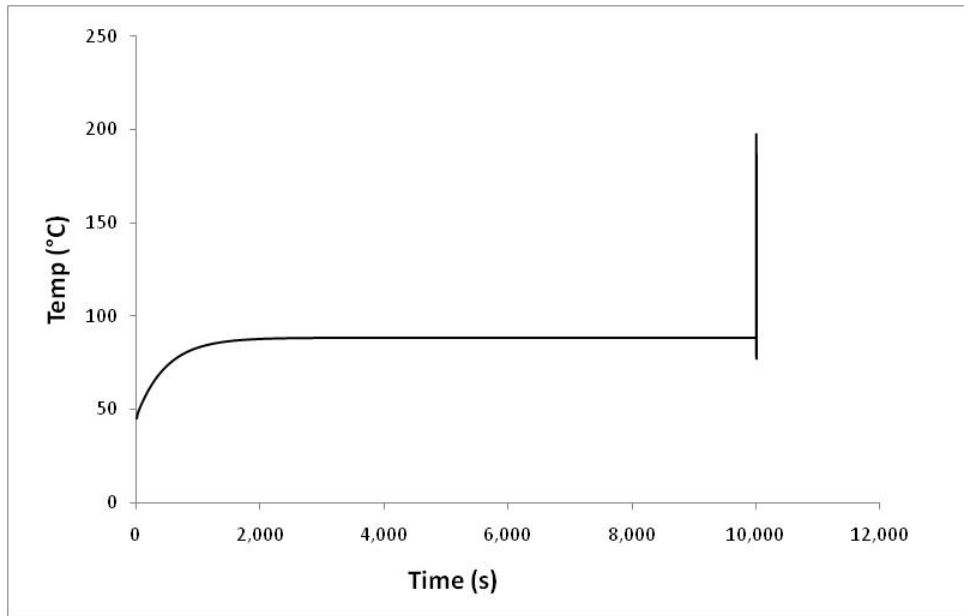
Figure 6.18 0.25 mm thick beryllium window 2 MW no cooling

Figure 6.19 shows that with 30°C flowing water applied to the circumference of the window, the temperature stabilises with a peak of around 132°C – a 55°C reduction on ambient cooling alone. For the 60 GeV beam case, where the frequency and average heat load are almost doubled, water cooling would certainly be necessary at 2 MW. However, these results are generated using a simple ANSYS model with an assumed constant heat transfer coefficient on the surface. A more thorough cooling analysis would be required when the LBNE beam window design is in a more advanced stage.
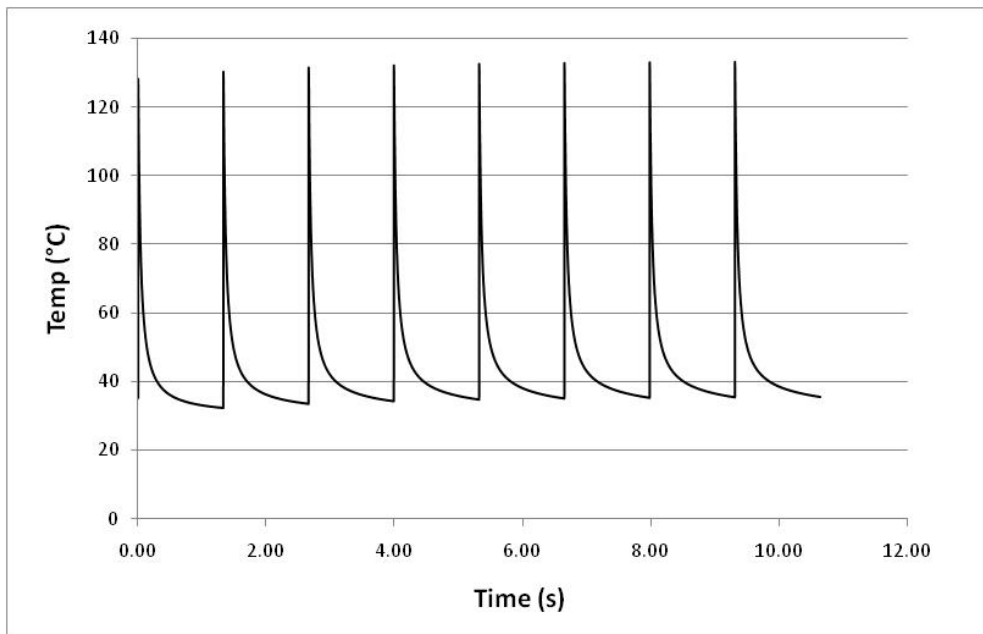

Figure 6.19 Temperature at centre of a 0.25 mm beryllium window with active water cooling on the periphery (assumed 1000 W/m².K plus air on internal surface at 10 W/m².K)

6.3.6 Effect of an off-centre beam

All window studies up to this point have looked at the situation of the proton beam striking the geometric centre of the partial hemisphere. This is because all models have been axi-symmetric to save computational cost and it's not possible to study an off-axis beam in this setup. To investigate the consequences of an off-centre beam, two 3D half-symmetrical models have been created: ANSYS AUTODYN has been used to study the stress waves resulting from one off-centre pulse; whilst a thermal-structural transient model was created using ANSYS Classic to study the quasi-static and longer term transient stresses resulting from multiple off-centre beam pulses. In both cases a simplified half-hemispherical shape has been used for ease of meshing (Figure 6.20 below).
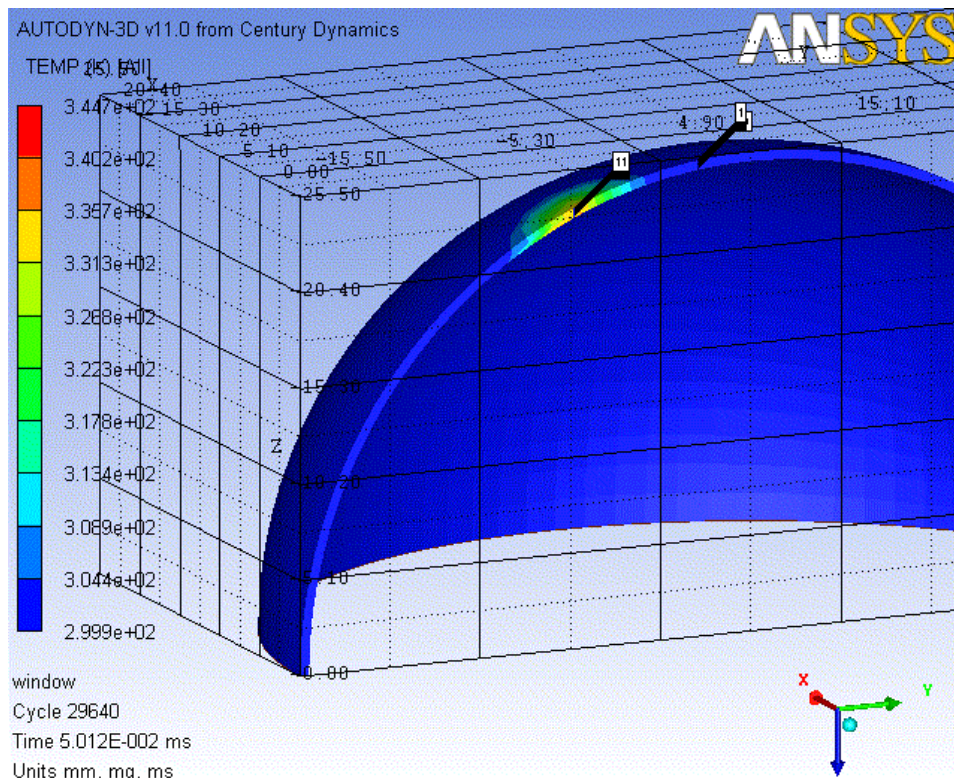

Figure 6.20 Temperature results from an off-centre beam simulation in AUTODYN

Figure 6.21 shows ANSYS AUTODYN results for the stress generated in a beryllium window when a single beam pulse strikes the geometric centre of the hemisphere and compares this with three off-centre beams – 3mm, 10mm and 15mm. There is very little difference between the results and it is likely that the small discrepancies are due to differences in the model mesh at these points, rather than any real effect.

Figure 6.22 shows the ANSYS Classic axisymmetric results for the same beam parameters as in Figure 6.21. The results agree reasonably well, although the magnitude of the stress in the ANSYS Classic results is around 5-10% higher. This may be due to a difference in the material properties used in ANSYS Classic, which were manually written into the model script and taken from the ITER Material Properties Handbook [4], and those used in AUTODYN, which are taken automatically from a material library that is written into the software.
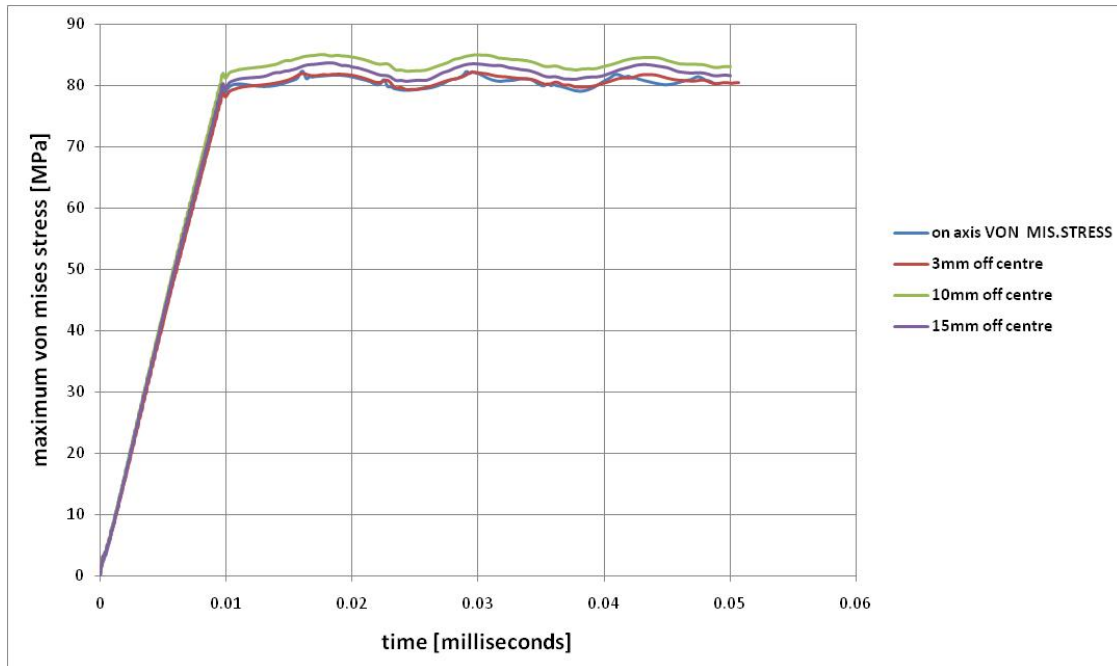
Figure 6.21 ANSYS AUTODYN results for stress in a 0.25 mm beryllium window for a central and various off-centre beams (700 kW, 1.5 mm beam sigma)
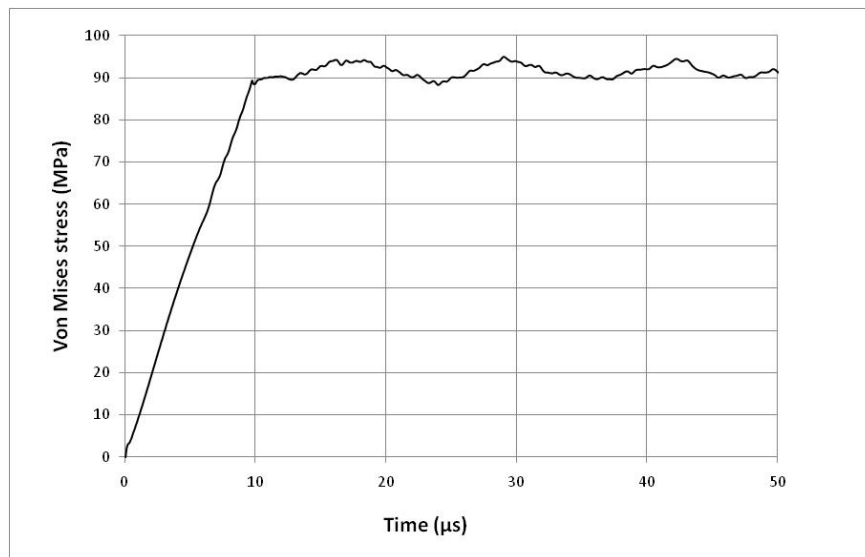

Figure 6.22 2D axisymmetric ANSYS Classic (Multiphysics, coupled-field elements) results for the same beam profile as Figure 6.21

The ANSYS Classic results derived using a three dimensional model shown in Figure 6.23 also seem to suggest that a hemispherical shaped window is quite resilient to an off-centre beam. In this case five beam pulses (1.1 mm sigma) were simulated to strike window centre then five more beam pulses strike 15 mm off-centre. In this case, again, the maximum stress due to the off-centre beam is almost identical as that generated due to an on-centre beam.

184
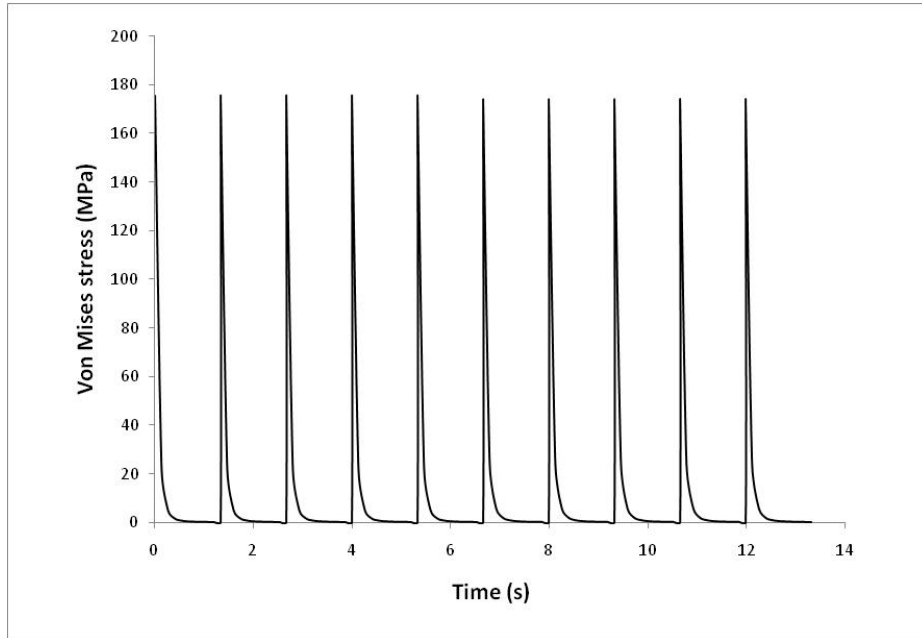
Figure 6.23 3D transient results for 5 central pulses then 5 pulses 15 mm off centre (1.1 mm sigma)

In both these models the window was modelled as a simple hemisphere with no constraints other than the mass of surrounding material and the maximum stress was measured at beam centre. It's possible that a large stress could be generated due to thermal expansion if the beam was so errant as to pass through the join between the thin beam window and the thick flange. But a more detailed model would be needed to study this.

6.4 AlBeMet

Figure 6.24 shows the Von Mises stress in identically shaped beryllium and AlBeMet beam windows due to a 700 kW 1.5 mm beam pulse (whilst Figure 6.25 shows the results for multiple pulses).
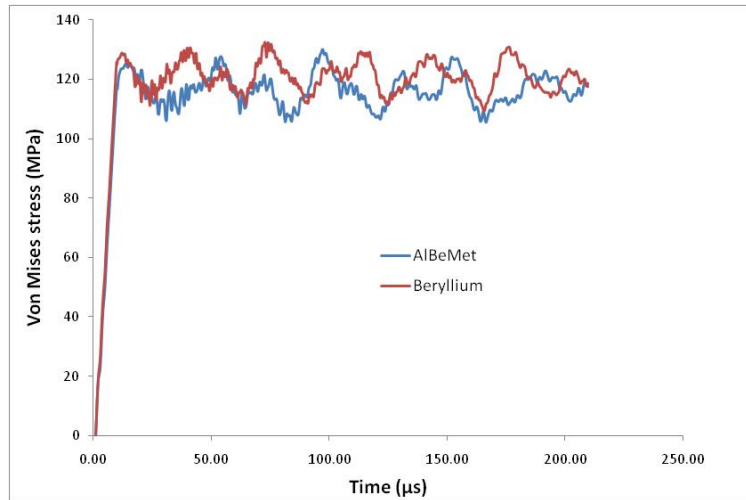

Figure 6.24 Stress in 0.25 mm thick beryllium and AlBeMet beam windows due to a 700 kW 1.5 mm beam pulse

For these two materials the peak stresses for a given beam pulse are almost identical. Although AlBeMet has a higher density and a lower specific heat capacity [6] – meaning that it has a larger temperature rise per pulse – it also has a lower Young's modulus than beryllium so the effect of the larger temperature jump on the peak stress is reduced.
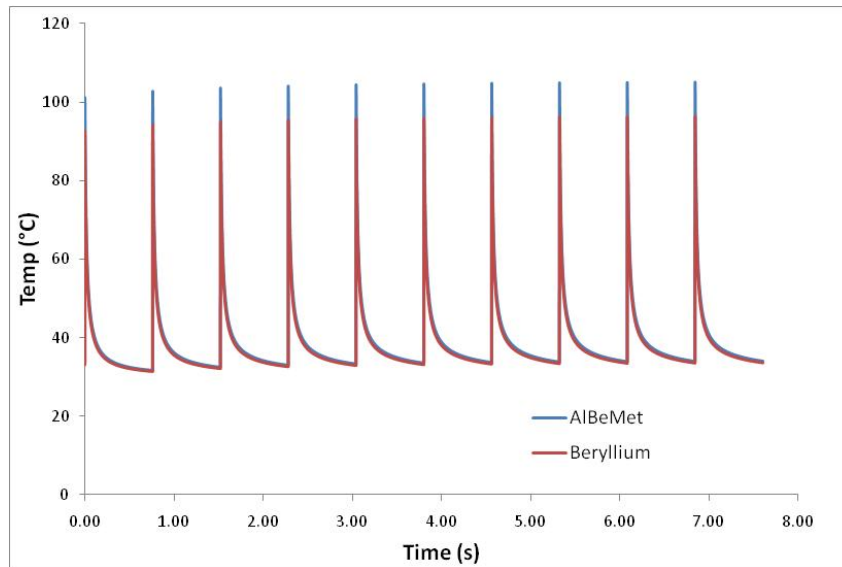

Figure 6.25 Transient temperature in 0.25 mm thick beryllium and AlBeMet beam windows due to a 700 kW, 1.5 mm beam pulse

Therefore AlBeMet seems to offer little benefit over beryllium as a beam window material for LBNE.

(NOTE: Results in this graph were obtained before a FLUKA data bug was fixed, so the stress values are slightly overestimated, but this does not change the conclusions).

6.5 Titanium alloy (Ti-6Al-4V)

6.5.1 Overview of results for titanium alloy

Figures 6.26 and 6.27 show the peak energy deposition and associated temperature rise in a titanium alloy beam window as a function of beam size. Energy deposition for titanium alloy has been scaled by density from FLUKA results for beryllium. Due to an increased density and lower specific heat capacity, the temperature rise per-pulse in titanium is estimated to be around four times greater than for beryllium given the same beam pulse.
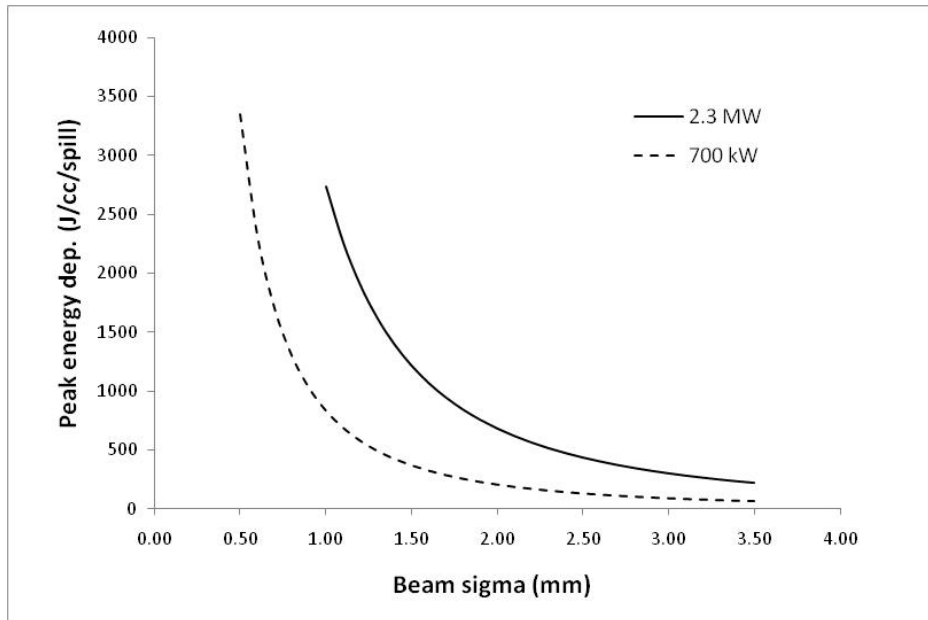
Figure 6.26 Peak energy deposition in Ti-6Al-4V windows for 120 GeV beams of varying size
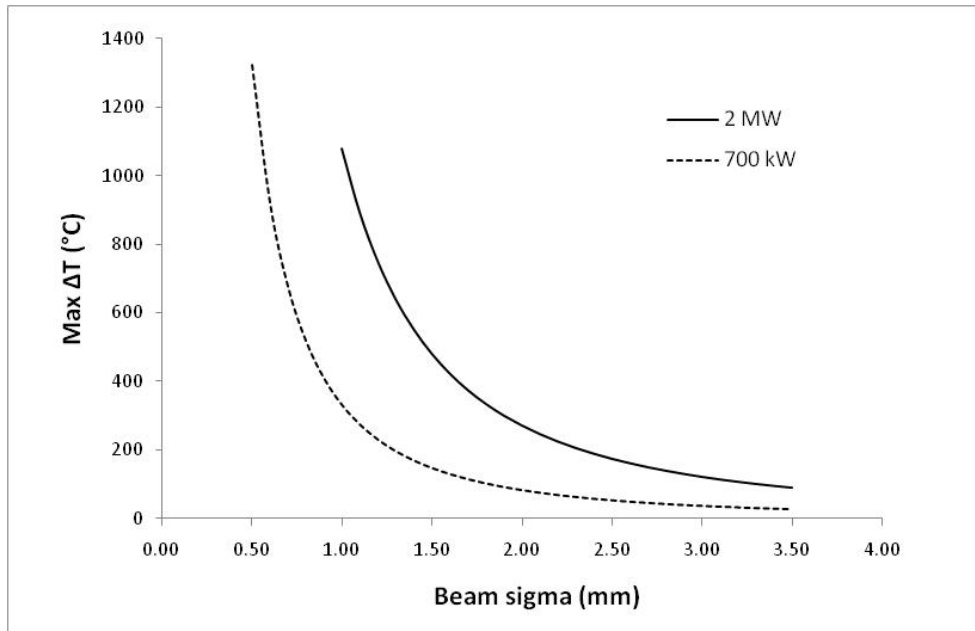
Figure 6.27 Temperature rise per pulse in Ti-6Al-4V windows for a 120 GeV beams of varying size
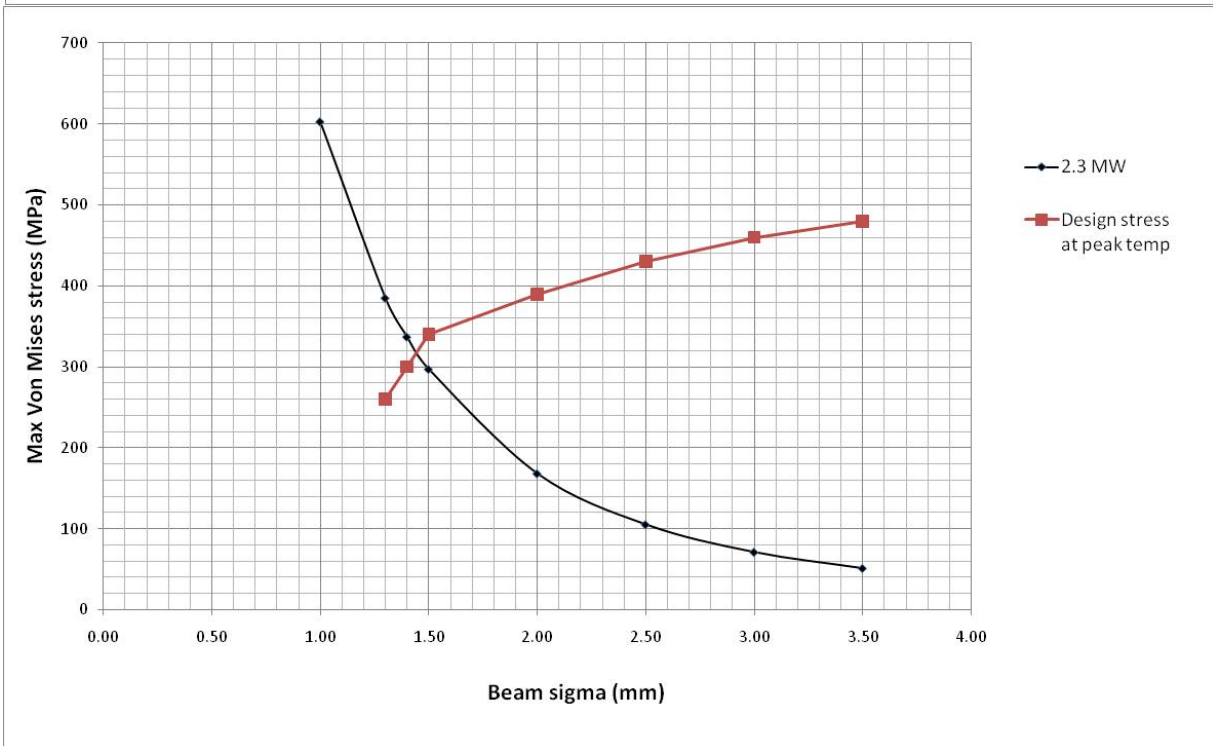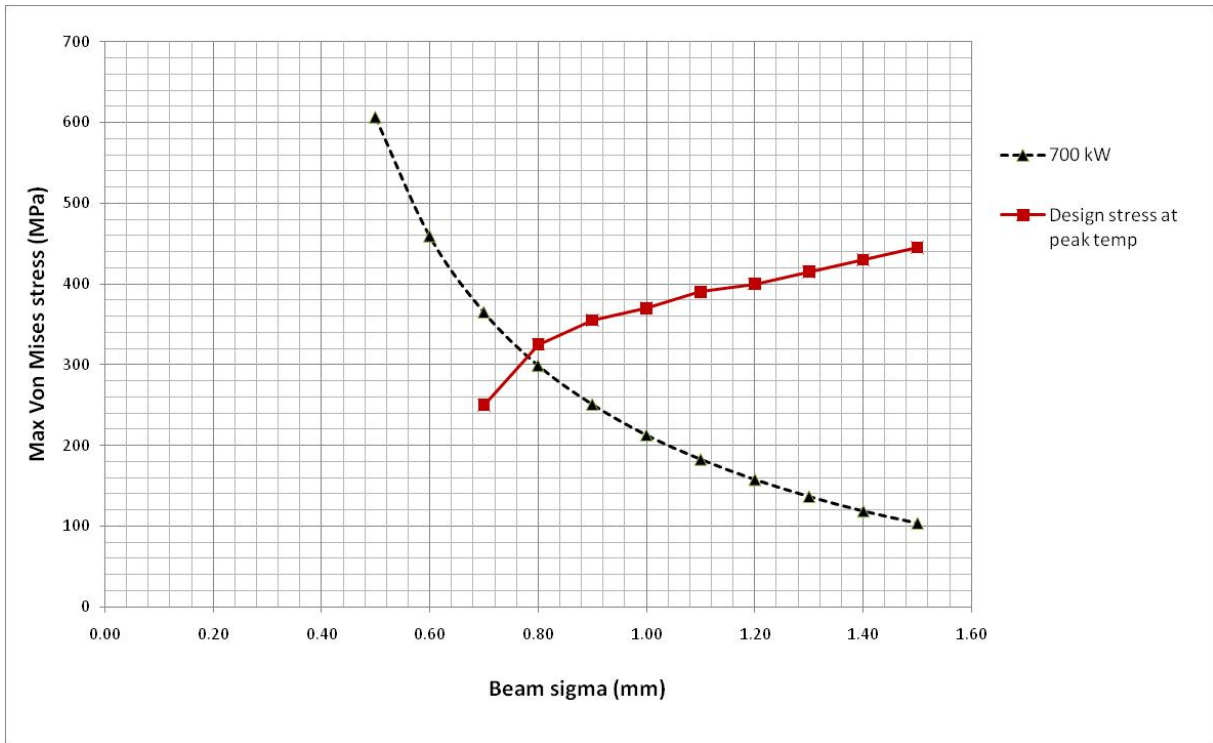
Figure 6.28 Relationship between spot size and maximum stress due to single 700 kW 120 GeV beam pulse in a 0.25 mm thick half hemispherical titanium alloy window

The graphs in Figure 6.28 summarise ANSYS simulation results for the maximum stress in a titanium alloy window subjected to various size beams with powers of 700 kW and 2.3 MW.

The design stress is plotted as a function of peak temperature for that particular beam pulse. They show that the minimum tolerable beam sigma size for 700 kW is 0.8 mm, whilst for 2.3 MW the minimum sigma is 1.5 mm.

6.5.2 Elastic stress waves generated due to one pulse

Figure 6.29 shows the Von Mises stress in a titanium alloy window resulting from the passage of a single 2.3 MW 120 GeV beam (sigma of 1.5 mm). A titanium alloy beam window therefore looks like a possible candidate for even this most extreme case.

The elastic stress waves make up a larger component of the total than for the beryllium window due to the lower sound speed in titanium alloy. Figure 6.30 shows the corresponding surface displacement.
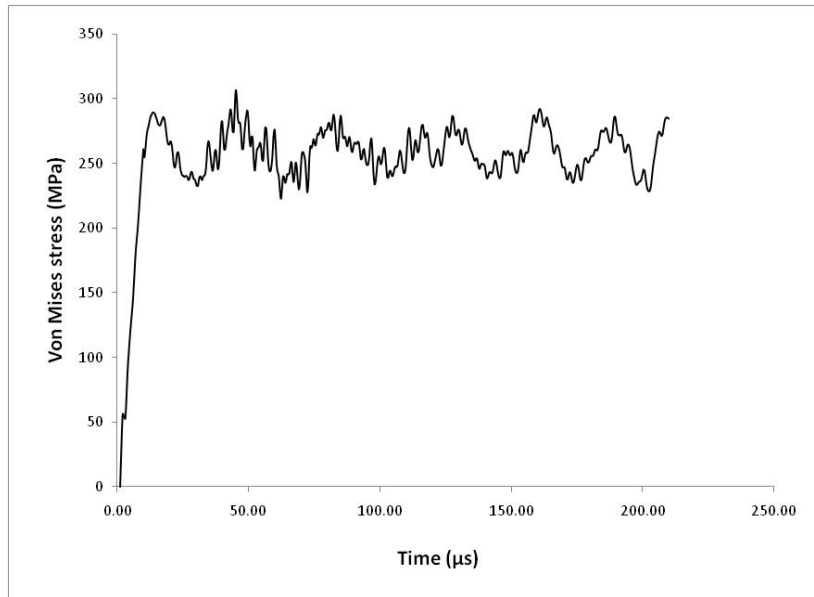
Figure 6.29 Stress in a 0.25 mm thick titanium alloy due to a single 2.3 MW beam pulse (1.5 mm sigma)
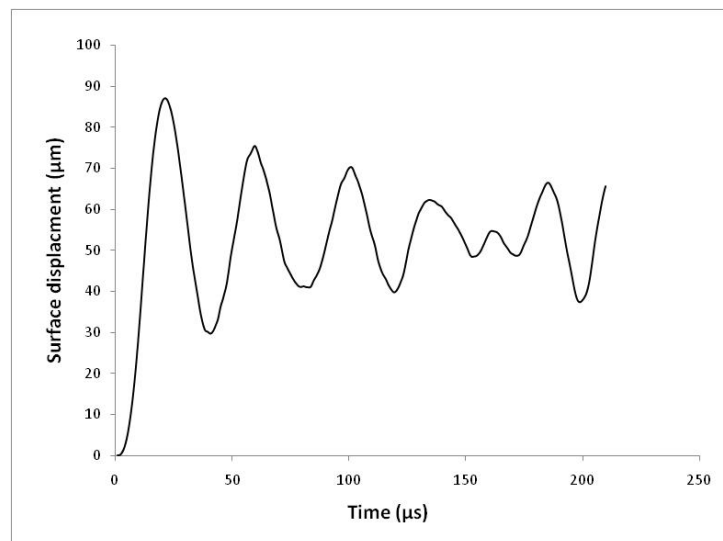
Figure 6.30 Surface displacement at window centre due to a single 2.3 MW beam pulse (1.5 mm sigma)

6.5.3 Transient thermal stress over many pulses and cooling requirement

Figure 6.31 shows the quasi-static stress peaks over multiple pulses in the case of the most extreme beam case of 2.3 MW with a sigma of 1.5 mm. The peak stress is 270 MPa.
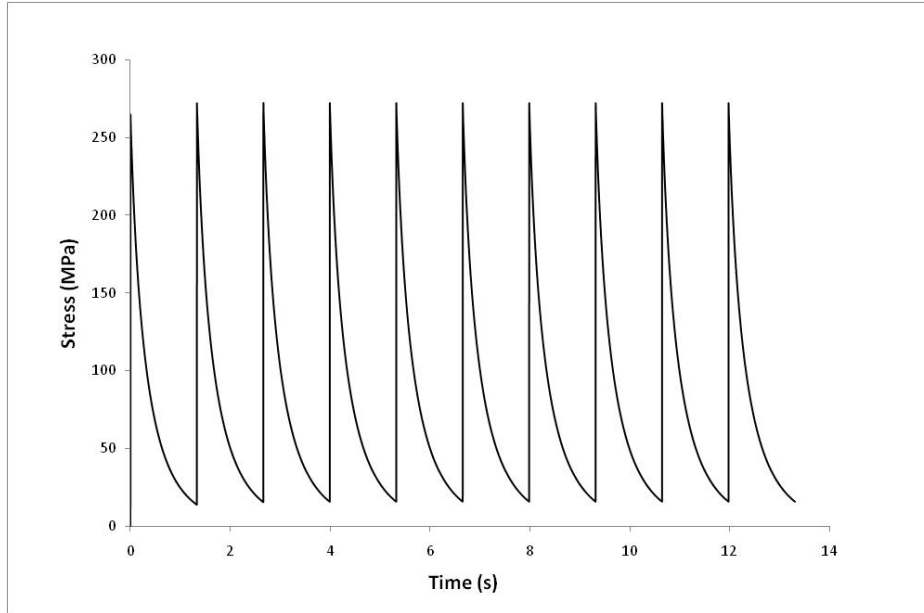
Figure 6.31 Quasi-static Von Mises stress peaks over ten 2.3 MW (1.5 mm beam sigma) pulses on the inner surface of a 0.25 mm thick titanium alloy window cooled by gaseous helium (assuming 500 W/m^2.K)

The 750 kW T2K target station beam window in J-PARC is made from titanium alloy (Ti-6Al-4V). The poor thermal conductivity of this metal – especially relative to beryllium – meant that ambient or external water cooling was not an option. A double-skinned window with helium cooling across the beam spot was required to keep the temperature to acceptable level. Should the LBNE window be made from titanium alloy this would also be the case.
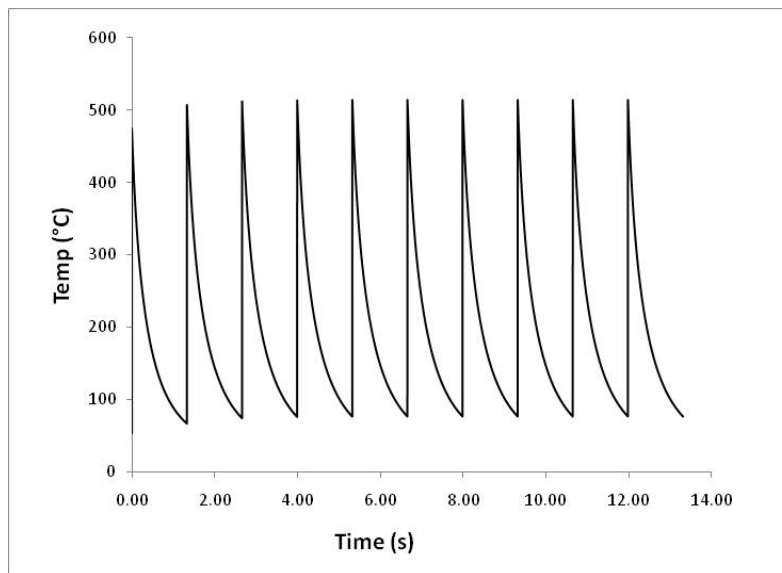
Figure 6.32 Temperature at beam centre of a 0.25 mm thick titanium alloy window subjected to a 2.3 MW (1.5 mm beam sigma) cooled by gaseous helium (assuming 500 W/m^2.K)

190

Figure 6.32 shows the peak temperature in such a 0.25 mm titanium alloy window subjected to a 2 MW 1.5 mm sigma beam. The temperature jump per pulse, at around 450°C, is very high. But the base temperature between pulses does not rise much above the starting temperature.

A double-skinned titanium alloy beam window cooled by high velocity helium gas would be an acceptable design of beam window for LBNE, even possibly in the extreme 2 MW, 1.5 mm beam sigma case. The disadvantages of this design compared with a beryllium window are: (a) the need for cooling and (b) it's a less proven material in radiation environments.

However, the large temperature jump per pulse and the difficulty in cooling the window beam spot between pulses will still present problems. The peak temperature will still be around 500°C. Figure 6.33 shows how the strength of this alloy will be lowered significantly at this temperature.

Figure 6.33 Reduction in strength with temperature of the titanium alloy Ti-6Al-4V [7]

6.6 Is the design stress too conservative?

The P-bar target at Fermilab has a beryllium cover that is thought to have experienced per-pulse energy densities exceeding 1000 J/cc [8]. Simple elastic stress simulations demonstrate that a single pulse of such intensity would induce a thermal stress in excess of the tensile strength of beryllium.

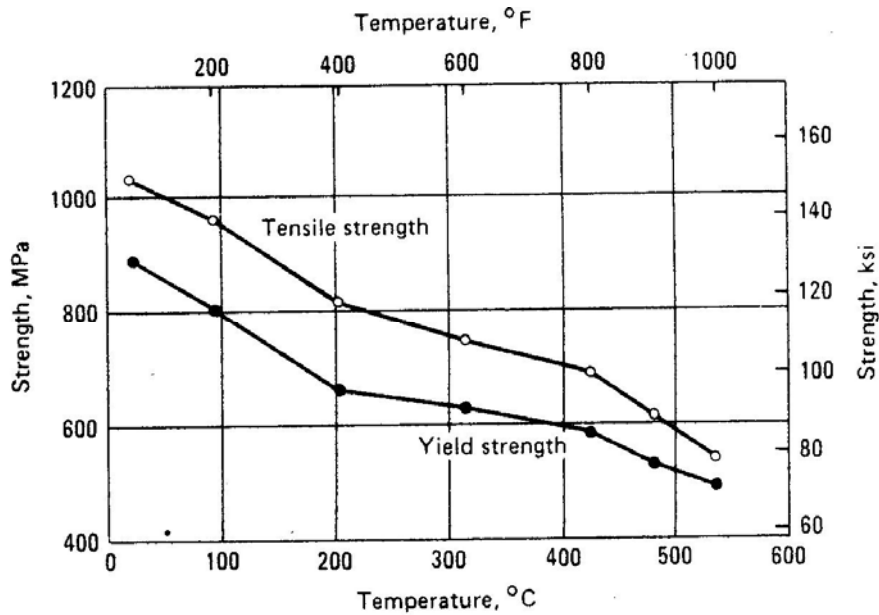However, plastic deformation in the beryllium may allow the window to survive such intense beams. If the initial beam pulse creates a plastic strain region at the centre window that leaves a residual tensile stress then each subsequent pulse needs to exceed this tensile stress before it induces a compressive stress in the material, thus allowing the beam window to survive more intense pulses than one might assume from a simple elastic analysis.

To study this effect, an elastic-plastic ANSYS model has been created. This simulation uses a bi-linear stress-strain curve, as illustrated in Figure 6.34, for beryllium to take account of plastic deformation when the yield strength is exceeded. The yield and ultimate tensile strengths and the elastic modulus have been taken from the ITER Material Properties Handbook (273 and 452 MPA) [4] and the yield strain has been calculated to be 8.8E-4.
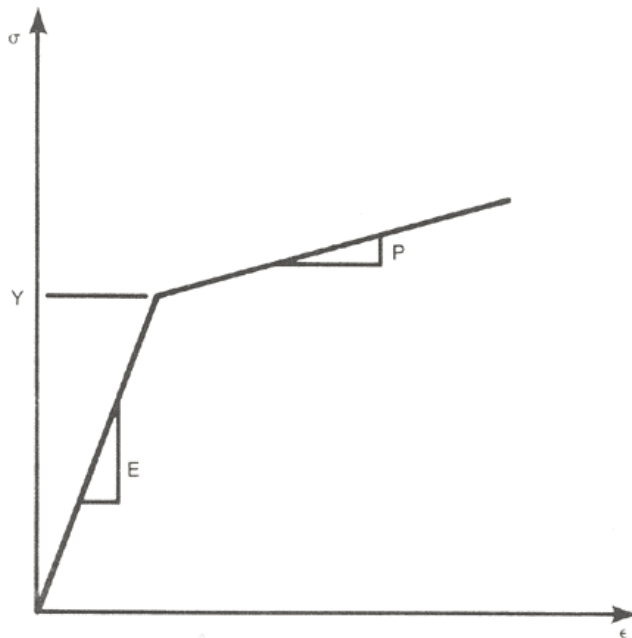
Figure 6.34 Bi-linear stress-strain curve

Figure 6.35 shows the residual hoop stress in a flat 0.5 mm thick flat beryllium window after 10 pulses with a peak intensity of 1000 J/cc. The plastic deformation leaves a tensile region in the centre surrounded circumferentially by a compressive region. The majority of the plastic deformation occurs during the first pulse and leaves a 256 MPa residual tensile stress that reduces the magnitude of the compressive stress generated in each subsequent pulse, as shown in figure 6.36 and 6.37.

Figure 6.35 Residual hoop stress in a beryllium window due to plastic deformation following a 1000 J/cc intensity beam

Figure 6.36 Plastic strain at beam centre over first 10 pulses
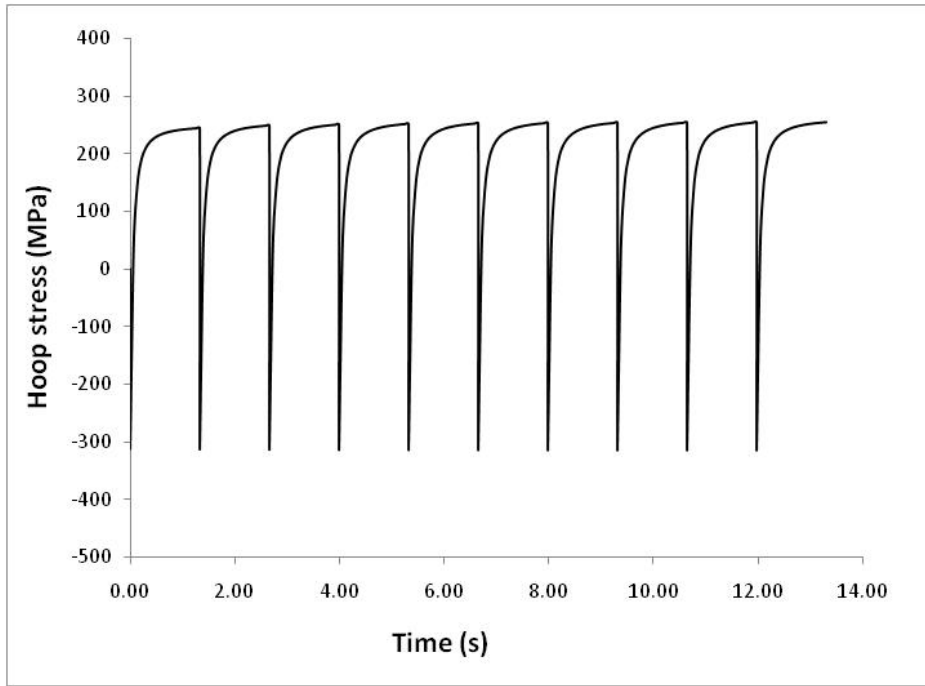
Figure 6.37 Hoop stress at beam centre (accounting for elastic and plastic stress/strain)

Figure 6.38 shows how a much larger compressive stress is induced in the window if plastic effects are not taken into account.
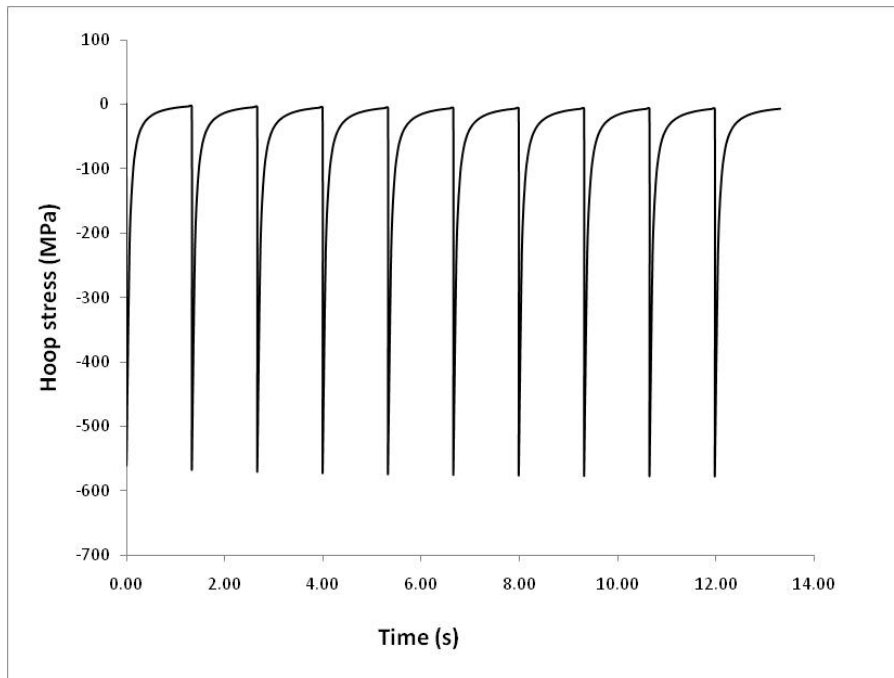
Figure 6.38 Hoop stress at beam centre (elastic only)

So a beryllium window or target may be capable of withstanding very high intensity beams without failure. However, one would be reluctant to recommend this as the baseline design for such a facility without extensive verification tests. An off-centre beam, for example, could be catastrophic for such a design due to the fact that the compression due to the beam could then be compounding the plastic compressive stress surrounding the tensile region. The stress field would no longer be isotropic and large shear stresses could be induced in the material resulting in failure.

6.7 Results summary and conclusions

- A beryllium window with circumferential water cooling could be an acceptable design for the LBNE window for 700 kW (larger than 1.1 mm beam sigma) and 2.3 MW (larger than 1.8 mm beam sigma). Forgoing water cooling and using only natural convection cooling to air may even be sufficient for 700 kW.

Beam window for 700 kW operation

- For 700 kW beam power operation at 120 or 60 GeV, a single partial hemispherical skin of pure beryllium is the recommended material for any beam size greater than a beam sigma of 1.1 mm. Water cooling at the external circumference is recommended, although natural convection cooling may be sufficient. The beryllium could be replaced with AlBeMet, however the alloy offers little benefit and raises the question of radiation damage resistance, so is not recommended.
- Titanium alloy Ti-6Al-4V would offer a slightly increased safety factor compared with beryllium for the same beam size, however its relatively poor thermal conductivity means it would require direct gas cooling (for which only helium has been considered) between two thin skins, in a design similar to that used for T2K.

Beam window for 2 – 2.3 MW operation

- For 2 – 2.3 MW operation at 120 or 60 GeV, a single partial hemispherical skin of pure beryllium is the recommended material for any beam size greater than a beam sigma of 1.8 mm. Water cooling at the external circumference is recommended. It may be possible to reduce the beam size if plastic deformation and consequent 'shakedown' for the first few beam pulses can be tolerated, although the consequences of a window failure would have to be carefully considered.

- A double skinned helium cooled titanium alloy Ti-6Al-4V beam window may permit a reduction in beam sigma to 1.5 mm with the material remaining within the elastic region. However there would need to be a study of the cooling to ensure sufficiently low temperatures can be achieved for the required material properties.

6.8 References

1. *FESHM Chapter 5033.1 – Vacuum Window Safety (2004).* Fermilab safety document.

2. US Department of Transport (2003). *Metallic Materials Properties Development and Standardisation Handbook.* Office of Aviation Research, Washington, D.C.

3. Davenne, T. STFC Rutherford Appleton Laboratory. *Personal Communication.*

4. ITER Material Properties Handbook (1997).

5. N. Simos, H. Kirk, K. McDonald, M. Cates, J. Tsai, D. Beshears, B. Riemer, C. Finfock, R. Prigl, K. Brown, S. Kahn and H. Ludewig. *Thermal Shock Induced by a 24 GeV Proton Beam in the Test Windows of the Muon Collider Experiment E951 – Test Results and Theoretical Predictions*. Brookhaven National Laboratory, Upton, NY 11973, USA

6. Brush Wellman Inc. *AlBeMet 162 Material Properties.*

7. American Society for Metals. *Metals handbook. Volume 2. Properties and selection: nonferrous alloys and pure metals.* Ninth edition.

8. Hurh, P. Fermilab National Accelerator Laboratory. *LBNE 2+ MW Target R&D Overview for NBI 2010*. Neutrino Beams and Instrumentation conference 2010, Tokai, Japan.

9. Young, W.C. (1989) *Roark's Formula's for Stress and Strain*. Sixth edition. McGraw-Hill.

Appendix 6.1 – Stress due to pressure alone

Figure 6.39 shows the stress induced in a flat window of diameter 50 mm (which is the required window aperture) with varying thicknesses under a pressure load of one atmosphere. The stress is calculated using the equation below [9], which assumes a flat circular disc with a clamped periphery.
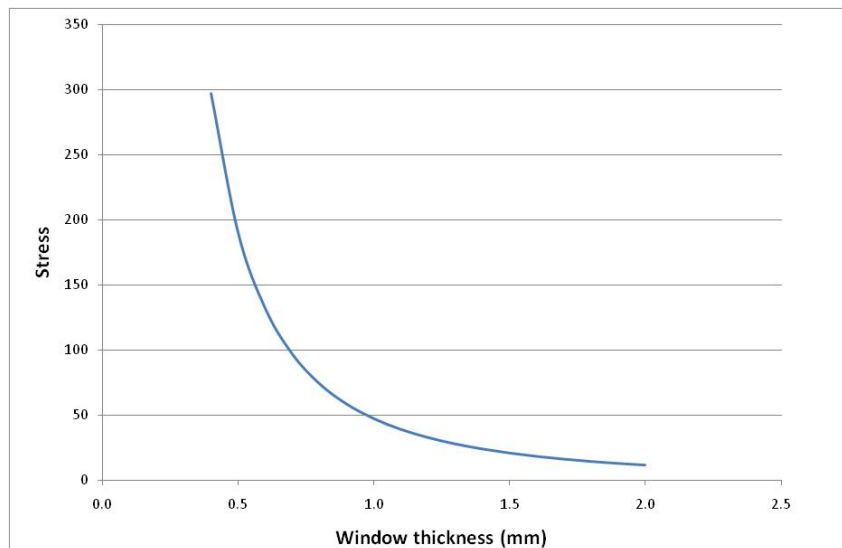
Figure 6.39 Stress in a flat circular plate with a clamped periphery when subject to a pressure force of 1 bar

Pressure (bending) stress in a flat plate with clamped periphery = $3Pr^2/4h^2$

Where: P is pressure
              r is the plate radius
              h is the thickness

Assuming the material is beryllium, it shows that even to meet the Fermilab beam window stress criterion (of half the ultimate tensile strength) on pressure stresses alone requires a thickness of over 0.5 mm. As thermal stresses will increase with window thickness, this makes a flat window an undesirable choice. Also, a flat window, although easy to manufacture, is not a desirable shape for accommodating thermal expansion due to beam heating.

A partial hemisphere shape has therefore been adopted as the baseline. Stresses in windows of varying curvature and thickness are showed in Figure 6.40, calculated using the equation below. All window simulations assume with a radius of curvature of 30 mm and a thickness of 0.25 mm. The only variables that change, in terms of the window structure, are the thickness and the material.

Figure 6.40 Stress in partially hemispheres (with an outer diameter of 50mm) of varying thickness and radii of curvature (R)

Pressure stress in a partial hemisphere = PR/2h

Where: *R* is radius of curvature

Appendix 6.2 – Discussion of the Vacuum Window Design Stress
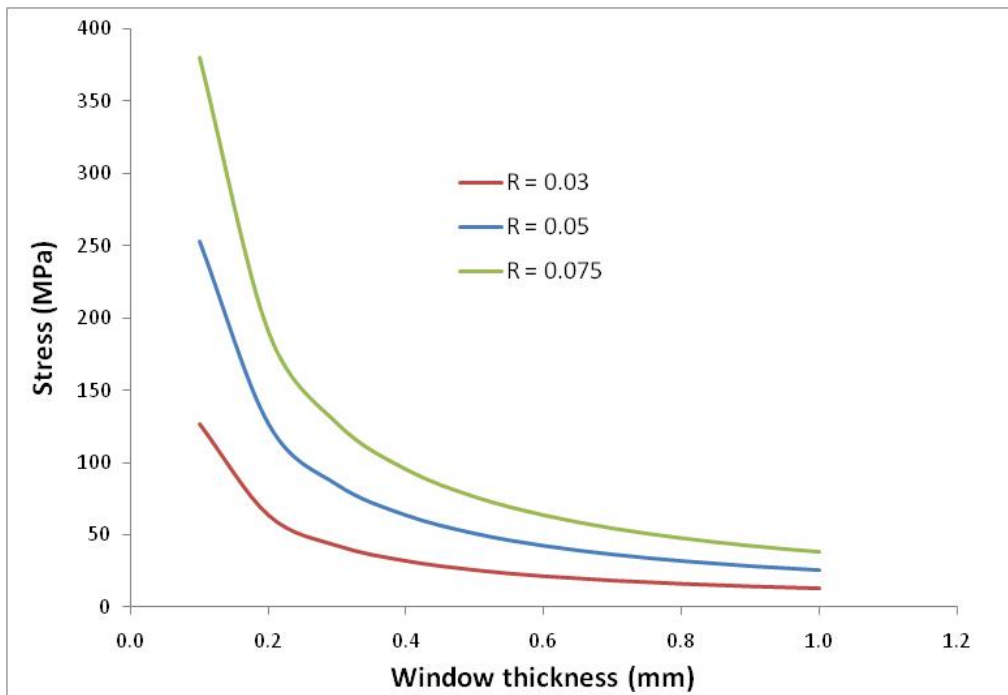
All vacuum windows used at Fermilab should be designed in accordance with the ASME Boiler and Pressure Vessel Code. Whilst the Fermilab Vacuum Window Safety document states that: "In addition to vacuum loading, window design shall take into account any other load which may affect window function. These loads include those resulting from variation of pressure on the window (due to normal operation, or possible faulty procedure), as well as all relevant effects of beam deposition such as thermal loading, cyclic mechanical shock due to very brief, high intensity beam pulsing, and material degradation from long term beam exposure." The Design Stress (DS) for vacuum windows at Fermilab has been set at half the Ultimate Tensile Stress (UTS).

The failure criterion therefore used in this report has been that the maximum combined Von Mises stress from pressure and beam effects, as derived from ANSYS simulations, should be less than half the UTS. This definition may, however, be conservative. Firstly, the membrane stress due to pressure can be made almost negligible by careful selection of window shape and thickness, as for all the cases studied in this report. This leaves the thermal stresses due to the passage of the pulsed proton beam as the dominant mode of stress. A thermal stress of this type is considered by the pressure vessel codes to be local and self-equilibrating. So the window may be more resistant to this type of stress and the codes allow thermal stresses of up to three times the design stress. The British Standard for pressure vessels BS5500 states that these types of stress may result in incremental distortion, rather than catastrophic failure.

However, the situation is made more complicated again by the pulsed nature of the beam as these thermal stresses may result in premature failure due to fatigue when subjected to stresses much lower than three times DS.

So, in conclusion, the limit of half the UTS for all combined stresses might well be conservative and the pressure vessel codes would suggest that it is. However, a determination of the ultimate design stress of the final window design must take into account an analysis of the fatigue life of the window as well as the likely degradation of material properties due to radiation damage.

7. Conclusions, Recommendations, Outstanding Issues

7.1 General comments

This study has made conclusions on all the technical goals of the Accord. This has covered beam powers of 0.7 MW and 2 - 2.3 MW for 60 GeV and 120 GeV proton beams, over a range of beam and target sizes, for a beam sigma in the range of 1.5 mm - 3.5 mm together with target diameters of 9 mm - 21 mm respectively. In terms of the analysis, all the phenomena identified have been successfully modelled, studied and summaries of the findings are listed at the end of each of the above sections for both 0.7 and 2 - 2.3 MW beam powers. The aim of this summary is to draw these conclusions together and identify suitable candidates for further study.

Beryllium and beryllium alloys are considered as the most likely alternative candidate target materials to the baseline graphite due to a significantly increased tolerance to radiation damage [1]. Pure beryllium gives a slightly higher Figure of Merit compared with other target materials and generates slightly lower thermal stresses. Since radiation damage effects are expected to be lower for a pure metal compared with an alloy, Structural Grade pure beryllium (S-65) is the recommended material.

Comparing the Figure of Merit for the given limits, the larger beam size and target reduces the FoM by up to 20% compared with the smaller beam size. However it is clear that as far as the engineering is concerned, in all cases a larger diameter target and beam spot size is preferred. Rather than make predictions of target lifetimes, this study has assessed the minimum target dimensions that can be permitted for the stresses to be within a Safety Factor of 1.5 against the yield stress.

The beam window conclusions are to be found at the end of Section 6.

7.2 Conclusions on Integrated Target and Horn

The interim report [2] suggested the combined target and horn may be an attractive option for 700 kW operation. Water spray cooling appears feasible for this beam power, although probably not for the higher beam powers. However, the completion of the study as presented in Section 5 has identified two further issues that are critical to the feasibility of such a design. These are:

1. The required target/inner conductor diameter is dominated by the cross-sectional area required to carry the longitudinal Lorentz force generated by the horn current pulse. As described in detail in Section 5, this leads to the requirement of a 21 mm diameter target regardless of beam power. This is considerably greater than would be required from the pulsed beam effects for the lower beam power and also a larger diameter than would be preferred from consideration of the Figure of Merit.

2. The longitudinal stress waves, particularly for an off-centre beam, limit operation at higher beam powers. While acceptable for a 21 mm diameter target operating at 700 kW, an increase in beam power would require an unacceptable increase in the target/inner conductor diameter.

Since an integrated target and horn design would be limited to 700 kW operation, and only then at the cost of a reduction in pion yield, it is suggested that this option is not investigated further.

7.3 Conclusions on Separate Target and Horn

This study indicates that a separate target supported within the bore of the first magnetic horn is preferred for any beryllium target for operation at up to 2 - 2.3 MW beam power. Two simple design concepts are proposed for both 700 kW and 2 MW cases, however since these were only considered in the later stages of this study, it has not been possible to develop either of these concepts into detailed designs. Although the two concepts are similar for both beam powers, forced convection air cooling is found to be sufficient for both at 700 kW, whereas helium and water cooling respectively are recommended for the 2 MW concepts.

The attractions of separating the target from the horn include:

- Optimisation of pion yield as a function of energy is possible since the target and horn dimensions and their relative positions can be separately optimised

- Structural independence from horn, meaning that (i) stresses are not combined and (ii) the risk of combined failure modes is reduced.

- Easy integration of target with horn, permitting the replacement of failed targets and re-use of horn, thereby minimising costs of target failures.

All target concepts subdivide the material along the length of the target. Due to the beam pulse length being significantly shorter than the longitudinal stress wave oscillation period, a longitudinally segmented target reduces the magnitude of the dominant longitudinal stress waves.

7.4 Target Concepts for 700 kW Beam Power:

Air-cooling is suggested as a possibility for targets operating at up to 700 kW beam power since:

- Air cooling fits well with the stated preference for the LBNE facility of an atmospheric pressure, air-cooled target station. At exit from the downstream end of the target, the heated air would enter the decay volume, or 'chase', where it would mix with the air cooling the inner wall of the chase.

- Absence of contained water avoids problems of stress waves being generated by interaction of secondary particles with the water.

- No additional active water or helium cooling circuit would be required.

However, serious consideration should be given to the safety aspects of operating beryllium at elevated temperatures in air. The suggested alternatives to the air cooled target options are the 2 – 2.3 MW helium or water cooled target designs outlined later.

Although neither of the options below have been subjected to detailed analysis for the 700 kW beam power case, inspection of the results that were generated for other cases leads one to anticipate that the smallest beam and target sizes investigated may be implemented, namely a beam sigma of 1.5 mm radius and a target diameter of 9 mm. Further investigation

is recommended before either concept could be selected for detailed design. The outline concepts are shown schematically below.

Outline Concept 1a (700 kW)

- Separate spherical or nearly spherical beryllium lumps supported by a triple-helix structure within a thin titanium alloy or beryllium tube.

- Direct, single pass air cooling of the lumps with the air passing inside the tube bore, with the flow directed around the separate pieces by the triple helix structure.
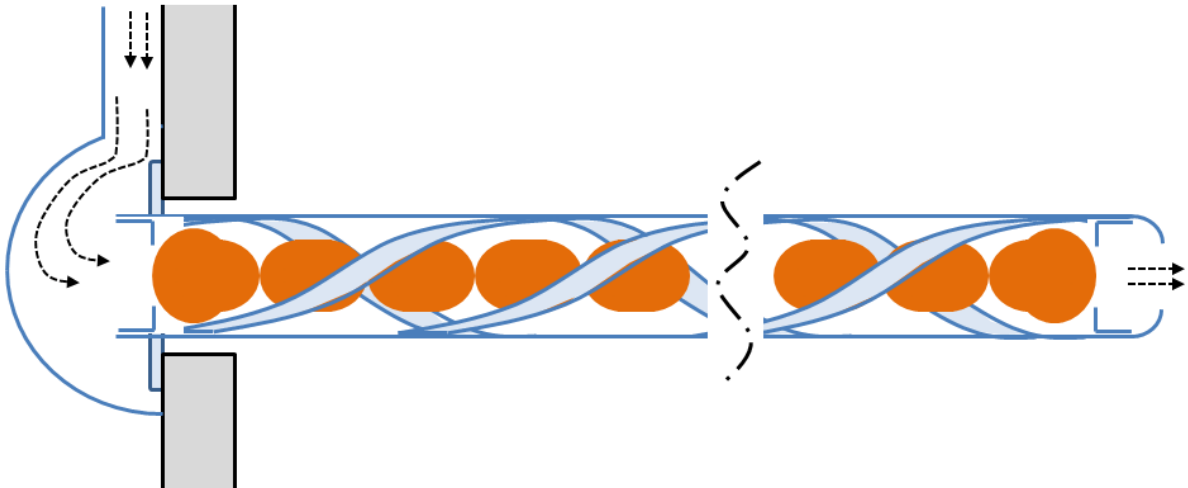

Figure 7.1. Concept 1a. Single pass helical flow air cooled sphere target design concept.

This geometry is naturally tolerant to an off-centre beam pulse since (i) the separate target pieces are naturally resistant to any beam misalignment and (ii) the target pieces are substantially independent of the external tube supports. The only deflection of the assembly may come from (i) secondary interactions with the target tube or (ii) from non-uniform air heating of the target tube.

The throttle profile suggested at the downstream end of the target tube in Figure 7.1 is intended to permit higher pressure gas flow, with a possible increase in permissible beam power. It also has the effect of enclosing the target pieces within the assembly.

This cooling configuration has neither been studied for air nor for the small (9 mm diameter) target, however the results obtained for helium cooling of a 13 mm diameter target operating at 2.3 MW indicate this is an attractive possibility.

Outline Concept 2a (700 kW)

- Cylindrical beryllium segments closely fitting so as to have good thermal contact with the inside bore of a beryllium or thin titanium alloy tube.

- Single-pass air cooling of the external surface of the tube, with the air passing between the annular space between the target and horn inner conductor.
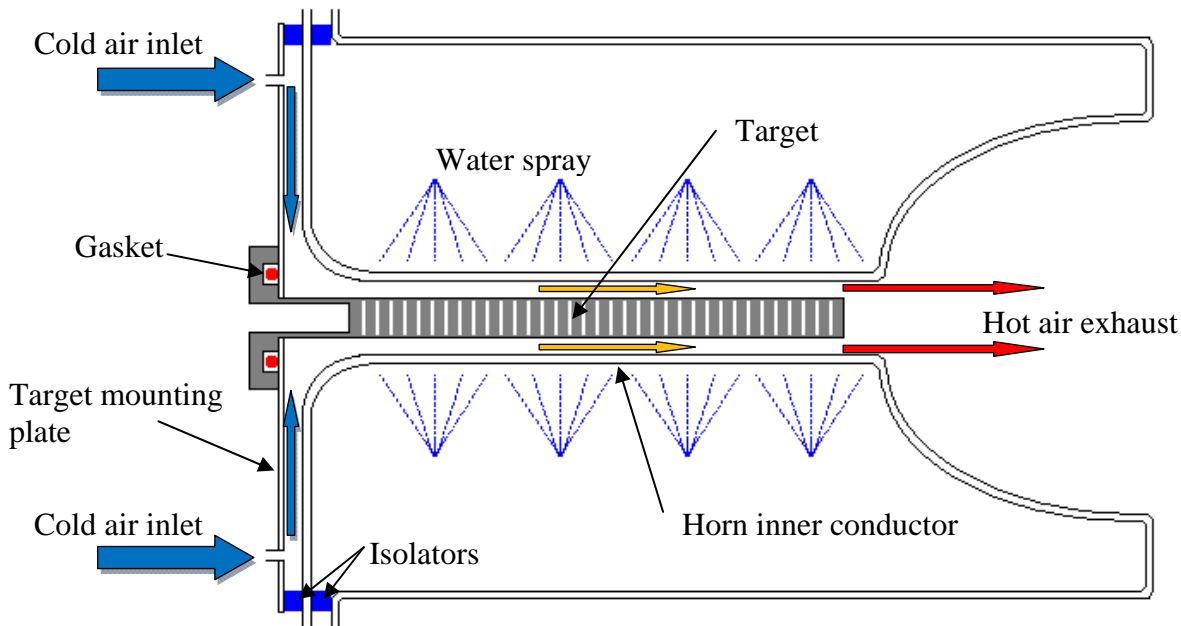
Figure 7.2. Concept 2a: Air cooled rod target

The study has not considered the thermal stresses or stress waves of this option for a 9 mm diameter target operating at 700 kW, and it can only be stated with certainty that the air cooling method itself is sufficient. However inspection of the combined results that were generated for an off-centre beam applied to continuous cylindrical and to spherical ball targets, together with the results from segmentation of a larger diameter cylinder operating at 2.3 MW indicates that this may be an attractive possibility.

7.5 Target Summary: 2 – 2.3 MW Beam Power

As for the 700 kW target, the most viable beryllium technology for operation at 2 – 2.3 MW is found to be a separate target supported within the horn bore. The design concepts proposed are similar to those for options 1 and 2 above, however with different layouts to permit different cooling methods. The dimensions are governed by the engineering requirements, namely the diameter needs to be larger than indicated by consideration of the pion yield alone in order to bring the stresses down to within allowable limits.

Outline Target Concept 1b (2 - 2.3 MW)

- Separate spherical or nearly spherical beryllium lumps supported by a triple-helix structure within a thin titanium alloy or beryllium tube, supported within an outer tube closed with end windows of the same material.

- Direct cooling of the beryllium lumps by passing pressurised helium inside the tube bore, with the flow directed around the separate pieces by the triple helix structure. Supply of helium achieved via the annular space between the inner and outer tubes.

This is similar to Concept 1a for the 700 kW target, however with a separate helium circuit operating at a nominal 10 bar pressure. This requires the external tube with beam windows at entry and exit to the target. A schematic layout of this concept is shown in Figure 7.3
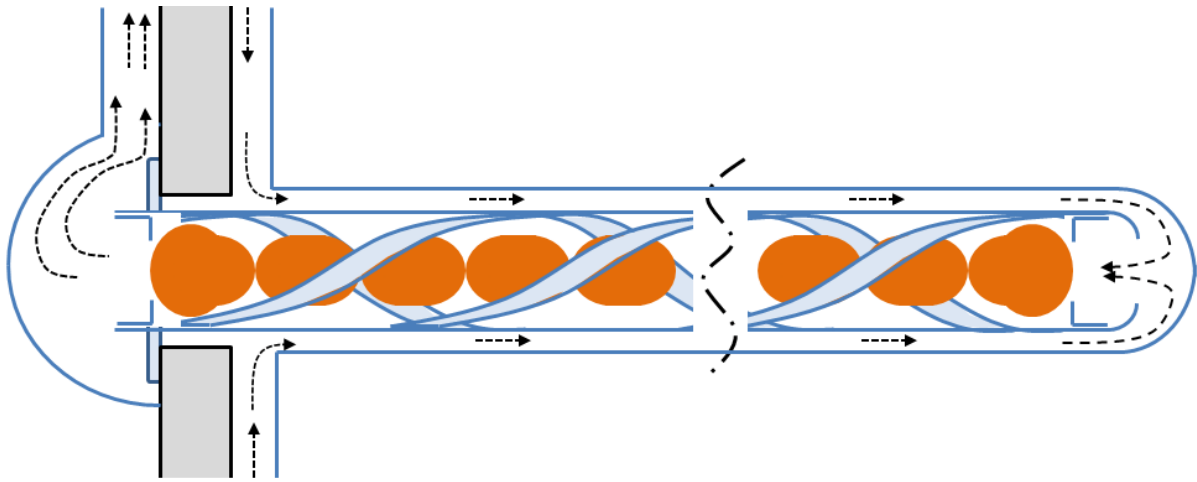
Figure 7.3 Concept 1b: Pressurised recirculating helical flow helium cooling of target spheres

CFD simulations have been performed demonstrating the feasibility of the kernel of this concept with the parameters shown in Table 7.1.

Table 7.1

Beryllium sphere diameter	13 mm
Beam sigma	2.2 mm
Helium mass flow rate	17 g/s
Inlet helium pressure	11.1 bar
Outlet helium pressure	10 bar
Inlet velocity	40 m/s
Maximum velocity	185 m/s
Total heat load	9.4 kW
Maximum beryllium temperature	178 C
Helium temperature rise, ΔT (T_{in}-T_{out})	106 C

Air Cooling

A single pass air cooling channel appears unrealistic for any target geometry similar to that proposed for the 700 kW target options. However, it may be possible to develop a feasible transverse flow design and so air cooling remains a possibility for a sphere-based target design.

Outline Target Concept 2b

- Short cylindrical beryllium segments inserted with an interference fit within the inside bore of a beryllium or thin titanium alloy cylindrical cooling jacket.

- Water cooled jacket with the water entrained with a sufficient void fraction of gas bubbles to minimise and mitigate the effects of secondary particle induced pressure waves [3].

The dimensions required for this target concept cannot be stated with confidence at the conclusion of this study, however indications are that a 21 mm diameter target may be possible. The longitudinal divisions are found to significantly reduce the magnitude of longitudinal stress resonances generated in a solid rod.

The separate short cylinders that comprise the target material are required to be a close fit with the inside bore of the water jacket so as to maintain a good thermal contact. The concept cooling jacket design consists of a single layer duct to minimise pion absorption. The duct is split into four channels to allow both inlet and outlet of the cooling water to be located at the upstream end of the target. The Beryllium core is sub divided into small cylinders. The cylinders have a raised ring of approximately 100 microns at one end to prevent face to face contact of the cylinders. The cylinders also have small vent channels to aid in the target assembly and to allow gases to escape from the target during operation.
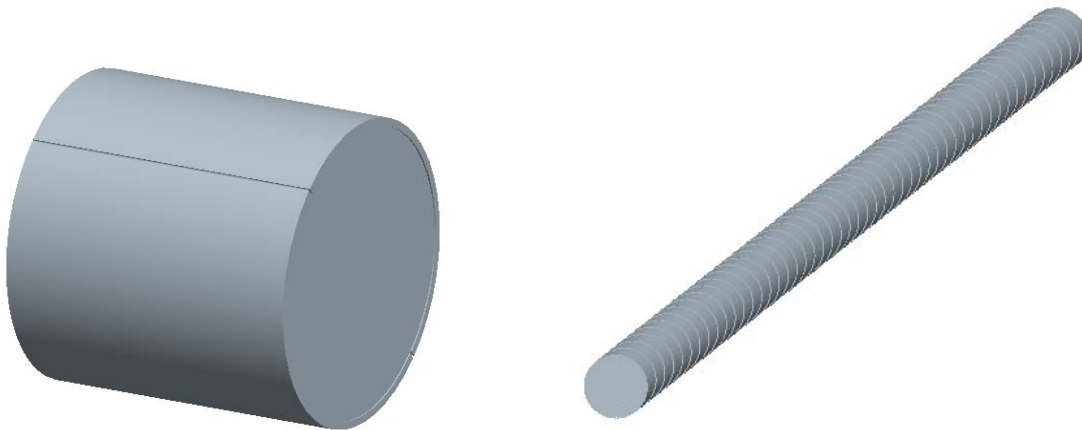

Figure 7.4 Concept 2b showing i) single target cylinder, ii) complete target stack

The Beryllium cylinders are installed into a tube with an interference fit. This tube is then machined down to a wall thickness around 0.5mm, but leaving four "fins" to hold the outer tube concentric and to act as flow guides. The fins end before the downstream end of the target so the flow can return to the upstream end of the target (Figure 7.5).
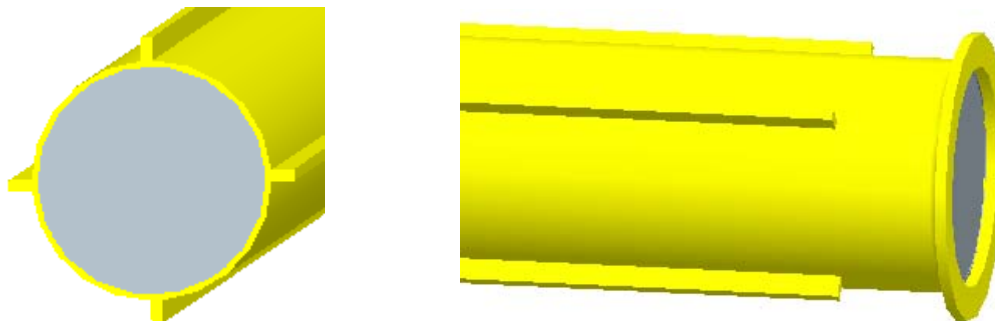

Figure 7.5 Concept 2b. Target inner tube with fins. a) upstream end, b) downstream end

This assembly is then inserted into a close fitting outer tube. The inner and outer tubes are sealed at the downstream end by welding. This forms a single duct around the target which is

divided into four channels which connect at the downstream end. Two opposite channels are used for cooling water inlet and the other two are for water outlet (Figure 7.6). Figure 7.7 shows a cross section of the complete target design.
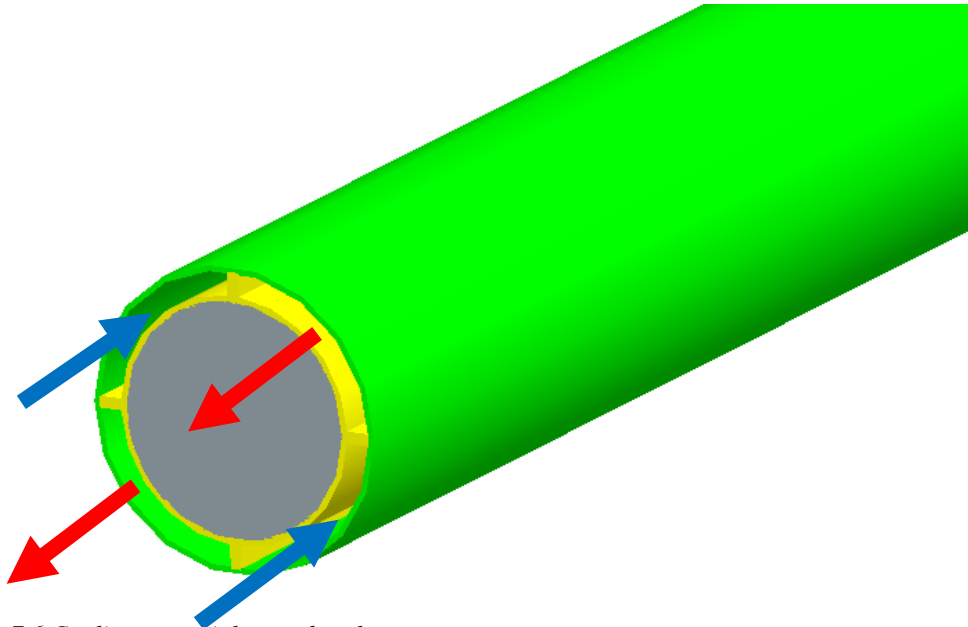

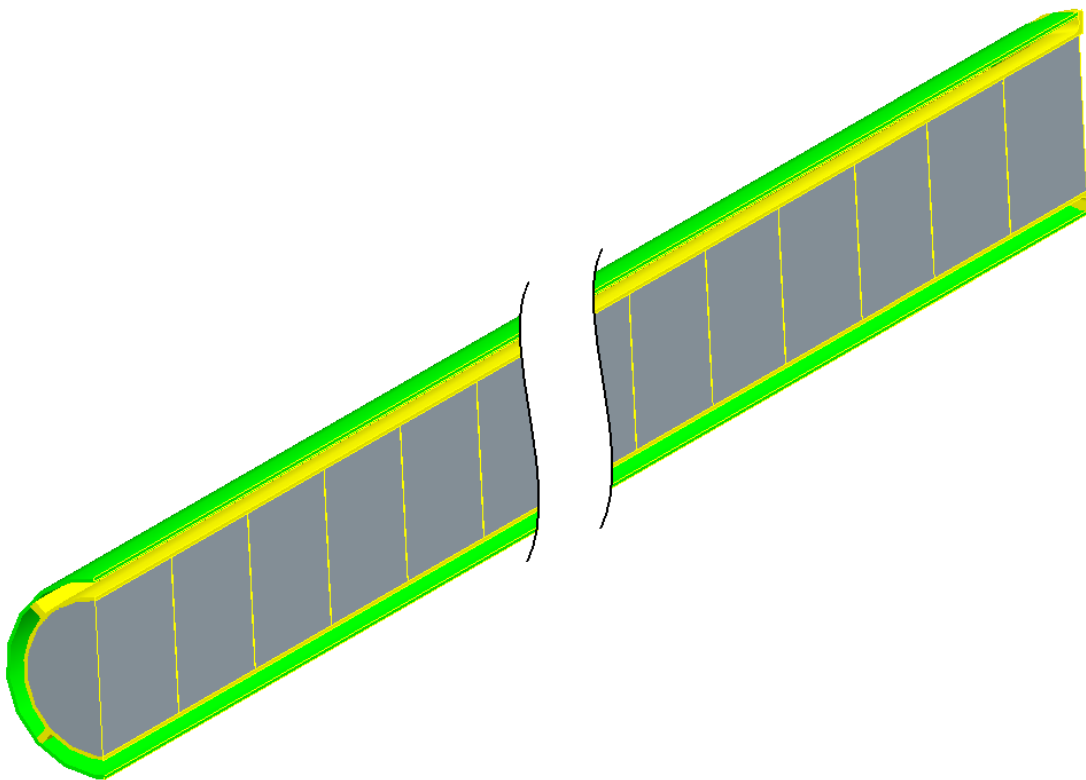*Figure 7.6 Cooling water inlets and outlets.*

Figure 7.7 Cross sectional view of target assembly.

Gas Cooling

Helium cooling via a double annular flow duct is also a viable method of cooling the outer cylinder of this arrangement. However a considerably higher flow rate would be required in this configuration than for Concept 1b in order to generate sufficient heat transfer for the beryllium material to be maintained within reasonable temperature limits. Consequently helium cooling is not as attractive an option. This option is detailed in Section 4.

At these high heat loads, air cooling discharging at atmospheric pressure is not realistically viable for this configuration.

Summary of Relative merits of different target concepts and beam powers

Table 7.2 Summary of the different target concepts for different beam powers with a simple assessment of relative merits where 1 = good, 2 = fair or some issues identified, 3 = poor or significant further study required. Brackets indicates that this is not verified.

Issue	Description	700 kW concepts		2–2.3 MW concepts	
		1a	2a	1b	2b
		Rating			
Pion yield	Smallest beam spot and target sizes possible	1	(1)	2	3
	Absorption of the pions by the coolant / jacket.	1	1	1	2
	Further optimisation of pion yield as a function of energy is possible since the target and horn dimensions and their relative positions can be separately optimised.	1	1	1	1
Tolerance to beam induced stress waves	Longitudinal stress waves	1	2	1	2
	Lateral stress waves from off-centre beam	(1)	(2)	(1)	(2)
	Stress waves in coolant	1	1	1	3
Integration with horn	Structural independence from horn, meaning that (i) stresses are not combined and (ii) the risk of combined failure modes is reduced.	1	1	1	1
	Easy integration of target with horn, permitting the replacement of failed targets and re-use of horn, thereby minimising costs of target failures.	1	1	2	2
Integration with target station infrastructure	**Air-cooling** fits well with the stated preference for the LBNE facility of an atmospheric pressure, air-cooled target station.	1	1		
	Water cooling requires an extra cooling circuit but considerable experience exists at Fermilab				2
	Helium cooling would require new infrastructure and new expertise			3	

7.6 Outstanding issues

Due to the short but wide-ranging nature of this study, it has not been possible to develop any of the options to any level of detailed design. If a beryllium target is to be pursued then further work is recommended to investigate the practical implementation of all target options leading to a complete design. If it is preferred to avoid air cooling for 700 kW targets, then the 2 MW helium or water-cooled concepts could be optimised for the lower beam power. Below is a non-exhaustive list of outstanding design and analysis issues.

Beam window

1. Final selection of window material.

2. Determine the minimum beam spot size that can be tolerated for a selected window material allowing for plastic deformation, with a full assessment of the consequences of a miss-steered beam.

General target issues

1. Study to choose beryllium or titanium alloy as preferred target tube material, and beam window material where appropriate

2. Selection of preferred cooling method for 700 kW operation with decision on possible upgrade path to 2 MW

3. Analysis and design of target supports within horn bore if required

4. Detailed engineering of all components

5. Integration with magnetic horn including remote handling engineering

Specific 700 kW target issues

1. Concepts 1a and 2a: Study off-centre beam on target (separate spheres) and possible need for support from horn

2. Confirmation that 1.5 mm radius beam sigma is possible for Concepts 2a (segments within tube)

3. Study and possible mitigation of stress concentrations in target Concepts 2a (segments within tube)

4. For air-cooled targets, study fire and contamination risks. While solid beryllium does not burn easily in air, if radiation damage were to cause the target material were to break up into a powder, then this would burn easily. Oxidation of beryllium e.g. in a fire could cause toxic beryllium oxide dust to contaminate the target station, transported by the cooling medium. This may lead to a preference for helium or water cooled target.

Specific 2 - 2.3 MW target issues

1. Concept 1b: Design of helix support/inner tube

2. Concept 1b: Optimisation of helium flow and sphere/lump profile to minimise helium pressure while maintaining pressure drop within reasonable limits.

7.7 References

[1] 'Operating Experience With Meson Production Targets At TRIUMF', E.W. Blackmore, A. Dowling, R. Ruegg, M. Stenning, TRIUMF, Vancouver, BC, Canada, Proceedings of 2005 Particle Accelerator Conference, Knoxville, Tennessee.

[2] 'Conceptual Design Study of the LBNE Target and Beam Window', CJ Densham, O Caretta, TR Davenne, MD Fitton, P Loveridge, M Rooney (STFC Rutherford Appleton Laboratory), Interim report

[3] 'Acoustic attenuation, phase and group velocities in liquid-filled pipes: Theory, experiment, and examples of water and mercury', Kyungmin Baik, Jian Jiang, and Timothy G. Leighton, J. Acoust. Soc. Am, accepted 11 September 2010.